Femtosecond Real-Time Dynamics of Solvation:
Molecular Reactions in Clusters and Supercritical Fluids

Thesis by

Qianli Liu

In Partial Fulfillment of the Requirements

for the Degree of

Doctor of Philosophy

California Institute of Technology
Pasadena, California

1997

(Submitted August 12, 1996)

Acknowledgments

A great many people deserve to be acknowledged for their help during my graduate education. To all those, not mentioned specifically here, you have my deepest gratitude for your efforts. A number of people deserve a special mentioning and I would like to take this opportunity to express my appreciation.

First and foremost, I would like to thank my parents for their love and support, without which I would not have gotten as far as I have.

I owe special thanks to my advisor, Ahmed Zewail, for his support, encouragement, and friendship. His scientific insight and seemingly endless enthusiasm has led me through all these years of research work.

I would like to thank all past and present members of the Zewail group with whom I have worked through the years. Especially, I wish to thank Earl Potter, Juen-Kai Wang, Jennifer Herek, Soren Pedersen, Arnolf Materny, Chris Hyland, Chao-Zhi Wan, and Manish Gupta for their collaborations in some of the research projects. I also want to thank Martin Gruebele, Garith Robert, Christopher Lienau, Hua Guo and Spencer Baskin for their helpful discussions on various research subjects.

Finally, I owe my gratitude to Prof. Thomas Tombrello for supporting me in my first year at Caltech, and to Prof. Vincent McKoy for providing me with the access to necessary computing facilities.

Abstract

This thesis presents two distinct applications of femtosecond laser spectroscopy combined with molecular dynamics (MD) simulations. The first application is the study of the dissociation and geminate recombination dynamics of iodine in argon clusters. By using different size distributions of the clusters in a molecular beam, and tuning the central frequencies of the pump and probe beams, the dynamics over a wide range of energies, states and reaction coordinates have been resolved. A microscopic picture of solvation has been established. The MD simulations in this study have covered the femtosecond to picosecond time scales which are essential for characterizing the evolution of solvation and its equilibration in clusters. The second application is the study of vibrational energy and phase relaxation dynamics of iodine in the gas-to-liquid transition region of rare gases (He, Ne, and Ar). The pressure of the system has been continuously varied from 0 to 4000 bar, allowing the relaxation dynamics to be examined across a wide dynamic range. The usual near-linear density dependence has been found for the energy relaxation rate, while a striking non-linear behavior with density has been discovered for the dephasing rate. The MD simulations in this study adopted both a classical model and a semi-classical model, and have reproduced the experimental observations. The novel density dependence of the dephasing rate is attributed to the combined influence of the solute-solvent forces and the vibration-rotation couplings which have opposite trends with density in the intermediate and high density regimes.

Table of Contents

Chapter 1

Introduction

The advent of femtosecond lasers has made it possible to resolve microscopic processes on atomic time scales. With temporal resolutions on the order of 10^{-14} to 10^{-13} seconds, molecular reactions can now be examined during the course of transition from reactants to products. Typically, an ultrafast laser pulse (pump) excites the reactants and prepares a coherent wave packet along the reaction coordinate. A second (or more) laser pulse (probe), delayed in time, then probes the transition state and the products. As the pump-probe delay time is varied consecutively, the dynamic process of reaction is captured in real time. The introduction of such pump-probe transition-state detection techniques to the study of chemical reaction dynamics has led to the exciting field of femtochemistry.[1]

Since its first application to the study of uni-molecular dissociation dynamics,[2] the femtosecond real-time detection technique has been applied to a wide variety of molecular systems (for reviews, see recent books by Zewail,[3] and by Manz and Wöste[4]). One particularly fruitful area of research is the study of solvation dynamics in dense media. Here the time scales of the solute-solvent couplings are typically on the order of 10^{-12} to 10^{-10} seconds), which is much shorter than the radiative lifetimes (~ 10^{-9} seconds). The random fluctuations of the solvent can quickly bury the spectroscopic characteristics of the reaction with a thermal distribution. It is, therefore, difficult to extract unique transition-state information from such solvated systems by traditional spectroscopic means. With femtosecond pulses, however, the solute molecule can be excited and probed on time scales shorter than that of the solvent fluctuations. The

nuclear wave packet motions of the solute can then be resolved and the gradual influence of the solvent can be monitored as the system evolves with time.

To study the solvation dynamics in a controlled manner, two types of solvent systems are particularly adequate, representing two different approaches. One is supercritical fluids; the other is molecular clusters. In the first approach, the pressure and, hence, the density of the solvent can be continuously varied from virtually zero to liquid-like values, allowing the degree of solvation to be a controllable variable.[5] Combined with femtosecond real-time techniques, the continuous variation of solvent densities can systematically link gas phase characteristics to condensed phase behaviors. In the second approach, the cluster systems offer an opportunity to examine solute-solvent interactions in a confined environment, potentially bridging the gap between isolated systems and the condensed phase in a different manner from the supercritical fluids. Molecular clusters have both microscopic and macroscopic properties which have been studied as a function of size and composition.[6-8] On the femtosecond time scale it should be possible to examine the elementary motions of reactions in these clusters and elucidate the effect of the solvent shells and compositions on the wave packet motion.[9]

In this thesis, the real-time techniques are applied to the study of reaction dynamics of iodine both in supercritical rare-gas fluids (He, Ne, and Ar) and in argon clusters. In the former, the focus is on the vibrational coherence (phase) and energy relaxation; in the latter, the focus is on the dynamics of dissociation and recombination. The molecular iodine is chosen in these studies for a number of reasons. The

femtosecond dynamics of I_2 have been studied in a gas cell, and in a molecular beam.[10-12] Also, the dynamics of the isolated molecules have been contrasted with those of high-pressure gases[13,14] and in clusters with one or few rare-gas atoms.[15,16] In addition, earlier studies have examined the process of caging at high pressures,[17] in liquids,[18-22] and in matrices.[23,24] The attractiveness of iodine as a solute lies in its simplicity as a diatomic molecule and in the characterization of its potential energy curves.[25-29]

For the supercritical system, the pressure of the rare gases is changed from 0 to 4000 atmospheres (bar). The coherence and population of a nuclear wave packet and their decay with time are directly examined as the system transitions from gas phase to a supercritical fluid with liquid-like densities. While the energy relaxation rate demonstrates a near-linear behavior with the density, the phase relaxation rate shows a striking non-linear density-dependence. For the cluster system, the average size of the clusters and the pump and probe wavelengths are varied, and the bond-breaking and bond-reforming dynamics are resolved across a broad dynamics range. A coherent caging is observed for the first time in neutral clusters, and is associated with the coherent dissociation and the rigid structure of large clusters.

Besides the experiments, a molecular dynamics (MD) simulation program has been developed and used to study the above systems computationally. Based on simple classical and semi-classical models, the simulation can reproduce the experimental observations and thereby provide an intuitive interpretation. It also offers an opportunity

to link theoretical concepts to experimental observations and provides insight into the microscopic processes that govern the reaction dynamics.

The MD simulation program is developed by myself. Most of the theoretical analysis, modeling, and computation is also carried out by myself. The experimental work presented in this thesis has been performed in collaboration with several coworkers; their contributions to the relevant projects are described wherever applicable..

Chapter two introduces vibrational dephasing theories, including previous theoretical models and a general approach. The formula developed in this chapter will be used in the MD simulations of the phase relaxation dynamics in supercritical rare-gas fluids.

Chapter three describes the MD simulations designed for the supercritical systems. The methodology, solvent structures and dynamics as well as a classical and a semi-classical models used for the dephasing dynamics are described in detail.

Chapter four presents the experimental studies of the coherence and energy relaxation dynamics of I_2 in supercritical rare gases. The combination of a femtosecond laser system with a high-pressure cell apparatus has allowed a direct measurement of dephasing and relaxation times, as the solvent density was varied from zero to liquid-like density. A striking density dependence of the dephasing rate was discovered. The MD simulation results are also described and compared with the experimental observations and with other theoretical predictions. The MD simulations have both reproduced the experimental observations and revealed the underlying microscopic picture of dephasing.

The novel phenomena observed experimentally was attributed to the combined influence of solute-solvent forces and vibration-rotation couplings which had opposite trend with density in a motion-narrowing regime. The experimental data presented here were mainly obtained by Dr. Chaozhi Wan. Mr. Chris Hyland and Mr. Manish Gupta have both contributed to this work during its early stage.

Chapter five presents the experimental studies of the dissociation and caging dynamics of I_2 in argon clusters. The molecular clusters were generated in a molecular beam and the average size of the clusters can be controlled by varying the backing pressure. Both direct dissociation (on the A state) and indirect pre-dissociation (on the B state) of iodine were studied as the pump wavelength was tuned. The bond-breaking time was found to be a key parameter in determining the time scale and behavior of the subsequent bond-reforming. In large clusters, following the direct dissociation, a coherent caging was observed and was attributed to both the coherent nature of the bond-breakage and the rigid structure of the cluster cage. The text of this chapter has been taken directly from a published paper.[30] This work was done through collaboration with Dr. Juen-Kai Wang, and was a continuation of an early project which was done through collaboration with Dr. Earl Potter.[31]

Chapter six presents the MD studies on the dissociation and caging dynamics of I_2 in argon clusters. This work is closely related to the one presented in the previous chapter. The simulation results presented in this chapter has provided support to the interpretation given in the previous chapter. The microscopic processes of bond breakage

and bond reformation have been visualized with the help of simple classical models. The effect of local structures, cluster sizes and temperature, bond distance and the excitation energies were also examined in the MD simulations. The text of this chapter has also been taken from a published paper.[32]

As evidenced by the brief summaries above, the combination of femtosecond real-time methods with MD simulations provides a powerful means to achieve in-depth understandings of molecular reaction dynamics and to reveal the underlying microscopic pictures. Not surprisingly, such approach is being applied to an even broader class of experiments now and will probably see continued applications in the years to come.

1.1 References

1 A. H. Zewail, in *Phys. Today*, Vol. 33 (1980), pp. 27.

2 M. Dantus, M. J. Rosker, and A. H. Zewail, *J. Chem. Phys.* **87,** 2395 (1987).

3 A. H. Zewail, *Femtochemistry: Ultrafast Dynamics of the Chemical Bond* (World Scientific, Singapore, 1994).

4 *Femtochemistry*, Vol. , edited by L. Manz and L. Woste (VCH Verlagsgellschaft mbH, Weinheim (Germany), 1995).

5 J. Jonas, *J. Chem. Soc. Faraday Trans. 2* **83,** 1777 (1987).

6 M. Kappes and S. Leutwyler, in *Atomic and Molecular Beam Methods*, edited by G. Scoles (Oxford University Press, New York, 1988), pp. 380.

7 J. Jortner, D. Scharf, N. Ben-Horin, U. Even, and U. Landman, in *Proceedings of the International School of Physics: The Chemical Physics of Atomic and Molecular Clusters*, edited by G. Scoles (North-Holland, New York, 1990), pp. 43.

8 R. S. Berry, in *Proceedings of the International School of Physics: The Chemical Physics of Atomic and Molecular Clusters*, edited by G. Scoles (North-Holland, New York, 1990), pp. 3.

9 A. H. Zewail, *Faraday Discuss. Chem. Soc.* **91,** 207 (1991).

10 R. M. Bowman, M. Dantus, and A. H. Zewail, *Chem. Phys. lett.* **161,** 297 (1989).

11 M. Dantus, M. H. M. Janssen, and A. H. Zewail, *Chem. Phys. Lett.* **181,** 281 (1991).

12 M. Gruebele and A. H. Zewail, *J. Chem. Phys.* **98,** 883 (1993).

13 Y. Yan, R. M. Whitnell, K. R. Wilson, and A. H. Zewail, *Chem. Phys. Lett.* **193,** 402 (1992).

14 A. H. Zewail, M. Dantus, R. M. Bowman, and A. Mokhtari, *J. Photochem. Photobiol.* **A 62,** 301 (1992).

15 J. J. Breen, D. M. Willberg, and A. H. Zewail, *J. Chem. Phys.* **93,** 9180 (1990).

16 D. M. Willberg, M. Gutmann, J. J. Breen, and A. H. Zewail, *J. Chem. Phys.* **96,** 198 (1992).

17 J. Schroeder and J. Troe, *Ann. Rev. Phys. Chem.* **38,** 163 (1987).

18 T. J. Chuang, G. W. Hoffman, and K. B. Eisenthal, *Chem. Phys. Lett.* **25,** 201 (1974).

19 D. J. Nesbitt and J. T. Hynes, *J. Chem. Phys.* **77,** 2130 (1982).

20 P. Bado, C. Pupuy, D. Magde, and K. Wilson, *J. Chem. Phys.* **80,** 5531 (1984).

21 A. L. Harris, J. K. Brown, and C. B. Harris, *Ann. Rev. Phys. Chem.* **39,** 341 (1988).

22 N. F. Scherer, L. D. Ziegler, and G. R. Fleming, *J. Chem. Phys.* **96,** 5544 (1992).

23 P. B. Beeken, E. A. Hanson, and G. W. Flynn, *J. Chem. Phys.* **78,** 5892 (1983).

24 M. Macler and M. C. Heaven, *Chem. Phys.* **151,** 219 (1991).

25 R. S. Mulliken, *J. Chem. Phys.* **55,** 288 (1971).

26 J. C. D. Brand and A. R. Hoy, *Appl. Spectry. Rev.* **23,** 285 (1987).

27 J. Tellinghuisen, *J. Chem. Phys.* **76,** 4736 (1982).

28 X. Zheng, S. Fei, M. C. Heaven, and J. Tellinghuisen, *J. Chem. Phys.* **96,** 4877 (1992).

29 X. Zheng, S. Fei, M. C. Heaven, and J. Tellinghuisen, *J. Mol. Spectry.* **149,** 399 (1991).

30 J.-K. Wang, Q. Liu, and A. H. Zewail, *J. Phys. Chem.* **99,** 11309 (1995).

31 E. D. Potter, Q. Liu, and A. H. Zewail, *Chem. Phys. Lett.* **200,** 605 (1992).

32 Q. Liu, J.-K. Wang, and A. H. Zewail, *J. Phys. Chem.* **99,** 11321 (1995).

Chapter 2

Theory of Vibrational Dephasing

2.1 Background

The microscopic process of molecular vibration can be observed macroscopically if the vibration is made coherent, i.e., if all the molecules vibrate in phase. This can be achieved experimentally by exciting a vibrational mode using femtosecond laser pulses. In time domain, the laser pulse initiates the vibrational motion momentarily for all molecules involved. In phase space, it prepares a coherent wave packet on the corresponding potential energy surface. Once generated, the coherence of the wave packet decays with time in solvent, as random fluctuations in the solute-solvent interactions gradually destroy the phase correlation. Fundamental to the solvation dynamics, the phase relaxation may serve as a sensitive probe of local structures and details of intermolecular potentials. The time scale of dephasing also establishes a time frame, within which the reaction dynamics can be made coherent.

In this chapter the origin of dephasing for a diatomic molecule embedded in dense solvents is considered. The focus is on the phase coherence and its decay by the so called pure dephasing process (T_2'). Since the energy relaxation process (T_1) is not included here, it is assumed that $T_2 = T_2'$ in this chapter. Later in Chapter 4 we consider both processes. There are two principle causes of dephasing: one is the external forces, directly associated with the random solute-solvent collisions, and the other is the vibration-rotation couplings. The former contribution to the dephasing rate can be estimated based on the independent binary collision model (IBC) in which the solute-solvent collisions are assumed to be binary and independent of one another.[1] Under this

assumption, the total phase spread (uncertainty) $\delta\phi$ is proportional to the product of the phase shift $\Delta\phi$ caused by one collision and the fluctuations in the collision number N, i.e.,

$$\delta\phi \sim \Delta\phi \cdot N^{1/2}. \tag{2.1}$$

The collision number N over time t is given by:

$$N = t \cdot \tau_{coll}^{-1}, \tag{2.2}$$

where τ_{coll}^{-1} is the collision rate. The dephasing time T_2 is estimated by equating the phase spread $\delta\phi$ to 2π, i.e.,

$$T_2 \approx 4\pi^2 \tau_c / (\Delta\phi)^2. \tag{2.3}$$

The dephasing rate is, therefore, given by

$$T_2^{-1} \approx \left[(\Delta\phi)^2 / 4\pi^2\right] \cdot \tau_{coll}^{-1}, \tag{2.4}$$

which is linearly proportional to the collision rate τ_{coll}^{-1}. According to the hard-sphere theory, the collision rate has a linear density behavior at low densities and becomes nonlinear at higher densities due to the increased role of the solvent volume (packing).

Based on the IBC theory and model potentials, analytical expressions for the dephasing rate can be derived rigorously. Assuming an anharmonic potential for the vibrational mode:

$$V_0(Q) = \frac{1}{2}\mu\omega_0^2 Q^2 + \frac{1}{6} f Q^3, \tag{2.5}$$

and an exponential function for the solute-solvent potential, Oxtoby obtained the following expression for the dephasing rate:[2]

$$T_{2;coll}^{-1} = \frac{\mu^* k_B T}{8\omega_0^2 L^2 \mu^2}\left(1-\frac{2fL}{\mu\omega_0^2}\right)^2 \tau_{coll}^{-1}. \tag{2.6}$$

In the above equations, Q is the vibrational coordinate of the oscillator, μ is the reduced mass of the solute, ω_0 is the unperturbed vibrational frequency, f is the cubic force constant, L is the range of the solute-solvent potential, μ^* is the reduced mass of the solvent relative to the solute, and τ_{coll}^{-1} is the collision rate. The linear dependence of the dephasing rate on the collision rate is also predicted by the hydrodynamic theory, in which a modified Langevin equation is solved for the vibration of a homo-nuclear molecule (anharmonic) in a viscous media.[3]

Schweizer and Chandler developed a theory of dephasing which takes into account both repulsive and attractive forces and vibration-rotation couplings. Using the general integral expression for the vibration correlation function (see below) and separating forces based on their time scales, they were able to obtain expressions for the dephasing rates induced by different forces. For the repulsive force in the motion narrowing regime, Schweizer and Chandler have obtained the following expression using a hard-sphere description:[4]

$$T_{2;R}^{-1} = \frac{\left[1-(r_e/2\bar{\sigma})^2\right]^2}{4\left[1+(r_e/2\bar{\sigma})\right]}\cdot\frac{3mk_BT}{16\omega_0^2L^2\mu^2}\cdot\left(1-\frac{2fL}{\mu\omega_0^2}\right)^2\tau_E^{-1}, \tag{2.7}$$

where m is the solvent mass, r_e is the equilibrium bond length of the diatomic molecule, τ_E^{-1} is the Enskog hard-sphere collision rate for a sphere of diameter σ_a at infinite dilution in a solvent of diameter σ_s, given by:

$$\tau_E^{-1} = \frac{8}{3}(\pi k_B T/2\mu_s)^{1/2} \rho \bar{\sigma}^2 g(\sigma_a, \sigma_s, \bar{\sigma}; \rho) \tag{2.8}$$

in which ρ is the number density of the solvent, $\mu_s = mM/(m+M)$ is the reduced mass of the solvent, $\bar{\sigma} = (\sigma_a + \sigma_s)/2$, and $g(\sigma_a, \sigma_s, \bar{\sigma}; \rho)$ is the contact value of the radial distribution function for a solute atom and the solvent, given by:[5]

$$g(\sigma_a, \sigma_s, \bar{\sigma}; \rho) = \frac{(1-\eta)\left[\frac{\sigma_a}{\bar{\sigma}}(1+2\eta) + \frac{\sigma_s}{\bar{\sigma}}(1-\eta)\right] + \eta^2\left(\frac{\sigma_a}{\bar{\sigma}}\right)^2}{2(1-\eta)^3} \tag{2.9}$$

where $\eta \equiv \pi\rho\sigma_s^3$ is the packing factor of the solvent. As $\rho \to 0$, $g(\sigma_a, \sigma_s, \bar{\sigma}; \rho) \to 1$, and $\tau_E^{-1} \to \frac{2}{3}\pi\bar{\sigma}^2\bar{v}_s\rho$, which is the collision rate for an ideal gas. According to both Eqs. (2.6) and (2.7), the dephasing rate induced by collision forces *increases with increasing density.*

In contrast, dephasing by vibration-rotation coupling has a very different behavior. The molecular rotation exerts a virtual force, the centrifugal force F_{VR}, along the vibrational coordinate. The solute-solvent collisions cause the angular momentum to change randomly. The corresponding force fluctuation ΔF_{VR} causes a momentary shift $\Delta\omega_{VR}$ to the vibrational frequency. The resulting phase shift is ~ $\Delta\omega_{VR} \cdot \tau_{VR}$, where τ_{VR} corresponds to the time duration of the force fluctuation. τ_{VR} is of the same order of

magnitude as the time interval between collisions, i.e. τ_{coll}.[4] The total phase spread is given by:

$$\delta\varphi \sim \Delta\omega_{VR} \cdot \tau_{coll} \cdot N^{1/2} = \Delta\omega_{VR} \cdot \tau_{coll}^{1/2} \cdot t^{1/2}. \tag{2.10}$$

As done previously for the IBC case, the dephasing rate is obtained by equating the total phase spread to 2π. Thus,

$$T_{2;VR}^{-1} \sim \left(\Delta\omega_{VR}/2\pi\right)^2 \cdot \tau_{coll}. \tag{2.11}$$

Analytical expressions for $T_{2;VR}^{-1}$ have been derived by Brueck[6] and Schweizer and Chandler[4] by considering the correlation functions of rotation. In the motion narrowing regime, for diatomic molecules with an anharmonic potential, the expression is as follows:[4]

$$T_{2;VR}^{-1} = \frac{\left(3k_BT\right)^2}{2\mu^2\omega_0^2 r_e^4}\left(1+\frac{fr_e}{3\mu\omega_0^2}\right)^2 \gamma\tau_E, \tag{2.12}$$

where again r_e is the equilibrium bond length of the diatomic molecule, τ_E is the molecular Enskog collision time, and γ is an adjustable parameter, which is on the order of one. The above equation predicts that the vibration-rotation coupling contribution to the dephasing rate *decreases with increasing density* in the motion narrowing regime.

Besides the collision force and vibration-rotation coupling, Schweizer and Chandler have also considered the contribution from the attractive force F_A. It is defined as the induction force caused by vibration-induced polarization and dipole moment fluctuations.[4] The relaxation time scale of F_A was assumed to be on the order of the solvent diffusion time over a molecular bond length, which is much longer than the time

scale of dephasing. Its contribution to the dephasing rate, $T_{2;A}^{-1}$, could, therefore, be evaluated using a slow modulation approximation. Their result indicated that $T_{2;A}^{-1}$ scaled with $(\rho\chi)^{1/2}$, where ρ is the solvent density and χ is the compressibility. It should be noted that F_A is different from the attractive part of the static solute-solvent potential, rather it is the change of the potential parameter due to the vibration of the solute. For the iodine-rare gas system under study, the static attractive force, which is reflected in the magnitude of the van der Waals binding energy, has been included in the MD simulations reported here; its contribution to the dephasing rates has been found to be negligible in comparison with that of the repulsive force.

In this study, the solvent density changes from low, gas-phase values to liquid-like values, causing the time scales and nature of relevant microscopic processes to vary over a wide dynamical range. Accordingly, the previous theoretical results can not be directly applied. Instead, general expressions will be derived in the following and will be used in the MD simulations to evaluate the corresponding dephasing rates and separate the influence of the different forces, as prescribed below.

2.2 General Theory

The coherence and dephasing characteristics of an oscillator is described by its vibration correlation function, $\langle Q(t)Q(0)\rangle$, where, Q is the coordinate of the I–I vibration and $\langle\cdots\rangle$ represents an ensemble average. Classically, $\langle Q(t)Q(0)\rangle$ can be evaluated by averaging the product $Q(t)\cdot Q(0)$ over all possible solvent configurations. Such direct classical calculations are generally not applicable to quantum systems of molecular vibrations, unless the condition $\hbar\omega << k_B T$ is satisfied. Here, $\hbar\omega$ represents the characteristic quantum energy of the vibrational mode, and $k_B T$ is the thermal energy of the system. For the I_2 vibration of the B state, we have $\hbar\omega$ ~ 100 cm^{-1} and $k_B T$ ~ 200 cm^{-1} (at room temperature). Classical approximation may, therefore, be applicable in this case. Generally, however, the vibration correlation function and, hence, the dephasing rate must be formulated on a quantum mechanical basis.

The equation of motion for a weakly perturbed oscillator[7] can be used to describe the solvated molecular vibration in the weak-coupling regime:

$$\dot{Q} = i[\omega_0 + \omega_1(t)]Q \tag{2.13}$$

where, Q is the coordinate along the normal mode of vibration, ω_0 is the un-perturbed vibrational frequency, and $\omega_1(t)$ is the instantaneous frequency shift induced by the solute-solvent forces. The time dependence of $\omega_1(t)$ arises from the classical bath dynamics of solvent molecules. The solution to Eq. (2.13) is given by:

$$Q(t) = Q(0)\exp(i\omega_0 t)\exp\left[i\int_0^t \omega_1(t')dt'\right]. \tag{2.14}$$

The vibration correlation function, normalized to the initial value $\langle Q^2 \rangle$, is given by:

$$\langle Q(t)Q(0)\rangle = \exp(i\omega_0 t)\left\langle \exp\left[i\int_0^t \omega_1(t')dt'\right]\right\rangle, \tag{2.15}$$

which is exact through second order in the vibration-bath interaction. The pointed bracket $\langle\cdots\rangle$ denotes an equilibrium ensemble average over the initial conditions associated with the bath coordinates. The second factor on the right-hand side of Eq. (2.15), i.e.,

$$\phi(t) \equiv \left\langle \exp\left[i\int_0^t \Delta\omega(t')dt'\right]\right\rangle, \tag{2.16}$$

characterizes the phase relaxation and frequency shift of the oscillator and is called the relaxation function of the oscillator.[7] By the fluctuation dissipation theorem, the resonance absorption spectrum at the frequency ω is given by

$$I(\omega-\omega_0) = \frac{1}{2\pi}\int_{-\infty}^{\infty} e^{-i(\omega-\omega_0)t}\phi(t)dt\,. \tag{2.17}$$

Evaluation of the relaxation function or the vibration correlation function is, therefore, essential to the resolution of the line shape or dephasing rate. According to a cumulant expansion theorem developed by Kubo,[7] the relaxation function can be expanded as

$$\left\langle \exp\left[i\int_0^t \omega_1(t')dt'\right]\right\rangle = \exp\left[\sum_{n=1}^{\infty}(i)^n\int_0^t dt_1\cdots\int_0^{t_{n-1}} dt_n\langle\omega_1(t_1)\cdots\omega_1(t_n)\rangle_C\right] \tag{2.18}$$

where $\langle\omega_1(t_1)\cdots\omega_1(t_n)\rangle_C$ is a cumulant average, and the first two orders are given by:

$$\langle\omega_1(t_1)\rangle_C = \langle\omega_1(t_1)\rangle \tag{2.19}$$

$$\langle\omega_1(t_1)\omega_1(t_2)\rangle_C = \langle\omega_1(t_1)\omega_1(t_2)\rangle - \langle\omega_1(t_1)\rangle\langle\omega_1(t_2)\rangle. \tag{2.20}$$

In the weak field limit, the cumulant expansion is truncated at the second order, i.e.,

$$\phi(t) = \exp\left[-\int_0^t dt_1 \int_0^{t_1} dt_2 \left\langle \omega_1(t_1)\omega_1(t_2)\right\rangle\right], \tag{2.21}$$

in cases where $\langle \omega_1(t)\rangle = 0$, i.e., the mean frequency shift is zero. If a stationary condition: $\langle \omega_1(t+\tau)\omega_1(t)\rangle = \langle \omega_1(\tau)\omega_1(0)\rangle$ is satisfied, then the double integral in Eq. (2.21) can be simplified as given in the following:

$$\int_0^t dt_1 \int_0^{t_1} dt_2 \left\langle \omega_1(t_1)\omega_1(t_2)\right\rangle \equiv \int_0^t d\tau \int_\tau^t dt_2 \left\langle \omega_1(\tau+t_2)\omega_1(t_2)\right\rangle \equiv \int_0^t d\tau (t-\tau)\left\langle \omega_1(\tau)\omega_1(0)\right\rangle, \tag{2.22}$$

where the first equality is obtained by changing variables, i.e., $(t_1, t_2) \rightarrow (\tau = t_1 - t_2, t_2)$, and the second equality is based on the stationary condition mentioned above. The relaxation function is then reduced to:

$$\phi(t) = \exp\left[-\int_0^t d\tau (t-\tau)\left\langle \omega_1(\tau)\omega_1(0)\right\rangle\right]. \tag{2.23}$$

In general, if $\langle \omega_1 \rangle \neq 0$, we can define a fluctuating frequency $\Delta\omega(t) = \omega_1(t) - \langle \omega_1(t)\rangle$ and, following similar procedures, obtain the following expression:

$$\phi(t) = \exp\left(i\langle \omega_1 \rangle t\right)\exp\left[-\int_0^t d\tau (t-\tau)\left\langle \Delta\omega(\tau)\Delta\omega(0)\right\rangle\right]. \tag{2.24}$$

The objective is now to transform from the frequency correlation function to the correlation functions of the acting forces. Two perturbation terms are considered here: one is the solute-solvent interaction potential $V_R(Q;\bar{r})$ where $\bar{r}$ represents the solvent coordinates; the other is the vibration-rotation coupling $V_{VR}(Q) \equiv J^2/2I(Q)$, where J is the

angular momentum and $I(Q) \equiv \mu \cdot r_{I-I}^2(Q) \equiv \mu(r_e + Q/2)^2$ is the moment of inertia of I_2. To a second order in Q, $V_R(Q;\vec{r})$ can be Taylor expanded to

$$V_R(Q;\vec{r}) = F_R Q + G_R Q^2, \tag{2.25}$$

where $F_R \equiv (\partial V_R/\partial Q)_0$ and $G_R \equiv (1/2)(\partial V_R^2/\partial Q^2)_0$ are functions of the bath coordinates $\vec{r}$ only, and represent the forces exerted by solvent molecules along the normal coordinate Q of the solute. Following Oxtoby,[2] F_R and G_R are related for an exponential potential of the solute-solvent interaction: $V_R(Q;\vec{r}) \propto \exp[-(r - Q/2)/L]$ where the Q dependence is now included to indicate the effective solute-solvent distance. Accordingly, $G_R = F_R/4L$, where L is the range of the repulsive force determined by the inter-molecular potential, and $V_R(Q;\vec{r})$ is given by

$$V_R(Q;\vec{r}) = F_R(Q + Q^2/4L). \tag{2.26}$$

The change of the moment of inertia during a molecular vibration will lead to an effective force, the centrifugal force F_{VR}. Similarly, as for the collision term of Eq. (2.26), the vibration-rotation coupling can be expanded to the second order in Q, i.e.,[4,8]

$$V_{VR} = F_{VR}(Q - 3Q^2/2r_e), \tag{2.27}$$

where,

$$F_{VR} = (\partial V_{VR}/\partial Q)_0 = 2E_{Rot}/r_e, \tag{2.28}$$

and r_e is the equilibrium distance between the two solute atoms. $E_{Rot} = J^2/2\mu r_e^2$ is the rotational energy of the solute. The general form of both collision and vibration-rotation couplings is then given by:

$$V(Q)=F\left(Q+\lambda Q^2\right), \tag{2.29}$$

where $\lambda=1/4L$ for the collision force and $\lambda=-3/2r_e$ for the vibration-rotation coupling.

The solute-solvent couplings will cause time-dependent energy shifts for the vibrational levels, given by the matrix element $V_{n,n}(t)$ for the nth vibration level. For a transition involving two adjacent vibrational levels, n and n - 1, the instantaneous frequency shift $\omega_1(t)$ induced by the coupling is then given by:

$$\omega_1(t)=\left(V_{n,n}(t)-V_{n-1,n-1}(t)\right)/\hbar=F(t)\left(Q_{n,n}-Q_{n-1,n-1}+\lambda\left(Q^2_{n,n}-Q^2_{n-1,n-1}\right)\right), \tag{2.30}$$

where the last equality is based on Eq. (2.29).

The task now is to evaluate the coupling matrix elements. For an anharmonic oscillator, described by Eq. (2.5), its eigenstates can be expanded in terms of the corresponding harmonic wave functions. To a first order in the cubic force constant f, the eigenstate of the nth level is given by:[9]

$$\begin{aligned}\left|\psi_n\right\rangle=&\left|\varphi_n\right\rangle-3\xi\left(\frac{n+1}{2}\right)^{3/2}\left|\varphi_{n+1}\right\rangle+3\xi\left(\frac{n}{2}\right)^{3/2}\left|\varphi_{n-1}\right\rangle\\&-\frac{\xi}{3}\left(\frac{(n+3)(n+2)(n+1)}{8}\right)^{1/2}\left|\varphi_{n+3}\right\rangle+\frac{\xi}{3}\left(\frac{n(n-1)(n-2)}{8}\right)^{1/2}\left|\varphi_{n-3}\right\rangle\end{aligned} \tag{2.31}$$

where $\left|\varphi_n\right\rangle$ is the wave function for the nth vibrational level of the corresponding harmonic oscillator, and the parameter ξ is given by

$$\xi = \frac{f}{6\hbar\omega_0}\left(\frac{\hbar}{\mu\omega_0}\right)^{3/2}. \tag{2.32}$$

According to Eq. (2.31), the coupling matrix elements are given by:

$$Q_{n,n} = -6\lambda\left[\left(\frac{n+1}{2}\right)^{3/2}\langle\varphi_{n+1}|Q|\varphi_n\rangle - \left(\frac{n}{2}\right)^{3/2}\langle\varphi_n|Q|\varphi_{n-1}\rangle\right] \equiv -\left(n+\frac{1}{2}\right)\frac{f\hbar}{2\mu^2\omega_0^3}, \tag{2.33}$$

and

$$Q_{n,n}^2 = \langle\varphi_n|Q^2|\varphi_n\rangle = \left(n+\frac{1}{2}\right)\frac{\hbar}{\mu\omega_0}. \tag{2.34}$$

Substituting Eqs. (2.33) and (2.34) into Eq. (2.30), one obtains the following expression for the instantaneous frequency shift:

$$\omega_1(t) = (\Delta z/\hbar)F(t), \tag{2.35}$$

where,

$$\Delta z = \frac{\lambda\hbar}{\mu\omega_0}\left(1 - \frac{f}{2\lambda\mu\omega_0^2}\right). \tag{2.36}$$

The frequency fluctuation $\Delta\omega(t)$ is given by

$$\Delta\omega(t) = \omega_1(t) - \langle\omega_1(t)\rangle = (\Delta z/\hbar)\Delta F(t), \tag{2.37}$$

where $\Delta F(t) \equiv F(t) - \langle F(t)\rangle$ is the force fluctuation, and $\langle\omega_1(t)\rangle$ is again the average frequency shift. The relaxation function is then given by

$$\phi(t) = \exp\left(i\langle\omega_1\rangle t\right)\exp\left[-(\Delta z/\hbar)^2\int_0^t d\tau(t-\tau)\langle\Delta F(\tau)\Delta F(0)\rangle\right], \tag{2.38}$$

which is now expressed in terms of the force correlation function (in contrast with Eq. (2.24) for the frequency correlation functions). Consequently, the time correlation

function of $\langle \Delta F(\tau)\Delta F(0)\rangle$ is the central element in the determination of the dephasing rate. Equation (2.38) can be further simplified in the two limiting regimes of *slow* and *fast* modulation of the forces:

A) Slow modulation:

One notices from Eq. (2.38) that the integral of the force correlation function can be carried out if $\langle \Delta F(\tau)\Delta F(0)\rangle$ is a constant of time. In this case, the decay of $\phi(t)$ will be governed by a Gaussian function. In general, the correlation function $\langle \Delta F(\tau)\Delta F(0)\rangle$ decays with time. Its correlation time τ_c, defined by

$$\tau_c \equiv \frac{1}{\langle (\Delta F)^2 \rangle}\int_0^\infty d\tau \langle \Delta F(\tau)\Delta F(0)\rangle, \tag{2.39}$$

characterizes the speed of the modulation and corresponds, generally, to the decay time of $\langle \Delta F(\tau)\Delta F(0)\rangle$. For example, if $\langle \Delta F(\tau)\Delta F(0)\rangle$ decays exponentially, i.e.,

$$\langle \Delta F(\tau)\Delta F(0)\rangle = \langle (\Delta F)^2 \rangle e^{-t/\tau_d}, \tag{2.40}$$

then it can be shown that $\tau_c = \tau_d$. The upper limit of the integral in Eq. (2.38) is on the order of the dephasing time T_2 of interest. In the limiting case where τ_c is much longer than T_2, $\langle \Delta F(\tau)\Delta F(0)\rangle$ can be approximated by its constant amplitude term $\langle (\Delta F)^2 \rangle$ for the whole range of the integral in Eq. (2.38), and the relaxation function takes again a Gaussian functional form given by:

$$\phi(t) \propto \exp\left[-(\Delta z/\hbar)^2 \langle (\Delta F)^2 \rangle t^2/2\right] \equiv e^{-t^2/2T_2^2}. \tag{2.41}$$

The dephasing rate is, therefore, given by

$$T_2^{-1} = (\Delta z/\hbar)\left\langle (\Delta F)^2 \right\rangle^{1/2} \equiv \left\langle (\Delta\omega)^2 \right\rangle^{1/2}. \tag{2.42}$$

The last equality was based on Eq. (2.37), and indicates that T_2^{-1} is governed by the amplitude of frequency fluctuation in the slow modulation limit.

In the slow modulation regime, the relaxation function $\phi(t)$ may be mainly represented by the Gaussian type function as given by Eq. (2.41). The line shape in this case is also Gaussian, i.e.,

$$I(\omega-\omega_0) = \frac{1}{\sqrt{2\pi}\left\langle (\Delta\omega)^2 \right\rangle^{1/2}} \exp\left[-\frac{(\omega-\omega_0)^2}{2\left\langle (\Delta\omega)^2 \right\rangle} \right] \tag{2.43}$$

where the line width is given by

$$\left\langle (\Delta\omega)^2 \right\rangle^{1/2} \equiv (\Delta q/\hbar)\left\langle (\Delta F)^2 \right\rangle^{1/2}, \tag{2.44}$$

which is equal to the amplitude of frequency fluctuations.

B) Fast Modulation:

On the other hand, if τ_c is much shorter than T_2, then $\langle \Delta F(\tau)\Delta F(0)\rangle \to 0$ for $\tau >> \tau_c$. Since the upper limit t of the integral in Eq. (2.38) is comparable to or longer than the dephasing time T_2 of interest, one obtains

$$\begin{aligned} \int_0^t d\tau (t-\tau)\langle \Delta F(\tau)\Delta F(0)\rangle &\approx \int_0^\infty d\tau (t-\tau)\langle \Delta F(\tau)\Delta F(0)\rangle \\ &\equiv t\int_0^\infty d\tau \langle \Delta F(\tau)\Delta F(0)\rangle - \int_0^\infty \tau d\tau \langle \Delta F(\tau)\Delta F(0)\rangle \end{aligned} \tag{2.45}$$

where the approximation $\int_t^\infty d\tau(t-\tau)\langle\Delta F(\tau)\Delta F(0)\rangle \approx 0$ is taken, and the second term is a constant independent of time t. The relaxation function is then represented by an exponential form:

$$\phi(t) \propto \exp\left[-(\Delta z/\hbar)^2 t\int_0^\infty d\tau\langle\Delta F(\tau)\Delta F(0)\rangle\right] \equiv e^{-t/T_2}. \tag{2.46}$$

The dephasing rate in this case is given by:

$$T_2^{-1} = (\Delta z/\hbar)^2\int_0^\infty d\tau\langle\Delta F(\tau)\Delta F(0)\rangle, \tag{2.47}$$

which, according to Eq. (2.39), is equivalent to the following expression:

$$T_2^{-1} = (\Delta z/\hbar)^2\langle(\Delta F)^2\rangle\tau_c \equiv \langle(\Delta\omega)^2\rangle\tau_c. \tag{2.48}$$

The last equality is based on Eq. (2.37).

In the fast modulation limit, the relaxation function $\phi(t)$ is mainly represented by a single exponential as given by Eq. (2.46). The line shape is Lorentzian

$$I(\omega-\omega_0) = \frac{1}{\pi}\frac{\gamma_e}{(\omega-\omega_0)^2+\gamma_e^2}. \tag{2.49}$$

The line width in this case is given by

$$\gamma_e \equiv \langle(\Delta\omega)^2\rangle\tau_c. \tag{2.50}$$

Since $\tau_c << T_2$, one obtains $\langle(\Delta\omega)^2\rangle\tau_c << \langle(\Delta\omega)^2\rangle T_2$, which leads to the relations:

$$T_2^{-1} << \langle(\Delta\omega)^2\rangle^{1/2}, \tag{2.51}$$

and

$$\gamma_e \equiv \langle(\Delta\omega)^2\rangle\tau_c << \langle(\Delta\omega)^2\rangle^{1/2}. \tag{2.52}$$

The dependence of the dephasing rate and line width on τ_c is distinctively different from the results in Eqs. (2.42) and (2.44), respectively, indicating the origin of the so called motion narrowing. The short time of τ_c has reduced the full range of modulation and thus reduced the T_2^{-1} and the line width.

The correlation time τ_R of $\langle \Delta F_R(\tau)\Delta F_R(0)\rangle$ corresponds to the time duration of the collision. As shown in the MD simulations, τ_R is much shorter than the correlation time τ_{VR} of $\langle \Delta F_{VR}(\tau)\Delta F_{VR}(0)\rangle$. Following Schweizer and Chandler,[4] we assume that the fluctuations in the inter-molecular forces and vibration-rotation couplings are uncorrelated, i.e.,

$$\langle \Delta F(\tau)\Delta F(0)\rangle \approx \langle \Delta F_R(\tau)\Delta F_R(0)\rangle + \langle \Delta F_{VR}(\tau)\Delta F_{VR}(0)\rangle. \tag{2.53}$$

Throughout the whole density range of interest, τ_R is also much shorter than T_2, so that Eq. (2.47) can be used to evaluate the dephasing rate induced by the collision forces, i.e.,

$$T_{2;R}^{-1} = (\Delta z/\hbar)^2 \int_0^\infty d\tau \langle \Delta F_R(\tau)\Delta F_R(0)\rangle, \tag{2.54}$$

with now

$$\Delta z = \frac{\hbar}{4\mu\omega_0 L}\left(1 - \frac{2fL}{\mu\omega_0^2}\right). \tag{2.55}$$

In the above case for collision forces, τ_R is always much shorter than T_2. However, for τ_{VR} the situation is different; it could be shorter or longer than T_2 depending on the density. At very low densities, τ_{VR} is longer than T_2, as shown in the MD simulations, so that the slow modulation approximation is applicable at these densities. At high

densities, however, τ_{VR} becomes shorter than T_2 and the fast modulation approximation becomes applicable. In general, the relaxation function is given by

$$\phi(t) = \exp\left[-4(\Delta z/\hbar r_e)^2 \int_0^t d\tau (t-\tau)\left\langle \Delta E_{Rot}(\tau)\Delta E_{Rot}(0)\right\rangle\right], \tag{2.56}$$

with now

$$\Delta z = \frac{3\hbar}{2\mu\omega_0 r_e}\left(1+\frac{f r_e}{3\mu\omega_0^2}\right) \tag{2.57}$$

and

$$\Delta E_{Rot}(t) = E_{Rot}(t) - \left\langle E_{Rot}(t)\right\rangle. \tag{2.58}$$

The dephasing time $T_{2;VR}$ is then determined from the decay time of the relaxation function.

2.3 References

1 S. F. Fischer and A. Laubereau, *Chem. Phys. Lett.* **35,** 6 (1975).

2 D. W. Oxtoby, *Adv. Chem. Phys.* **40,** 1 (1979).

3 D. W. Oxtoby, *J. Chem. Phys.* **70,** 2605 (1979).

4 K. S. Schweizer and D. Chandler, *J. Chem. Phys.* **76,** 2296 (1982).

5 S. Chapman and T. G. Cowling, *Mathematical Theory of Non-Uniform Gases* (Cambridge, Cambridge (England), 1970).

6 S. R. J. Brueck, *Chem. Phys. Lett.* **50,** 516 (1977).

7 R. Kubo, in *Fluctuations, Relaxation and Resonance in Magnetic Systems*, edited by D. t. Haar (Plenum, New York, 1962).

8 D. Levesque, J. J. Weis, and D. W. Oxtoby, *J. Chem. Phys.* **72,** 2744 (1980).

9 C. Cohen-Tannoudji, B. Diu, and F. Laloe, *Quantum Mechanics*, 2 ed. (Hermann, Paris, 1977).

Chapter 3

Molecular Dynamics Simulations

3.1 Methodology

In classical mechanics, the trajectory of a system is definite once the initial conditions and the interaction potentials are known. The trajectory, however, can not be analytically solved for systems with more than three particles. The difficulty lies in the fact that the interaction forces depend on the relative coordinates of all particles involved, the changes of which are in turn determined by the forces. This problem can be overcome numerically in MD simulations.

Considering only the translational motion for simplicity, the Hamilton's equations for a N-particle system ($N >> 1$) is given by:

$$\begin{cases} \dot{q}_{ij} = \partial H / \partial p_{ij} \\ \dot{p}_{ij} = -\partial H / \partial q_{ij} \end{cases} \quad (i = 1,2,\cdots,N; j = x,y,z), \tag{3.1}$$

where q_{ij} and p_{ij} are the ith particle's position and momentum respectively along the Cartesian coordinate j (x, y, or z). H is the Hamiltonian of the system, and is given by

$$H = \sum_{i=1}^{N} \sum_{j=x,y,z} \frac{p_{ij}^2}{2m_i} + V(q,p). \tag{3.2}$$

The potential function $V(q,p)$ generally depends on both the coordinates and momenta of all particles involved. For the system of interest, it will only depends on the relative coordinates of the particles. If one further assumes that the total potential is a sum over pair-wise interactions, and each pair-wise interaction is spherically symmetric, then $V(q,p)$ is reduced to the following form:

$$V = \sum_{i' \neq i} u_{ii'}(|\vec{q}_i - \vec{q}_{i'}|) \equiv \sum_{i' \neq i} u_{ii'}(r_{ii'}) \tag{3.3}$$

where $r_{ii'}$ is the distance between particle i and particle i', $u_{ii'}(r_{ii'})$ is their interaction potential. Combining Eqs. (3.1) to (3.3), at a given time t, the Newton's equations governing the motion of particle i are given by

$$\begin{cases} \dot{\bar{v}}_i(t) = \dfrac{1}{m_i}\sum_{i'\neq i} \nabla u_{ii'}(r_{ii'}(t)) \equiv \bar{a}_i(t) \\ \dot{\bar{q}}_i(t) = \bar{v}_i(t) \end{cases} \tag{3.4}$$

where $\bar{a}_i(t)$ is the acceleration of particle i at time t and can be evaluated according to the current positions of all particles. To first order, the velocity and position in a time step Δt is given by

$$\begin{cases} \bar{v}_i(t+\Delta t) = \bar{v}_i(t) + \bar{a}_i(t)\cdot\Delta t \\ \bar{q}_i(t+\Delta t) = \bar{q}_i(t) + \bar{v}_i(t)\cdot\Delta t \end{cases}. \tag{3.5}$$

Such calculation can be applied to all particles involved so that the acceleration at time $t+\Delta t$ can be evaluated. The time step Δt can be made small enough to ensure the accuracy of the calculation. The trajectory of the system is then obtained by iterating the above calculations for many time steps starting from a given set of initial positions and velocities.

In practice, Eq. (3.5) is not directly used for the integration because of its low convergence order (second order in time step). Numerous algorithms have been developed based on Eq. (3.4) to improve the accuracy and efficiency of the integration. For a review, see a recent book by Allen and Tildesley.[1] A simple yet efficient algorithm was proposed by Verlet,[2] as shown below

$$\bar{q}_i(t+\Delta t) = -\bar{q}_i(t-\Delta t) + 2\bar{q}_i(t) + \bar{a}_i(t)\cdot\Delta t^2 \tag{3.6}$$

which is correct except for errors of order Δt^4. The velocities do not appear in the above equation. The velocities are not needed to compute the trajectories, but they are useful for estimating various properties of the system, such as kinetic energy and velocity correlation function. Swope et al[3] modified the Verlet algorithm to include the velocities in the calculation as in the following:

$$\begin{cases} \vec{q}_i(t+\Delta t) = \vec{q}_i(t) + \vec{v}_i(t)\Delta t + \frac{1}{2}\vec{a}_i(t)\cdot\Delta t^2 \\ \vec{v}_i(t+\Delta t) = \vec{v}_i(t) + \frac{1}{2}\left[\vec{a}_i(t) + \vec{a}_i(t+\Delta t)\right]\Delta t \end{cases} \tag{3.7}$$

which is called "velocity Verlet" algorithm and is also accurate to the fourth order in Δt.

The Verlet and "velocity Verlet" algorithms are exactly reversible in time and, given conservative forces, are guaranteed to conserve momentum. They are numerically stable, convenient and simple and are particularly adequate for simulation of liquids or high pressure gases, where computation time is a major concern and relatively low accuracy is required.[1] If the pair-wise potential is represented by the Lennard-Jones function:

$$u_{ii'}(r_{ii'}) = 4\varepsilon_{ii'}\left[\left(\frac{\sigma_{ii'}}{r_{ii'}}\right)^{12} - \left(\frac{\sigma_{ii'}}{r_{ii'}}\right)^{6}\right] \tag{3.8}$$

then the numerically expensive square-root operations can be avoided in calculating the components of accelerations along a Cartesian coordinate:

$$a_{ij}(t) = \frac{1}{m_i}\sum_{i'\neq i} 24\varepsilon_{ii'}\frac{q_i - q_{i'}}{r_{ii'}^2}\left[2\left(\frac{\sigma_{ii'}}{r_{ii'}}\right)^{12} - \left(\frac{\sigma_{ii'}}{r_{ii'}}\right)^{6}\right] \tag{3.9}$$

which depends on the $r_{ii'}^2$ instead of $r_{ii'}$.

Classical trajectories depend on both the system Hamiltonian and the initial conditions, including initial positions and velocities of all particles involved. For the system of interest, molecular iodine is embedded in compressed rare gases. The initial positions and velocities must, therefore, represent a thermal distribution at room temperature and given density. Typically, the system is prepared in the following way:

First, all the atoms are randomly assigned to matrix sites. Two adjacent sites are assigned to I_2 — the molecule is treated as two individual atoms bonded by their potential well. The coordinates of the two iodine atoms are adjusted so that the I–I distance is equal to their ground state equilibrium value (2.67 Å). The total number of solvent atoms is determined by the density and the cell size used, as discussed below. The initial velocities are Monte Carlo sampled from a Maxwell distribution at room temperature (T_0 = 300 K).

Second, the system is allowed to relax by integrating the Hamilton's equations for a certain period of time (typically 10 ps). At the end of the relaxation, the average kinetic energy (equivalent to a temperature T) of the system is calculated.

Third, all velocities are scaled by a factor $\sqrt{T_0/T}$ and the system is allowed to relax again. The cycle will be repeated until the final temperature T is within 5% of the specified value, i.e., 300 K.

During the preparation, the two iodine atoms interact with each other according to the ground state, i.e., X state, potential. At the beginning of the simulation, the I–I potential is momentarily switched to the valence state, i.e., B state. In doing so, the potential energy of I_2 is set to be around the 8th vibrational level on the B state. The parallel component of the relative I–I velocity is set to be zero, while the perpendicular component remains unchanged.

The iodine X and B states, as well as the iodine-rare gas potentials are modeled by the following Morse function:

$$V(r) = D\left\{e^{-2\beta(r-r_e)} - 2e^{-\beta(r-r_e)}\right\} + E_\infty \tag{3.10}$$

where D is the binding energy, r_e is the equilibrium distance, r is the I–I distance, β characterizes the stiffness of the potential, and E_∞ is the asymptotic value of the potential energy when the two atoms are separated by a infinite distance. The solvent-solvent potentials are modeled by the Lennard-Jones functions given by Eq. (3.8). The parameters used for these potentials are listed in Table 1.

Since all the time correlation functions require ensemble averages, it is necessary to compute a large number of independent trajectories. The independence is achieved by using different sequences of random numbers in preparing the initial positions and velocities for each trajectory.

In the simulation, a finite number of atoms are used to represent the corresponding infinite physical system. A cubic cell of size L and with $N = L^3 \cdot \rho$ solvent atoms is

selected, where ρ is the given density. To avoid a surface effect near each face of the cell, a periodic boundary condition is used. The cubic cell is replicated throughout space to form an infinite lattice. In the course of the simulation, as a molecule moves in the original cell, its periodic image in each of the neighboring cells moves in exactly the same way. Thus, as a molecule leaves the central cell, one of its images will enter through the opposite face. There are no walls at the boundary of the central cell, and no surface molecules. During the simulation, it is only necessary to store the coordinates of molecules in the central cell. All the images can be produced by a translational transform:

$$(x,y,z) \leftrightarrow (x+i\cdot L, y+j\cdot L, z+k\cdot L);\ i,j,k = 0,\pm 1,\pm 2,\cdots \tag{3.11}$$

For efficiency, the potentials are cut off at half the size of the cell in evaluating the forces. To avoid serious cut-off errors,[1] the size of the cell is chosen to be $L \geq 6\sigma$, where σ is the range parameter for the Lennard-Jones potential.

It is important to notice the difference between a small, infinitely periodic system and the isotropic macroscopic system which it is designed to represent. The significance of the difference depends on the range of the intermolecular potential and the phenomenon under investigation. For a fluid of Lennard-Jones atoms, the particle is not able to "sense" the symmetry of the periodic lattice if the cell size is around or greater than 6σ as the potential scales with $(\sigma/r)^6$ at long distance, which is relatively short-ranged. The use of periodic boundary conditions inhibits the occurrence of long-wavelength fluctuations. For a cube of side L, the periodicity will suppress any density

waves with a wavelength greater than L. Pratt and Haan[4] have developed theoretical methods for investigating the effects of boundary conditions on equilibrium properties. For the relaxation dynamics under study, the time scale of interest is on the order of 10 ps or less. The time scales for density fluctuations with wavelength greater than $L \sim 24\text{Å}$ are orders of magnitude longer. The influence of the lattice periodicity is, therefore, expected to be negligible.

3.2 Solvent Structure and Dynamics

3.2.1. Snapshots:

To help visualize the system under study, snapshots generated from the simulation are plotted in Fig. 1, Fig. 2 and Fig. 3 for He, Ne, and Ar systems, respectively. In these figures, the larger and darker spheres, which are visible at low densities, are iodine atoms. The lighter and smaller spheres are He, Ne, and Ar atoms. The centers of the spheres correspond to the coordinates obtained in the trajectory calculation. The sizes of iodine and solvent atoms are scaled to their van der Waals diameters (4.30 Å for I, 2.44 Å for He, 3.20 Å for Ne, and 3.82 Å for Ar).

3.2.2. Radial distribution function:

The radial distribution function $g(R)$ of rare gas atoms with respect to the iodine atom is calculated based on the snapshots obtained from the trajectories. Such distributions, normalized by R^{-2}, are plotted in Fig. 3, Fig. 4 and Fig. 5 for He, Ne, and Ar, respectively. The function quickly drops to zero at short distances in these figures indicating the finite sizes of the atoms and the steep repulsive forces among them at close contact.

At long distance, $g(R)$ is almost constant for helium at pressures up to 600 bar (see Fig. 4). At high pressures, a peak near 3.5 Å appears, which is followed by a valley at 4.75 Å and a second peak at 6.0 Å. These two peaks represent the first two packing shells. Their very existence indicative of a short-range correlation among solvent atoms.[5] For neon, the peaks are visible even at 100 bar. The fist peak is near 4.2 Å, valley near

5.25 Å, and the second peak near 6.75 Å. For argon, the first peak, prominent even at very low pressures (50 bar), is located near 3.8 Å. The second peak is at 7.0 Å. At pressures near and above 600 bar, a third peak appears which is located at 10 Å. At 3200 bar, the radial distribution appears almost identical to the one obtained for liquid argon at 94.4 K.[5] Notice that the density at this pressure is the same as that of liquid argon, i.e., 1.374 g/cm^3 or 20.7 atoms/nm^3.[6]

3.2.3. Velocity correlation function and collision rate:

The auto-correlation function of solvent velocity, $\langle \bar{v}(t) \cdot \bar{v}(0) \rangle$, characterizes the dynamical properties of the solvent. It has been calculated by averaging the dot product $\bar{v}(t) \cdot \bar{v}(0)$ over all the solvent atoms in the box and more than 10^5 snapshots. The results are shown in Fig. 7, Fig. 8, and Fig. 9 for He, Ne, and Ar, respectively. For He and Ne at low densities, $\langle \bar{v}(t) \cdot \bar{v}(0) \rangle$ can be fit by an exponential function at short times. At high densities, the correlation functions become non-exponential. For argon, $\langle \bar{v}(t) \cdot \bar{v}(0) \rangle$ can be described by a Gaussian function at short times. As shown in Fig. 9, the correlation function becomes negative near 0.2 ps at pressures higher than 1200 bar. For liquid argon at 94.4 K, a similar negative minimum around 0.33 ps has been reported.[5] The negative region that occurs at high densities is interpreted as the back scattering that occurs when a molecule collides with one of the neighboring molecules forming a cage around the central one.[7]

The decay of $\langle \bar{v}(t) \cdot \bar{v}(0) \rangle$ over time is mainly caused by random collisions among solvent atoms. If one assumes that an solvent particle loses its memory once it undergoes

a collision, then the decay time of $\langle \bar{v}(t) \cdot \bar{v}(0) \rangle$ will represent the time interval τ_{coll} between collisions. For simplicity, we assigned the time at which $\langle \bar{v}(t) \cdot \bar{v}(0) \rangle$ drops to one half its initial value to τ_{coll}; the inverse value was taken to be the collision rate τ_{coll}^{-1}. In Fig. 10 we have plotted the collision rates thus obtained for all three solvents. The behavior of the collision rates with density is similar for He and Ne. Both show a near-linear increase at low densities and a non-linear increase at high densities. For argon, the behavior of so-defined collision rates is somewhat different. The rate increases drastically until reaching a saturate value at densities around 5 atoms/nm^3. This appears to be caused by the fact that at high densities argon tend to cluster around each other to form pseudo-stable van der Waals complexes. According to the simulation, some of these complexes can exist for longer than several picoseconds. The lines in Fig. 10 are polynomial fits to the simulated collision rates (see Table 2).

In Fig. 10, the corresponding Enskog hard-sphere collision rates are also plotted for comparison. The values shown were calculated based on the following equation derived in previous theoretical works (see Eq. (2.8) in Chapter 2 , or Ref. [8]):

$$\tau_E^{-1} = \frac{4}{3}\left(\pi k_B T/m\right)^{1/2} \rho\sigma^2 \frac{2-\pi\rho\sigma^3}{\left(1-\pi\rho\sigma^3\right)^3}. \qquad (3.12)$$

In the calculation, the hard sphere diameter was approximated by the Lennard-Jones σ parameter listed in Table 1. For helium and neon, the hard sphere collision rates are similar to the simulation results, particularly at low densities. For argon, however, the results differ significantly. This may indicate that the hard sphere assumption is not valid

for compressed argon gas because of the significant van der Waals attractions among argon atoms. It is also possible that the decay time of the velocity correlation function is no longer accurate measure of the collision time in this case.

3.2.4. Mean square displacement and diffusion coefficient:

The mean square displacement of solvent atoms, which undergo Brownian motions in a thermal system, is related to their diffusion coefficient D by the Einstein relation:

$$\left\langle x^2(t)\right\rangle \equiv \left\langle \left|\vec{r}(t)-\vec{r}(0)\right|^2 \right\rangle = 6Dt + C, \tag{3.13}$$

where $\left[\vec{r}(t)-\vec{r}(0)\right]$ is the displacement of an individual particle from time zero to time t. In the simulation, the mean square displacement is calculated by averaging the displacement square, $\left|\vec{r}(t)-\vec{r}(0)\right|^2$, over all solvent atoms and 512 trajectories. The results obtained are shown in Figs. 11, to 13 for the rare gases at several different pressures.

At high densities, the asymptotic linear behavior of $\left\langle x^2(t)\right\rangle$ with time is achieved in less than 1 ps. For low densities, however, the linear dependence occurs only after several picoseconds. Fitting the asymptotes of these curves to straight lines, numerical values of the diffusion coefficients are obtained. The results are plotted in Fig. 14. As density increases, the diffusion coefficient decreases rapidly.

3.3 Solvation Dynamics

3.3.1. Vibration correlation function

According to Ehrenfest's theorem,[9] a wave packet always moves like a classical particle insofar as the expectation values of its position and momentum are concerned. Moreover, a quantum system approaches the classical limit if its characteristic quantum energy, i.e., $\hbar\omega$, is small relative to the kinetic energy. For the iodine-rare-gas system under study, the thermal energy is about 208 cm^{-1} (300 K), which is much higher than the quantum energies of the translational (continuum) and the rotational modes. It is, therefore, fully justified to describe these modes classically. The quantum energy of the iodine vibrational mode is ~ 100 cm^{-1} which is about half the thermal energy. The iodine vibration may, therefore, be treated classically as well.

In the simulation, the vibration correlation function $\langle Q(t)Q(0)\rangle$ was directly evaluated by averaging the product $Q(t)\cdot Q(0) \equiv [R_{I-I}(t) - r_e]\cdot[R_{I-I}(0) - r_e]$ over 512 trajectories. Here $R_{I-I}(t)$ is I–I separation at time t and r_e = 3.03 Å is the equilibrium distance of I_2 (on B state). Some of the results are shown in Figs. 15 to 17 for the rare gases at several different pressures. These correlation functions indicate damped oscillations which are slightly asymmetric with respect to the equilibrium position because of the anharmonicity of the B state potential. To reduce the anharmonicity-induced dispersion effect, the initial vibrational energy of the iodine molecule is set to be the same for all the trajectories. The damping of the oscillation is, therefore, mainly caused by the dephasing process.

The envelope of the oscillation decay corresponds to the relaxation function introduced in Chapter 2. At low densities, the relaxation function is mainly composed of a Gaussian function, which indicates that a "slow modulation" channel dominates. At densities near or higher than the liquid values (20 atoms/nm^3), an exponential component becomes significant, indicating that a fast modulation channel becomes more important at higher densities. At intermediate densities, the relaxation function is a combination of Gaussian and exponential functions. The two channels will be attributed to two different types of dephasing process in the following discussion.

3.3.2. Correlation function of collision forces

The force correlation functions were calculated in the simulation based on the solute and the solvent positions and their model potentials. For the collision force F_R, introduced in the previous chapter, the time correlation function $\langle \Delta F_R(t) \Delta F_R(0) \rangle$ was calculated by averaging the product $\left[F_Q(t+t_k) - \overline{F}_Q(t+t_k)\right] \cdot \left[F_Q(t_k) - \overline{F}_Q(t_k)\right]$ over 512 trajectories and over 800 different t_k values. Here $F_Q(t)$ is the total solvent force projected along the I–I coordinate obtained by summing over all the pair-wise I-Rg forces at time t. $\overline{F}_Q(t)$ is the average value of $F_Q(t)$ among the 512 trajectories. The variable t_k was varied from 0 to 8 ps at the increment of 10 fs and was used for a temporal average of the product value. The time average is based on the ergodicity hypothesis and has been widely used in computation of correlation functions (see, for example, Ref. [10]). The correlation functions obtained are shown in Fig. 18, Fig. 19, and Fig. 20 for He, Ne, and Ar, respectively. These force correlation functions will be used to evaluate the collision

force induced dephasing rates, according to the equations derived in Chapter 2. The corresponding results will be detailed in the next chapter.

At short times, the force correlation function was fit by a Gaussian function

$$\langle \Delta F_R(t)\Delta F_R(0)\rangle = f(\rho)\exp\left(-\gamma_F^2 t^2\right). \tag{3.14}$$

The fitting results for the amplitude $f(\rho)$ and decay rate $\gamma_F(\rho)$ are plotted in Fig. 21. The lines are polynomial fit to $f(\rho)$ and linear fit to $\gamma_F(\rho)$, respectively. The fit parameters are listed in Table 3. The amplitude of $\langle \Delta F_R(t)\Delta F_R(0)\rangle$ increases rapidly and non-linearly with density across the whole density region of interest. The correlation time τ_R of $\langle \Delta F_R(t)\Delta F_R(0)\rangle$, which is the inverse of $\gamma_F(\rho)$, is, however, not sensitive to the change of solvent densities. For helium, $\gamma_F(\rho)$ slightly increases with the number density. For neon and argon, $\gamma_F(\rho)$ is virtually a constant over the whole density range of interest. This is consistent with the fact that τ_R represents the time it takes for atoms to remain in close contact. Within the density range of interest, we have $\tau_R \sim 0.1\,ps << T_2 \sim 1\,ps$, which justifies the "fast modulation" approximation to be used in evaluation of the dephasing rate.

At longer times, the force correlation function displays an oscillation about the zero level, the amplitude of which is greater at higher densities. The feature is also more significant for neon and argon than for helium. The period of the oscillation is identical to vibrational period of iodine on the B state. As the vibrational mode of iodine stretches, the two iodine nuclei extend further into the solvent bath. A stronger repulsion will be

imposed by the surrounding solvent. The direction of the force at this moment will be opposite to the motion of the vibration. As the vibrational mode contracts, the repulsive force will be reduced and the direction of the residue force becomes parallel to the motion of the contraction. The oscillatory feature is caused by this correlation of vibration to the solute-solvent forces.

At low densities, the solute-solvent collision is relatively independent of the solute vibration, because the stretching amplitude (about 0.2 Å) of the iodine molecule is negligible comparative to the average distance between solute and solvent. At higher densities, as the solvent atoms become closely packed around the iodine molecule, the local displacement of 0.2 Å will becomes more important. This explains why the oscillatory feature becomes more significant at higher densities.

3.3.3 Correlation function of vibration-rotation coupling:

The dephasing rate induced by the vibration-rotation coupling is related to the correlation function $\langle \Delta E_{rot}(t)\Delta E_{rot}(0)\rangle$ as shown in Chapter 2. In the simulation, it was calculated by averaging the product $\left[E_{rot}(t+t_k)-\overline{E}_{rot}(t+t_k)\right]\cdot\left[E_{rot}(t_k)-\overline{E}_{rot}(t_k)\right]$ over 512 trajectories and 800 t_k values. Here $E_{rot}(t)$ is the rotational energy of I_2 at time t, and $\overline{E}_{rot}(t)$ is the corresponding average value. Some of the correlation functions are shown in Figs. 22 to 24 for the rare gases at several different pressures. The amplitude $\left\langle (\Delta E_{rot})^2 \right\rangle$ and decay time τ_{VR} of the correlation function $\langle \Delta E_{rot}(t)\Delta E_{rot}(0)\rangle$ have also been obtained. $\left\langle (\Delta E_{rot})^2 \right\rangle$ was taken as the initial value of $\langle \Delta E_{rot}(t)\Delta E_{rot}(0)\rangle$, and τ_{VR} was

taken as the time at which $\langle \Delta E_{rot}(t)\Delta E_{rot}(0)\rangle$ dropped to half its initial value. The results for $\left\langle (\Delta E_{rot})^2 \right\rangle$ and τ_{VR} are plotted in Fig. 25 for all three solvents. The amplitude $\left\langle (\Delta E_{rot})^2 \right\rangle$ increases drastically with density until reaching a limiting value of about 40,000 cm^{-2} at densities around 5 atoms/nm^3, above which, it remains relatively constant. The correlation time τ_{VR}, on the other hand, decreases continuously with density across the whole range of interest. The limiting value of $\left\langle (\Delta E_{rot})^2 \right\rangle$ is expected as the maximum fluctuation in rotational energy is limited by the thermal energy of the system, i.e., $k_B T \approx 200\, cm^{-1}$. The decrease of τ_{VR} with density is consistent with the fact that it is related to the time interval between collisions.

3.3.4 Energy relaxation:

In the simulation, the iodine vibrational energy E_v, as a sum of the kinetic and the potential energies, was also monitored. In general, it decreases with time as a consequence of solvent-induced vibrational relaxation. Averaged over 512 trajectories, the behaviors of $E_v(t)$ with time are shown in Figs. 26 to 28 for He, Ne, and Ar, respectively. The decay of $E_v(t)$, which increases with density, represents the energy relaxation rate. The results will be discussed in Chapter 4 along with the experimental measurements.

3.4 Pressure to Density Conversion

It is worth noting that the relation between pressure and number density is no longer linear for the supercritical fluids at densities above certain values (~ 5 atoms/nm^3). For ease of discussion, the pressure-to-density conversion rates are plotted in Fig. 29, Fig. 30, and Fig. 31 for He, Ne, and Ar, respectively, based on data from previous works (see Refs. 11,.12, and 13).

3.5 References

1 M. P. Allen and D. J. Tildesley, *Computer Simulation of Liquids* (Oxford University Press, New York, 1992).

2 L. Verlet, *Phys. Rev.* **159,** 98 (1967).

3 W. C. Swope, H. C. Andersen, P. H. Berens, and K. R. Wilson, *J. Chem. Phys.* **76,** 637 (1982).

4 L. R. Pratt and S. W. Haan, *J. Chem. Phys.* **74,** 1864 (1981).

5 A. Rahman, *Phys. Rev.* **136,** A405 (1964).

6 J. Naghizadeh and S. A. Rice, *J. Chem. Phys.* **36,** 2710 (1962).

7 B. J. Alder, D. M. Gass, and T. E. Wainwright, *J. Chem. Phys.* **53,** 3813 (1970).

8 D. Chandler, *J. Chem. Phys.* **60,** 3504 (1974).

9 P. Ehrenfest, *Z. Physik* **45,** 455 (1927).

10 J. Chesnoy and J. J. Weis, *J. Chem. Phys.* **84,** 5378 (1986).

11 R. D. McCarthy, *J. Phys. Chem.* **R.2,** 923 (1973).

12 A. Michels, T. Wassenaar, and P. Louwerse, *Physica* **26,** 539 (1960).

13 R. B. Stewart and R. T. Jacobsen, *J. Phys. Chem. Ref. Data* **18,** 639 (1989).

14 G. C. Schatz, V. Buch, M. A. Ratner, and R. B. Gerber, *J. Chem. Phys.* **79,** 1808 (1983).

15 A. Garcia-Vela, P. Villarreal, and G. Delgado-Barrio, *J. Chem. Phys.* **94,** 7868 (1991).

16 Z. Li, A. Borrmann, and C. C. Martens, *J. Chem. Phys.* **97,** 7234 (1992).

17 D. J. Nesbitt and J. T. Hynes, *J. Chem. Phys.* **77,** 2130 (1982).

18 A. Garcia-Vela, P. Villarreal, and G. Delgado-Barrio, *J. Chem. Phys.* **92,** 6504 (1990).

19 F. G. Amar and B. J. Berne, *J. Phys. Chem.* **88,** 6720 (1984).

20 K. S. Schweizer and D. Chandler, *J. Chem. Phys.* **76,** 2296 (1982).

3.6 Tables

Table 1 Potential parameters used in the simulation

a) Morse Potentials

State/pair	D (cm^{-1})	r_e (Å)	β ($Å^{-1}$)	E_∞ (cm^{-1})	Reference
I-He	14.0	4.0	1.47	0	14
I-Ne	44.0	4.36	1.9	0	15
I-Ar	130.24	4.06	1.5	0	16
X	12547.2	2.67	1.91	0	17
B	4381.8	3.03	1.75	7605	17

b) Lennard-Jones Potentials

Pair	ε (cm^{-1})	σ (Å)	Reference
He-He	7.61	2.64	18
Ne-Ne	29.36	2.764	15
Ar-Ar	83.3	3.405	19

Table 2 Density dependence of collision rate - simulation result.

$$\tau_{coll}^{-1}(\rho) = C_0 + C_1\rho + C_2\rho^2 + C_3\rho^3$$

(ρ is in unit of nm^{-3})

Solvent	C_0 (ps^{-1})	C_1 ($ps^{-1}\cdot nm^3$)	C_2 ($ps^{-1}\cdot nm^6$)	C_3 ($ps^{-1}\cdot nm^9$)
He	-8.84×10^{-4}	0.333	-1.30×10^{-4}	1.67×10^{-4}
Ne	-1.07×10^{-2}	0.240	-8.11×10^{-3}	5.68×10^{-4}
Ar	-2.58	3.02	-0.236	6.02×10^{-3}

Table 3 Density dependence of $f(\rho)$ and $\gamma_F(\rho)$ - (MD).

a) $f(\rho) = f_0 + f_1\rho + f_2\rho^2 + f_3\rho^3 + f_4\rho^4$

(ρ is in unit of nm^{-3})

Solvent	f_0 ($cm^{-2}\text{Å}^{-2}$)	f_1 ($cm^{-2}\text{Å}^{-2}nm^3$)	f_2 ($cm^{-2}\text{Å}^{-2}nm^6$)	f_3 ($cm^{-2}\text{Å}^{-2}nm^9$)	f_4 ($cm^{-2}\text{Å}^{-2}nm^{12}$)
He	0.125	0.125	5.80×10^{-3}	0	0
Ne	-0.437	-0.704	-3.00×10^{-2}	1.15×10^{-3}	0
Ar	0.111	0.887	-3.05×10^{-2}	-5.93×10^{-3}	3.90×10^{-4}

b) $\gamma_F(\rho) = C_0 + C_1\rho$

(ρ is in unit of nm^{-3})

Solvent	$C_0(ps^{-1})$	$C_1(ps^{-1}\cdot nm^3)$
He	16.6	0.105
Ne	12.1	0.018
Ar	8.03	-0.019

3.7 Figure Captions and Figures

Fig. 1 Snapshots of the I_2-**helium** system at four different pressures as indicated in the figure. These snapshots are plotted in accordance to the positions calculated in the MD simulation. The coordinates are in the unit of Å.

Fig. 2 Snapshots of the I_2-**neon** system at four different pressures as indicated in the figure. These snapshots are plotted in accordance to the positions calculated in the MD simulation. The coordinates are in the unit of Å.

Fig. 3 Snapshots of the I_2-**argon** system at four different pressures as indicated in the figure. These snapshots are plotted in accordance to the positions calculated in the MD simulation. The coordinates are in the unit of Å.

Fig. 4 Normalized radial distribution functions of **helium** (arbitrary unit). The horizontal coordinate is the distance of solvent atoms to one of the iodine nuclei.

Fig. 5 Normalized radial distribution functions of **neon** (arbitrary unit). The horizontal coordinate is the distance of solvent atoms to one of the iodine nuclei.

Fig. 6 Normalized radial distribution functions of the **argon** (arbitrary unit). The horizontal coordinate is the distance of solvent atoms to one of the iodine nuclei.

Fig. 7 $\langle \bar{v}(t) \cdot \bar{v}(0) \rangle$ of **helium** (in the unit of $10^4\ m^2/s^2$), obtained by MD simulations at several different pressures, as indicated.

Fig. 8 $\langle \bar{v}(t) \cdot \bar{v}(0) \rangle$ of **neon** (in the unit of $10^4\ m^2/s^2$), obtained by MD simulations at several different pressures, as indicated.

Fig. 9 $\langle \bar{v}(t) \cdot \bar{v}(0) \rangle$ of **argon** (in the unit of $10^4\ m^2/s^2$), obtained by MD simulations at several different pressures, as indicated.

Fig. 10 Collision rates: a) MD simulation results, obtained from the calculated velocity correlation functions. b) Enskog hard sphere collision rates for He, Ne, and Ar calculated according to Eq. (3.12). [20]

Fig. 11 The mean square displacement $\langle x^2(t) \rangle$ of **helium** (in the unit of $\dot{A}^2$), obtained by MD simulations at several different pressures, as indicated.

Fig. 12 The mean square displacement $\langle x^2(t) \rangle$ of **neon** (in the unit of $\dot{A}^2$), obtained by MD simulations at several different pressures, as indicated.

Fig. 13 The mean square displacement $\langle x^2(t) \rangle$ of **argon** (in the unit of $\dot{A}^2$), obtained by MD simulations at several different pressures, as indicated.

Fig. 14 Diffusion coefficients (in the unit of $\dot{A}^2/fs$.) obtained by MD simulations for He (open circle), Ne (cross), and Ar (filled diamond).

Fig. 15 MD simulation results for $\langle Q(t)Q(0) \rangle$ (in the unit of $\dot{A}^2$), evaluated classically for iodine vibration in **helium**.

Fig. 16 MD simulation results for $\langle Q(t)Q(0) \rangle$ (in the unit of $\dot{A}^2$), evaluated classically for iodine vibration in **neon**.

Fig. 17 MD simulation results for $\langle Q(t)Q(0) \rangle$ (in the unit of $\dot{A}^2$), evaluated classically for iodine vibration in **argon**.

Fig. 18 $\langle \Delta F_R(t) \Delta F_R(0) \rangle$ for I_2 in **helium** (in the unit of $cm^{-2}/\dot{A}^2$), obtained by MD simulations at several pressures, as indicated.

Fig. 19 $\langle \Delta F_R(t) \Delta F_R(0) \rangle$ for I_2 in **neon** (in the unit of $cm^{-2}/\dot{A}^2$), obtained by MD simulations at several pressures, as indicated.

Fig. 20 $\langle \Delta F_R(t) \Delta F_R(0) \rangle$ for I_2 in **argon** (in the unit of $cm^{-2}/\dot{A}^2$), obtained by MD simulations at several pressures, as indicated.

Fig. 21 The behavior of: a) the amplitude and b) the correlation time of $\langle \Delta F_R(\tau) \Delta F_R(0) \rangle$ with density for He (open circle), Ne (open square), and Ar (filled circle) (see the text).

Fig. 22 $\langle \Delta E_{rot}(\tau)\Delta E_{rot}(0)\rangle$ for iodine in **helium** (in the unit of cm^{-2}). More than 10^5 snapshots were used for the ensemble average.

Fig. 23 $\langle \Delta E_{rot}(\tau)\Delta E_{rot}(0)\rangle$ for iodine in **neon** (in the unit of cm^{-2}). More than 10^5 snapshots were used for the ensemble average.

Fig. 24 $\langle \Delta E_{rot}(\tau)\Delta E_{rot}(0)\rangle$ for iodine in **argon** (in the unit of cm^{-2}). More than 10^5 snapshots were used for the ensemble average.

Fig. 25 The behavior of: a) the amplitude and b) the correlation time of $\langle \Delta E_{rot}(t)\Delta E_{rot}(0)\rangle$ with density for He, Ne, and Ar systems, as indicated.

Fig. 26 The behavior of iodine vibrational energy (in the unit of cm^{-1}) with time, obtained by MD simulations for iodine in solvent **helium**. The results were averaged over 512 trajectories. The zero energy corresponds to the B state minimum.

Fig. 27 The behavior of iodine vibrational energy (in the unit of cm^{-1}) with time, obtained by MD simulations for iodine in solvent **neon**. The results were averaged over 512 trajectories. The zero energy corresponds to the B state minimum.

Fig. 28 The behavior of iodine vibrational energy (in the unit of cm^{-1}) with time, obtained by MD simulation for iodine in solvent **argon**. The results were averaged over 512 trajectories. The zero energy corresponds to the B state minimum.

Fig. 29 Pressure to density conversion for compressed **helium** at room temperature. The plot was based on data taken from Ref. [11].

Fig. 30 Pressure to density conversion for compressed **neon** at room temperature. The plot was based on data taken from Ref. [12].

Fig. 31 Pressure to density conversion for compressed **argon** at room temperature. The plot was based on data taken from Ref. [13].

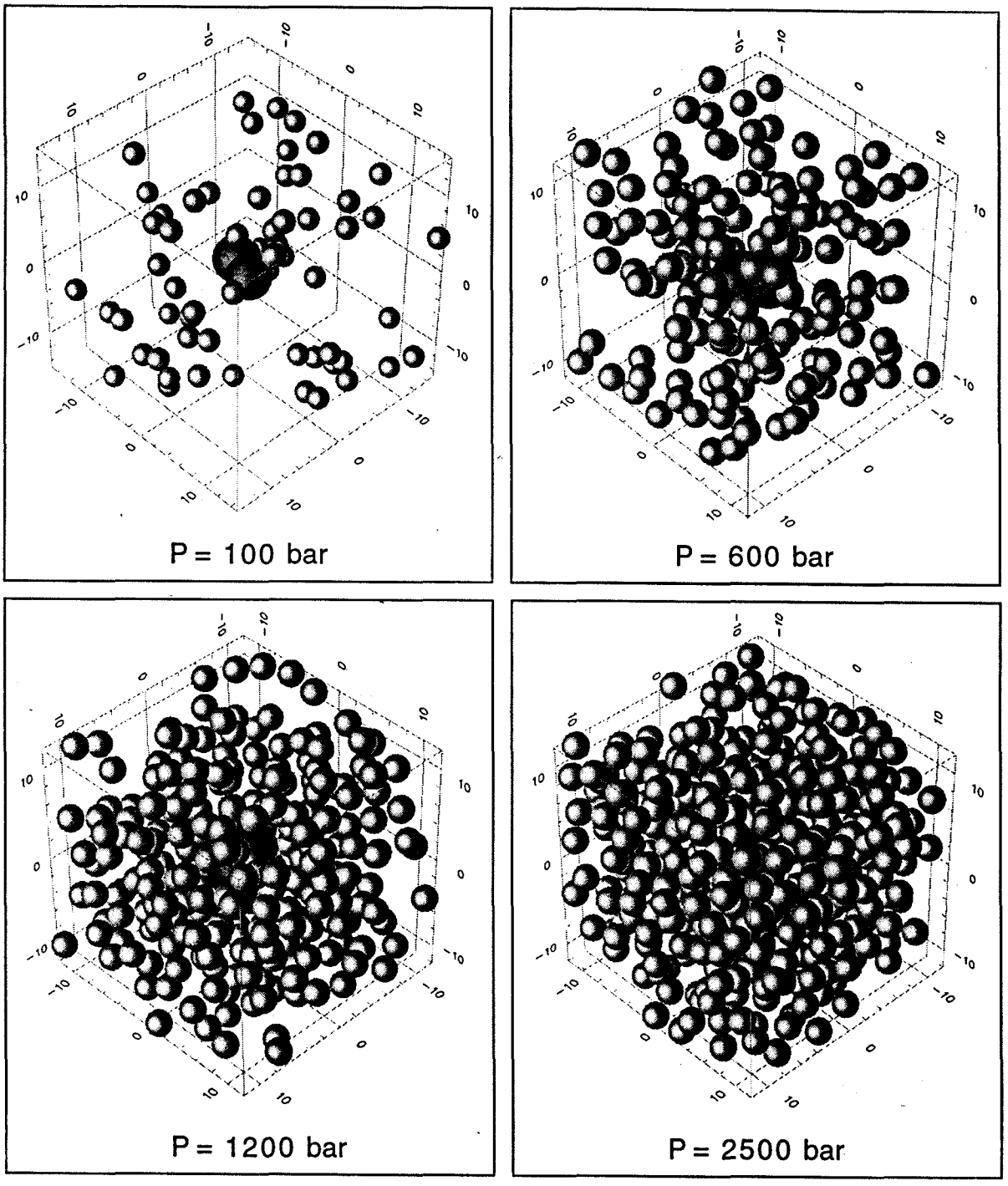

Figure 1

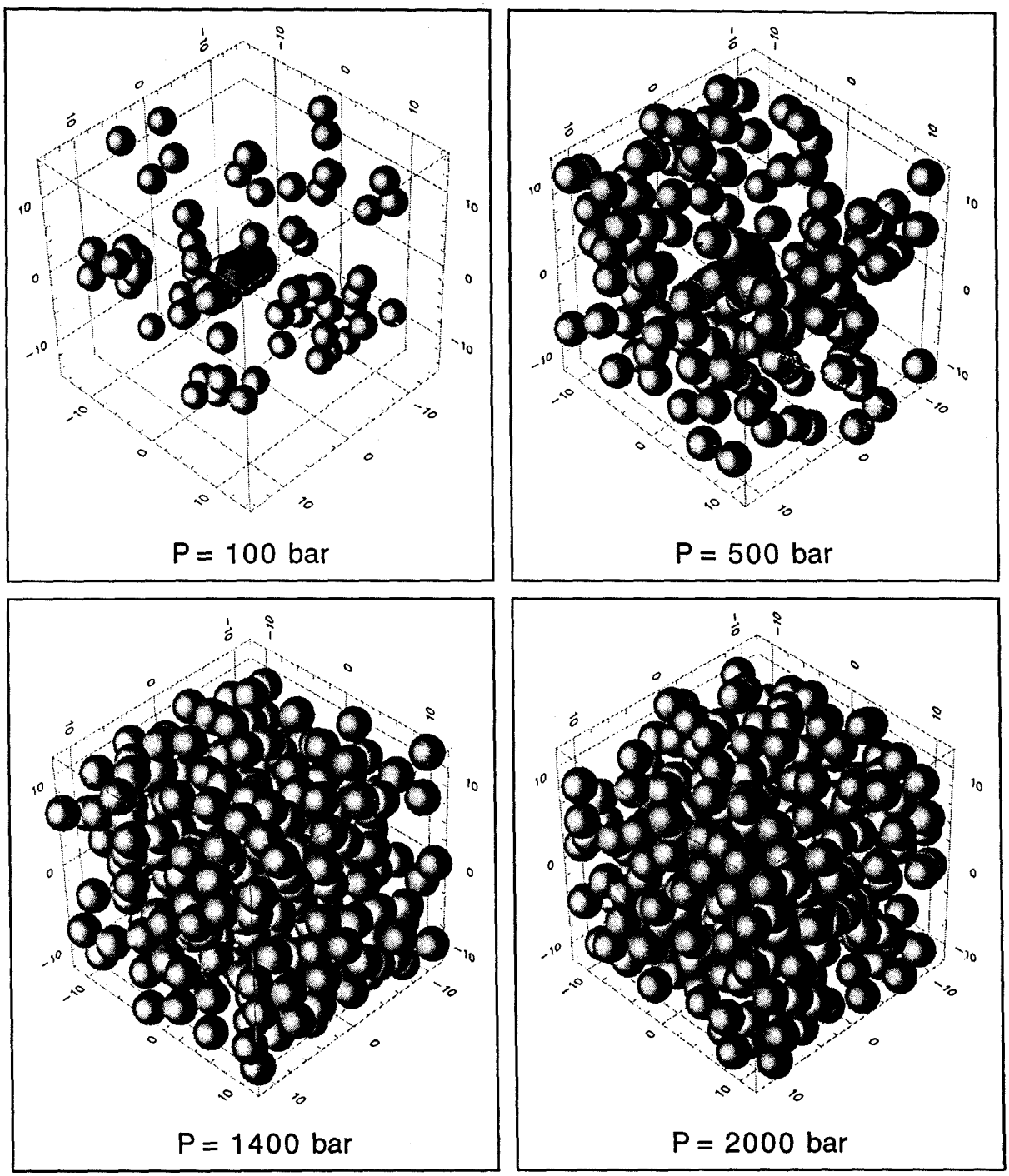

Figure 2

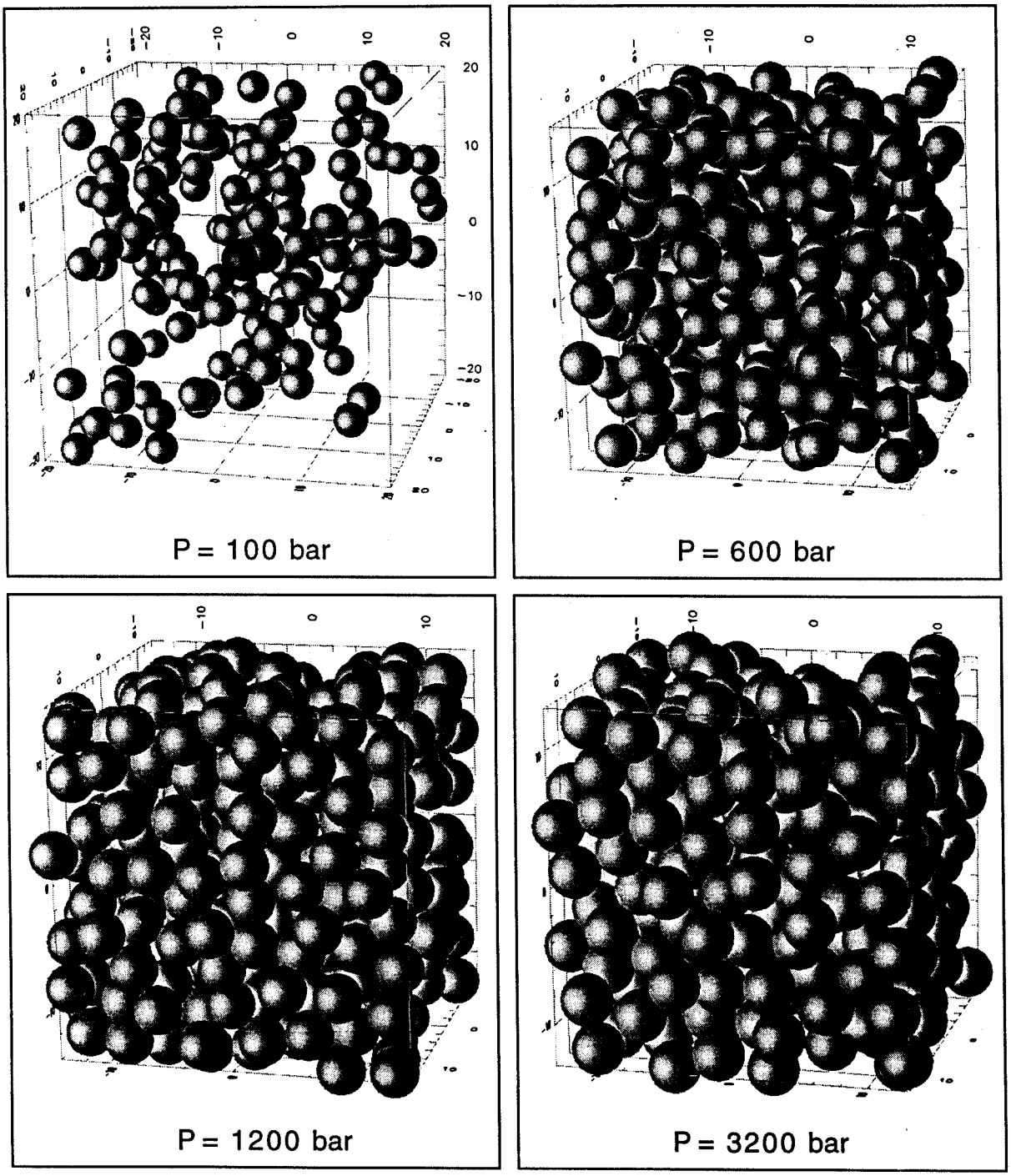

Figure 3

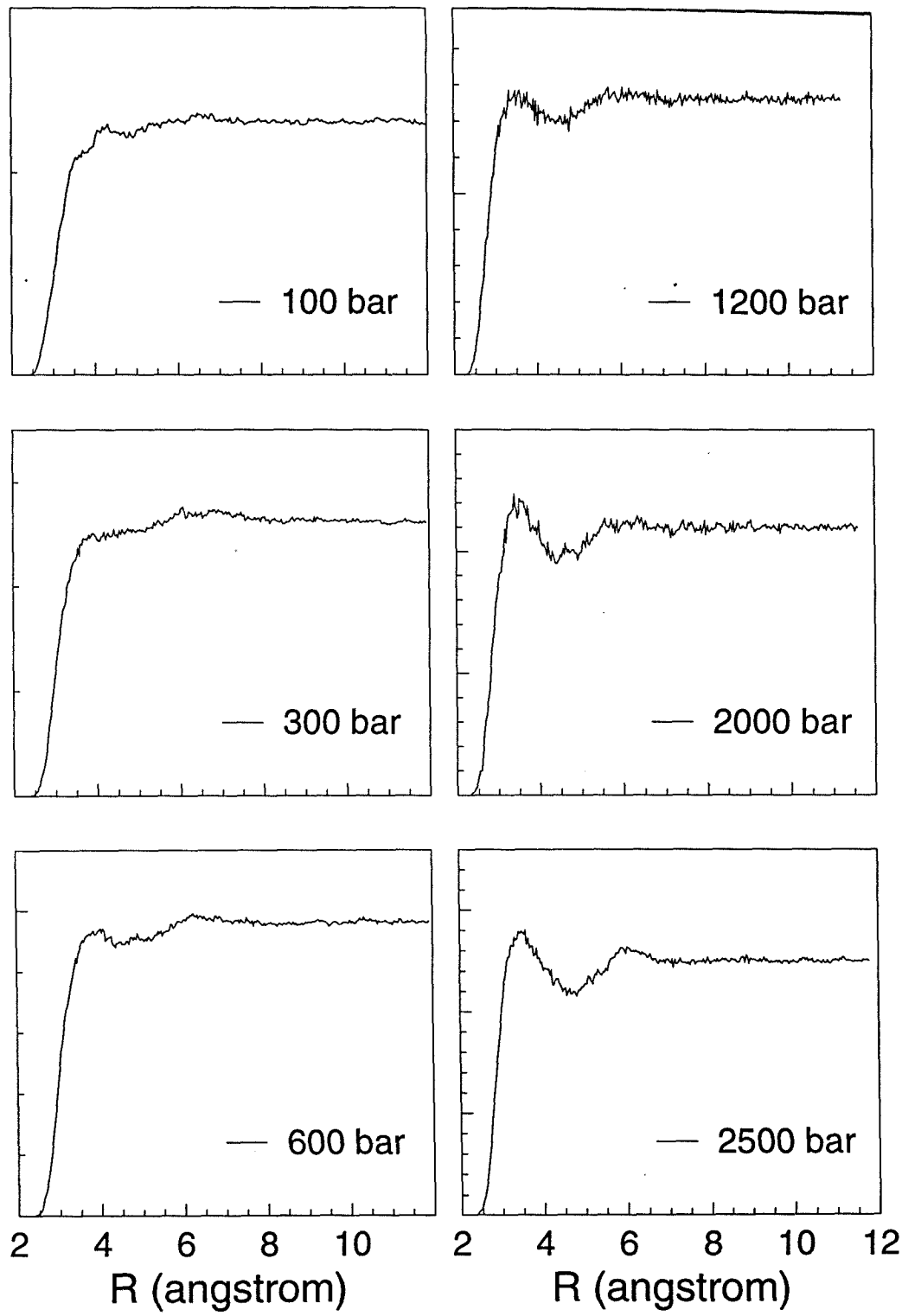
100 bar
1200 bar
300 bar
2000 bar
600 bar
2500 bar
2
4
6
8
10
R (angstrom)
2
4
6
8
10
12
R (angstrom)

Figure 4

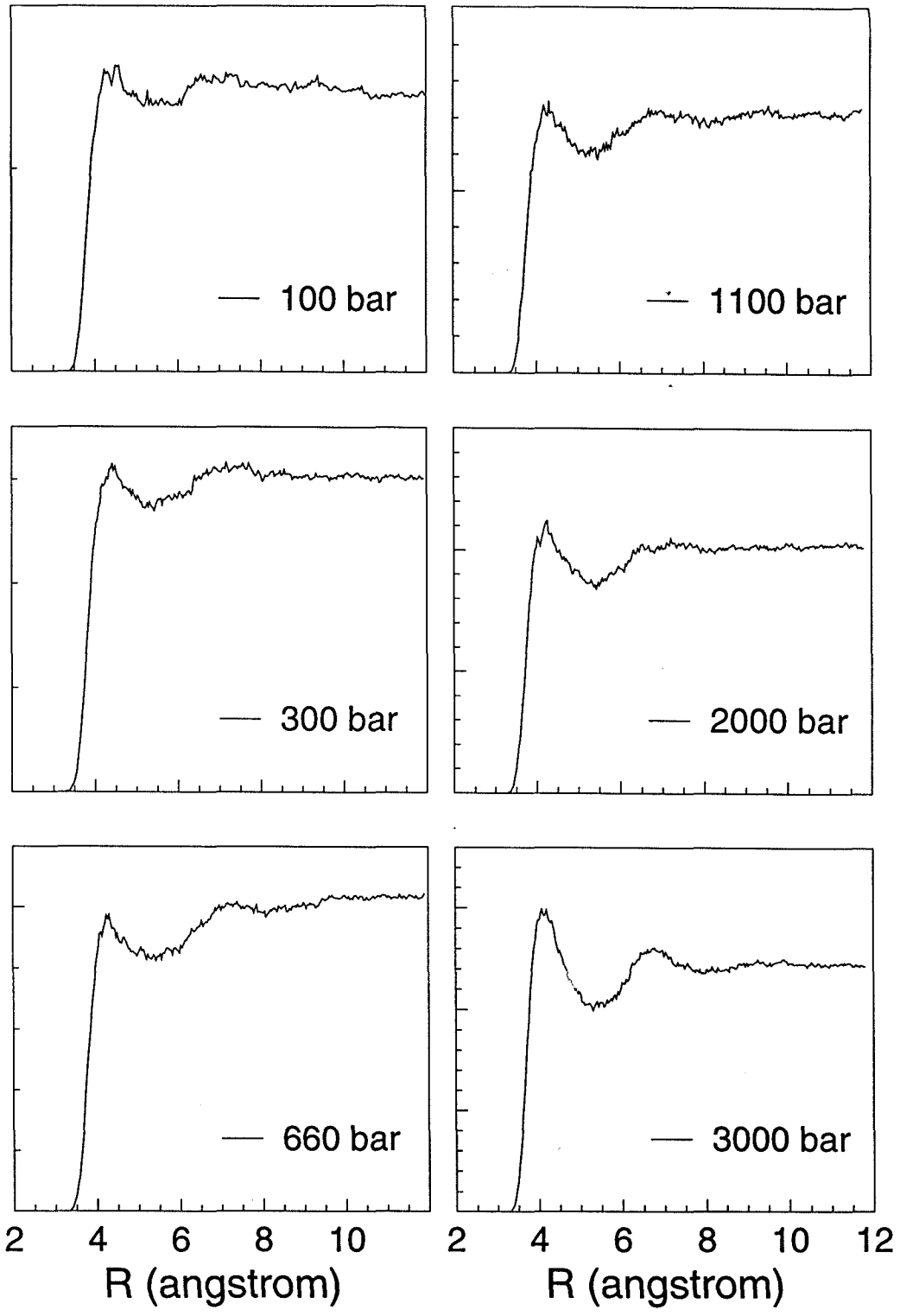
100 bar
1100 bar
300 bar
2000 bar
660 bar
3000 bar
2
4
6
8
10
12
R (angstrom)
R (angstrom)

Figure 5

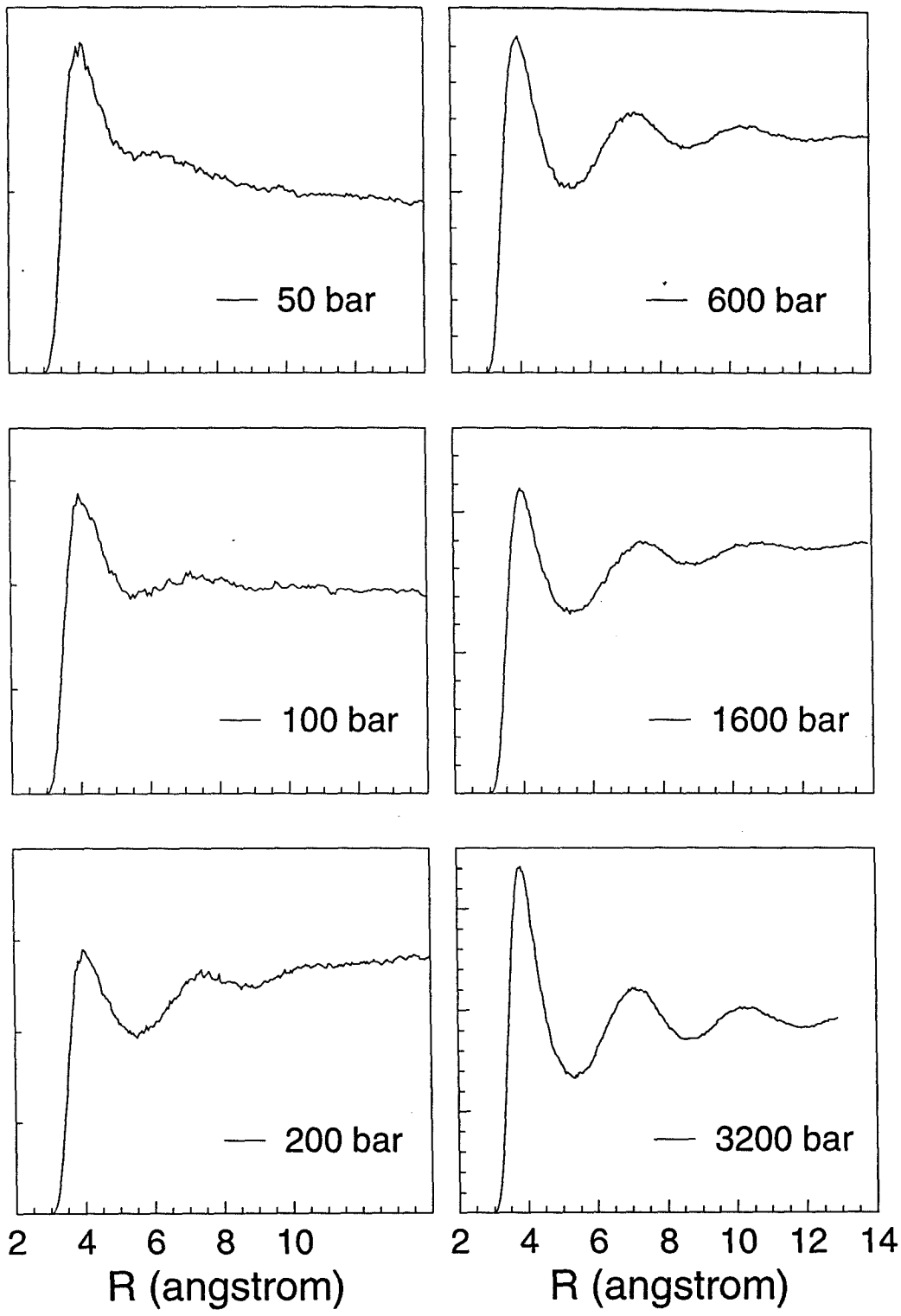
50 bar
600 bar
100 bar
1600 bar
200 bar
3200 bar
2 4 6 8 10
R (angstrom)
2 4 6 8 10 12 14
R (angstrom)

Figure 6

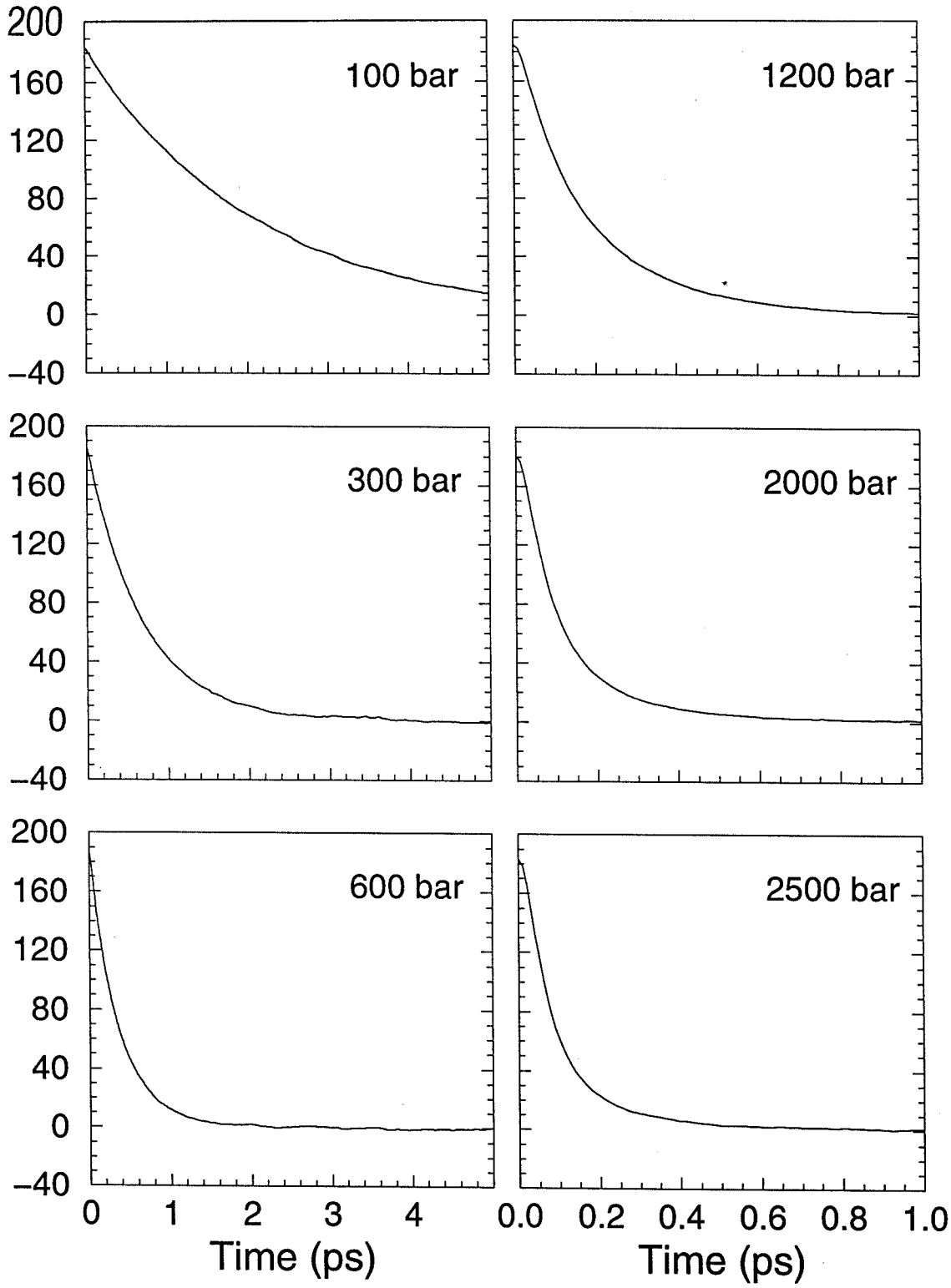
100 bar
1200 bar
300 bar
2000 bar
600 bar
2500 bar
200
160
120
80
40
0
−40
0
1
2
3
4
0.0
0.2
0.4
0.6
0.8
1.0
Time (ps)
Time (ps)

Figure 7

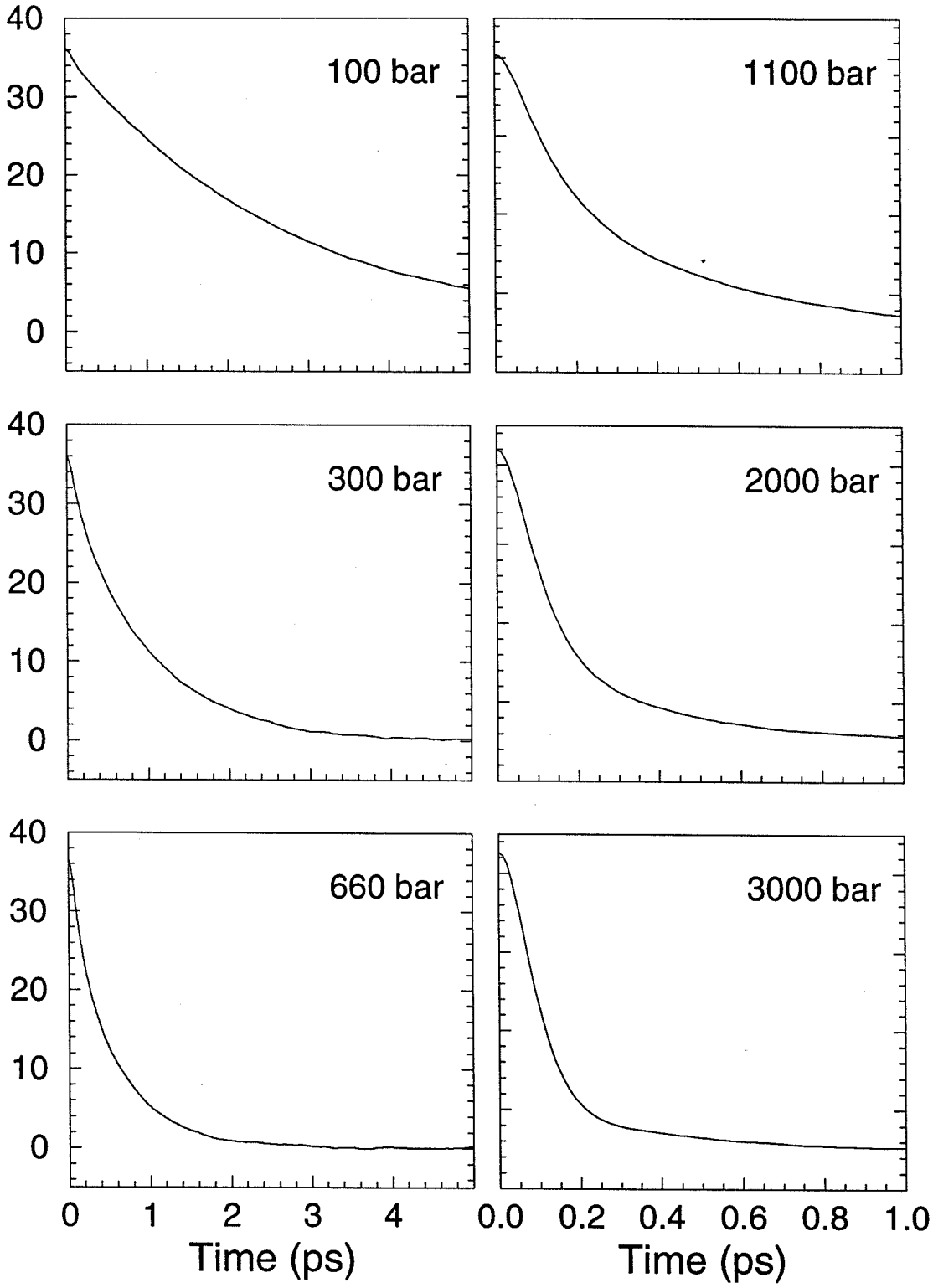
100 bar
1100 bar
300 bar
2000 bar
660 bar
3000 bar
40
30
20
10
0
0 1 2 3 4
0.0 0.2 0.4 0.6 0.8 1.0
Time (ps)
Time (ps)

Figure 8

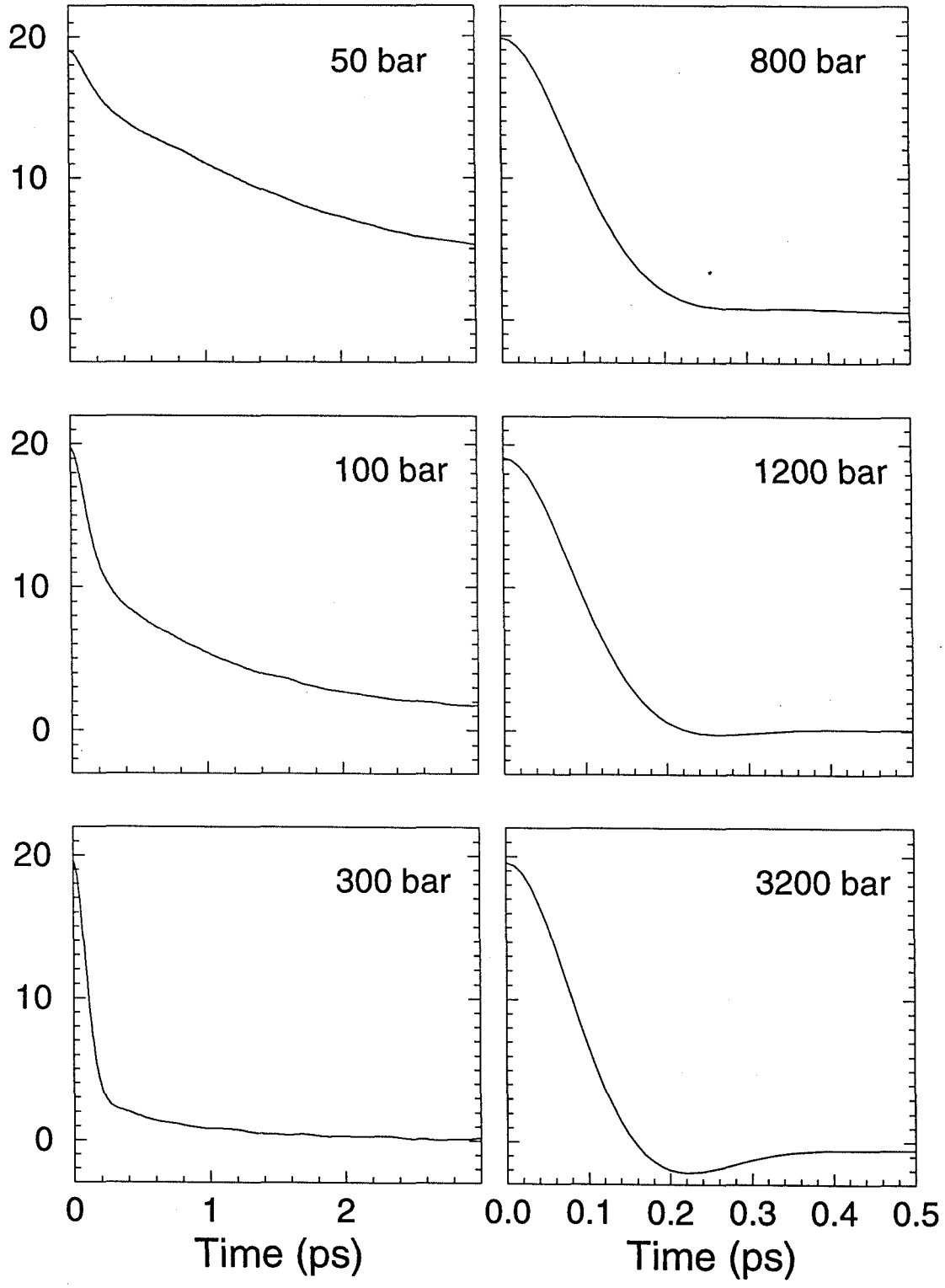
50 bar
800 bar
100 bar
1200 bar
300 bar
3200 bar
20
10
0
0
1
2
Time (ps)
0.0
0.1
0.2
0.3
0.4
0.5
Time (ps)

Figure 9

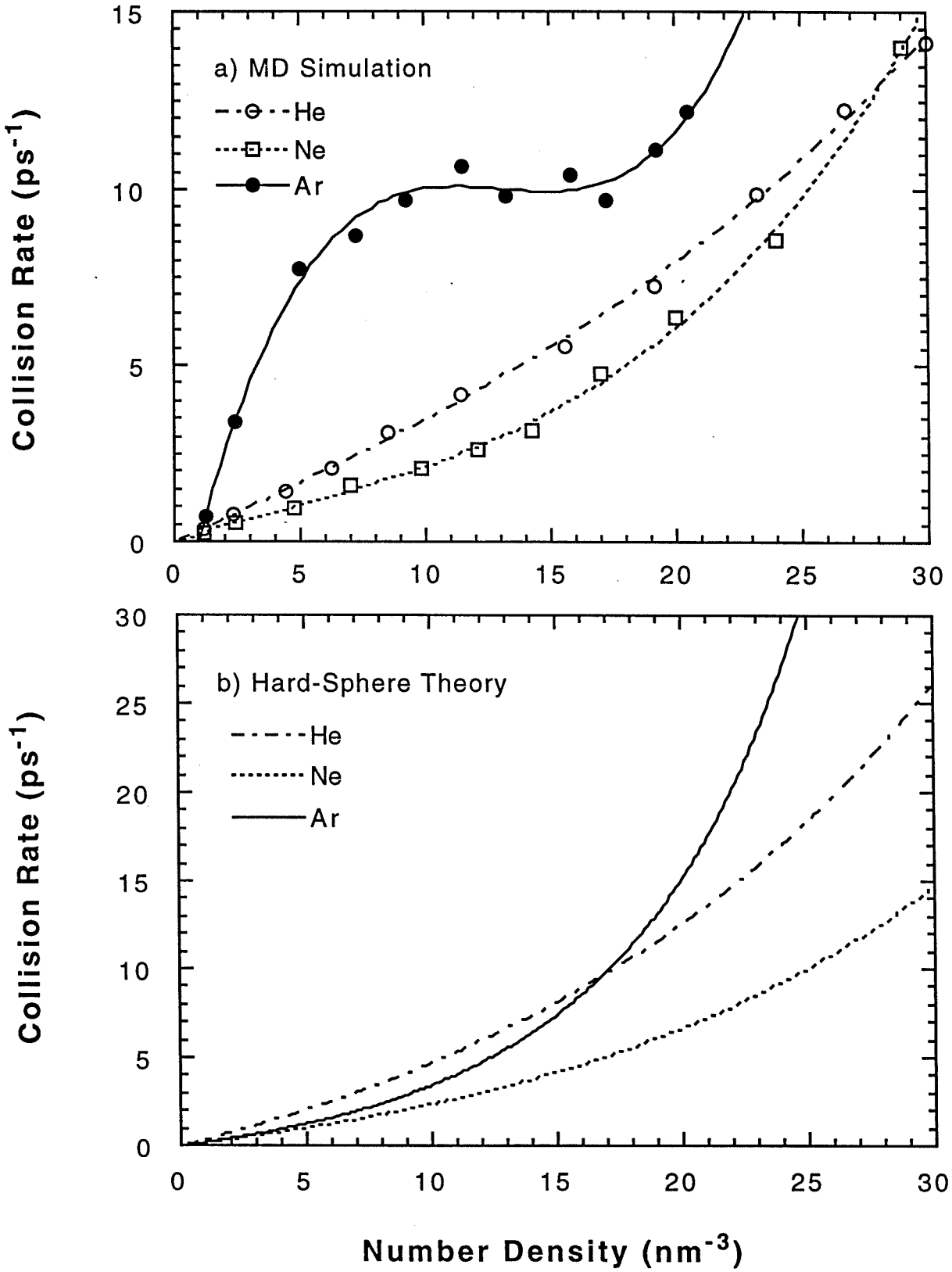
a) MD Simulation
He
Ne
Ar
Collision Rate (ps^{-1})
b) Hard-Sphere Theory
He
Ne
Ar
Collision Rate (ps^{-1})
Number Density (nm^{-3})

Figure 10

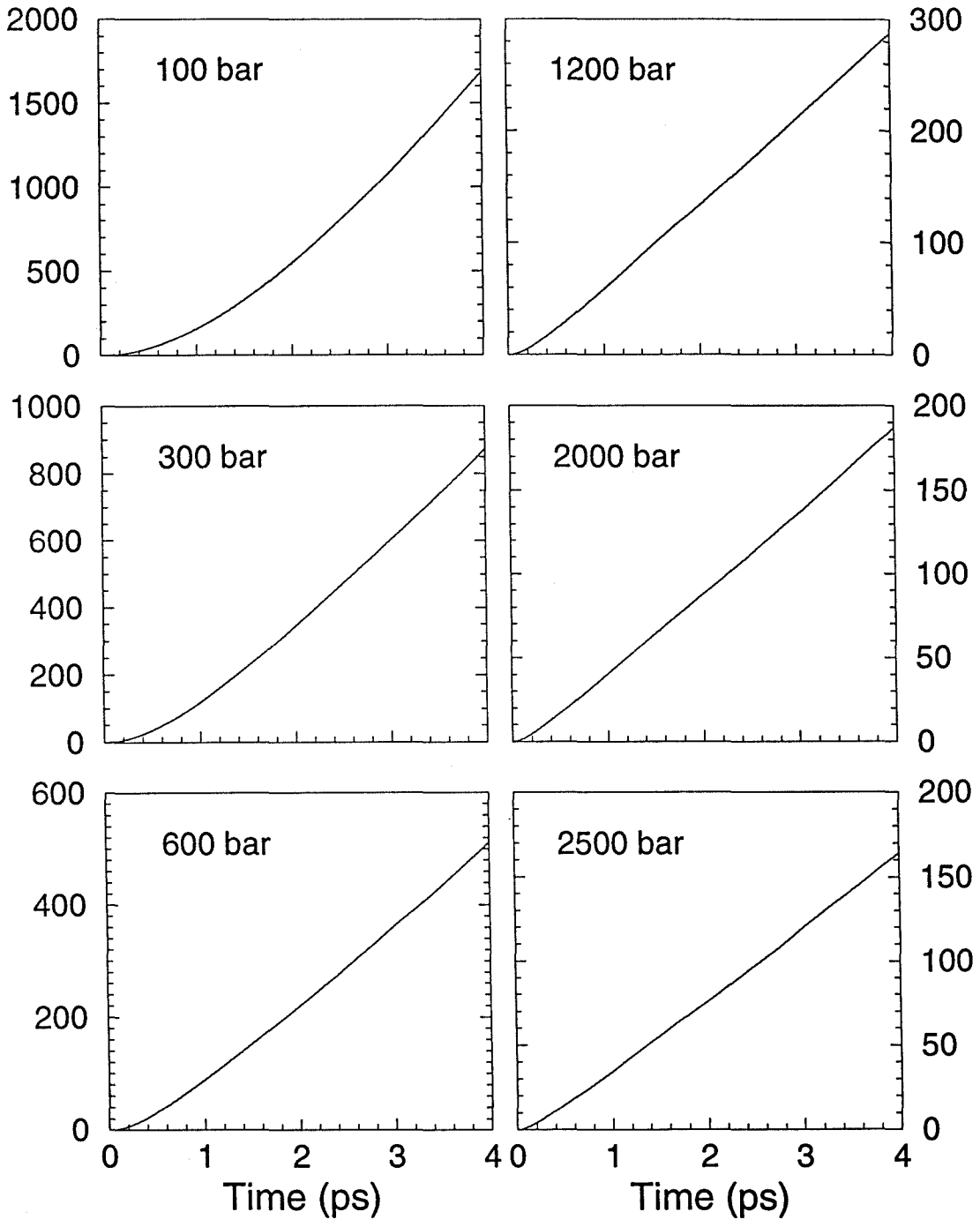
100 bar
1200 bar
300 bar
2000 bar
600 bar
2500 bar
Time (ps)
Time (ps)

Figure 11

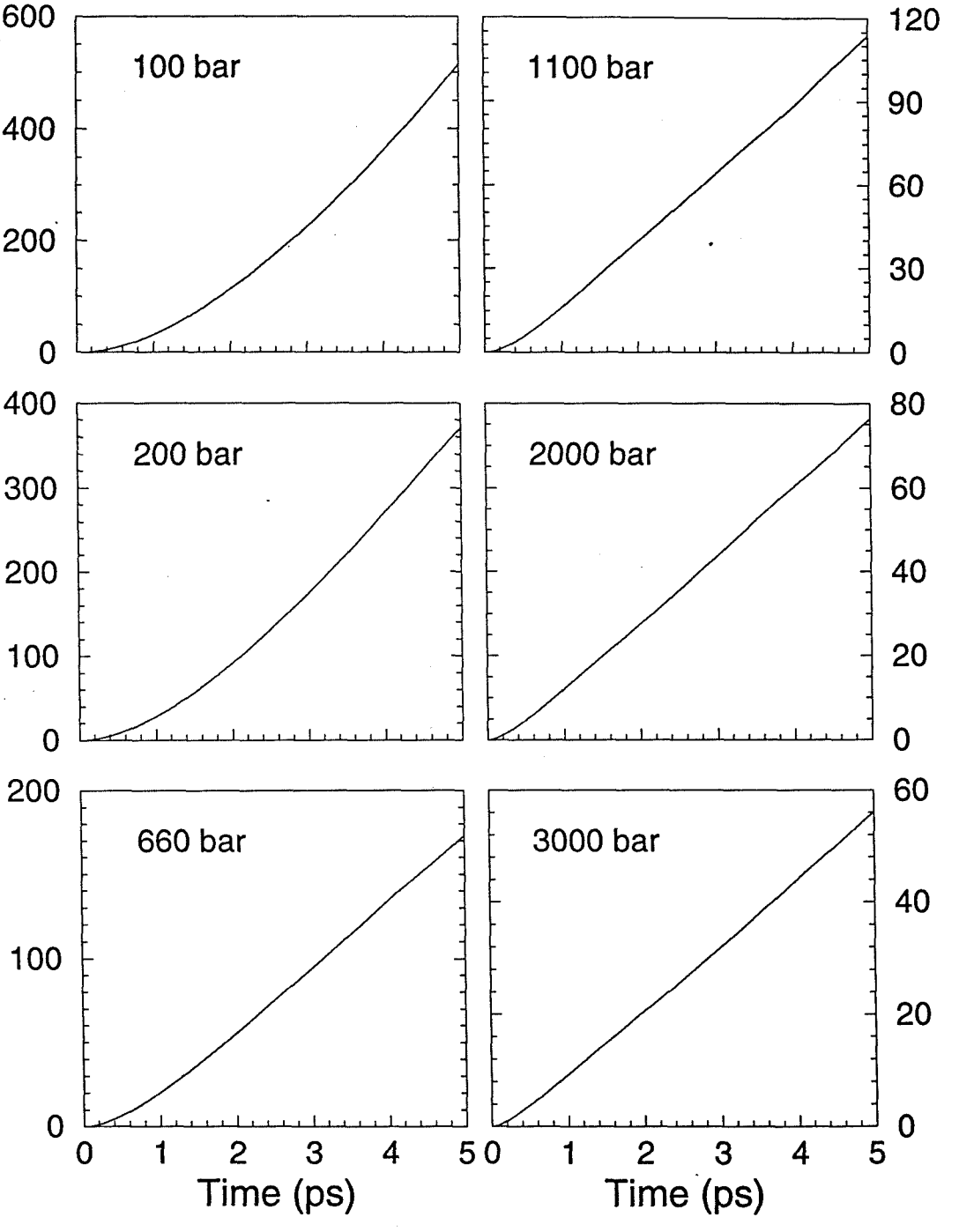
100 bar
1100 bar
200 bar
2000 bar
660 bar
3000 bar
600
400
200
0
120
90
60
30
0
400
300
200
100
0
80
60
40
20
0
200
100
0
60
40
20
0
0 1 2 3 4 5
Time (ps)
0 1 2 3 4 5
Time (ps)

Figure 12

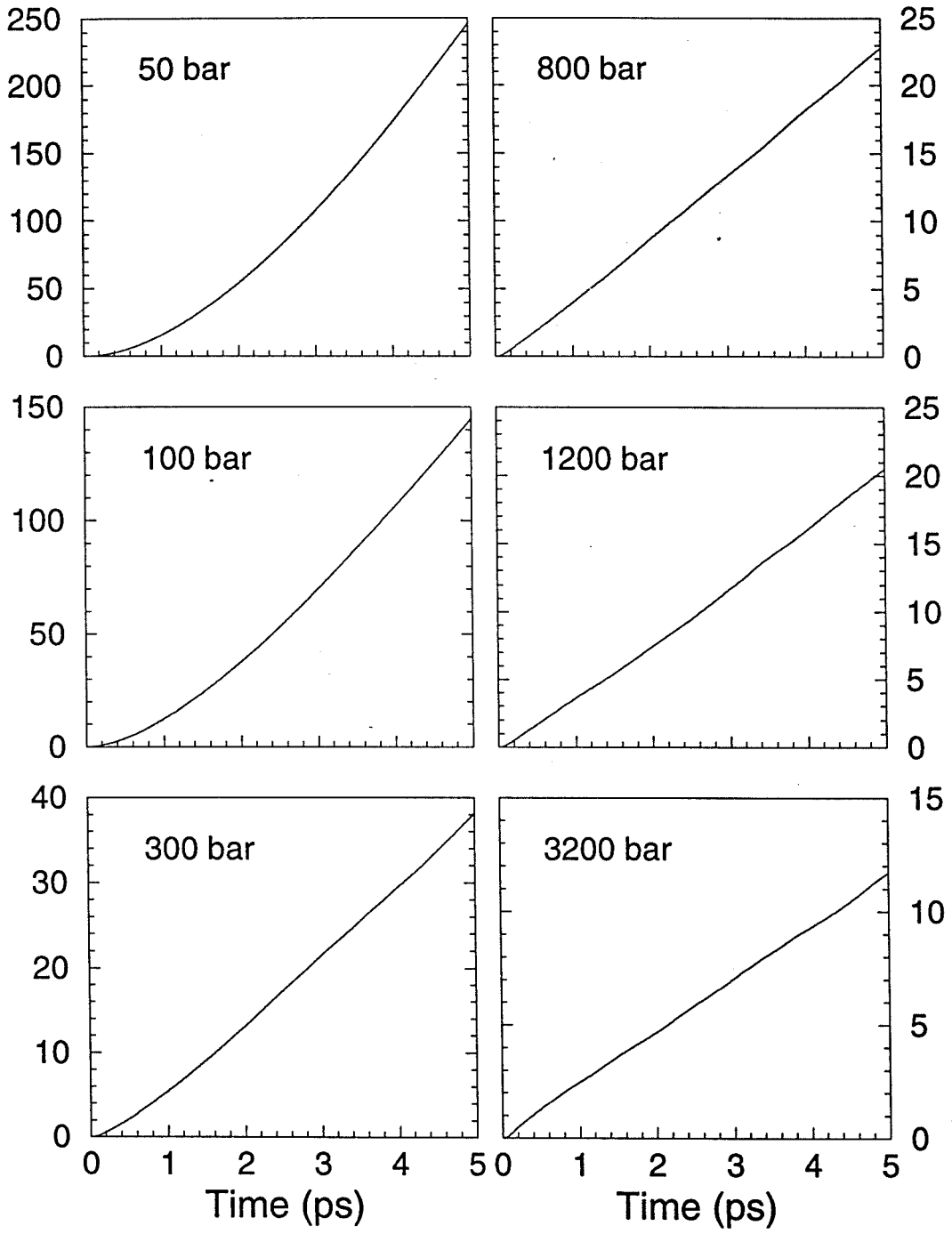

Figure 13

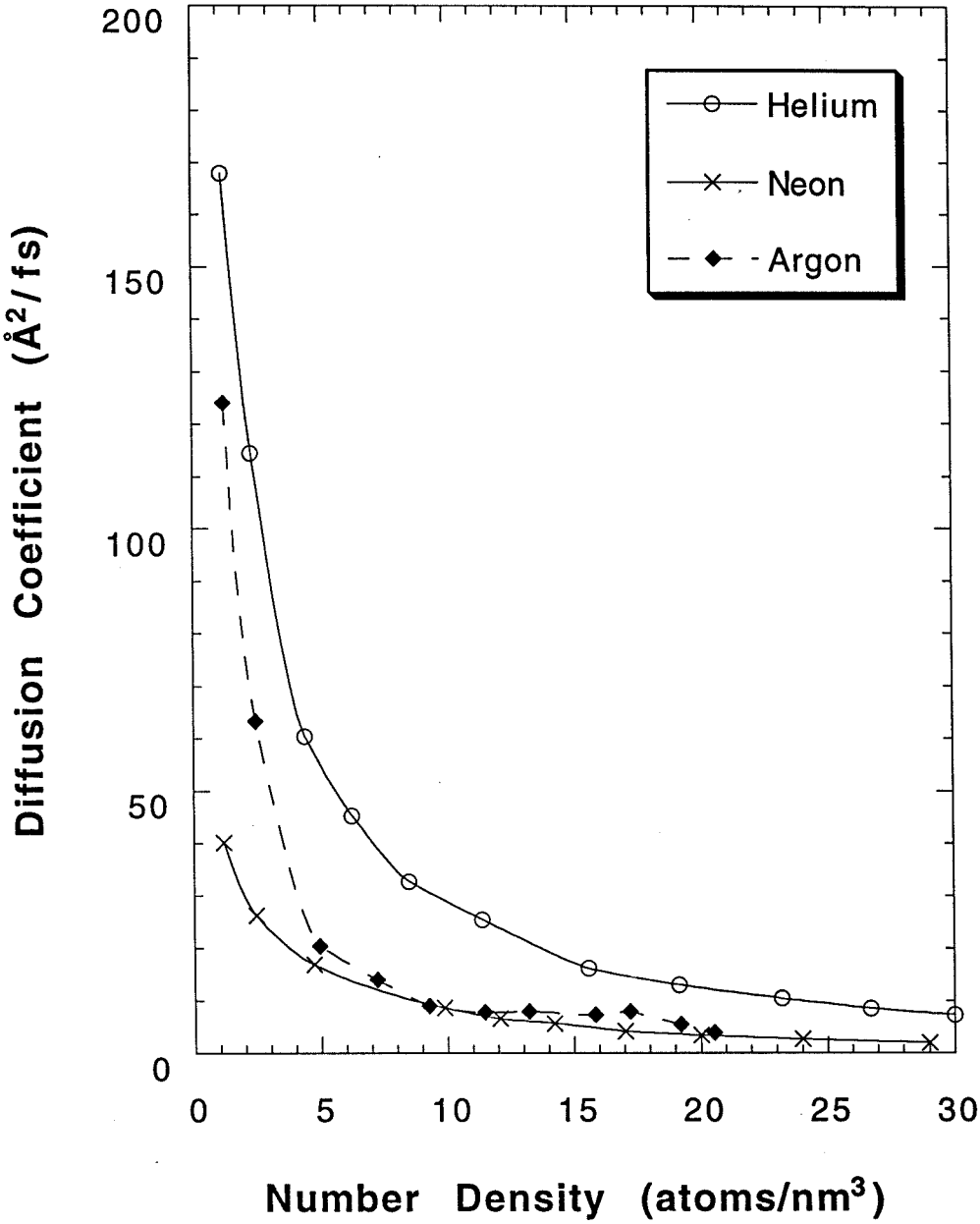
200
150
100
50
0
0
5
10
15
20
25
30
Helium
Neon
Argon
Diffusion Coefficient (Å²/fs)
Number Density (atoms/nm³)

Figure 14

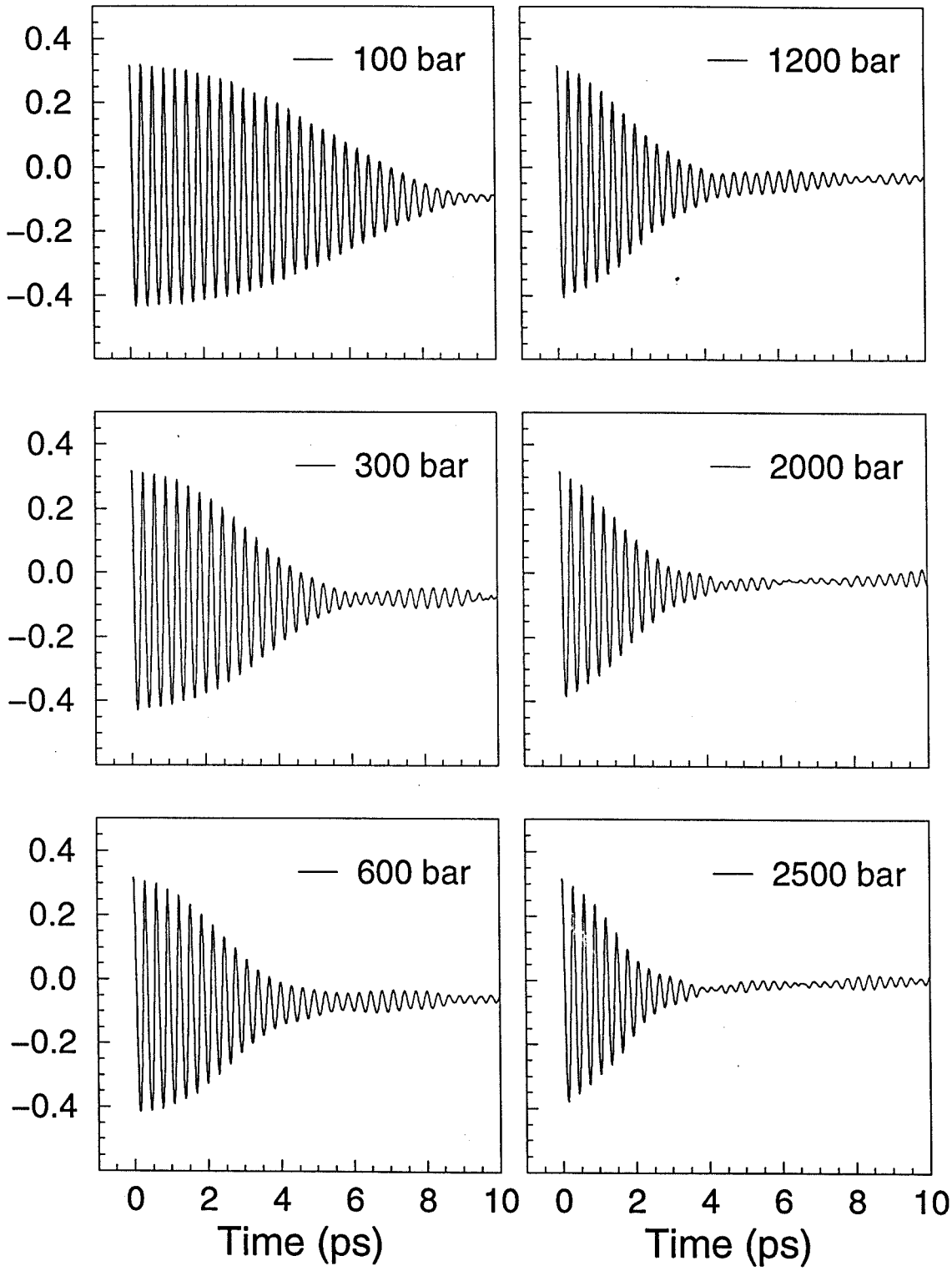
0.4
0.2
0.0
−0.2
−0.4
— 100 bar
— 1200 bar
— 300 bar
— 2000 bar
— 600 bar
— 2500 bar
0
2
4
6
8
10
Time (ps)
Time (ps)

Figure 15

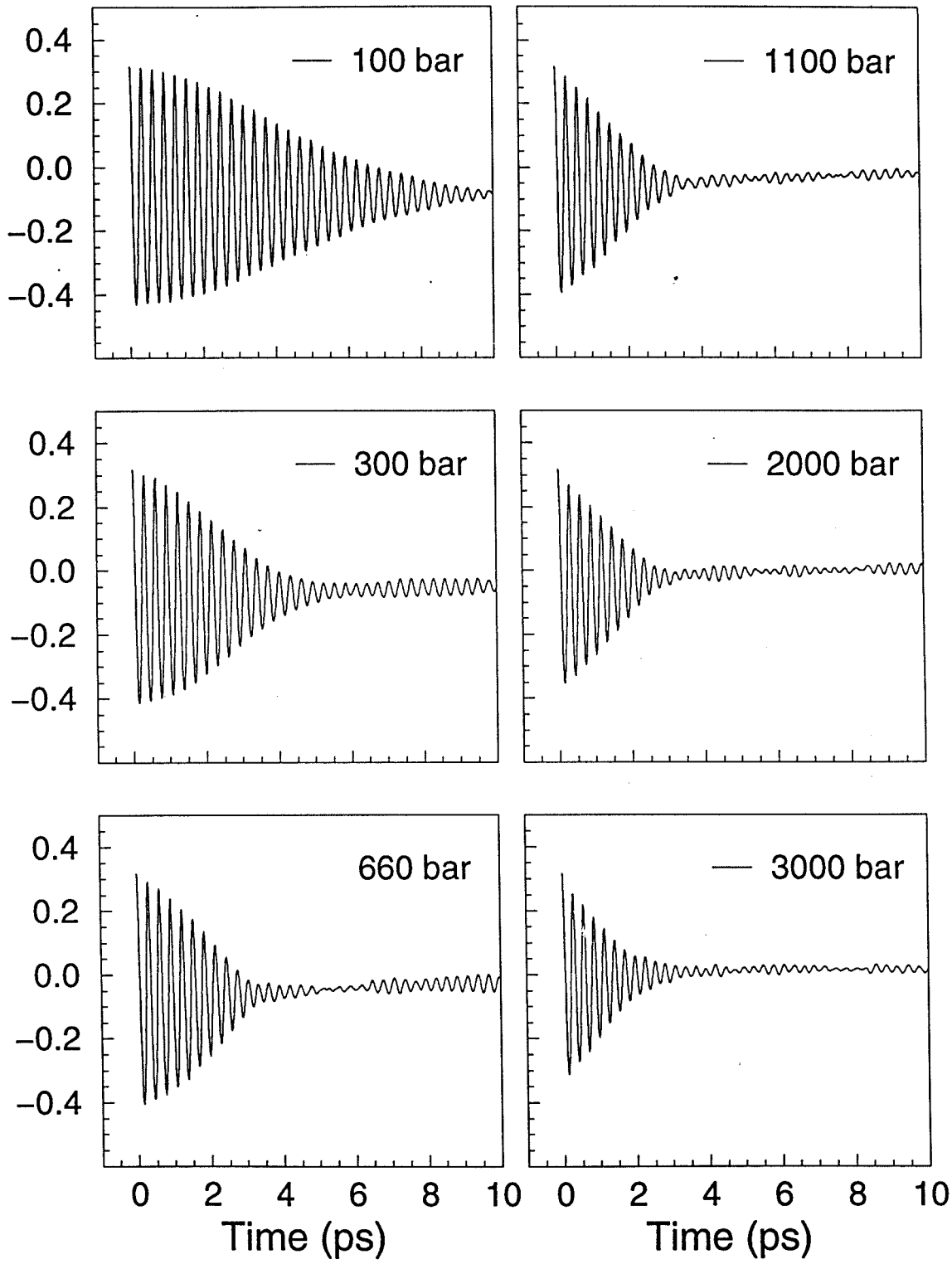
0.4
0.2
0.0
−0.2
−0.4
100 bar
1100 bar
300 bar
2000 bar
660 bar
3000 bar
0
2
4
6
8
10
Time (ps)
Time (ps)

Figure 16

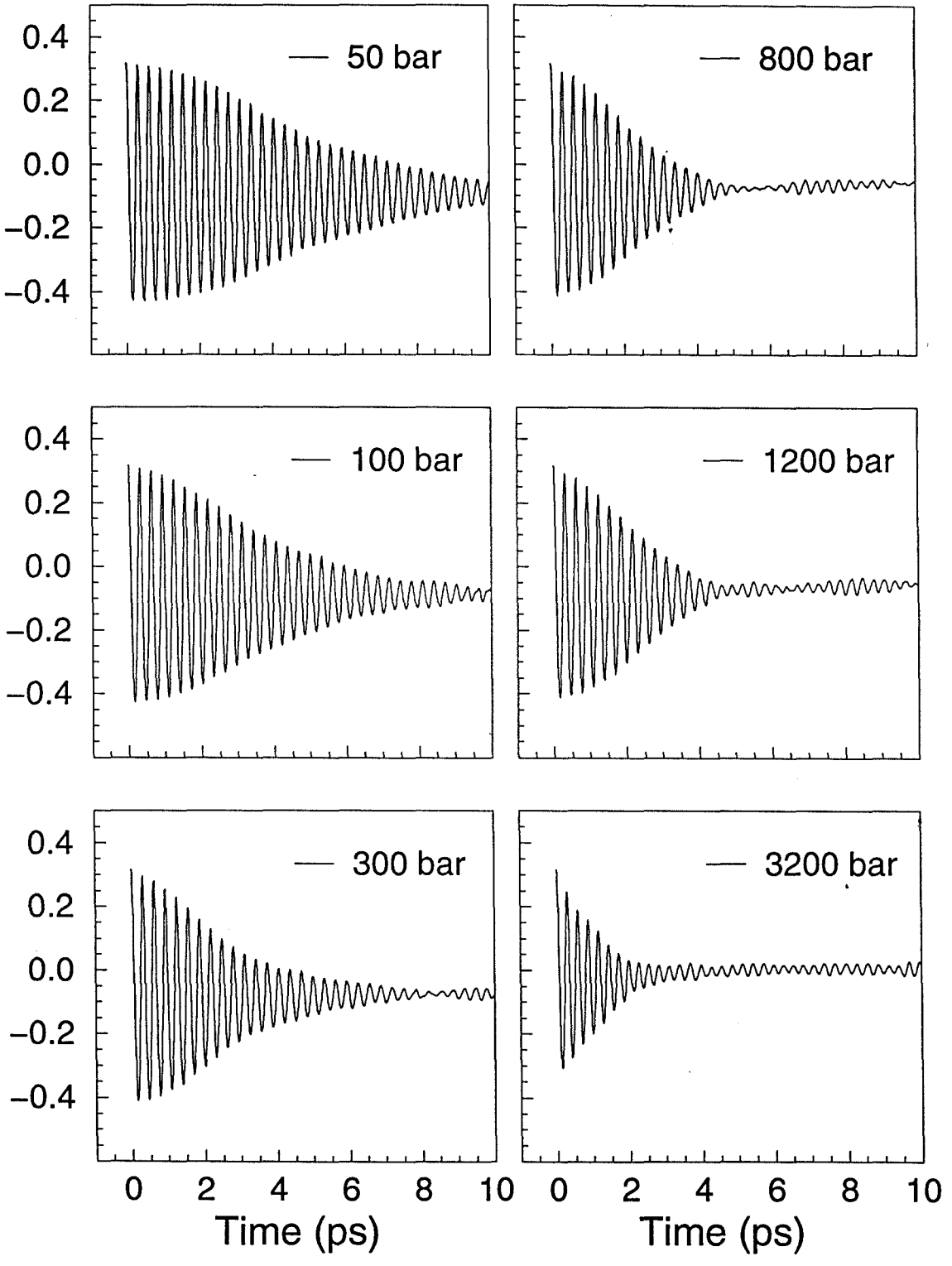
0.4
0.2
0.0
−0.2
−0.4
— 50 bar
— 800 bar
— 100 bar
— 1200 bar
— 300 bar
— 3200 bar
0
2
4
6
8
10
Time (ps)
Time (ps)

Figure 17

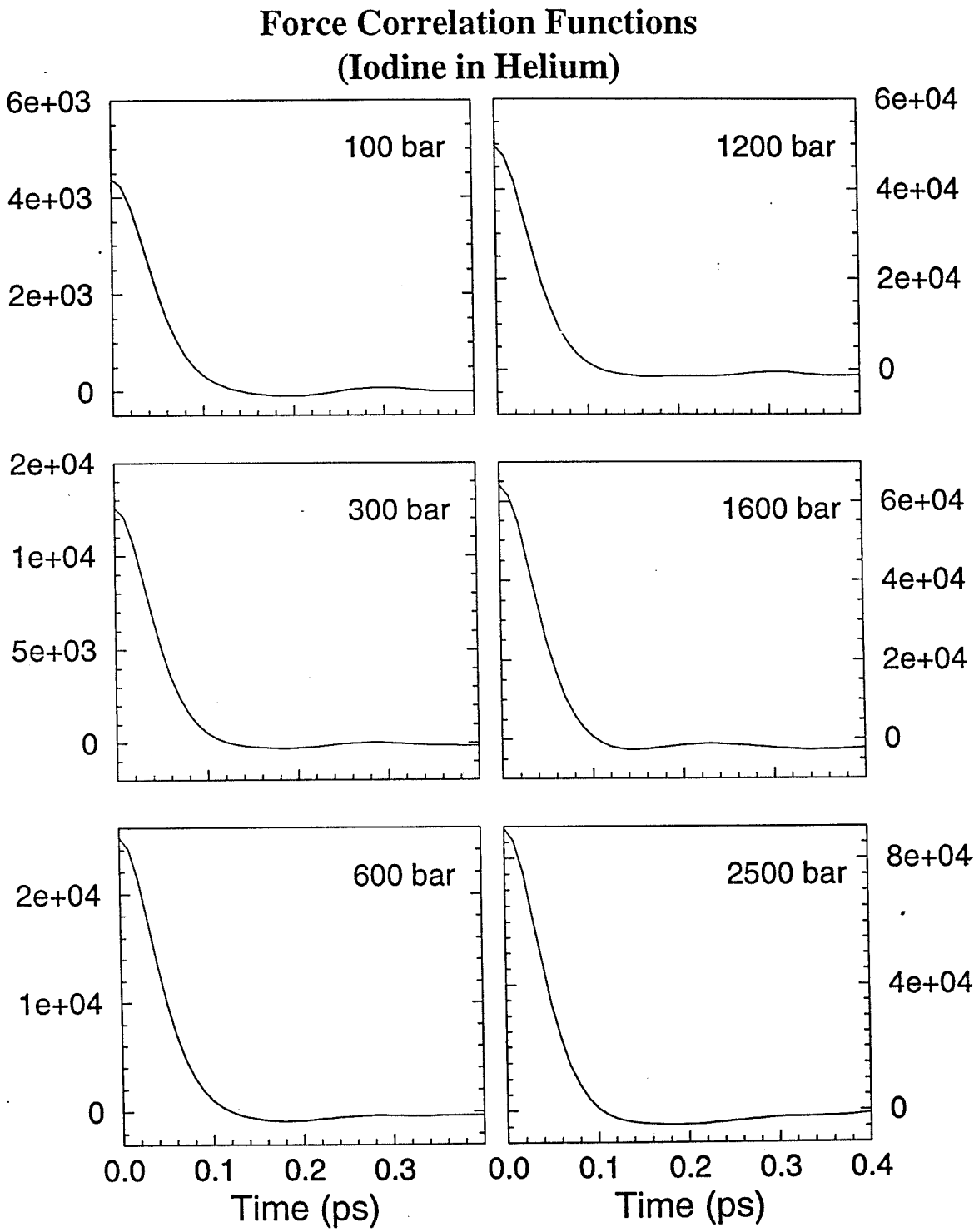
Force Correlation Functions
(Iodine in Helium)
100 bar
1200 bar
300 bar
1600 bar
600 bar
2500 bar
6e+03
4e+03
2e+03
0
6e+04
4e+04
2e+04
0
2e+04
1e+04
5e+03
0
6e+04
4e+04
2e+04
0
2e+04
1e+04
0
8e+04
4e+04
0
0.0
0.1
0.2
0.3
0.4
Time (ps)
Time (ps)

Figure 18

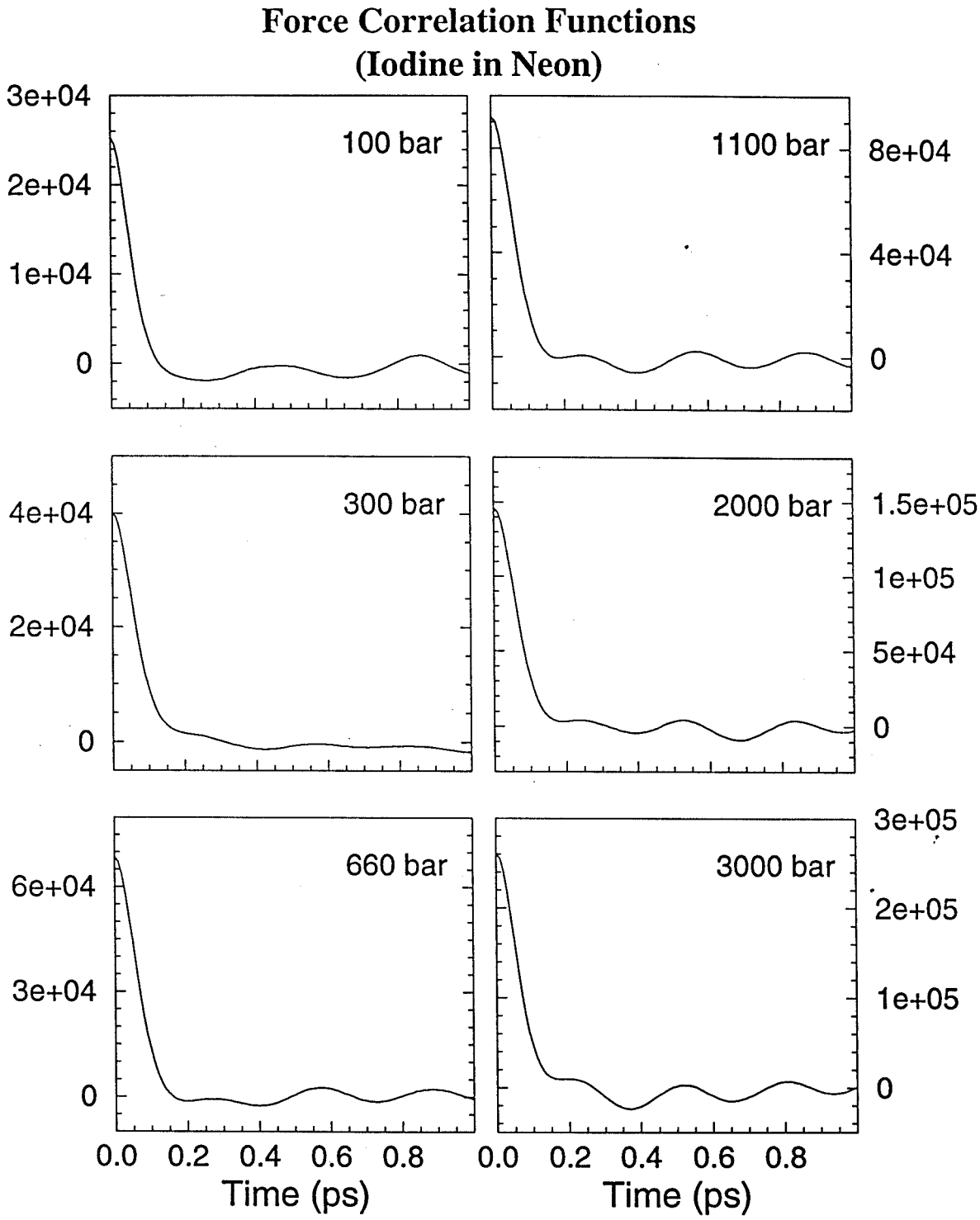
Force Correlation Functions
(Iodine in Neon)
100 bar
1100 bar
300 bar
2000 bar
660 bar
3000 bar
3e+04
2e+04
1e+04
0
8e+04
4e+04
4e+04
2e+04
0
1.5e+05
1e+05
5e+04
6e+04
3e+04
3e+05
2e+05
1e+05
0.0 0.2 0.4 0.6 0.8
Time (ps)

Figure 19

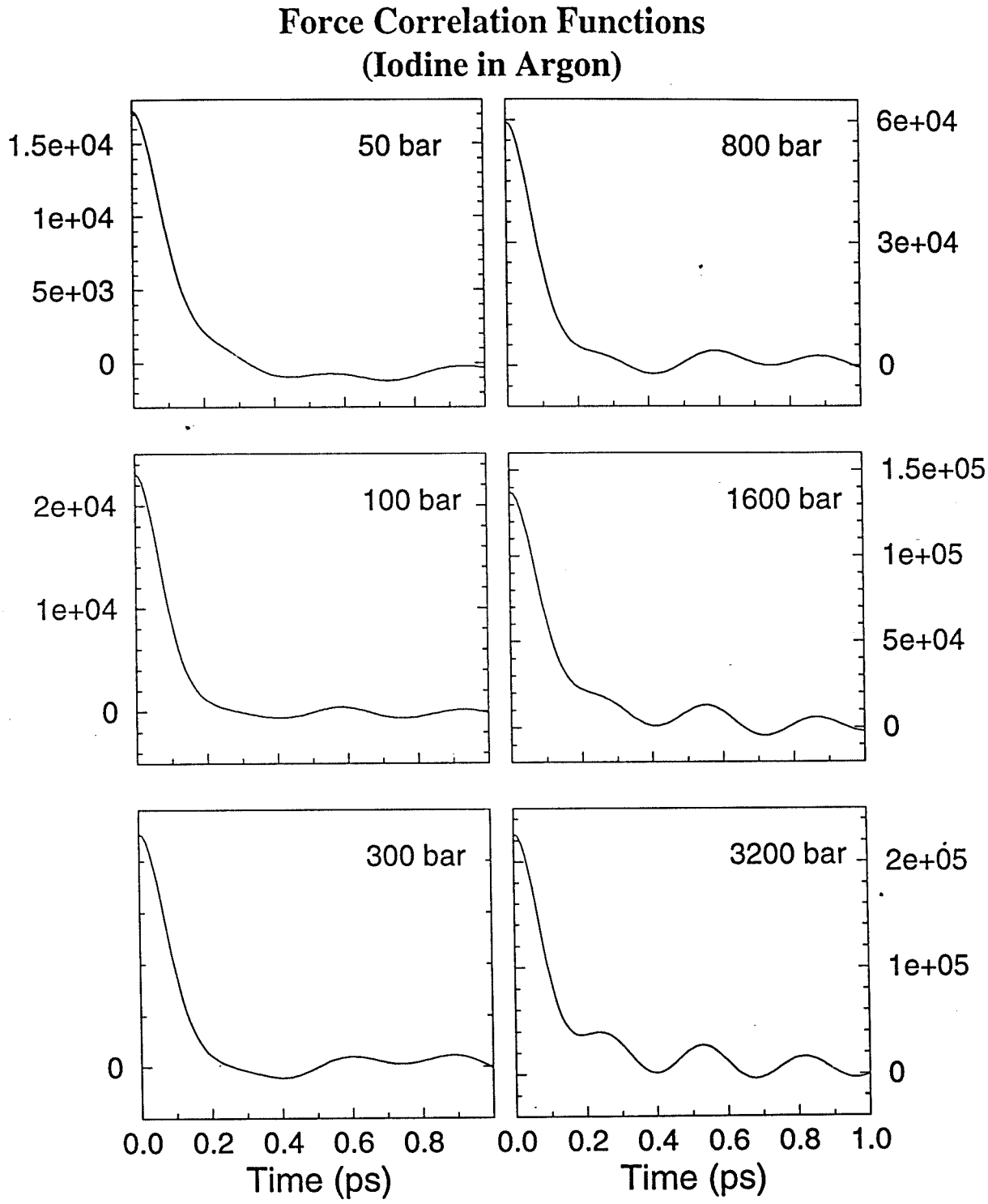
Force Correlation Functions
(Iodine in Argon)
50 bar
800 bar
100 bar
1600 bar
300 bar
3200 bar
1.5e+04
1e+04
5e+03
0
6e+04
3e+04
0
2e+04
1e+04
0
1.5e+05
1e+05
5e+04
0
0
0.0
0.2
0.4
0.6
0.8
Time (ps)
0.0
0.2
0.4
0.6
0.8
1.0
Time (ps)
2e+05
1e+05
0

Figure 20

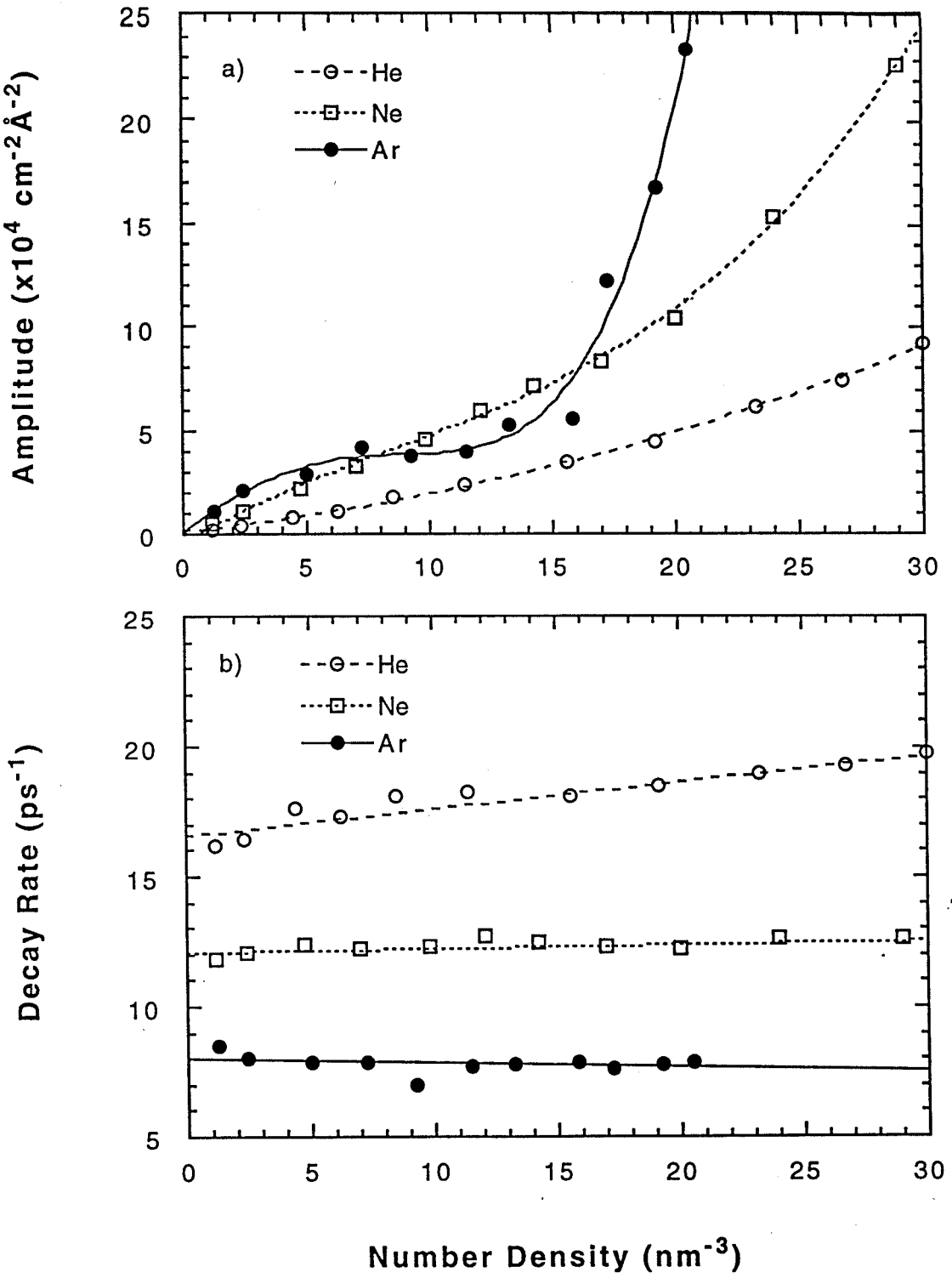
a)
He
Ne
Ar
Amplitude (x10^4 cm^{-2}Å^{-2})
b)
He
Ne
Ar
Decay Rate (ps^{-1})
Number Density (nm^{-3})

Figure 21

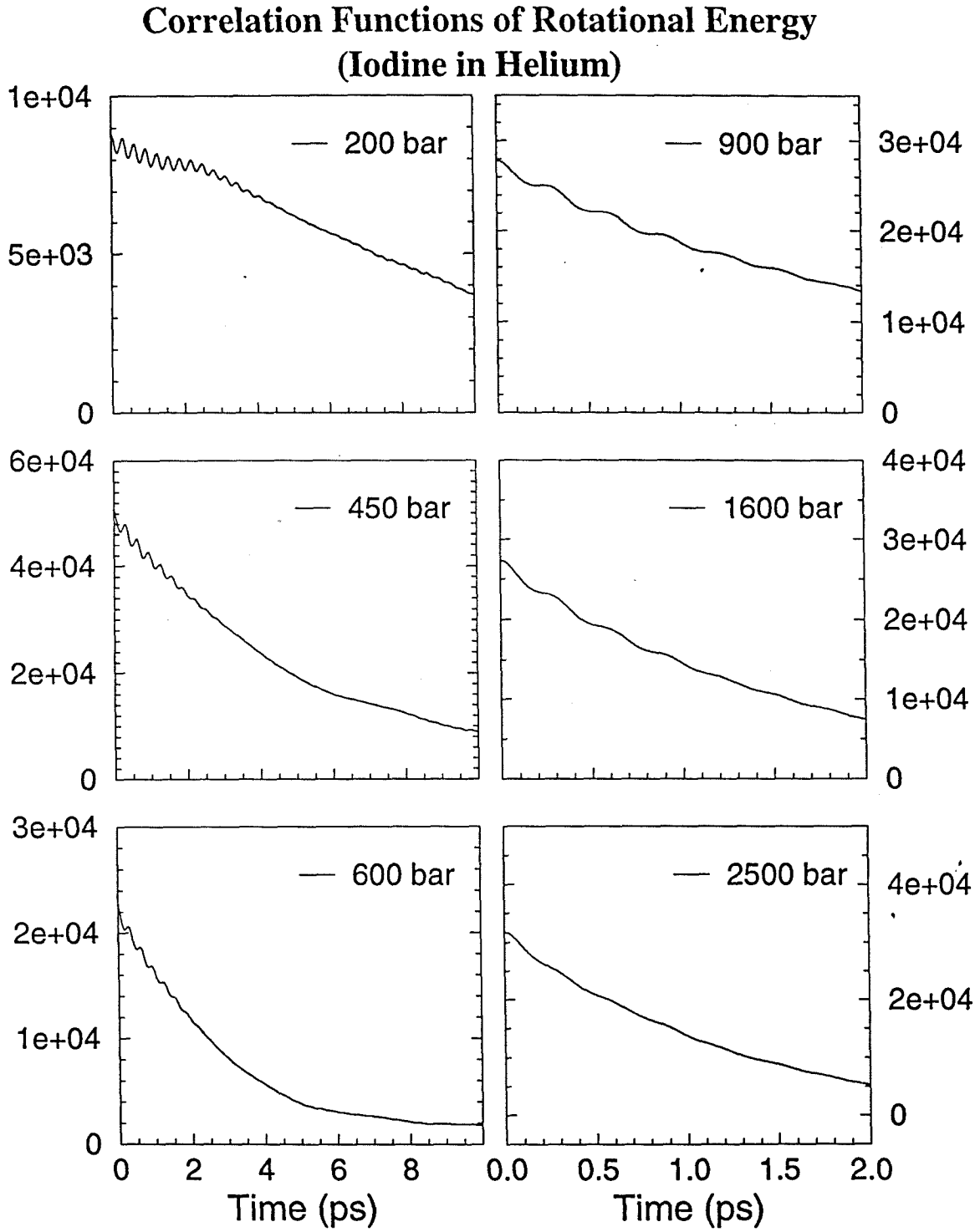
Correlation Functions of Rotational Energy
(Iodine in Helium)
200 bar
900 bar
450 bar
1600 bar
600 bar
2500 bar
1e+04
5e+03
0
3e+04
2e+04
1e+04
6e+04
4e+04
2e+04
0
4e+04
3e+04
2e+04
1e+04
0
3e+04
2e+04
1e+04
0
4e+04
2e+04
0
0 2 4 6 8
Time (ps)
0.0 0.5 1.0 1.5 2.0
Time (ps)

Figure 22

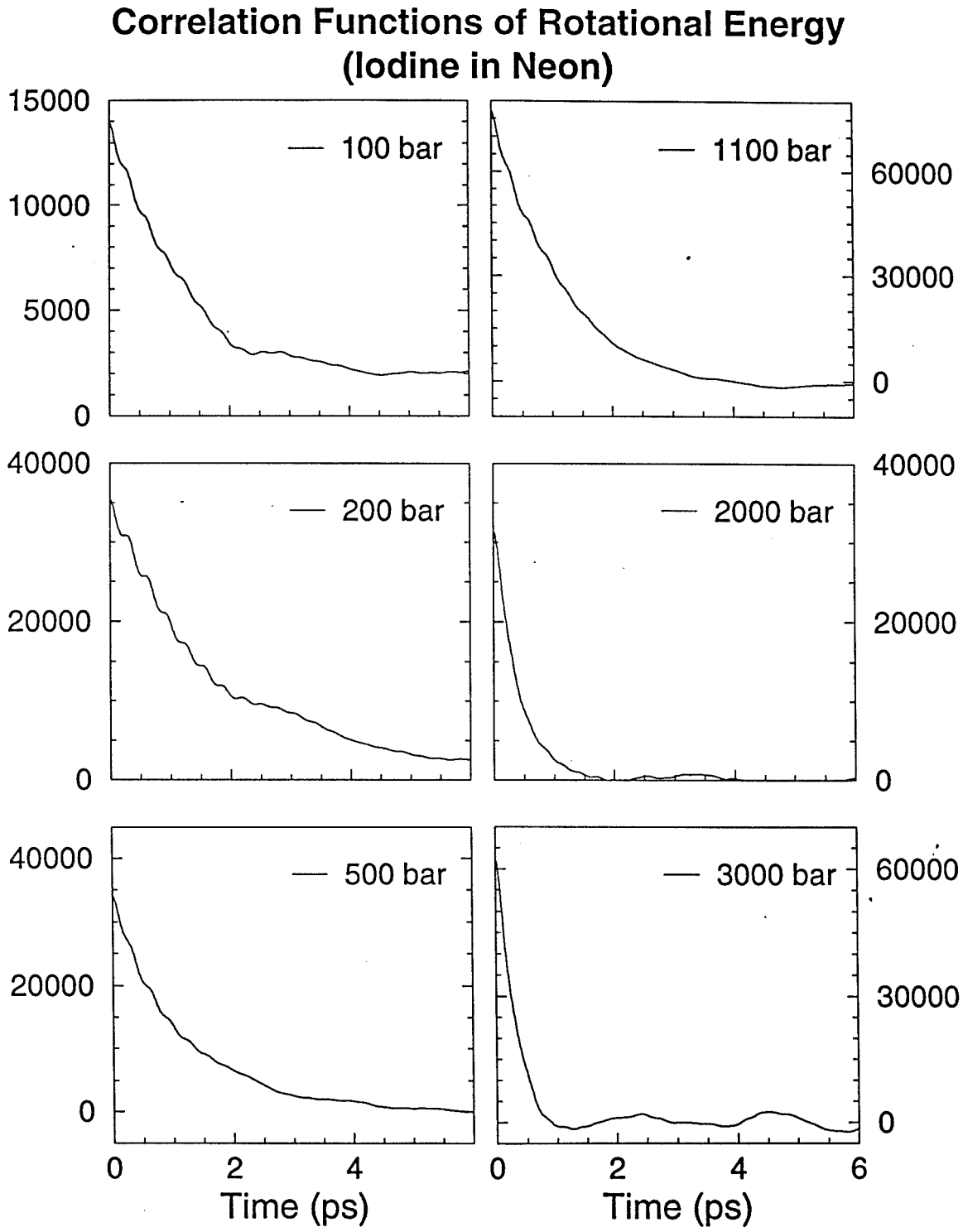
Correlation Functions of Rotational Energy
(Iodine in Neon)
100 bar
1100 bar
200 bar
2000 bar
500 bar
3000 bar
15000
10000
5000
0
60000
30000
40000
20000
0
2
4
6
Time (ps)

Figure 23

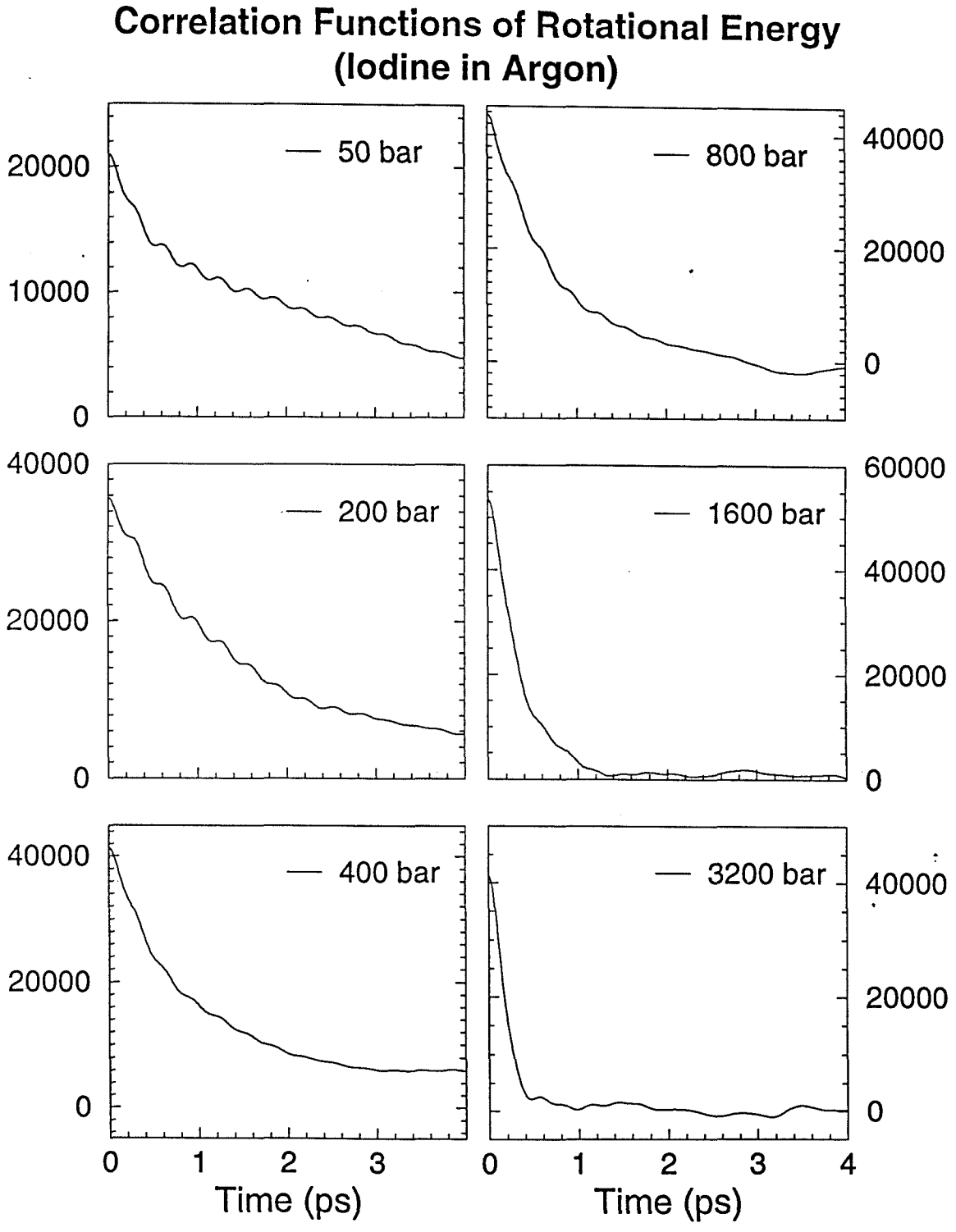
Correlation Functions of Rotational Energy
(Iodine in Argon)
50 bar
800 bar
200 bar
1600 bar
400 bar
3200 bar
20000
10000
0
40000
20000
0
40000
20000
0
60000
40000
20000
0
40000
20000
0
40000
20000
0
0 1 2 3
Time (ps)
0 1 2 3 4
Time (ps)

Figure 24

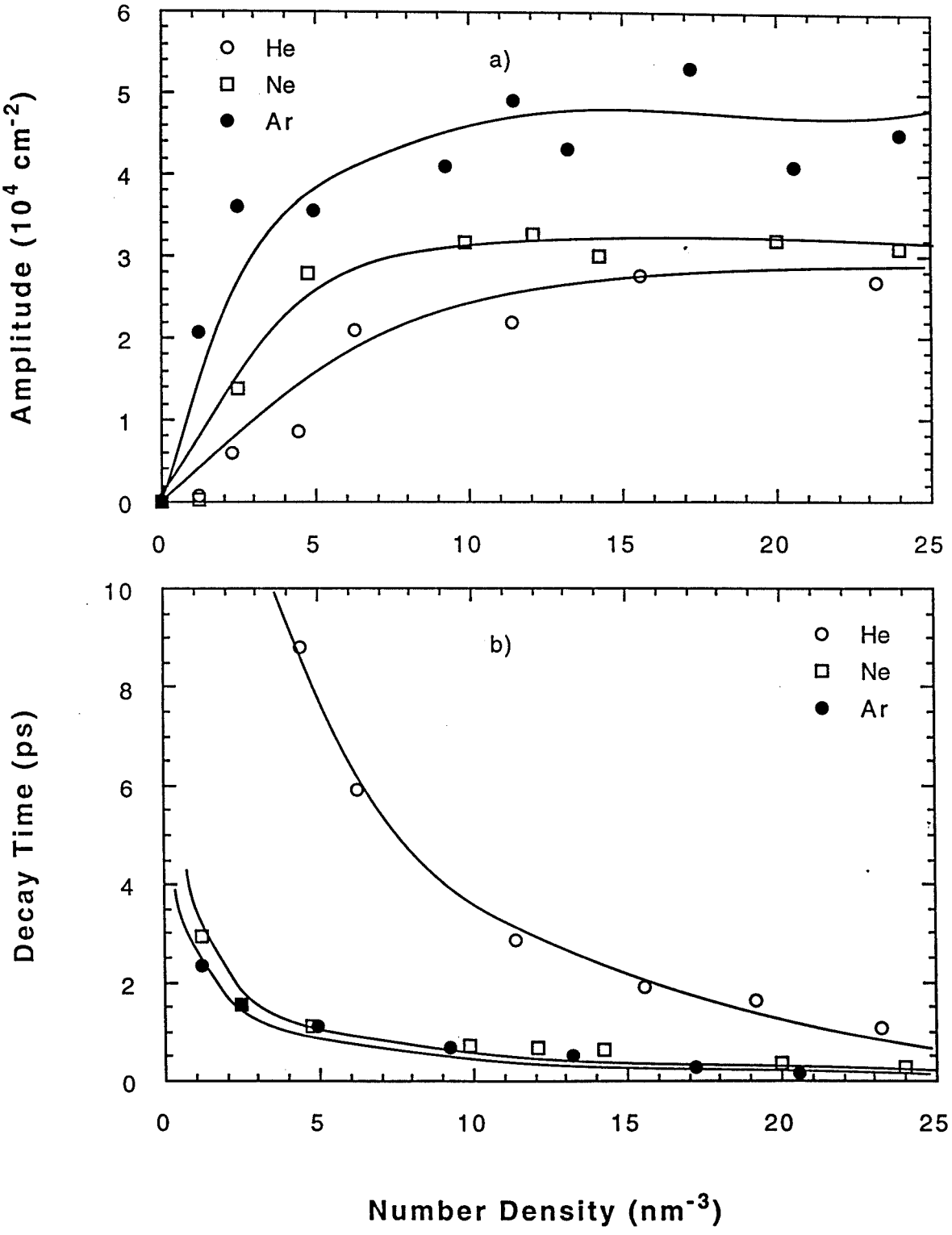
a)
He
Ne
Ar
Amplitude (10^4 cm^{-2})
0
1
2
3
4
5
6
0
5
10
15
20
25
b)
He
Ne
Ar
Decay Time (ps)
0
2
4
6
8
10
0
5
10
15
20
25
Number Density (nm^{-3})

Figure 25

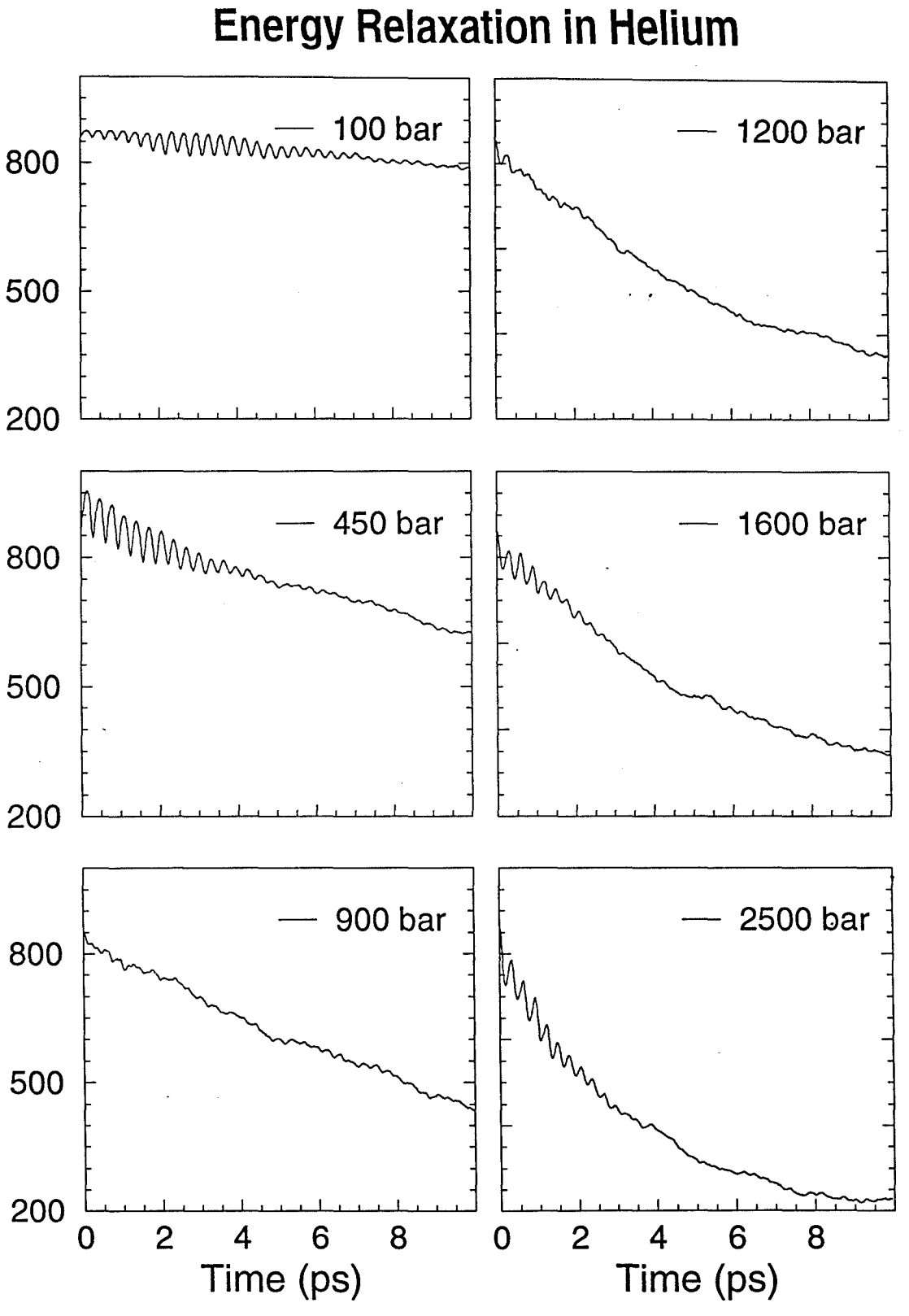
Energy Relaxation in Helium
100 bar
1200 bar
450 bar
1600 bar
900 bar
2500 bar
800
500
200
0
2
4
6
8
Time (ps)

Figure 26

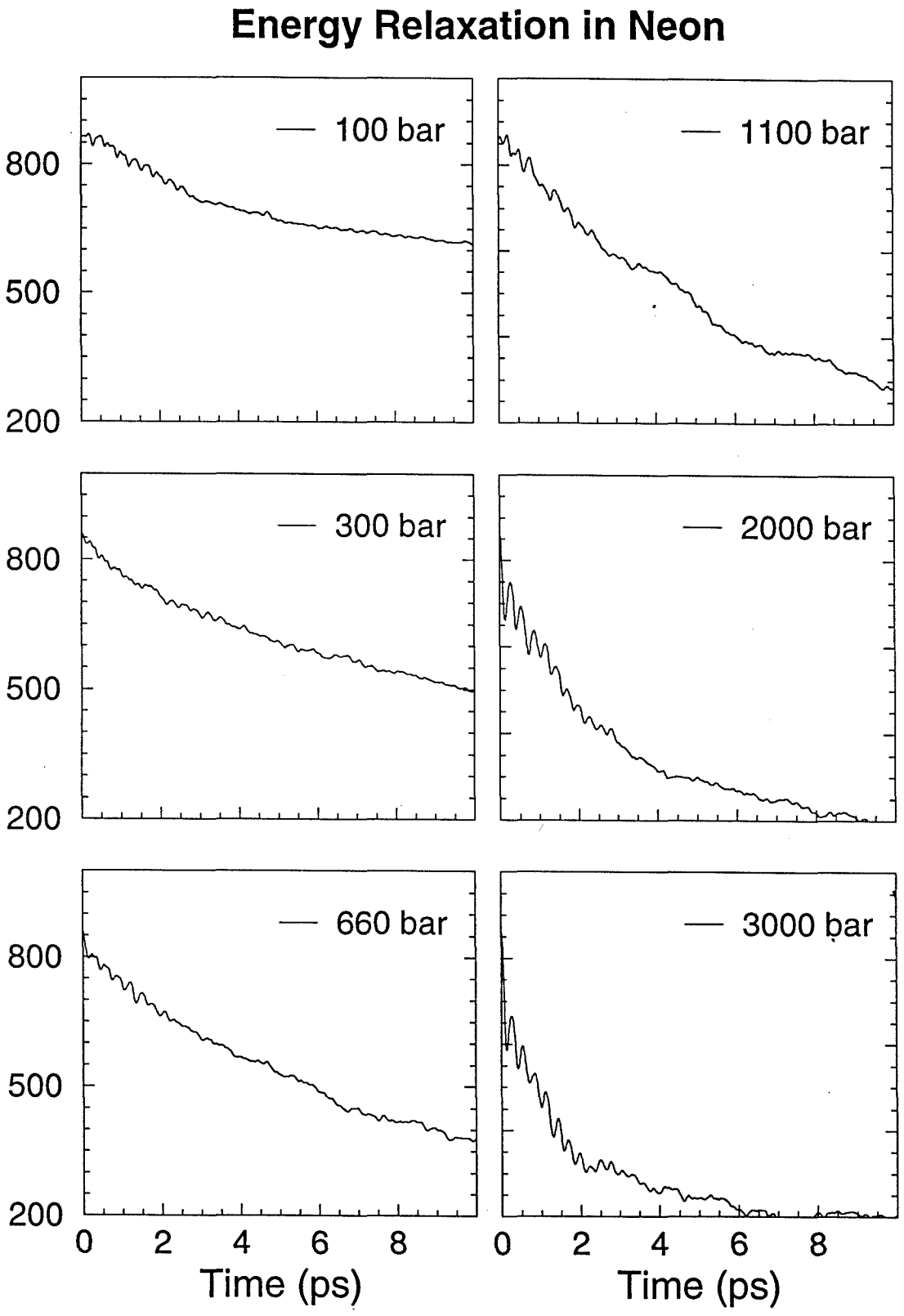
Energy Relaxation in Neon
100 bar
1100 bar
300 bar
2000 bar
660 bar
3000 bar
800
500
200
0
2
4
6
8
Time (ps)

Figure 27

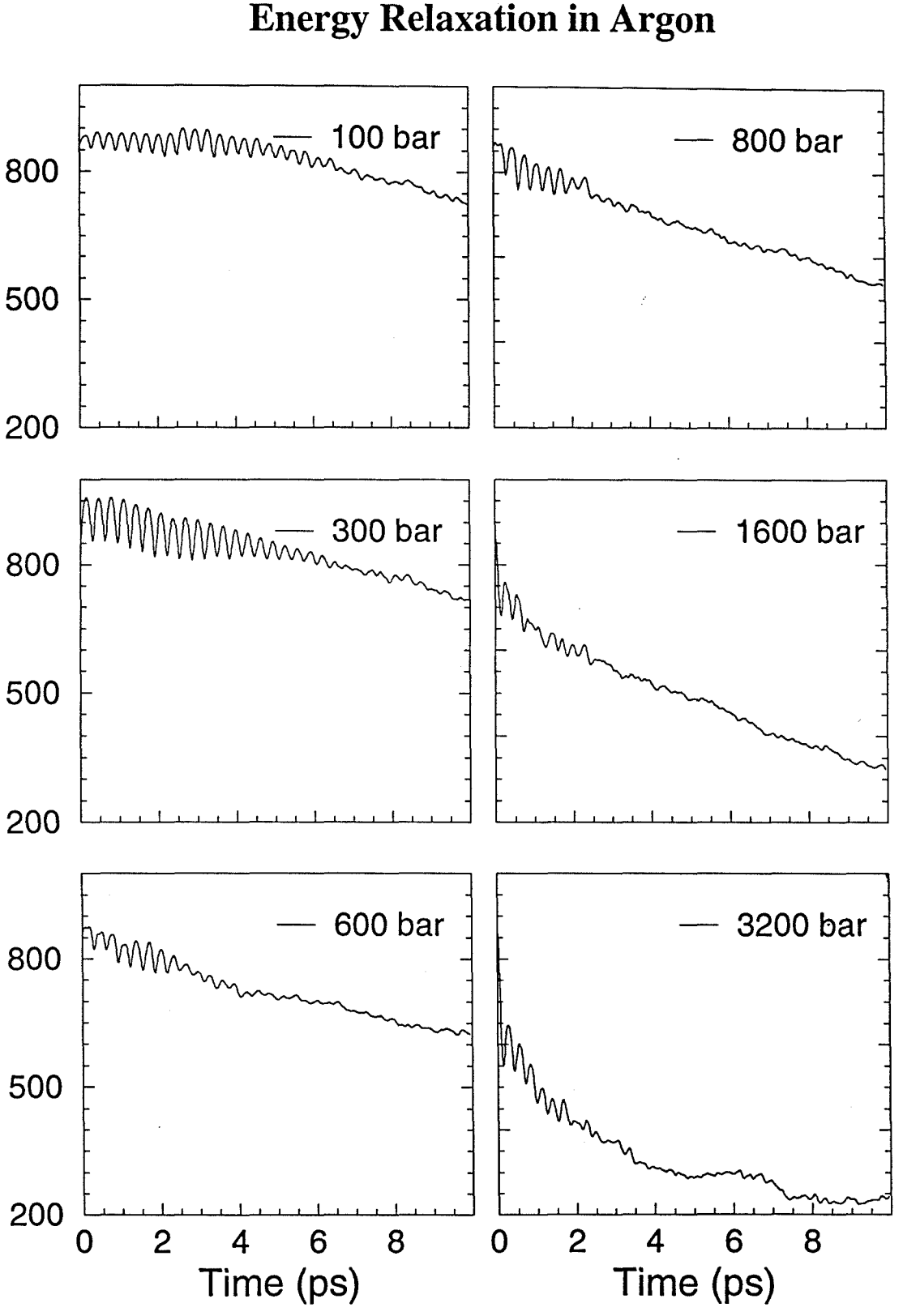
Energy Relaxation in Argon
100 bar
800 bar
300 bar
1600 bar
600 bar
3200 bar
800
500
200
0
2
4
6
8
Time (ps)

Figure 28

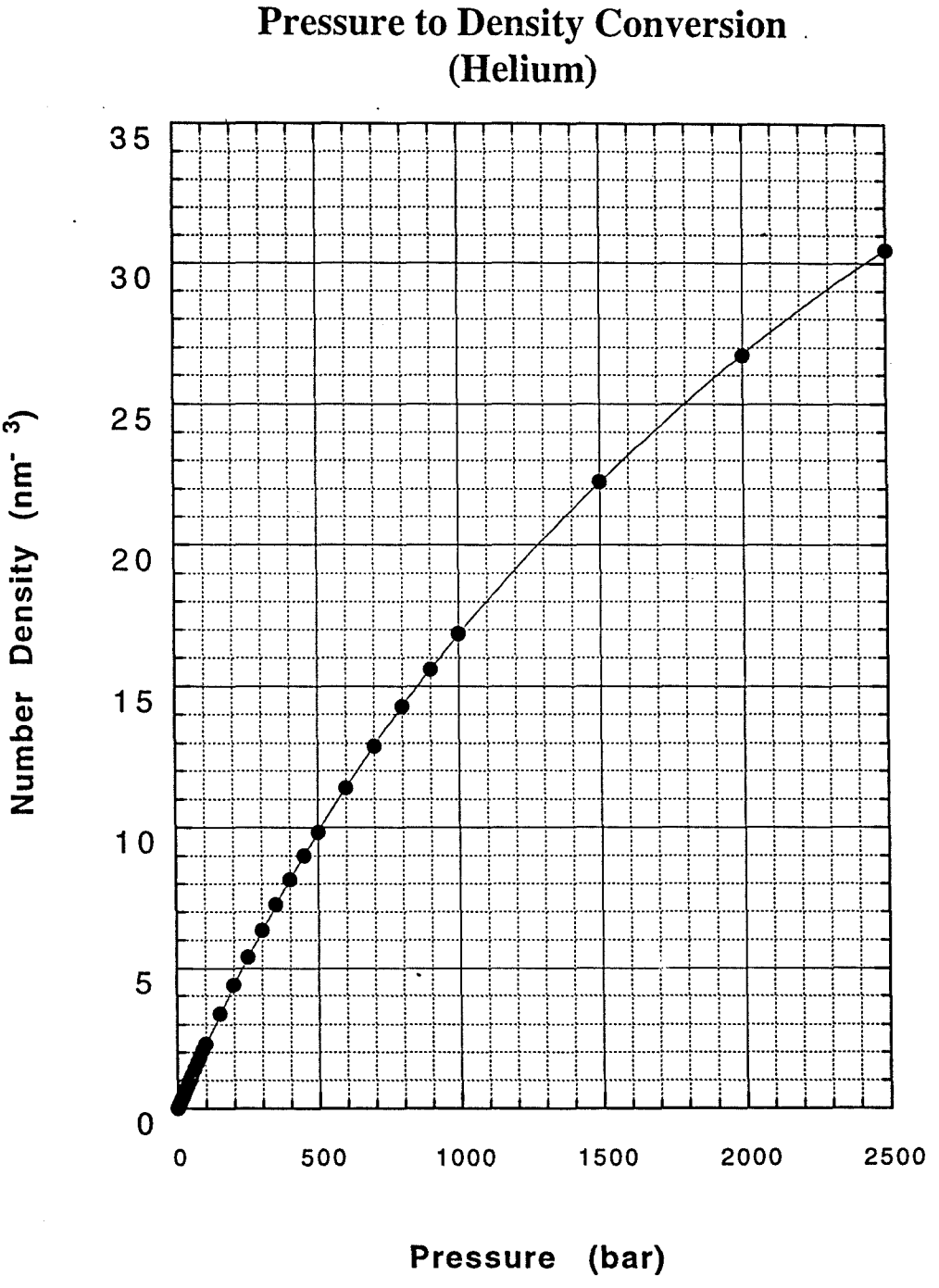
Pressure to Density Conversion
(Helium)
Number Density (nm^{-3})
35
30
25
20
15
10
5
0
0
500
1000
1500
2000
2500
Pressure (bar)

Figure 29

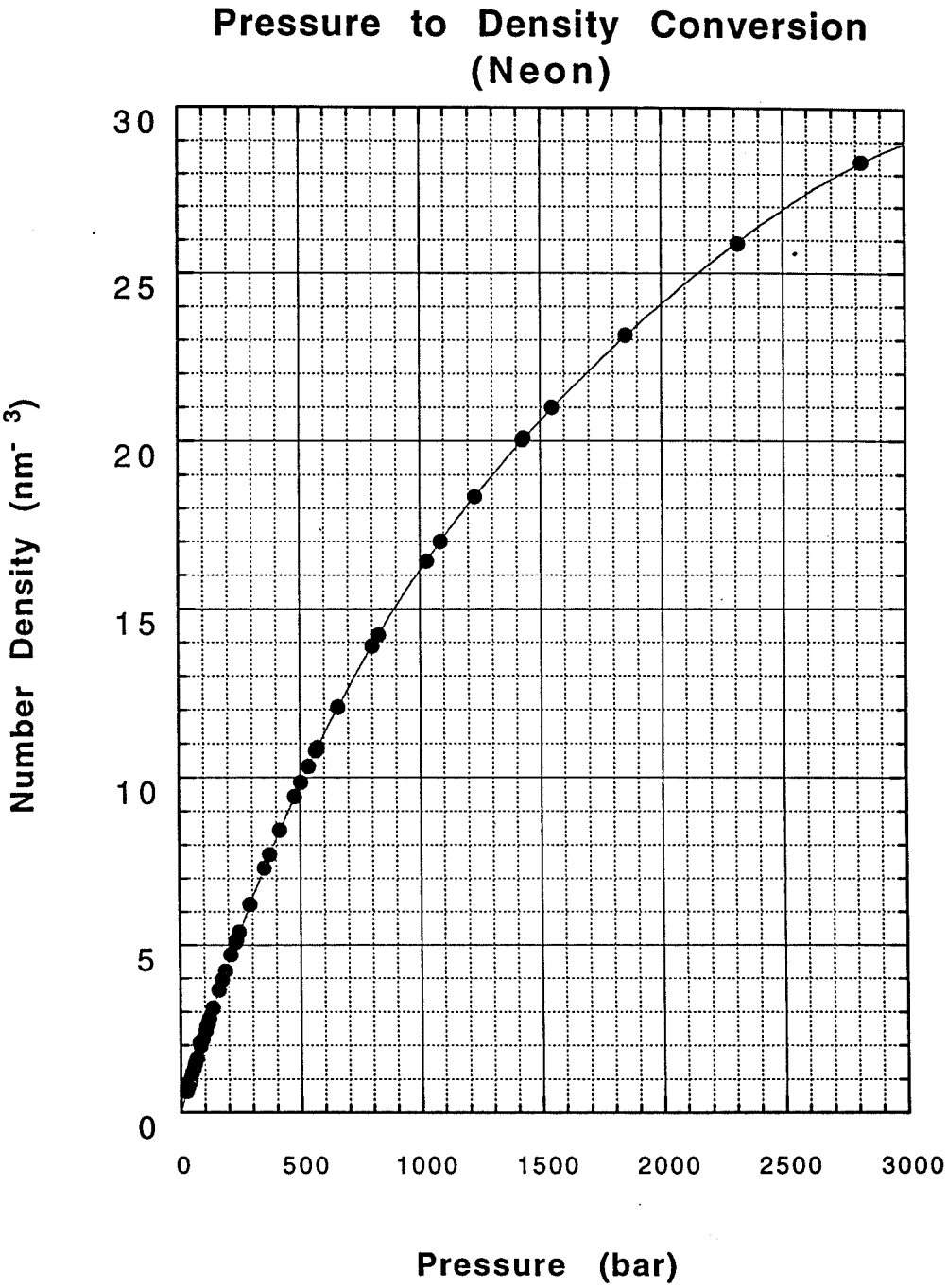
Pressure to Density Conversion
(Neon)
Number Density (nm^{-3})
30
25
20
15
10
5
0
0
500
1000
1500
2000
2500
3000
Pressure (bar)

Figure 30

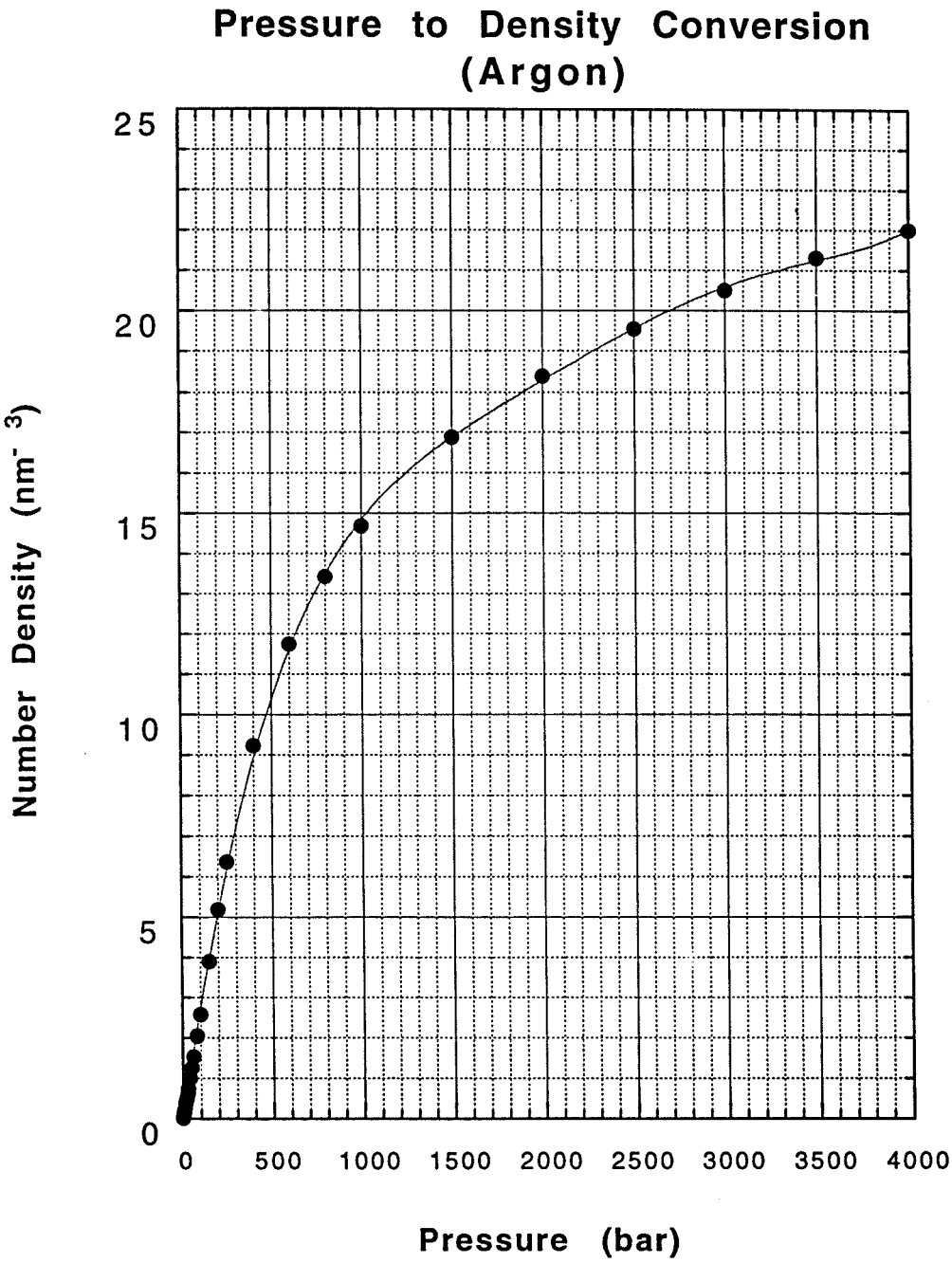
Pressure to Density Conversion
(Argon)
Number Density (nm- 3)
25
20
15
10
5
0
0
500
1000
1500
2000
2500
3000
3500
4000
Pressure (bar)

Figure 31

Chapter 4

Femtosecond Studies of Vibrational Phase and Energy Relaxation Dynamics of I_2 in Supercritical Fluids

4.1. Introduction

Femtosecond studies of molecular reactions in the gas-to-liquid transition region offer a unique opportunity to examine the solvation dynamics on the time scale of nuclear motions and as functions of solvent density. Previously, the pressure dependence of iodine dissociation and caging in rare-gas solvents was examined across a wide range from 0 up to 4000 bar.[1-4] Here, the vibrational coherence and relaxation dynamics are studied for solute iodine in solvent rare gases (He, Ne, and Ar) and across a similar pressure range. Specifically, by resolving the wave packet vibrational motion and the loss of its coherence, we are able to examine the density dependence of the different solvent forces controlling the reaction dynamics. Extensive molecular dynamics (MD) simulations of the radial distribution functions, force and velocity correlation functions, and correlation functions of the vibrational amplitude and energy give the microscopic picture.

In liquids, the subject of vibrational dephasing has attracted considerable attention over the past few decades (see, for example, Refs. [5-12]). Theoretically, based on a simple independent binary collision model, Fischer and Laubereau predicted a linear dependence of dephasing rate on the collision frequency and, hence, density.[6] Oxtoby derived a hydrodynamic theory which accounts for a linear dependence.[13] Brueck considered the effect of vibration-rotation coupling and predicted that its contribution to the dephasing rate is inversely proportional to the collision frequency in the motion narrowing regime.[7] Schweizer and Chandler developed a general theory to include the repulsive and attractive forces and the vibration-rotation couplings.[9] In the liquid density regime, they considered

the separate influence of the different forces based on different time scales of action. Their theory predicted a positive density dependence of dephasing rates induced by the repulsive force and negative density dependence of the rates induced by the attractive force and vibration-rotation couplings.[9]

MD simulations have been invoked to examine the theoretical predictions (see, e.g., Refs. [14-16]). For example, Michels et al recently examined the isothermal density dependence of dephasing dynamics in the nitrogen system.[16] Their simulations reproduced the experimental observation and revealed the significance of vibration-rotation coupling in the dephasing dynamics, particularly at low densities. Experimentally, the nitrogen system has been studied extensively;[10-12] the vibrational dephasing rate (line-width) displayed a negative density dependence at low density values and a positive density dependence at high density values. The negative density dependence was attributed to the vibration-rotation coupling effect.

Here, our focus is on femtosecond studies of the dephasing (T_2 process) and the relaxation (T_1 process) dynamics of solute iodine in solvent rare gases, obtained directly from the transient behavior of the wave packet motion. At room temperature, the solvent systems are above the critical point as shown in Fig. 1, for example, for argon (T_C = 150.70 K, P_C = 48.6 bar[17]) . As the pressure changes from 0 to 4000 atmospheres, the solvent density increases continuously with no phase transition. The phase diagrams are similar for He (T_C = 5.19 K, P_C = 2.27 bar for ^{4}He[17]) and Ne (T_C = 44.40 K, P_C = 26.53

bar[17]). The bulk density ρ can be changed continuously from zero and up to liquid-like densities.

As the solvent density is increased from $\rho = 0$ to about $\rho = 50$ *mol/l* (30 nm^{-3}), the reduced density $\rho^* \equiv \rho\sigma^3$, where σ is the solvent diameter, reaches values close to one. A near-linear behavior of $1/T_1$ with density (except at very high ρ) is observed, while a striking nonlinear behavior of $1/T_2$ with density is discovered. At low densities, $1/T_2$ increases rapidly with the density. At intermediate densities, $1/T_2$ is essentially constant. At densities near or above liquid values, $1/T_2$ increases rapidly again. Based on a simple classical model, the observed results are reproduced for all three solvents by considering the decay of the correlation function of the reaction nuclear coordinate $\langle Q(t)Q(0)\rangle$.

With semi-classical analysis, the observed density dependence of $1/T_2$ is found to be controlled by two different acting forces: the solute-solvent collision forces and the centrifugal forces (vibration-rotation couplings). The former dominates the dephasing dynamics only at very high densities. The latter contribution to dephasing is significant at densities up to the liquid-like values. The opposite trends of change with density for these two forces give rise to the seemingly "abnormal" density dependence observed experimentally. With MD simulations (see Chapter 3), we examined the different time scales for the correlation of these forces and for the solvent fluctuations, covering the two regimes of *slow* modulation and *fast* modulation (motion narrowing).

This chapter is organized as follows. In the next section, the experimental setup is briefly described and the results are presented. In Section 4.3, the results of MD

simulations are presented and compared with the experimental observations and with other theoretical predictions. Conclusions are given in Section 4.4.

4.2 Experimental

An overall schematic of the experimental setup is shown in Fig. 2,[18] and the laser system is shown in Fig. 3. The 60 fs laser pulses, centered at 620 nm, with a repetition rate of 100 Mhz and a pulse energy of 20 pJ, were generated from a home-built colliding-pulse mode-locked ring dye laser (CPM, see Fig. 3). The CPM laser consists of a gain jet (Rhodamine 6G/ethyleneglycol), a saturable absorber jet (DODCI/ethyleneglycol), seven single-stack dielectric mirrors, and four quartz prisms. It is pumped by a multi-line CW argon ion laser (Coherent Innova 310 with PowerTrack) running at ~ 3 Watt. The 20 pJ output pulses of the CPM were amplified to more than 1.5 mJ in a four-stage pulsed dye amplifier (PDA, see Fig. 3) pumped by the second harmonic output of a 30 Hz Nd:YAG laser (Spectra Physics GCR 4A). Sulforhodamine B dissolved in water was used in the first amplifier stage, while Rhodamine 640 dissolved in water was used in the last three stages. Amplified spontaneous emission was reduced by spatial filters after stages 1 and 3 and by a saturable absorber jet (Malachite Green/ethyleneglycol) placed after stage 2.

While the first three stages were pumped transversally, the fourth stage was a longitudinally pumped double-pass cell, and the YAG laser profile in this cell was expanded to a diameter of 1 cm. The amplified pulses were temporally re-compressed in a double-pass, two-prism sequence to a pulse width of 60 fs FWHM (assuming a Gaussian pulse profile) and then split by a 50/50 dichroic beam splitter into the pump and probe arms of a Michelson interferometer. In the probe arm, 310 nm pulses with a pulse duration of 60 fs were generated by frequency-doubling the attenuated red pulses in a 1 mm KDP crystal. The pump beam passed through two polarizers and a half-wave plate to

allow variation in the relative polarization of pump and probe lasers. The angle between pump and probe polarization was kept constant at 54.7° (the "magic" angle). Studies of the rotational anisotropy at high pressures will be discussed elsewhere.[19]

The pump and probe lasers were overlapped by means of a dielectric beam splitter and were focused slightly beyond the output window of the high-pressure cell in order to prevent white light continuum generation. Laser-induced fluorescence was collected at right angles to the laser propagation direction, collimated into a 20 cm, computer-controlled monochromator and detected with a photomultiplier tube (PMT). The slit width of the monochromator was kept at 2 mm, which corresponds to a spectral width of 6 nm (FWHM). The fluorescence signal from the PMT was averaged in a boxcar integrator and recorded as a function of delay between the pump and probe pulses. This delay was controlled using a high precision computer-controlled actuator that allowed for optical delays of up to 1 ns with a minimal stepsize of 0.7 fs. Five data points were accumulated at each actuator position. In a typical experimental scan, data were recorded at 200 to 400 different actuator positions. The scans were repeated until the desired signal-to-noise ratio was achieved, which required, in general, 10 to 80 scans.

The home-built high-pressure cell was constructed from heat-treated stainless steel (Vascomax 300, tensile strength 300,000 psi). Four optical windows (diameter 6 mm, clear aperture 2 mm) were centered in each of the four walls. The input window is 4.0 mm thick quartz, while the output and fluorescence collection windows are 2.8 mm thick sapphire. Quartz windows are advantageous in that they reduce the temporal

dispersion of the femtosecond pulses. The pressure in the cell was constantly monitored with a high precision strain gauge pressure transducer and the temperature inside the cell could be measured with a commercial high pressure thermocouple. The distance between input and output windows was chosen at 6 mm, so that the total cell volume was limited to 0.2 cm^3. Such a small cell volume is essential because it allows, even in the case of rare gases, the use of a small, manually operated, screw-type pressure generator. Pressure inside the cell was generated by flushing the rare gas into the pre-evacuated cell and manually compressing it to the desired pressure in an iterative process. To reach pressures above 1200 bar, the rare gas had to be pre-compressed to 300 bar by liquefication in a pressure-resistant cryotrap (see Fig. 2). The cell showed no decrease in pressure (less than 1 bar) during the course of an experiment.

The relevant potential energy surfaces of iodine are shown in Fig. 4. The pump pulse (620 nm) excites I_2 from its ground state $X\,0_g^+(^1\Sigma)^{20}$ to a valence state $B0_u^+(^3\Pi)$ and prepares a coherent wave packet around the 8th vibrational level.[3] The probe pulse (310 nm) further excites the wave packet to an ion-pair state (E or f) from where laser-induced fluorescence occurs.[18]

For iodine in helium, the laser-induced fluorescence transients are shown in Figs. 5 to 7 for pressures ranging from 0 to 2150 bar. The time zero in these transients corresponds to a zero time delay between the pump excitation and the probe detection. The positive time means that the probe pulse follows the pump pulse. In the absence of the solvent, i.e., at 0 bar, the fluorescence signal displays periodic oscillations. The

oscillation, with a period of about 300 fs, represents the periodic motion of the coherent wave packet near the excitation level (8th vibration level) on the B state. The modulation, with a long time recurrence at about 10 ps is caused by the anharmonicity of the B state potential[20]. The anharmonicity causes different components of the wave packet to become out of phase, by group velocity dispersion, and in phase again as the dispersion-induced phase shifts become integers of 2π. This dispersion induced phase modulation is fundamentally different from the dephasing effect to be discussed below in that the phase shifts are correlated in the case of dispersion. In the case of dephasing, the phase correlation is permanently lost.

The amplitude of recurrence is reduced as the helium pressure is increased. It almost disappears at 75 bar, indicating that the solvent induced dephasing has gradually destroyed the phase correlation among components of the wave packet (at the longer times of recurrences). At higher pressures the average signal level also decreases with time. This signal decay reflects the vibrational relaxation and electronic pre-dissociation of iodine on the B state, while the change of oscillation amplitude is indicative of a phase spread or dephasing of the wave packet. As the pressure is increased, both the energy relaxation rate (k_1) and the dephasing rate (k_2) increase, but differently. The transients obtained for neon are shown in Figs. 8 to 10 for pressures from 0 to 2550 bar; the transients for argon are shown in Figs. 11 to 13 for pressures from 0 to 3000 bar. The behaviors of these transients appear similar to those described for helium; their density dependencies are given below.

4.3. Results and Discussion

The wave packet, excited by the pump pulse, consists of several frequency components ω_i (i = 0, 1, 2, ...), corresponding to different vibrational levels. Neglecting the coherence between the ground (X) and the exited (B) state, the wave packet can be expressed as:[20]

$$|\psi\rangle = \sum_i b_i e^{-i\omega_i t - i\varphi_{i0} - i\int_0^t \omega_i'(t')dt'} |i\rangle \tag{4.1}$$

where b_i is the coefficient of the ith vibrational level, φ_{i0} is the initial phase, ω_i' is the solvent-induced instantaneous frequency shift, $\int_0^t \omega_i'(t')dt'$ is the accumulated phase shift, and $|i\rangle$ is the eigenstate of the ith vibrational level of the B state. The transient signal is given by

$$S(t) \propto \left|\langle ip|\vec{\mu}\cdot\vec{E}_{probe}|\psi\rangle\right|^2 \tag{4.2}$$

where $|ip\rangle$ represents the ion-pair state, and $\vec{\mu}\cdot\vec{E}_{probe}$ represents the probe-pulse induced dipole transition between the B and the ion-pair states. For a particular system, one obtains

$$S(t) \propto \left|\sum_i a_i e^{-i\omega_i t - i\varphi_{i0} - i\int_0^t \omega_i'(t')dt'}\right|^2 \equiv \mathrm{Re}\left(\sum_{i,j} a_i^* a_j e^{i\omega_{ij}t + i\varphi_{ij0} + i\delta\varphi_{ij}}\right), \tag{4.3}$$

where $\omega_{ij} \equiv \omega_i - \omega_j$, $a_i \equiv \langle ip|\vec{\mu}\cdot\vec{E}_{probe}|i\rangle b_i$, $\varphi_{ij0} \equiv \varphi_{i0} - \varphi_{j0}$, and $\delta\varphi_{ij} = \int_0^t \delta\omega_{ij}(t')dt'$ is the accumulated phase shift between the ith and jth levels with $\delta\omega_{ij}(t) \equiv \omega_i'(t) - \omega_j'(t)$.

The transient signal is then described by an ensemble average of Eq. (4.3), i.e.,

$$S(t) = \left\langle \mathrm{Re}\left[\sum_{i,j} a_i a_j \exp\left(i\omega_{ij}t + i\varphi_{ij0} + i\delta\varphi_{ij}\right)\right]\right\rangle. \tag{4.4}$$

Assuming that the relaxation rate k_1 is the same for all relevant components, i.e., $|a_i|^2 = a_{i0}^2 e^{-k_1 t}$, the above equation is reduced to

$$S(t) = e^{-k_1 t}\sum_i a_{i0}^2 + e^{-k_1 t}\sum_{i\neq j} a_{i0}a_{j0}\cos\left(\omega_{ij}t + \varphi_{ij0}\right)\phi(t). \tag{4.5}$$

The factor $\phi(t) \equiv \left\langle \mathrm{Re}\left(e^{i\int_0^t \delta\omega_{ij}(t')dt'} \right)\right\rangle$ is the relaxation function defined in Chapter 2. By using the cumulant expansion theorem[5], $\phi(t)$ reduces to an exponentially decaying function in the limit of fast modulation (see Chapter 2), i.e.,

$$\left\langle \mathrm{Re}\left(e^{i\int_0^t \delta\omega_{ij}(t')dt'} \right)\right\rangle = e^{-k_2' t} \tag{4.6}$$

where $k_2' \equiv 1/T_2'$ is the phase relaxation rate (pure dephasing rate). In this case, Eq. (4.5) is simplified to:

$$S(t) = Be^{-k_1 t} + e^{-k_2 t}\sum_{i\neq j} C_{ij}\cos\left(\omega_{ij}t + \varphi_{ij0}\right), \tag{4.7}$$

where B and C_{ij}'s are constants, and $k_1(1/T_1)$ is the energy relaxation rate while $k_2 \equiv k_1 + k_2'$ is the total dephasing rate $(1/T_1 + 1/T_2')$. In the limit of slow modulation, $\phi(t)$ reduces to a Gaussian form, as shown in Chapter 2. For simplicity, the exponential form was used to fit the experimental transients (for $t > 0$). For three frequency components, the following expression was used:

$$S(t) = A + Be^{-k_1 t} + e^{-k_2 t}\sum_{\alpha=1}^{3} C_\alpha \cos\left(\omega_\alpha t + \varphi_\alpha\right). \tag{4.8}$$

The parameter A is included to account for the signal offset of the transients. The experimental results and their fits, after subtraction of the second term in Eq. (4.8), are plotted in Fig. 14 for He at two densities. The features of coherent oscillations, recurrences, and dephasing have all been fit well by the simple model. Good fits were also achieved for the transients at higher densities and for other rare gases. To assess the range of uncertainty in the fits we have also invoked different treatments of the data, including the use of Fourier transform and fits of the entire data with or without subtraction of the diagonal term in Eq. (4.8).

It was noticed that the values of the three frequencies become closer to each other at higher pressures. At pressures higher than 100 bar, the transients could be well fitted by virtually a single damped cosine function. This is consistent with results from Fourier transformation given in the preceding paper.[4] Three separated peaks were shown at 0 bar. As the pressure increases, the peaks were gradually spread out and merged into one broad peak.

The fitting results for k_1 and k_2 are plotted in Fig. 15, Fig. 16, and Fig 17 for helium, neon, and argon, respectively. The lines in these figures are polynomial fits (filled circle for $k_2(\rho)$, open square for $k_1(\rho)$) with parameters listed in Table 1 for all three systems. The general behaviors of both the $k_1(\rho)$ and the $k_2(\rho)$ with density are very similar for the three rare gas solvents. The measured k_1 represents the pre-dissociation/vibrational relaxation rate, as discussed in the preceding papers. Its behavior with density is as expected: near linear increase at low densities and non-linear increase at

high densities. The $k_2(\rho)$ behavior, on the other hand, is very striking: it shows a three-phase density dependence. For comparisons, the classical simulation results for the dephasing and relaxation rates are also plotted in these figures.

The relaxation rate k_1 is obtained in the simulation by fitting the calculated $E_v(t)$ curves to exponential functions:

$$E_v(t) = E_0 e^{-k_1 t}. \tag{4.9}$$

The parameter k_1 thus obtained only represents the vibrational energy relaxation rate, since the non-adiabatic coupling of the B to dissociative states has not been included explicitly in the simulation. This coupling has recently been modeled in a series of papers by Ben-Nun et al.[21]

The simulation results for the dephasing rate k_2 were obtained by fitting the directly calculated correlation functions $\langle Q(t)Q(0)\rangle$ (see Chapter 3) to the following damped cosine function:

$$\langle Q(t)Q(0)\rangle = Q_0^2 \exp\left(-\frac{t}{\tau_e} - \frac{t^2}{2\tau_g^2}\right)\sum_{n=0}^{3} A_n \cos(n\omega t + \varphi_n), \tag{4.10}$$

where ω is the oscillation frequency, τ_g and τ_e are the dephasing time contributions from the Gaussian and exponential components, respectively. In the above equation, a double and a triple frequency components have been included to properly fit the anharmonic oscillations on the iodine B state. The value of τ_e approaches infinity at low densities and the exponential contribution becomes significant only at high densities. The dephasing

rate k_2 is defined as $k_2 = 1/\tau_{1/2}$, where $\tau_{1/2}$ is the time when $\langle Q(t)Q(0)\rangle$ decays to one half of its initial value.

The experimental results for k_2 are sums of the pure dephasing rates and the population relaxation rate k_1. Experimentally, k_1 is a measure of both vibrational and electronic (pre-dissociation) relaxation rates. To focus on the phase relaxation rate, we need to obtain the pure dephasing rates for both experiments and simulations. The experimental pure dephasing rate k_2' has been obtained by subtracting $k_1(\rho)$ from $k_2(\rho)$. The results are plotted in Fig. 18a, Fig. 19a, and Fig. 20a for He, Ne, and Ar, respectively. Similarly, the classical simulation results for k_2 also have a contribution from the vibrational energy relaxation rate. For a classical oscillator, its vibrational energy E_v is related to the amplitude of the oscillation $Q_{\max}$ by

$$E_v(t) = \frac{1}{2}\mu\omega^2 Q_{\max}^2(t). \tag{4.11}$$

If E_v decays in time according to Eq. (4.9), then $Q_{\max}$ will decay in time at half that rate ($k_1/2$). This decay of $Q_{\max}$ will lead to an equivalent decay component in the relaxation function obtained for an classical oscillator. To obtain the pure phase relaxation rate, this decay component has been subtracted from k_2. The pure dephasing rates obtained from classical simulations are plotted in Fig. 18b, Fig. 19b, and Fig. 20b for He, Ne, and Ar, respectively, to compare with the experimental counter-parts.

Besides the dephasing, the central frequency of the nuclear vibration was also obtained. It was found to be blue shifted due to solvation. From fitting of the

experimental transients, the frequency shifts have been obtained for all three solvents and are plotted in Fig. 21a. At 0 bar, the central frequency is about 113 cm^{-1}, close to the vibrational period around the 8th vibrational level[20]. The frequency shift is caused by both the mean solvent forces and the coherent vibrational relaxation. The MD simulation results for the frequency shift are plotted in Fig. 21b for comparison.

The most significant characteristics of the experimental results can be summarized as follows:

1) The density dependence of the dephasing rate is very different in three different regions of the number density. At low densities, i.e., $\rho < 5\ nm^{-3}$, the dephasing rate almost linearly increases with the density and the rate of change is fast: about 0.1 ps^{-1}/nm^{-3} for all three solvents. At intermediate densities, i.e., $6\ nm^{-3} < \rho < 20\ nm^{-3}$, the dephasing rate is not as sensitive to the change of number density: slightly increasing for neon while slightly declining for helium and argon. The slops of the curves in this range are between plus and minus 0.01 ps^{-1}/nm^{-3} for all three solvents. At very high densities, i.e., $\rho > 20\ nm^{-3}$, the dephasing rate increases again quickly with the density, reaching about 0.05 ps^{-1}/nm^{-3} for He, 0.06 ps^{-1}/nm^{-3} for Ne, and 0.12 ps^{-1}/nm^{-3} for Ar.

2) Throughout a broad density region, i.e., $0\ nm^{-3} < \rho < 20\ nm^{-3}$, the dephasing rates measured for the three different solvents are nearly identical: the differences are less than 20%. On the other hand, from He to Ar, the atomic mass of the solvent changes from 4 *amu* to 40 *amu*, while the I-Rg (Rg = He, Ne, or Ar) van der Waals binding energy changes from 14 cm^{-1} to more than 130 cm^{-1}.

3) The blue-shift of the vibrational frequency *increases* with the solvent density for all three solvents. The magnitude of the blue-shift is maximum for argon and minimum for helium.

The classical simulations have near-quantitatively reproduced all these observations, except for the frequency shift in argon. The difference in numerical values of the dephasing and relaxation rates is about 10%, which is surprisingly small considering the simple model used. In obtaining the classical vibration correlation functions, 512 trajectories were used in the ensemble average. The statistical errors involved are, therefore, expected to be about 10% as well. The agreement also confirms that the classical treatment of the iodine vibration seems valid for the system under study. Although the classical simulation has reproduced and, in a way, confirmed the seemingly "abnormal" density dependence of the dephasing rate, it has not provided an explicit description of the microscopic picture. The question of significance is: What microscopic processes have caused the three-phase behavior of the dephasing rates? The semi-classical simulation was carried out to provide the answer.

In the semi-classical approach, the collision force induced dephasing rate $T_{2;R}^{-1}$ was calculated according to Eq. (2.54). The vibration-rotation coupling induced dephasing rate $T_{2;VR}^{-1}$ was calculated according to Eq. (2.56). The total dephasing rate was taken to be the sum of $T_{2;R}^{-1}$ and $T_{2;VR}^{-1}$. The results are plotted in Fig. 22, Fig. 23, and Fig. 24 for He, Ne, and Ar, respectively. The behavior of the total dephasing rate with density was also plotted in Figs. 18 to 20 in order to compare with the experimental and classical

simulation results. From these results, it can be seen that the semi-classical MD simulations agree well with the experimental and classical simulation results, both for the general trends and for the absolute values.

In the semi-classical calculations, we separately considered the external solute-solvent forces and the vibration-rotation couplings. As shown in Figs. 22 to 24, the former contribution to the dephasing rate increases with the number density almost linearly at low densities. At high densities the dependence becomes nonlinear and the dephasing rate increases more drastically. This is because the solvent atoms start to pack closely with each other and the collision forces increase non-linearly with further density increase, as shown in Chapter 3.

However, the collision force induced dephasing rate is much less than that from vibration-rotation couplings, except for high densities. The latter shows a fast near-linear increase with the number density until a maximum value of about 0.4 ps^{-1} is reached at about 5 atoms/nm^3. In this region, the amplitude of the correlation function of the rotational energy fluctuation also increases near-linearly, as shown in Chapter 3. The correlation time, which is related to the time interval between collisions, is longer than the dephasing time in this region. The vibration-rotation coupling can, therefore, be described by the "slow modulation," which has caused the vibration correlation functions to be dominated by a Gaussian shape at low densities.

The amplitude of fluctuations in the vibration-rotation coupling, i.e., ΔE_{rot}, is on the order of $k_B T$ when thermal equilibrium is reached. At densities near or above 5

atoms/nm^3, the collision rate becomes fast enough for the solute rotational mode to be equilibrated with the solvent on the time scale of dephasing. At higher densities, the amplitude of fluctuations in the vibration-rotation coupling will not increase further, as shown by the MD simulations reported in Chapter 3. Because the key parameter here is the thermal energy (k_BT), which is the same for all three solvent systems studied, the maximum dephasing rate induced by the vibration-rotation coupling shall be very nearly the same for He, Ne, and Ar.

At higher densities, the correlation time τ_{VR} continues to decrease with density, while the amplitude of the coupling remains almost constant. In this density regime, τ_{VR} becomes shorter than the dephasing time, so that the integral in Eq. (2.57) start to decrease with the increase of the solvent density. As the density is increased further, the vibration-rotation coupling gradually shifts to the "fast modulation" regime, leading to a decrease in the dephasing rate as a consequence of the "motion narrowing" effect.

The decrease of the vibration-rotation coupling causes its contribution to the dephasing rate to become less significant at the high densities. As shown in Figs. 22 to 24, the decrease of the $T_{2;VR}^{-1}$ is partially compensated for by the increase of $T_{2;R}^{-1}$ in the intermediate density region. At densities near or above 20 atoms/nm^3, the latter contribution becomes dominant and increases quickly with the solvent density. The experimentally observed "three-phase" density dependence of the dephasing rate is, therefore, caused by the interplay of the two acting forces with opposing trend in the intermediate and high density regions.

It is also interesting to compare our results with predictions made by other theoretical models. The dephasing rate $T_{2;R}^{-1}$ predicted by the IBC theory[8] was calculated according to Eq. (2.6) and the results are plotted in Figs. 22 through 24. We have also applied Schweizer and Chandler's theory[9] and calculated the dephasing rates $T_{2;R}^{-1}$ and $T_{2;VR}^{-1}$ according to Eqs. (2.7) and (2.12), respectively. It is important to note that these equations were derived based on the fast modulation approximation and we maintained the $\tau_c < T_2$ criteria (from MD) in the calculation. The calculation, therefore, only covers the densities above 5 nm^{-3} for $T_{2;VR}^{-1}$, but is valid for all densities for $T_{2;R}^{-1}$. For the collision force induced dephasing rates, the IBC theory gives similar values to the simulation results. The results predicted by the Schweizer and Chandler's theory for $T_{2;R}^{-1}$ reproduce the correct trend; a scaling factor of ~ 3 is needed to bring the absolute values to those of the simulations. Qualitatively, the negative density dependence of $T_{2;VR}^{-1}$ is predicted, but the rate of change with density and the absolute magnitude are not consistent with our results, probably because the fast-modulation approximation is not valid throughout the density range.

The vibrational frequency shift is a measure of the influence of mean solvent forces, as shown by Eq. (2.35) of Chapter 2. Experimentally, the behavior of the frequency shift with density is nearly linear for the three rare gases (Fig. 21a). Such dependence has been reproduced by the MD simulations at densities of up to ~ 20 atoms/nm^3 for He and Ne (Fig. 21b). As mentioned in the preceding paper, the slope is larger than what is predicted by a hard-fluid model. Furthermore, at higher densities, a

non-linear behavior becomes significant in the MD simulations. We attribute this discrepancy to the coherent vibrational relaxation, which causes the wave packet to step down to lower vibrational levels with higher frequencies because of the anharmonicity. This transfer occurs impulsively on short time scales to maintain the phase coherence after relaxation.[22,23] In the case of Ar, the relatively higher van der Waals binding energy (about 250 cm^{-1} between I_2 and Ar; 130 cm^{-1} between I and Ar; 80 cm^{-1} between Ar and Ar) appears to cause pseudo-stable argon clusters to form at intermediate densities, in accordance with the MD simulations. The formation of such clusters results in a more efficient coherence transfer, as shown in Fig. 21b.

4.4. Conclusion

In this chapter, we have studied the femtosecond coherence dynamics of the dissociation reaction of iodine in rare gas solvents of He, Ne, and Ar at different densities. The phase coherence and energy relaxation rates are measured directly from the transient behavior of the wave packet motion. The separation of T_1 and T_2 type processes shows a striking density dependence and defines three phases of density behavior. With molecular dynamics simulations, we identify the forces controlling the behavior over the entire density range, from gas-phase binary collisions at low densities to liquid-like densities (ρ ~ 30 atoms/nm^3 ~ 50 mol/l; ρ^* ~ 0.8). We also studied the effect of the solvent force field on the resonance frequency of the wave packet. MD simulations reproduced the experimental results and revealed the microscopic elements of the dynamics. Studies of the radial distribution functions, velocity correlation functions, collision rates and force correlation functions, and their relevant time scales have established the origin of the density dependencies and indicated the transition from *slow* to *fast* modulation of solvent fluctuations. Finally, we invoked some analytical descriptions of dephasing and compared with the MD simulations and the experimental results. We identify the significance of two opposing forces, the usual collisional force due to inter-molecular interactions and the centrifugal force caused by the solute rotation in the solvent structure. The correlation times for these forces change differently with density and account for the novel phenomena investigated here.

4.5. References

1 A. H. Zewail, M. Dantus, R. M. Bowman, and A. Mokhtari, *J. Photochem. Photobiol.* **A 62,** 301 (1992).

2 Y.-J. Yan, R. M. Whitnell, K. R. Wilson, and A. H. Zewail, *Chem. Phys. Lett.* **193,** 402 (1992).

3 C. Lienau and A. H. Zewail, *J. Chim. Phys.* **92,** 566 (1995); C. Lienau and A. H. Zewail, *Chem. Phys. Lett.* **222,** 224 (1994); C. Lienau, J. C. Williamson, and A. H. Zewail, *Chem. Phys. Lett.* **213,** 289 (1993).

4 C. Lienau, A. Materny, and A. H. Zewail, *J. Phys. Chem.* (1996), in press; A. Materny, C. Lienau, and A. H. Zewail, *J. Phys. Chem.* (1996), in press.

5 R. Kubo, in *Fluctuations, Relaxation and Resonance in Magnetic Systems*, edited by D. t. Haar (Plenum, New York, 1962).

6 S. F. Fischer and A. Laubereau, *Chem. Phys. Lett.* **35,** 6 (1975).

7 S. R. J. Brueck, *Chem. Phys. Lett.* **50,** 516 (1977).

8 D. W. Oxtoby, *Adv. Chem. Phys.* **40,** 1 (1979).

9 K. S. Schweizer and D. Chandler, *J. Chem. Phys.* **76,** 2296 (1982).

10 R. Kroon, M. Baggen, and A. Lagendijk, *J. Chem. Phys.* **91,** 74 (1989).

11 B. Lavorel, B. Oksengorn, D. Fabre, R. Saint-Loup, and H. Berger, *Mol. Phys.* **75,** 397 (1992).

12 M. I. M. Scheerboom and J. A. Schouten, *Phys. Rev. E* **51,** R2747 (1995).

13 D. W. Oxtoby, *J. Chem. Phys.* **70,** 2605 (1979).

14 D. W. Oxtoby, D. Levesque, and J. J. Weis, *J. Chem. Phys.* **68,** 5528 (1978).

15 J. Chesnoy and J. J. Weis, *J. Chem. Phys.* **84,** 5378 (1986).

16 J. P. J. Michels, M. I. M. Scheerboom, and J. A. Schouten, *J. Chem. phys.* **103,** 8338 (1995).

17 R. K. Crawford, in *Rare Gas Solids*, Vol. 2, edited by M. L. Klein and J. A. Venables (Academic, London, 1977); see also R. B. Steward and R. T. Jacobson, J. Phys. Chem. Ref. Data, **18,** 639 (1989).

18 C. Lienau, J. C. Williamson, and A. H. Zewail, *Chem. Phys. Lett.* **213,** 289 (1993).

19 C. Wan, M. Gupta, and A. H. Zewail, *To be published* (1996).

20 M. Gruebele and A. H. Zewail, *J. Chem. Phys.* **98,** 883 (1993).

21 M. Ben-Nun and R. D. Levine, *Chem. Phys.* **201,** 163 (1995).

22 J. M. Jean and G. R. Fleming, *J. Chem. Phys.* **103,** 2092 (1995).

23 N. Pugliano, A. Z. Szarka, and R. M. Hochstrasser, *J. Chem. Phys.* **104,** 5062 (1996).

24 W. Wagner, *Cryogenics* **13,** 470 (1973).

25 A. Michels, J. M. Levelt, and W. D. Graaff, *Phsica* **24,** 659 (1958).

4.6. Tables

Table 1 Density dependence of $k_1(\rho)$ and $k_2(\rho)$ - experimental results.

a) $k_1(\rho) = A_0 + A_1\rho + A_2\rho^2 + A_3\rho^3$

(ρ is in unit of nm^{-3})

Solvent	$A_0\,(ps^{-1})$	$A_1\,(ps^{-1}\cdot nm^3)$	$A_2\,(ps^{-1}\cdot nm^6)$	$A_3\,(ps^{-1}\cdot nm^9)$
He	-0.01074	0.01735	-7.697×10^{-4}	2.655×10^{-5}
Ne	-0.02130	0.02257	-9.298×10^{-4}	3.348×10^{-5}
Ar	-0.04134	0.04247	-1.594×10^{-3}	4.929×10^{-5}

b) $k_2(\rho) = B_0 + B_1\rho + B_2\rho^2 + B_3\rho^3 + B_4\rho^4$

(ρ is in unit of nm^{-3})

Solvent	$B_0\,(ps^{-1})$	$B_1\,(ps^{-1}\cdot nm^3)$	$B_2\,(ps^{-1}\cdot nm^6)$	$B_3\,(ps^{-1}\cdot nm^9)$	$B_4\,(ps^{-1}\cdot nm^{12})$
He	0.06625	0.1194	-0.01155	4.120×10^{-4}	-4.543×10^{-6}
Ne	0.04688	0.1069	-0.007434	1.982×10^{-4}	-8.264×10^{-6}
Ar	-0.09692	0.1531	-0.009877	2.967×10^{-4}	-2.368×10^{-6}

Table 2 Density dependence of $k_1(\rho)$ and $k_2(\rho)$ - simulation result

a) $k_1(\rho) = A_0 + A_1\rho + A_2\rho^2 + A_3\rho^3$

(ρ is in unit of nm^{-3})

Solvent	$A_0\,(ps^{-1})$	$A_1\,(ps^{-1}\cdot nm^3)$	$A_2\,(ps^{-1}\cdot nm^6)$	$A_3\,(ps^{-1}\cdot nm^9)$
He	-6.09×10^{-3}	9.49×10^{-3}	-3.92×10^{-4}	1.34×10^{-5}
Ne	-1.01×10^{-2}	1.83×10^{-2}	-8.75×10^{-4}	3.36×10^{-5}
Ar	-8.76×10^{-3}	3.20×10^{-2}	-4.43×10^{-3}	1.87×10^{-4}

b) $k_2(\rho) = B_0 + B_1\rho + B_2\rho^2 + B_3\rho^3 + B_4\rho^4$

(ρ is in unit of nm^{-3})

Solvent	$B_0\,(ps^{-1})$	$B_1\,(ps^{-1}\cdot nm^3)$	$B_2\,(ps^{-1}\cdot nm^6)$	$B_3\,(ps^{-1}\cdot nm^9)$	$B_4\,(ps^{-1}\cdot nm^{12})$
He	2.96×10^{-2}	7.33×10^{-2}	-5.05×10^{-3}	1.22×10^{-4}	0
Ne	4.72×10^{-2}	7.28×10^{-2}	-4.17×10^{-3}	1.04×10^{-4}	0
Ar	3.43×10^{-2}	1.04×10^{-1}	-1.00×10^{-2}	-2.13×10^{-4}	7.61×10^{-6}

4.7 Figure Captions and Figures

Fig. 1 Phase diagram for argon. The plot is based on the results from Refs. [17,24,25].

Fig. 2 Overall schematic of the apparatus used in the high-pressure studies. CPM: colliding-pulse mode-locked dye laser; PDA: pulsed dye amplifier; BS: beam splitter; L: lens; SHG: second harmonic generation crystal; F: filter; P: polarizer; HW: half-wave plate; PMT: photomultiplier tube. (Courtesy of Chuck Williamson.)

Fig. 3 Femtosecond laser system. Top: CPM. M1 - M7: high-reflectivity mirrors; P1 - P4: prisms arranged to compensate group velocity dispersion; GJ: gain dye jet; SAJ: saturable absorber dye jet. Bottom: pulsed dye amplifier (PDA). C1 -C4: flow dye cells. (Courtesy of Jennifer Herek.)

Fig. 4 Relevant potential energy surfaces of iodine. Arrows are drawn to indicate the pump and probe excitation and the laser induced fluorescence.

Fig. 5 Laser induced fluorescence transients obtained at low pressures of **helium**, as indicated. The central wavelength of the pump pulse was at 620 nm and probe wavelength was at 310 nm.

Fig. 6 Laser induced fluorescence transients obtained at intermediate pressures of **helium**, as indicated. The central wavelength of the pump pulse was at 620 nm and probe wavelength was at 310 nm.

Fig. 7 Laser induced fluorescence transients obtained at high pressures of **helium**, as indicated. The central wavelength of the pump pulse was at 620 nm and probe wavelength was at 310 nm.

Fig. 8 Laser induced fluorescence transients obtained at low pressures of **neon**, as indicated. The central wavelength of the pump pulse was at 620 nm and probe wavelength was at 310 nm.

Fig. 9 Laser induced fluorescence transients obtained at intermediate pressures of **neon**, as indicated. The central wavelength of the pump pulse was at 620 nm and probe wavelength was at 310 nm.

Fig. 10 Laser induced fluorescence transients obtained at high pressures of **neon**, as indicated. The central wavelength of the pump pulse was at 620 nm and probe wavelength was at 310 nm.

Fig. 11 Laser induced fluorescence transients obtained at low pressures of **argon**, as indicated. The central wavelength of the pump pulse was at 620 nm and probe wavelength was at 310 nm.

Fig. 12 Laser induced fluorescence transients obtained at intermediate pressures of **argon**, as indicated. The central wavelength of the pump pulse was at 620 nm and probe wavelength was at 310 nm.

Fig. 13 Laser induced fluorescence transients obtained at high pressures of **argon**, as indicated. The central wavelength of the pump pulse was at 620 nm and probe wavelength was at 310 nm.

Fig. 14 LIF transients of iodine in helium (dots), and their fits (solid lines): a) 0 bar and b) 75 bar (see text).

Fig. 15 Density dependence of energy relaxation rate k_1 (open square) and dephasing rate k_2 (filled circle) for iodine in **helium**: a) Experimental results; b) Classical simulation results. The lines are polynomial fit to the relaxation rates.

Fig. 16 Density dependence of energy relaxation rate k_1 (open square) and dephasing rate k_2 (filled circle) for iodine in **neon**: a) Experimental results; b) Classical simulation results. The lines are polynomial fit to the relaxation rates.

Fig. 17 Density dependence of energy relaxation rate k_1 (open square) and dephasing rate k_2 (filled circle) for iodine in **argon**: a) Experimental results; b) Classical simulation results. The lines are polynomial fit to the relaxation rates.

Fig. 18 Phase relaxation rates as functions of number densities in **helium**: a) Experimental results; b) Classical simulation results; c) Semi-classical simulation results.

Fig. 19 Phase relaxation rates as functions of number densities in **neon**: a) Experimental results; b) Classical simulation results; c) Semi-classical simulation results.

Fig. 20 Phase relaxation rates as functions of number densities in **argon**. a) Experimental results; b) Classical simulation results; c) Semi-classical simulation results.

Fig. 21 Vibrational frequency shift as functions of the density: a) Experimental results; b) Classical simulation results. Open square for He, filled circle for Ne, and crossed square for Ar. The lines are drawn through the data points to guide the eyes.

Fig. 22 Dephasing rates of iodine in **helium** obtained from: a) semi-classical simulations; b) previous theoretical models.

Fig. 23 Dephasing rates of iodine in **neon** obtained from: a) semi-classical simulations; b) previous theoretical models.

Fig. 24 Dephasing rates of iodine in **argon** obtained from: a) semi-classical simulations; b) previous theoretical models.

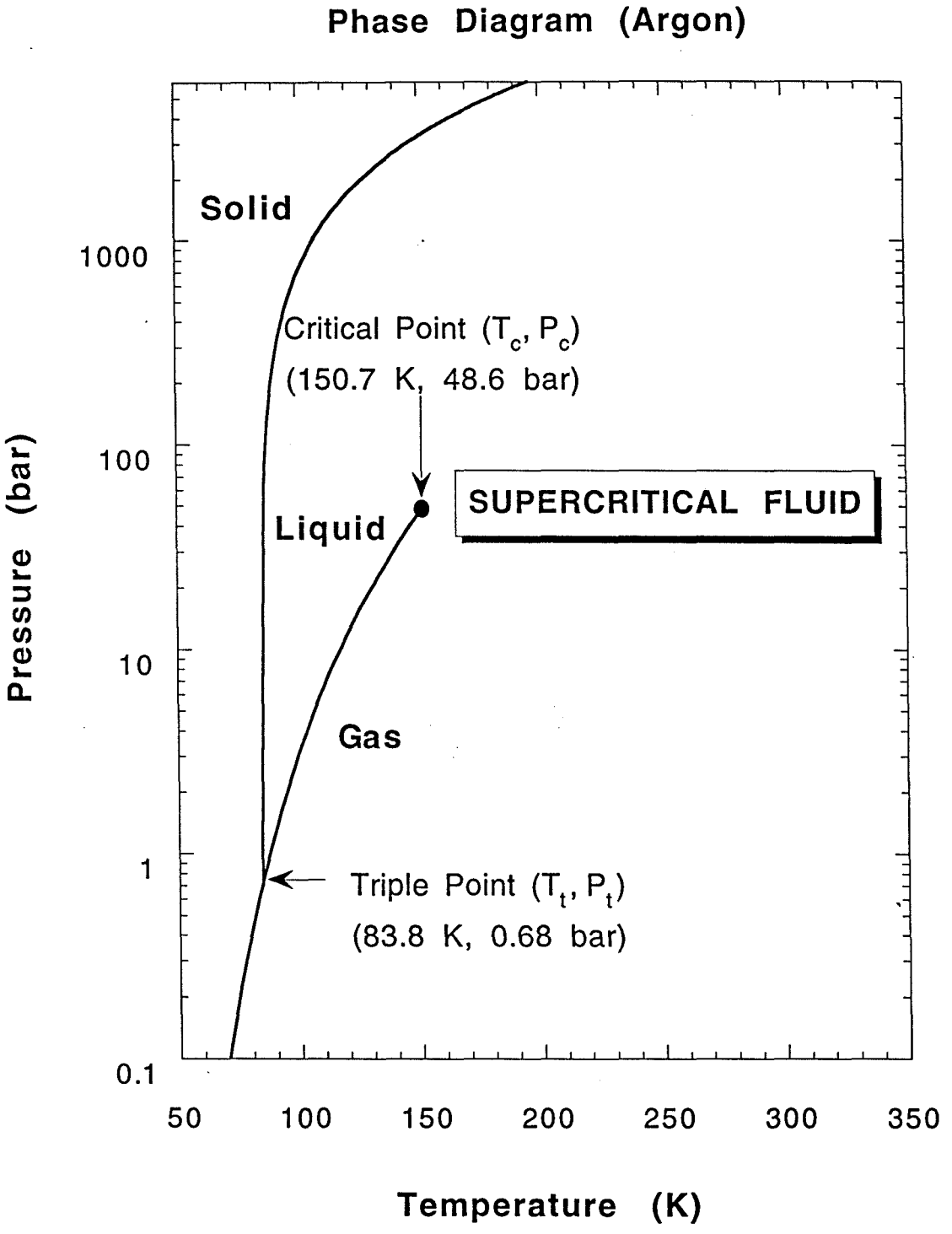
Phase Diagram (Argon)
Solid
Liquid
Gas
Critical Point (T_c, P_c)
(150.7 K, 48.6 bar)
SUPERCRITICAL FLUID
Triple Point (T_t, P_t)
(83.8 K, 0.68 bar)
Pressure (bar)
1000
100
10
1
0.1
50
100
150
200
250
300
350
Temperature (K)

Figure 1

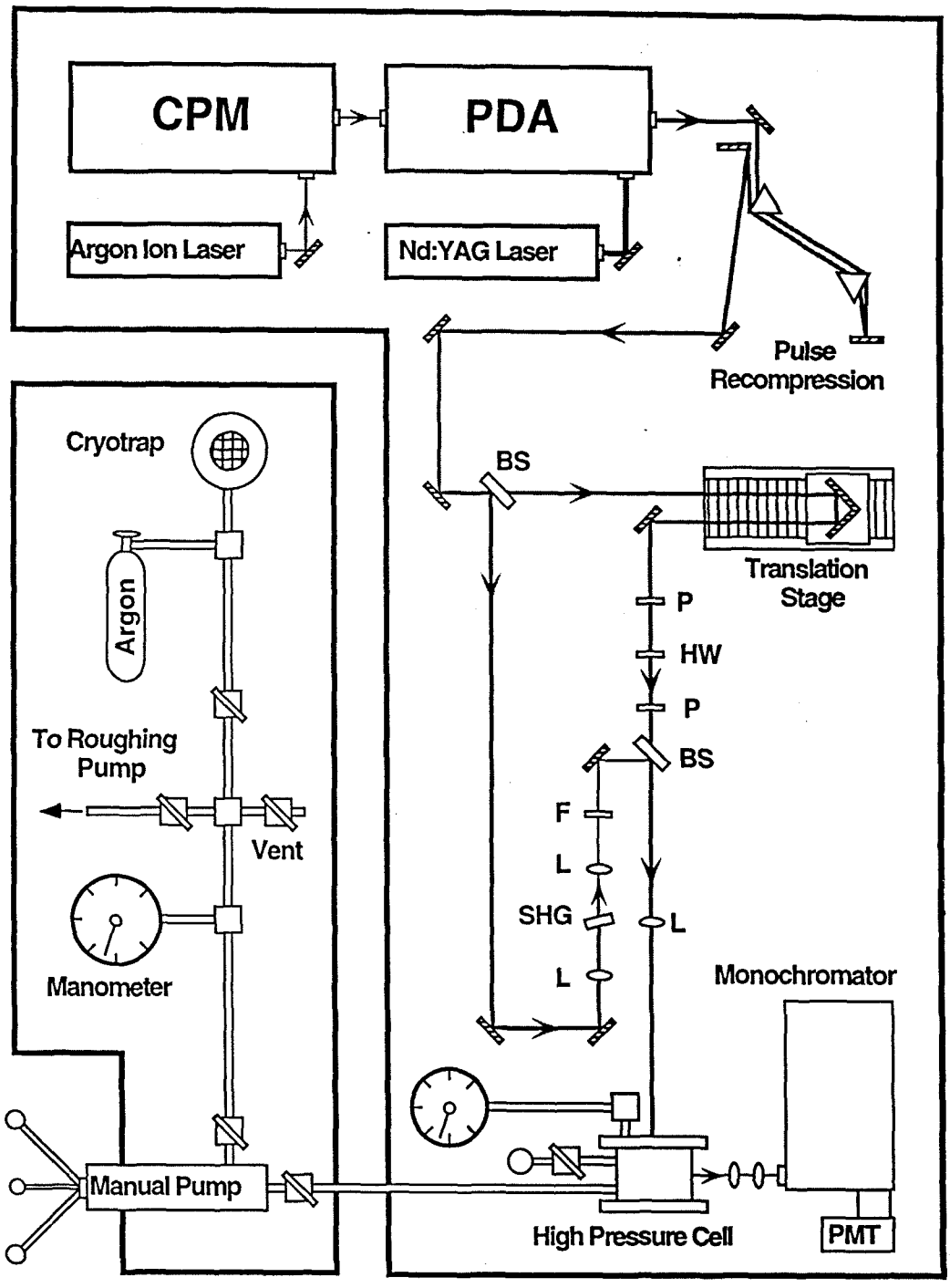
CPM
PDA
Argon Ion Laser
Nd:YAG Laser
Pulse
Recompression
Cryotrap
Argon
To Roughing
Pump
Vent
Manometer
BS
Translation
Stage
P
HW
P
BS
F
L
SHG
L
L
Monochromator
Manual Pump
High Pressure Cell
PMT

Figure 2

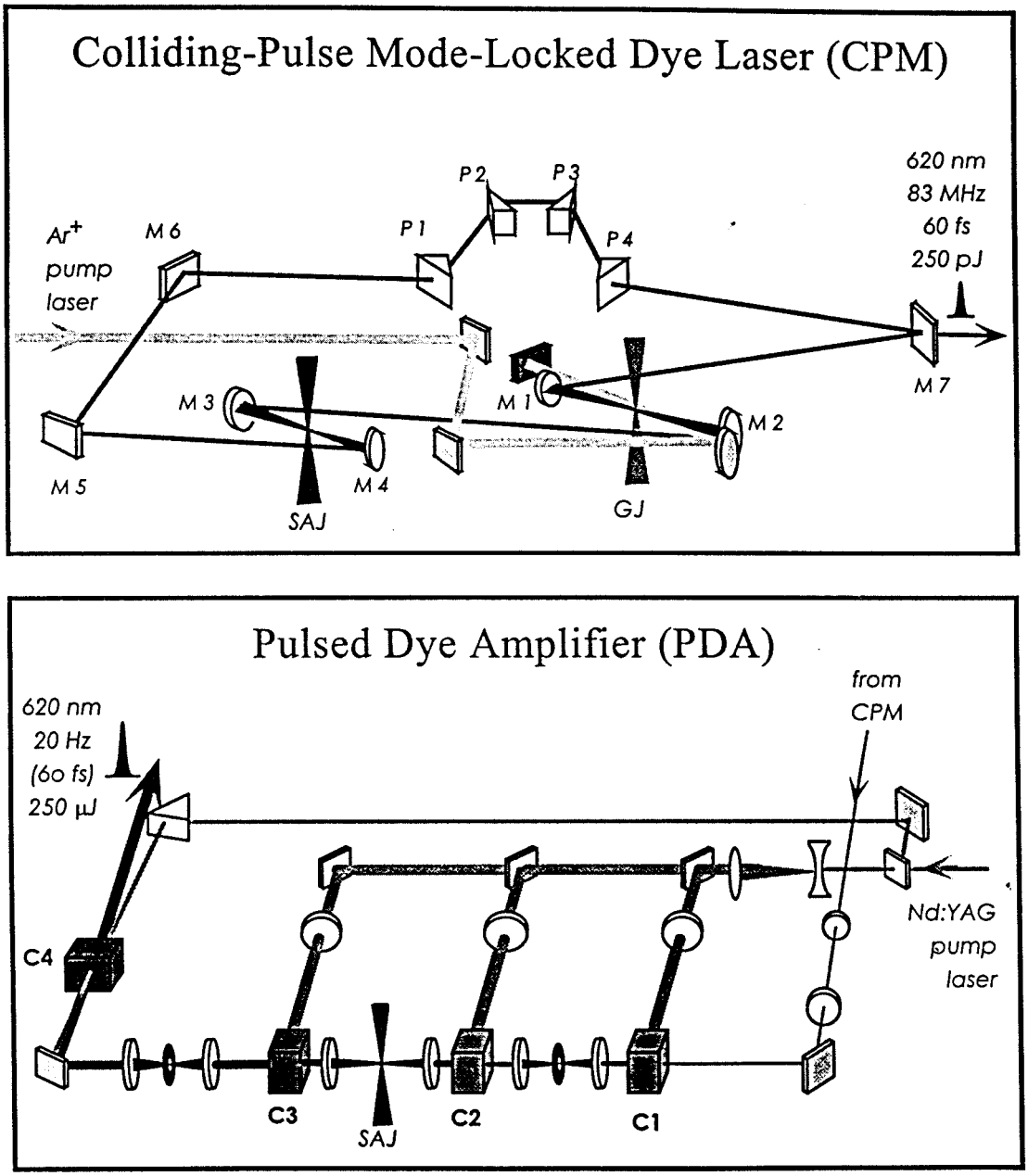
Colliding-Pulse Mode-Locked Dye Laser (CPM)
Ar+ pump laser
M 6
P 1
P 2
P 3
P 4
620 nm
83 MHz
60 fs
250 pJ
M 7
M 1
M 2
M 3
M 4
M 5
SAJ
GJ
Pulsed Dye Amplifier (PDA)
620 nm
20 Hz
(60 fs)
250 μJ
from
CPM
Nd:YAG
pump
laser
C4
C3
SAJ
C2
C1

Figure 3

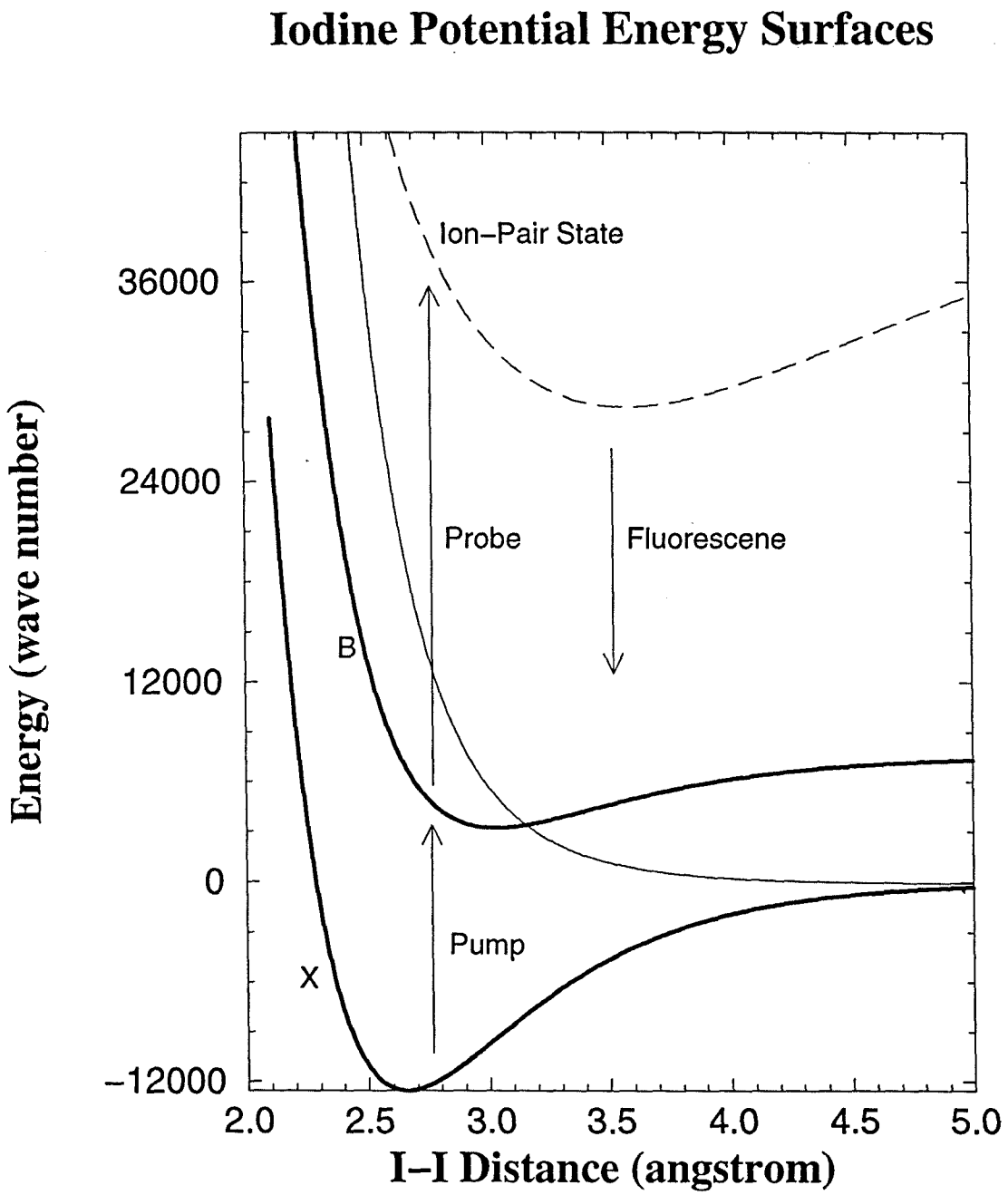
Iodine Potential Energy Surfaces
Ion–Pair State
Probe
Fluorescene
B
X
Pump
36000
24000
12000
0
–12000
Energy (wave number)
2.0
2.5
3.0
3.5
4.0
4.5
5.0
I–I Distance (angstrom)

Figure 4

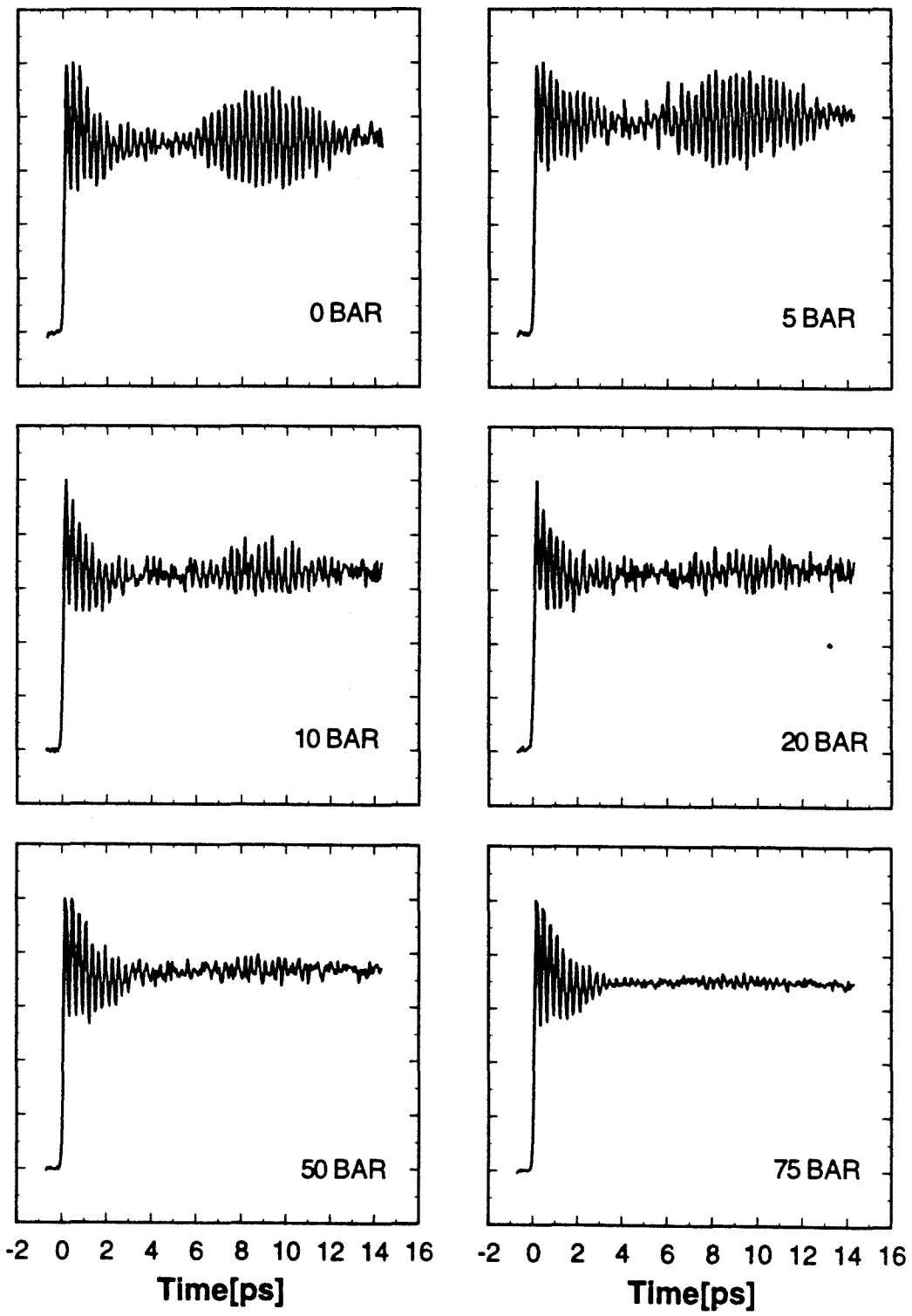
Dephasing of Iodine in Helium
0 BAR
5 BAR
10 BAR
20 BAR
50 BAR
75 BAR
-2 0 2 4 6 8 10 12 14 16
Time[ps]
-2 0 2 4 6 8 10 12 14 16
Time[ps]

Figure 5

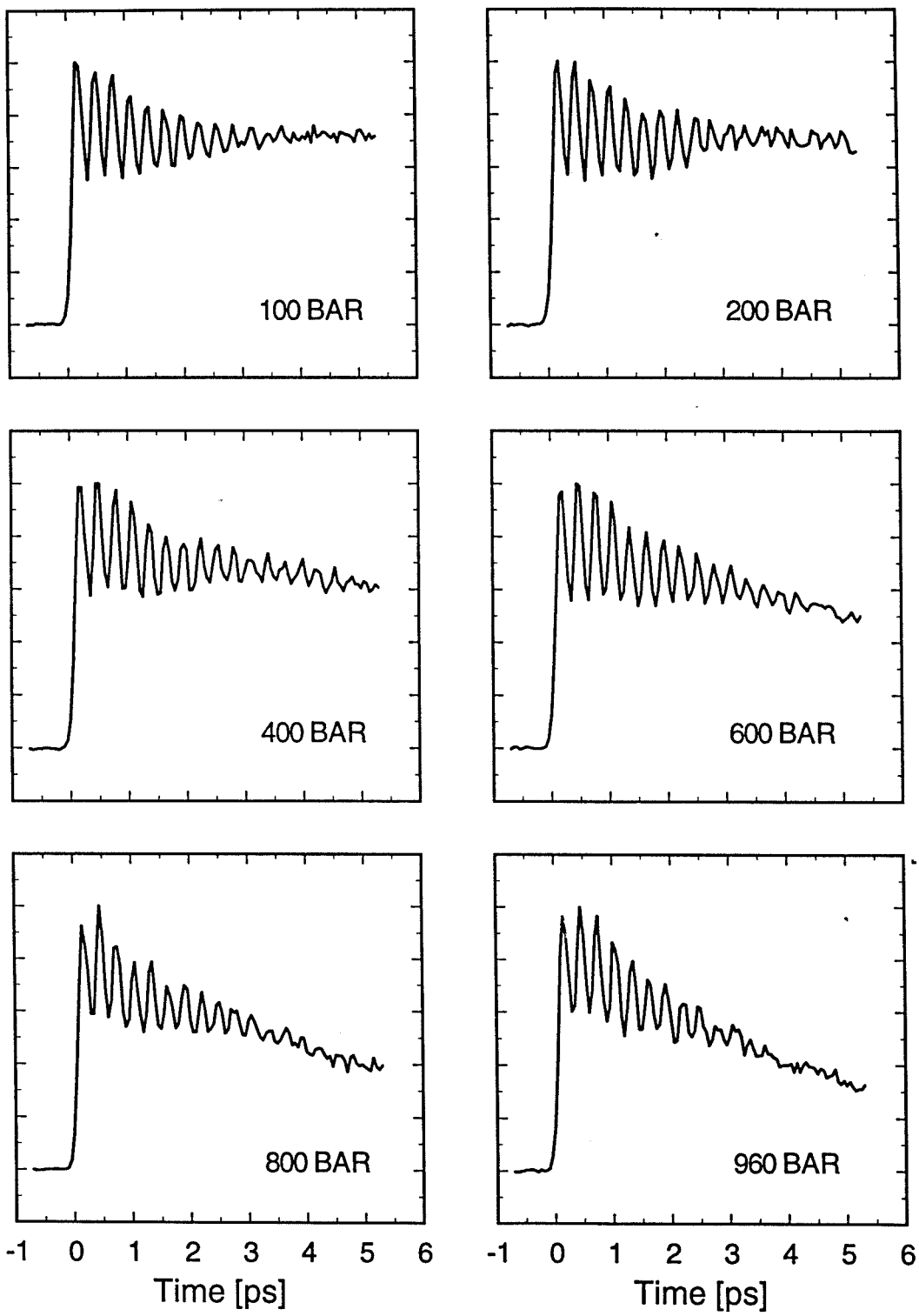
Dephasing of Iodine in Helium
100 BAR
200 BAR
400 BAR
600 BAR
800 BAR
960 BAR
-1 0 1 2 3 4 5 6
Time [ps]
-1 0 1 2 3 4 5 6
Time [ps]

Figure 6

Dephasing of Iodine in Helium

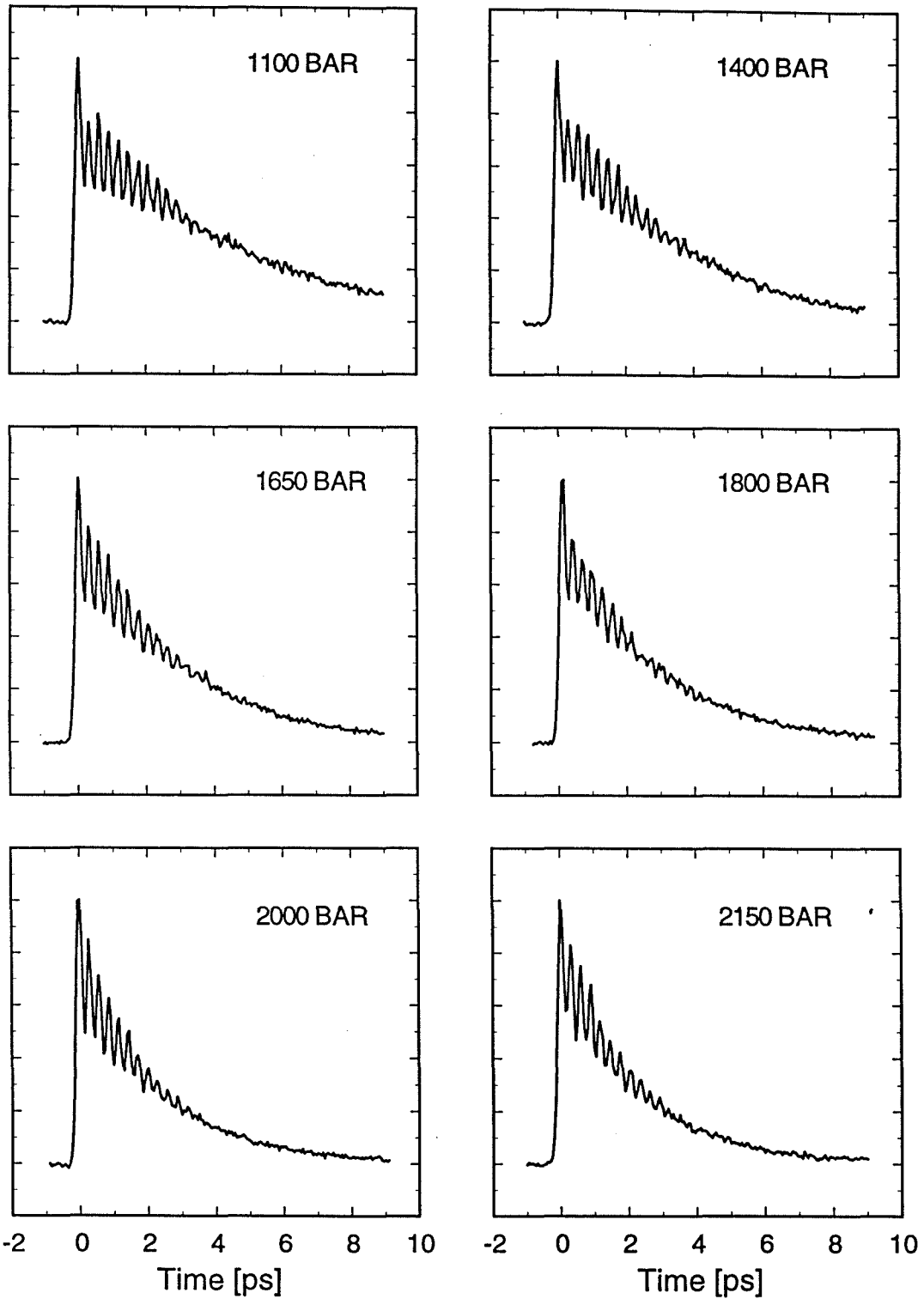

Figure 7

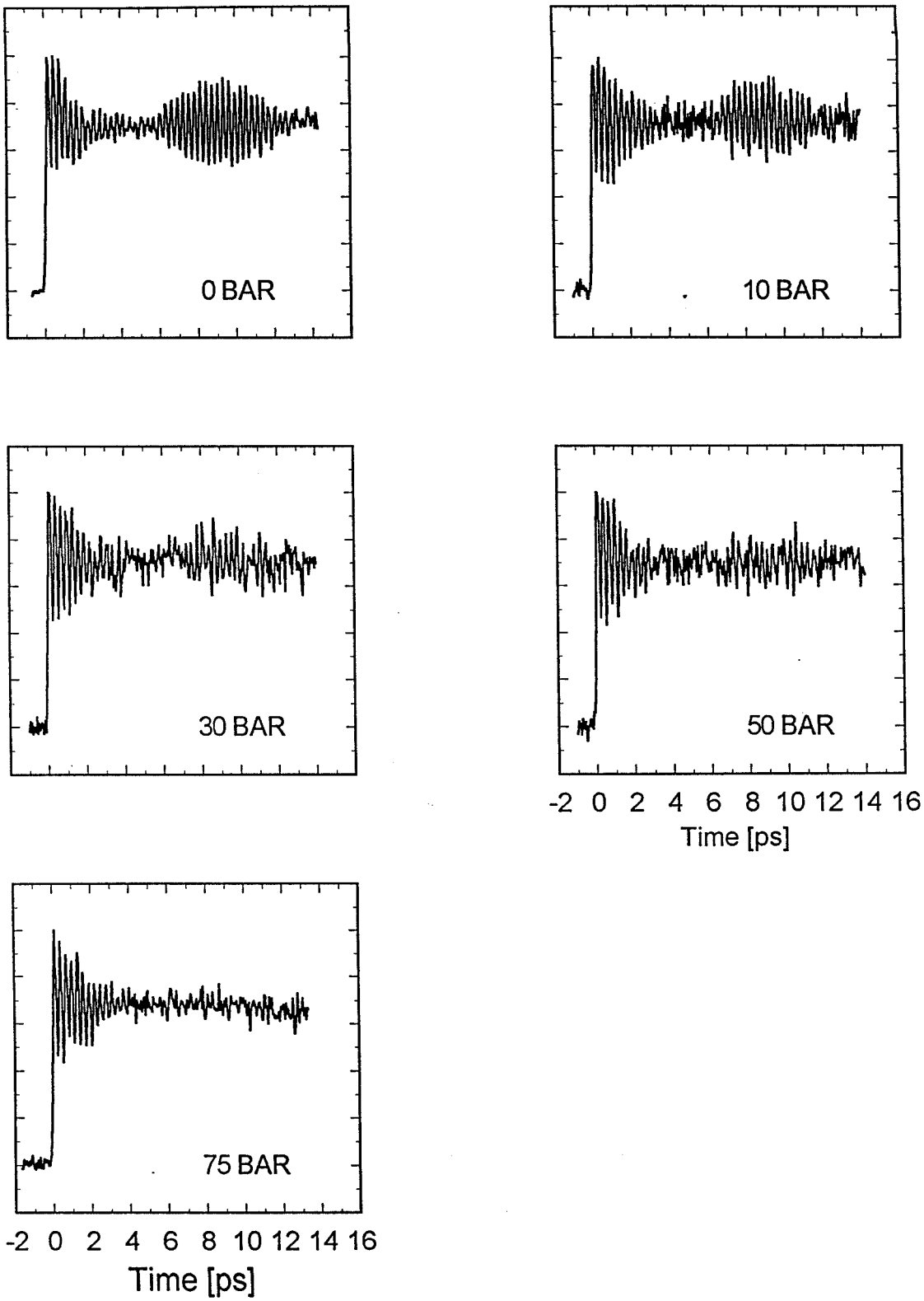
0 BAR
10 BAR
30 BAR
50 BAR
75 BAR
-2 0 2 4 6 8 10 12 14 16
Time [ps]
-2 0 2 4 6 8 10 12 14 16
Time [ps]

Figure 8

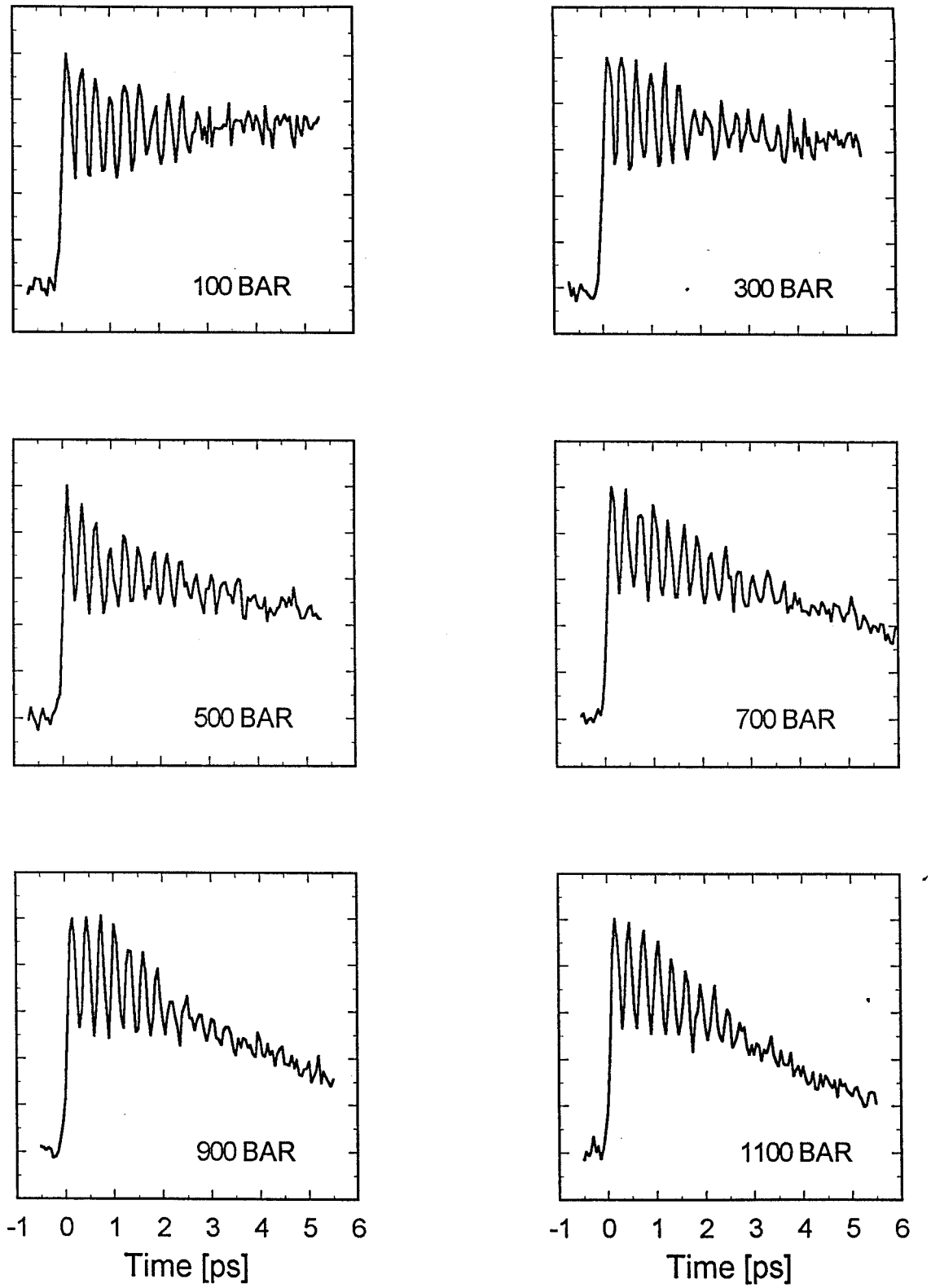
100 BAR
300 BAR
500 BAR
700 BAR
900 BAR
1100 BAR
-1 0 1 2 3 4 5 6
Time [ps]
-1 0 1 2 3 4 5 6
Time [ps]

Figure 9

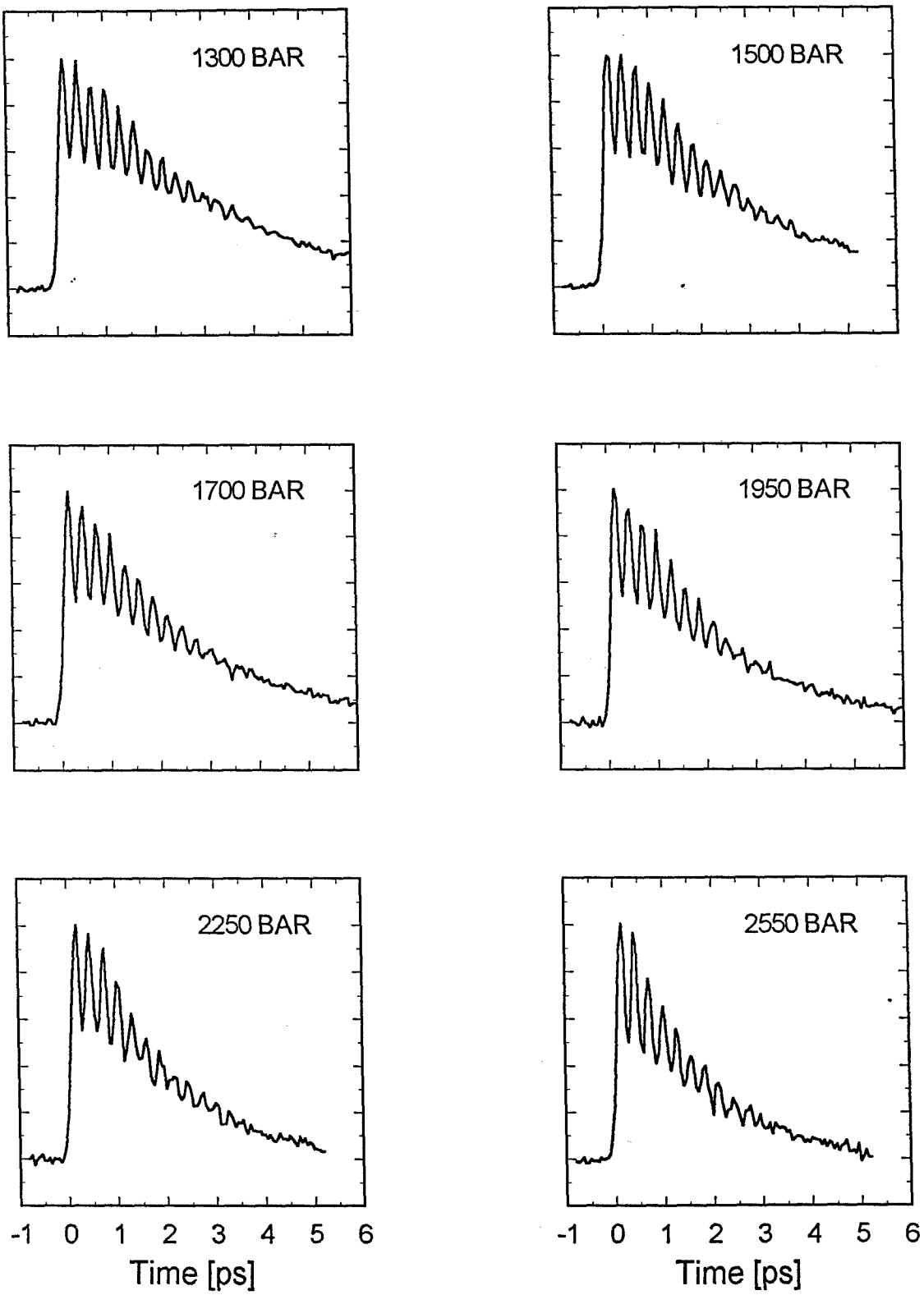
1300 BAR
1500 BAR
1700 BAR
1950 BAR
2250 BAR
2550 BAR
-1 0 1 2 3 4 5 6
Time [ps]
-1 0 1 2 3 4 5 6
Time [ps]

Figure 10

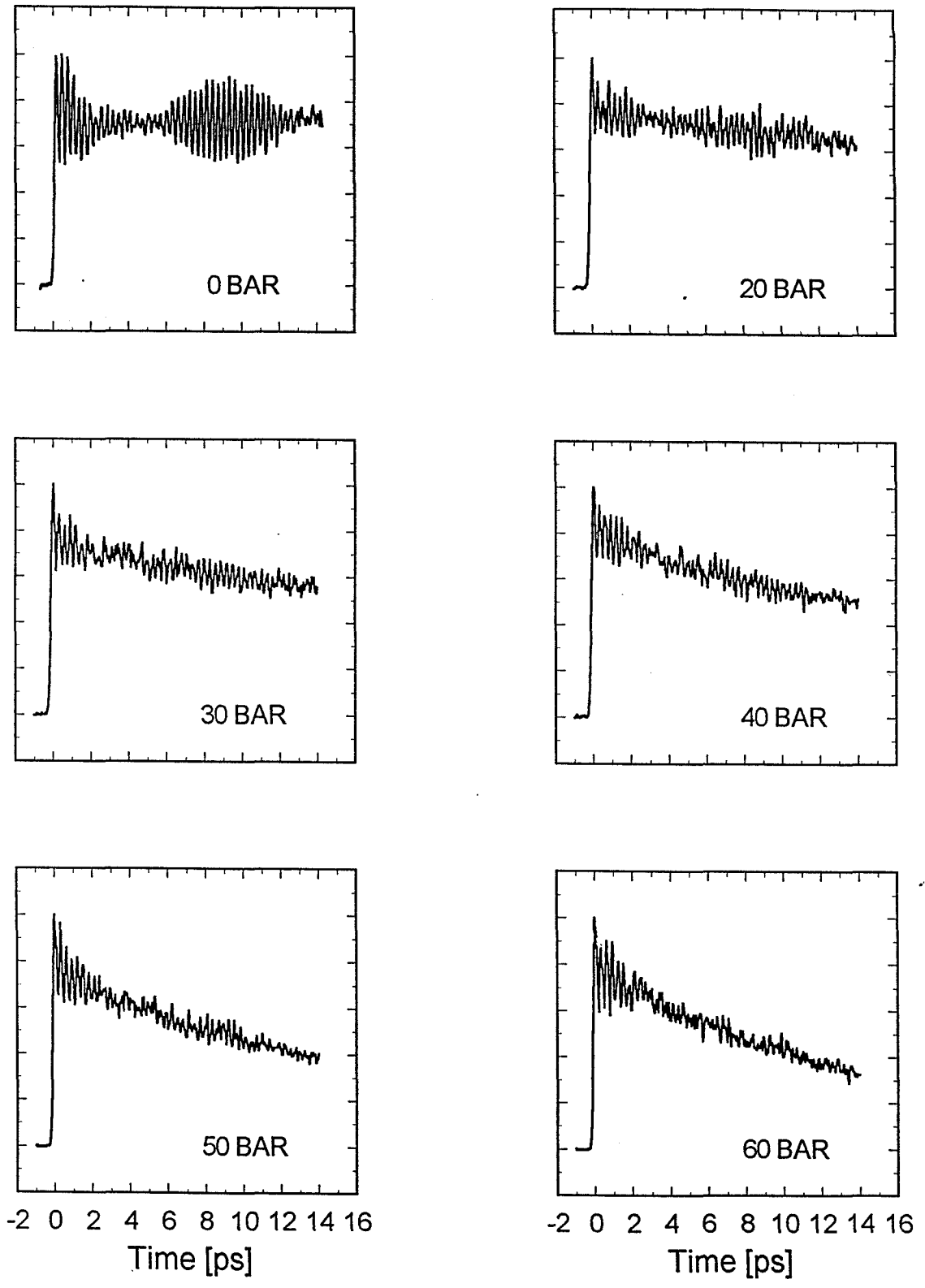
0 BAR
20 BAR
30 BAR
40 BAR
50 BAR
60 BAR
-2 0 2 4 6 8 10 12 14 16
Time [ps]
-2 0 2 4 6 8 10 12 14 16
Time [ps]

Figure 11

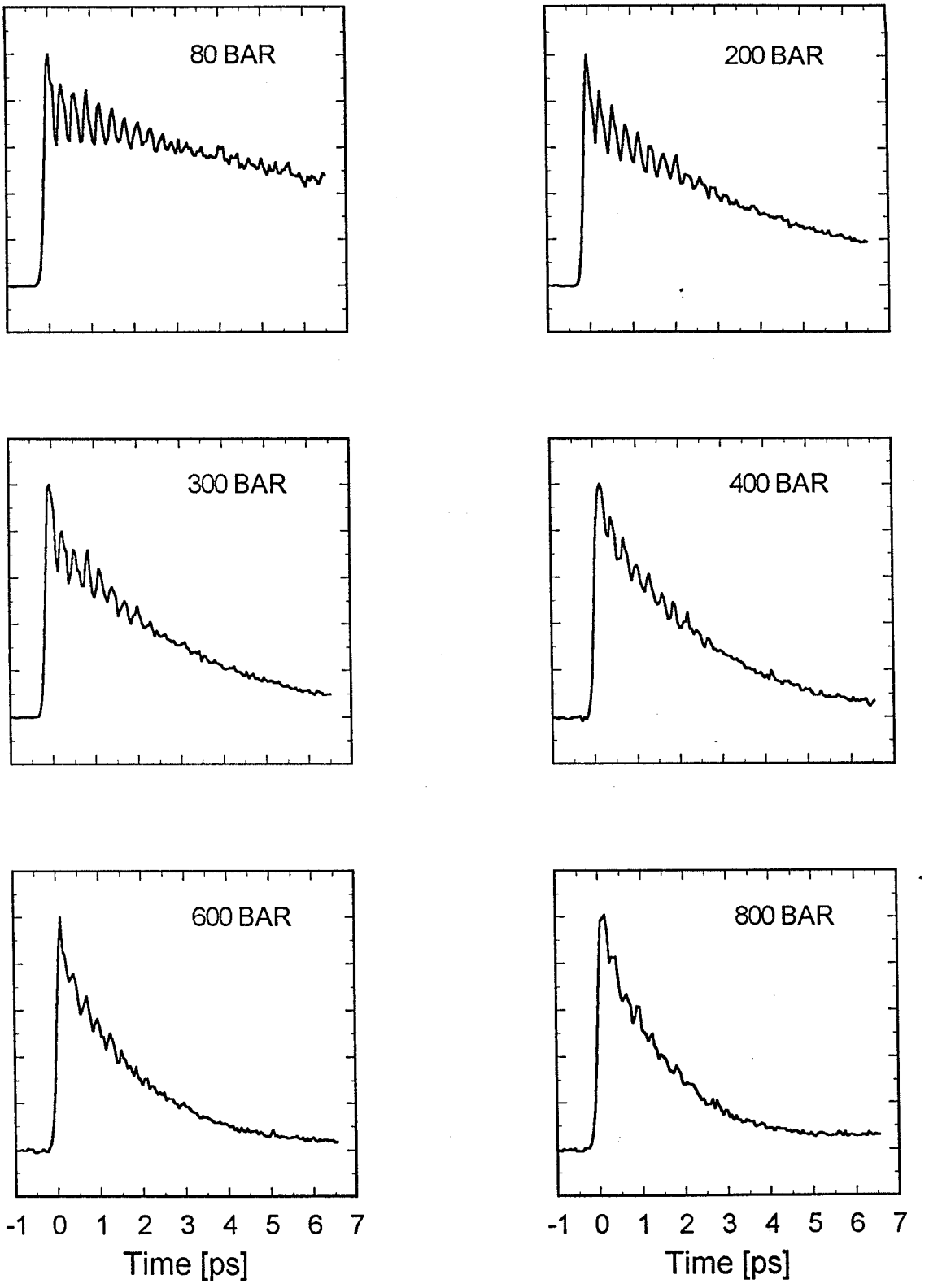
80 BAR
200 BAR
300 BAR
400 BAR
600 BAR
800 BAR
-1 0 1 2 3 4 5 6 7
Time [ps]
-1 0 1 2 3 4 5 6 7
Time [ps]

Figure 12

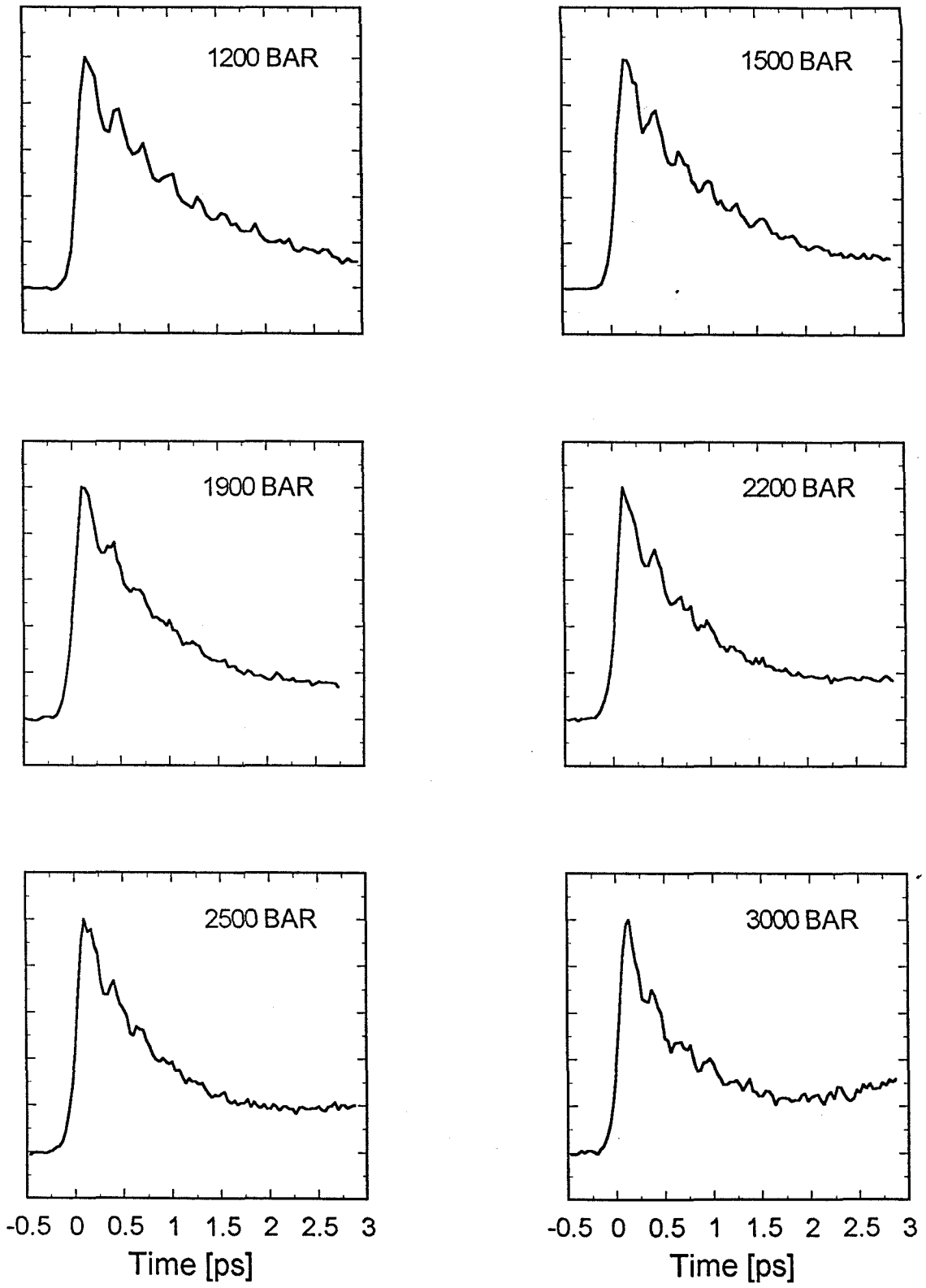
1200 BAR
1500 BAR
1900 BAR
2200 BAR
2500 BAR
3000 BAR
-0.5 0 0.5 1 1.5 2 2.5 3
Time [ps]
-0.5 0 0.5 1 1.5 2 2.5 3
Time [ps]

Figure 13

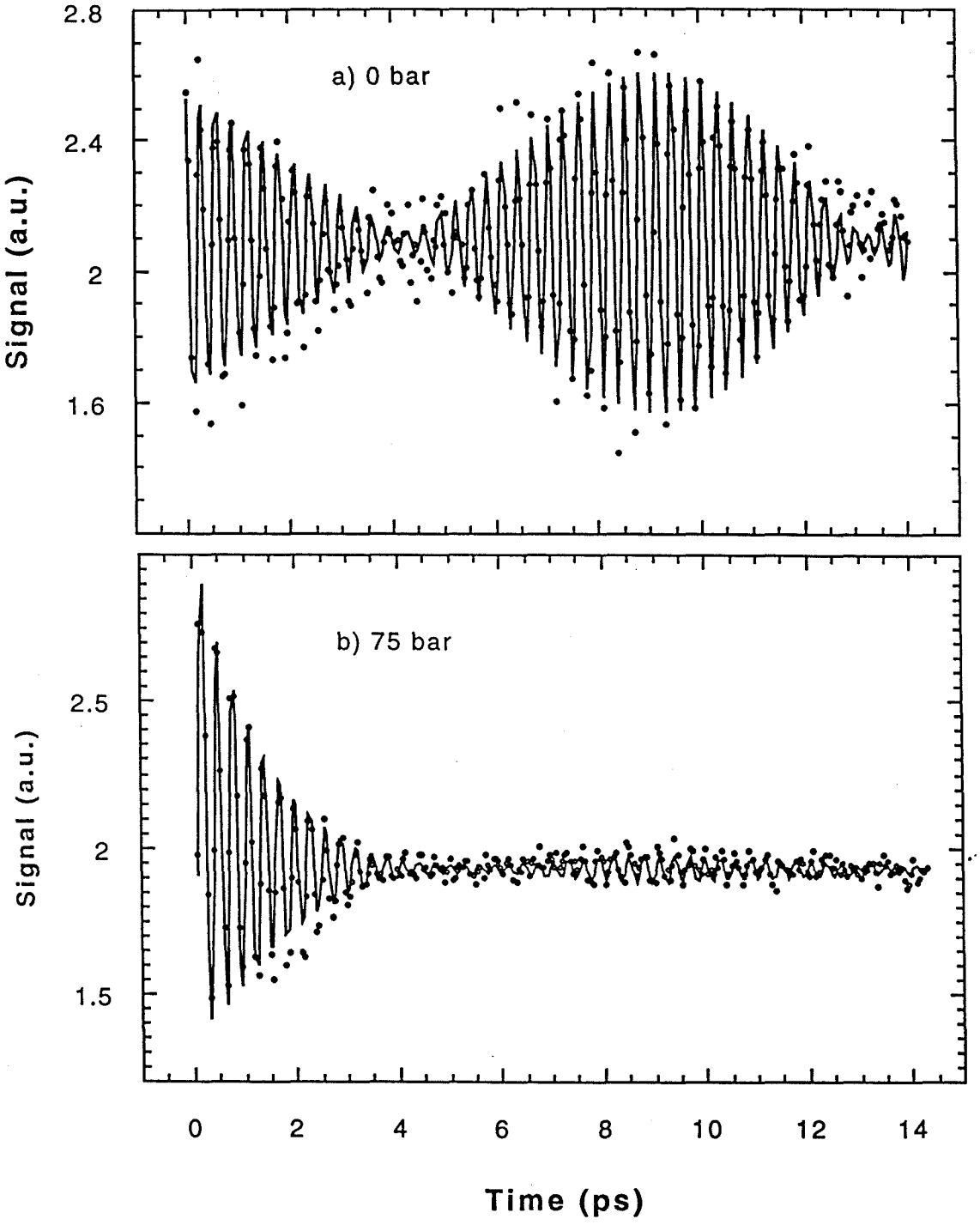
a) 0 bar
b) 75 bar
Signal (a.u.)
Signal (a.u.)
2.8
2.4
2
1.6
2.5
2
1.5
0
2
4
6
8
10
12
14
Time (ps)

Figure 14

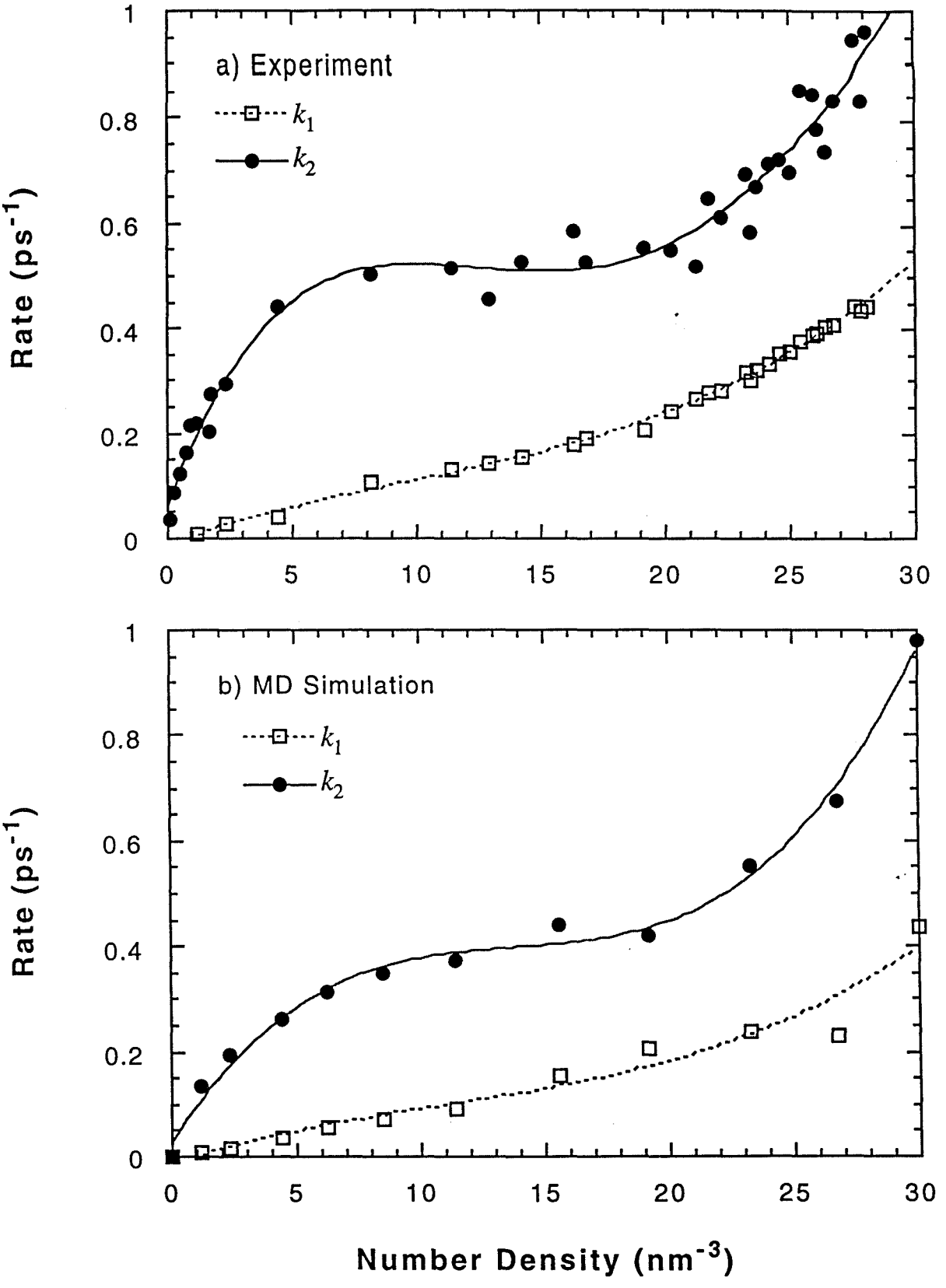
a) Experiment
k_1
k_2
b) MD Simulation
k_1
k_2
Rate (ps^{-1})
Rate (ps^{-1})
Number Density (nm^{-3})
0
0.2
0.4
0.6
0.8
1
0
5
10
15
20
25
30

Figure 15

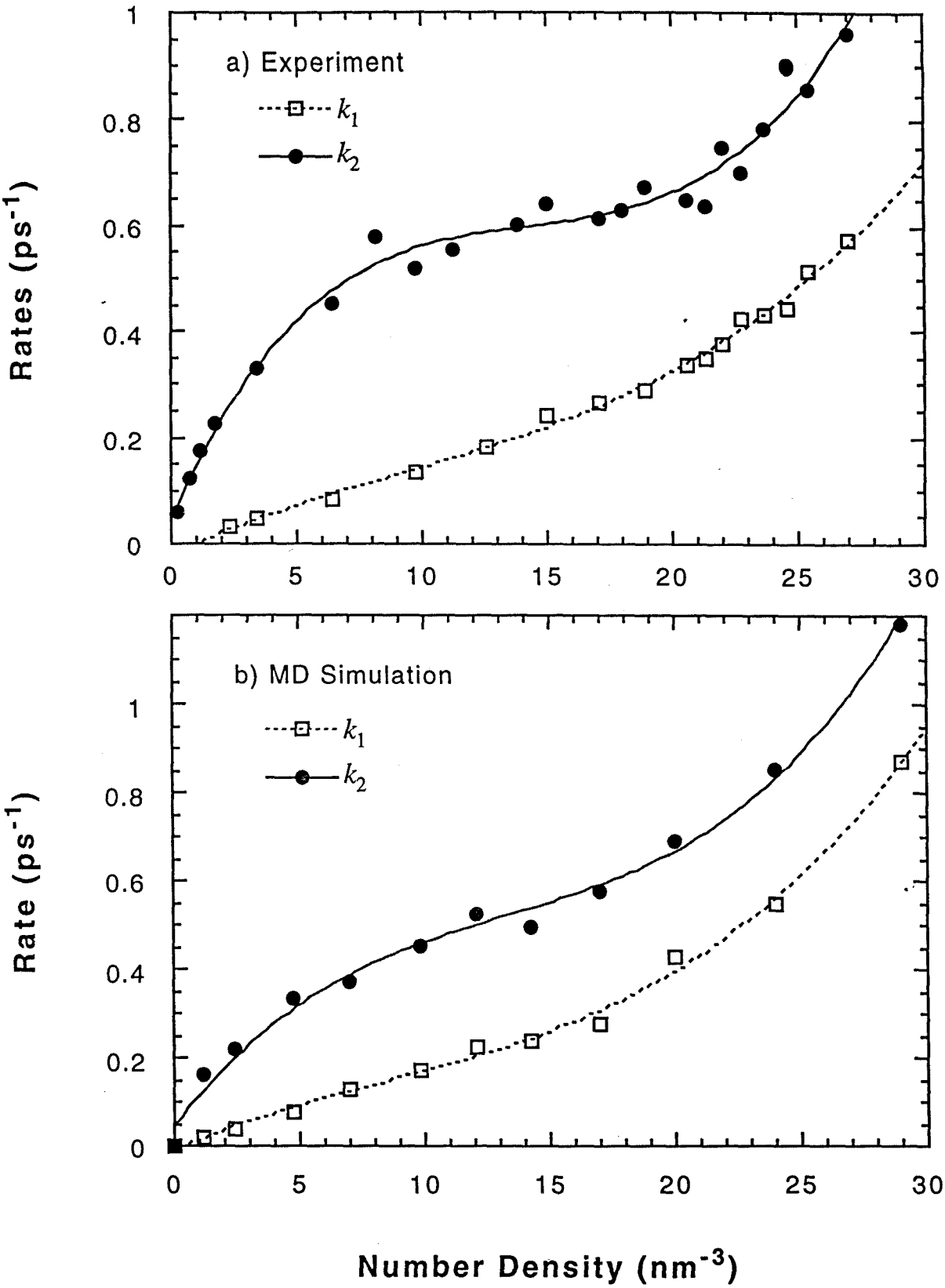
a) Experiment
k_1
k_2
Rates (ps^{-1})
b) MD Simulation
k_1
k_2
Rate (ps^{-1})
Number Density (nm^{-3})

Figure 16

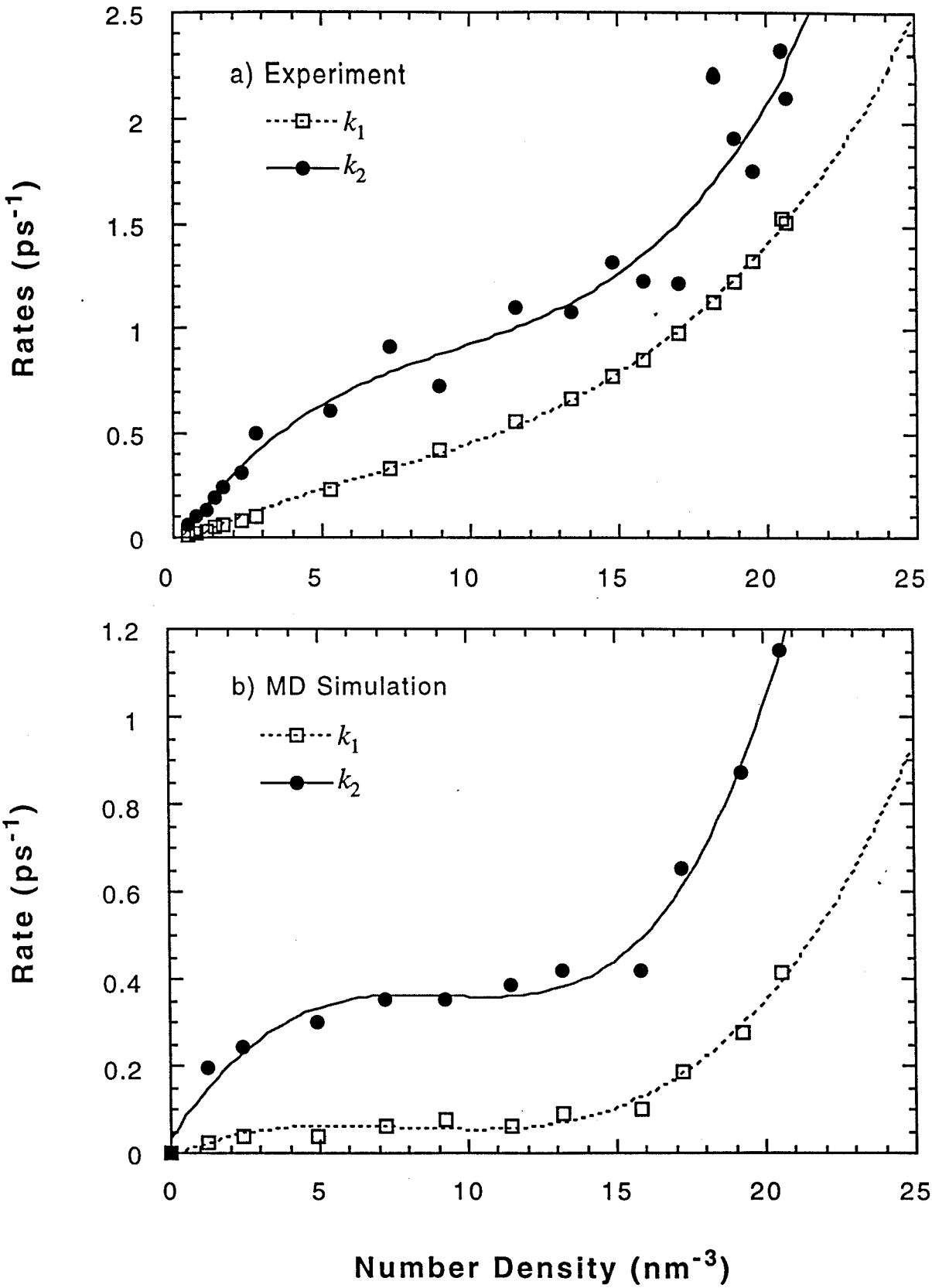
a) Experiment
k_1
k_2
Rates (ps^{-1})
2.5
2
1.5
1
0.5
0
0
5
10
15
20
25
b) MD Simulation
k_1
k_2
Rate (ps^{-1})
1.2
1
0.8
0.6
0.4
0.2
0
0
5
10
15
20
25
Number Density (nm^{-3})

Figure 17

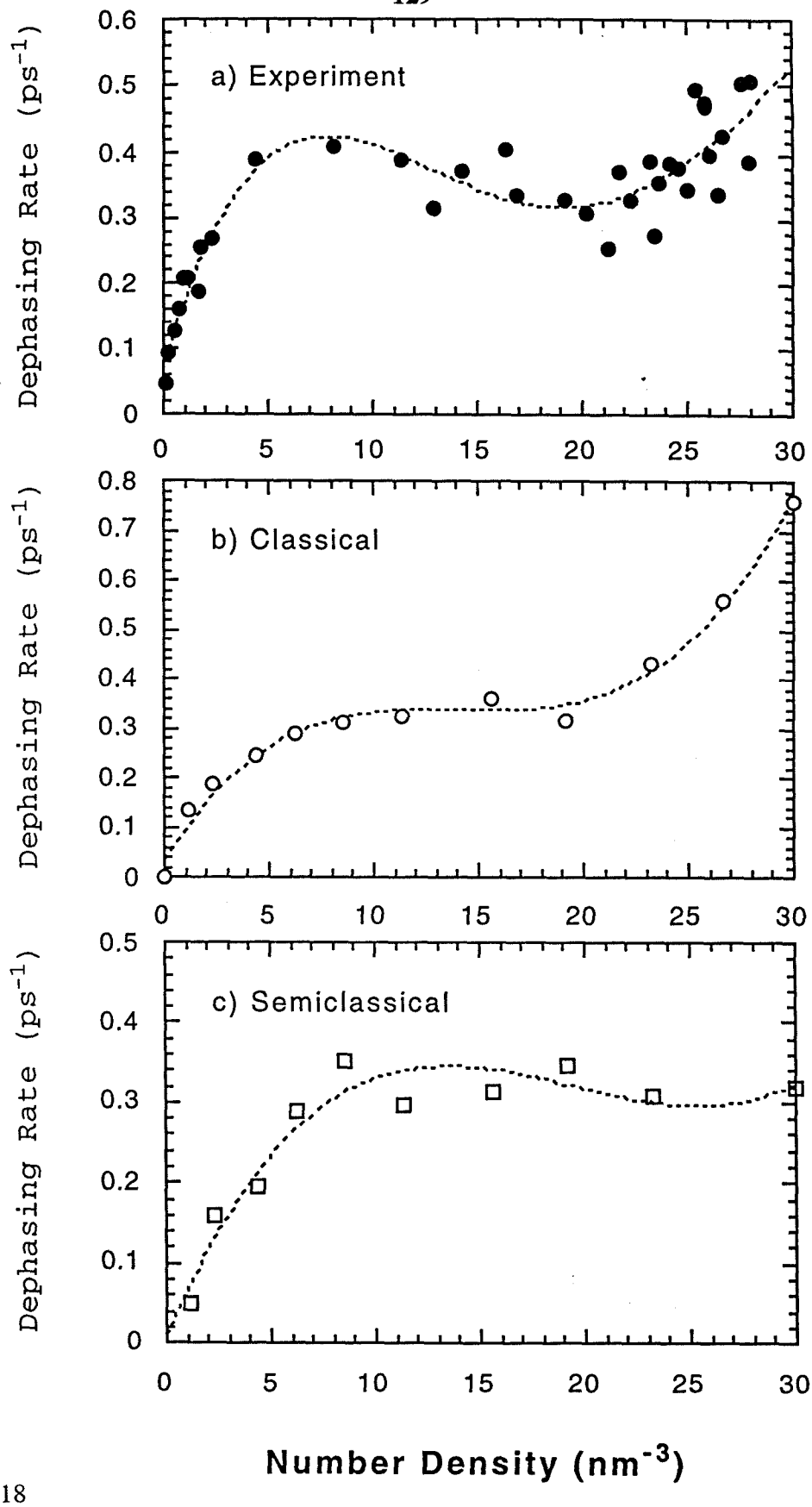
a) Experiment
b) Classical
c) Semiclassical
Dephasing Rate (ps^{-1})
Number Density (nm^{-3})

Figure 18

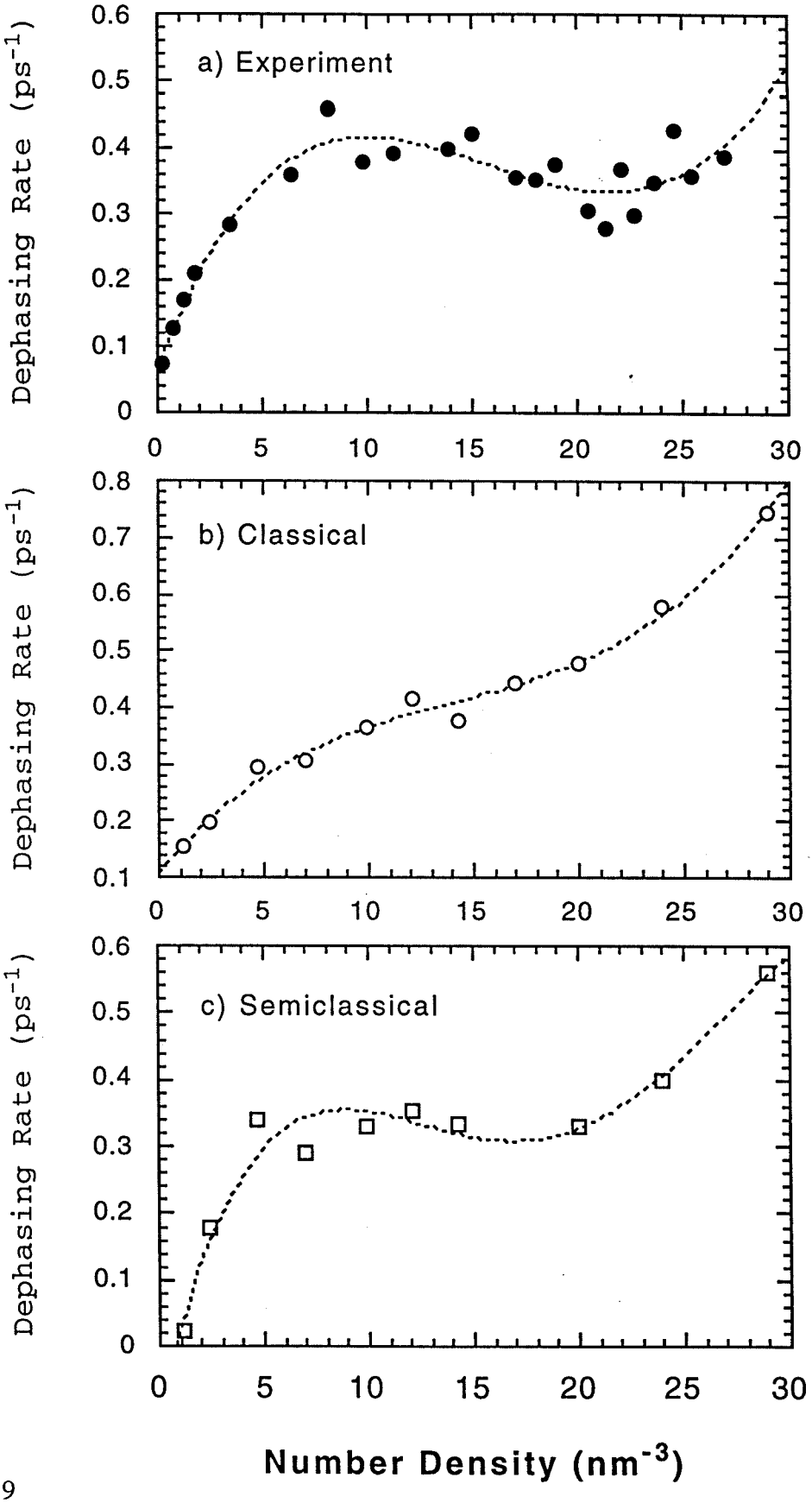
a) Experiment
b) Classical
c) Semiclassical
Dephasing Rate (ps^{-1})
Number Density (nm^{-3})

Figure 19

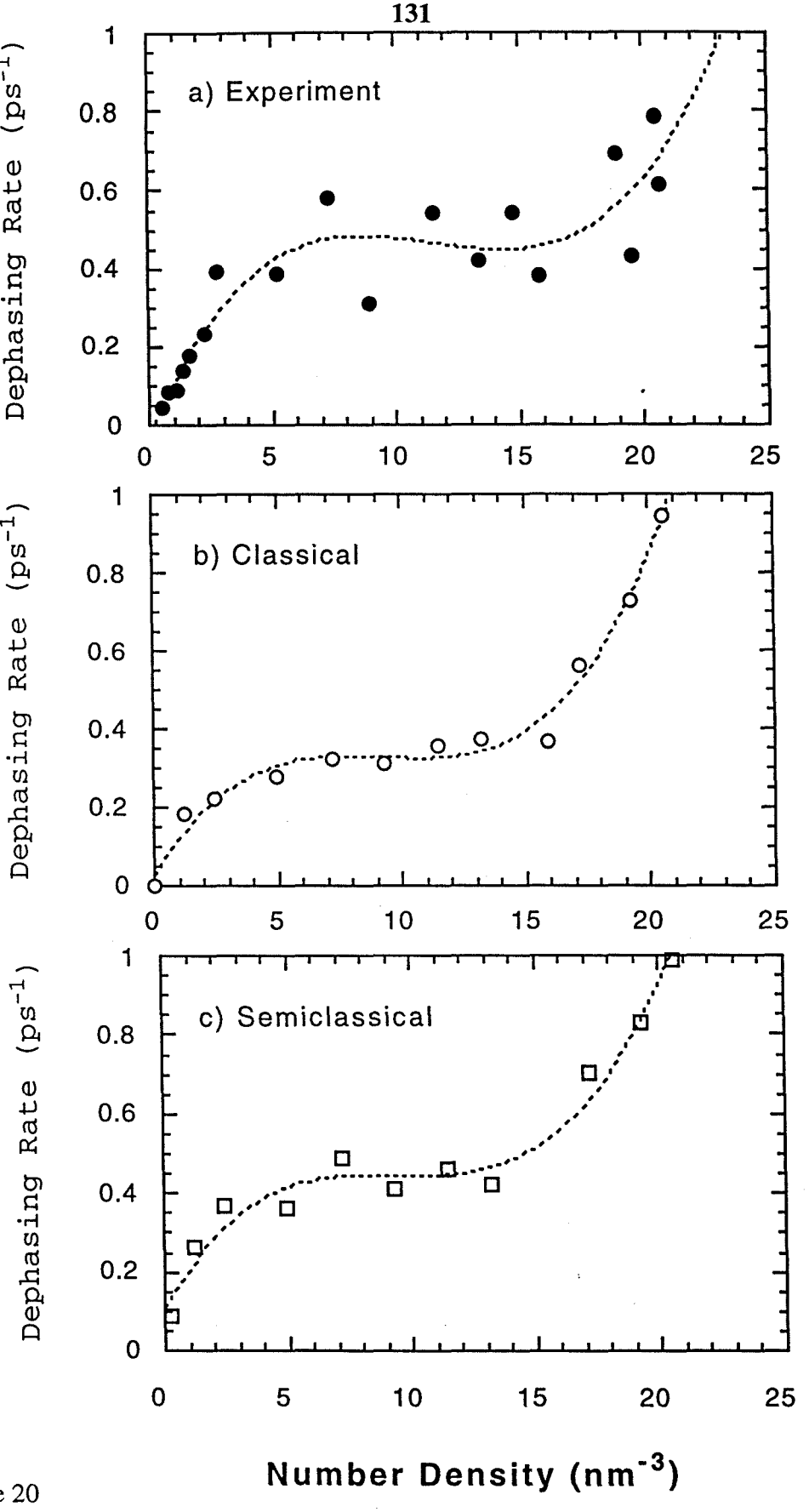
a) Experiment
b) Classical
c) Semiclassical
Dephasing Rate (ps^{-1})
Number Density (nm^{-3})
0
0.2
0.4
0.6
0.8
1
0
5
10
15
20
25

Figure 20

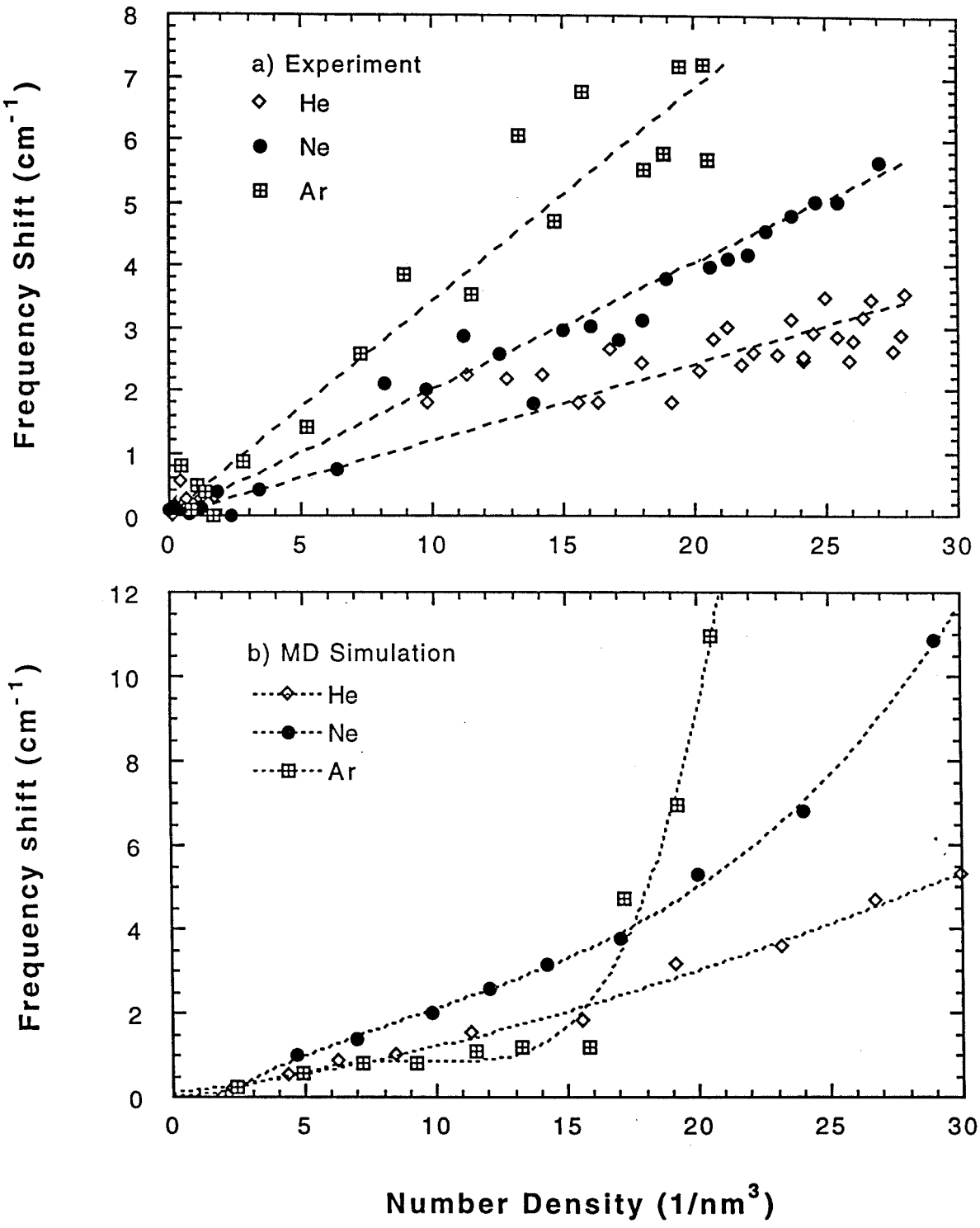
a) Experiment
He
Ne
Ar
Frequency Shift (cm^{-1})
b) MD Simulation
He
Ne
Ar
Frequency shift (cm^{-1})
Number Density (1/nm^3)

Figure 21

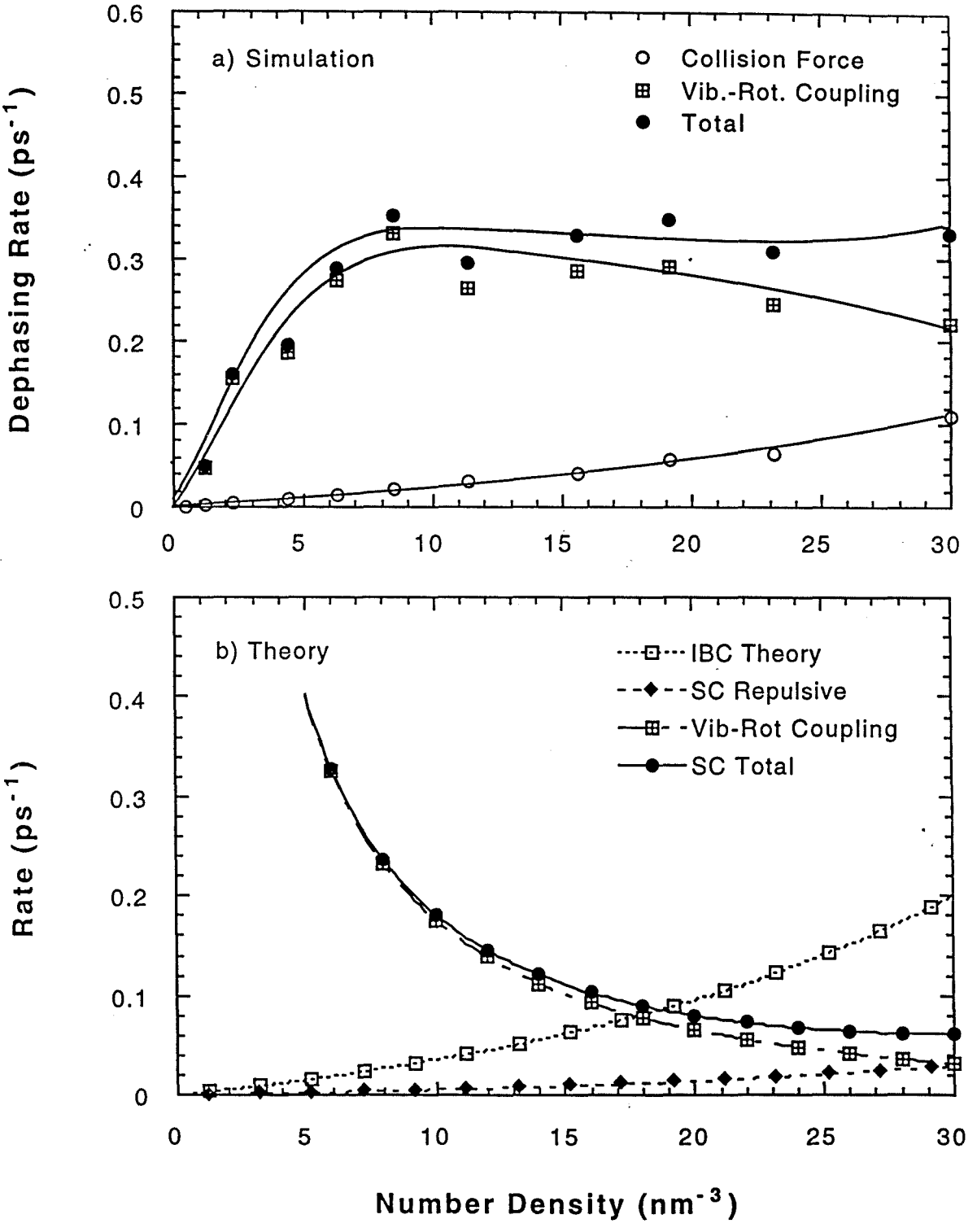
a) Simulation
Collision Force
Vib.-Rot. Coupling
Total
Dephasing Rate (ps^{-1})
0.6
0.5
0.4
0.3
0.2
0.1
0
0
5
10
15
20
25
30
b) Theory
IBC Theory
SC Repulsive
Vib-Rot Coupling
SC Total
Rate (ps^{-1})
0.5
0.4
0.3
0.2
0.1
0
0
5
10
15
20
25
30
Number Density (nm^{-3})

Figure 22

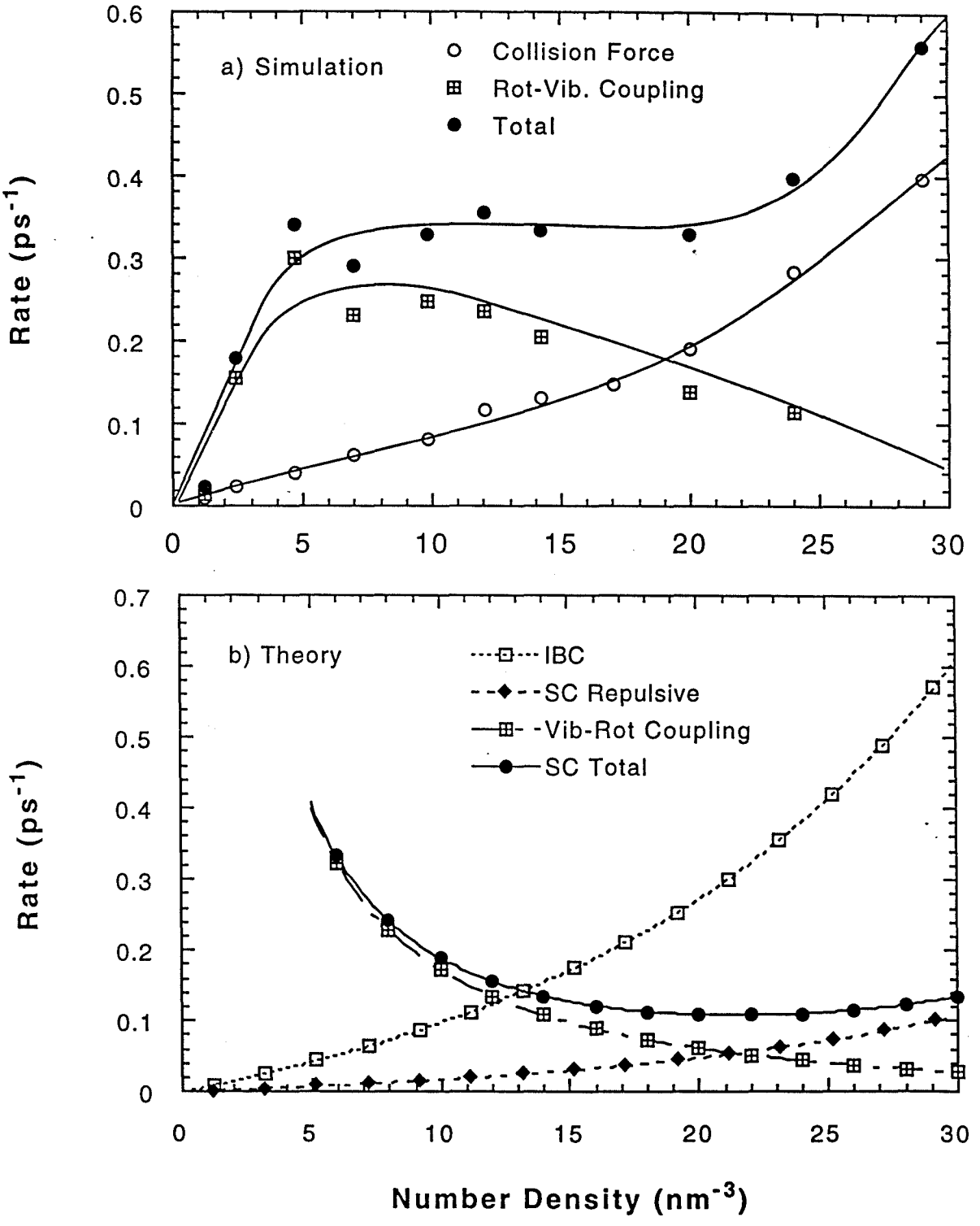
a) Simulation
Collision Force
Rot-Vib. Coupling
Total
Rate (ps^{-1})
0.6
0.5
0.4
0.3
0.2
0.1
0
0
5
10
15
20
25
30
b) Theory
IBC
SC Repulsive
Vib-Rot Coupling
SC Total
Rate (ps^{-1})
0.7
0.6
0.5
0.4
0.3
0.2
0.1
0
0
5
10
15
20
25
30
Number Density (nm^{-3})

Figure 23

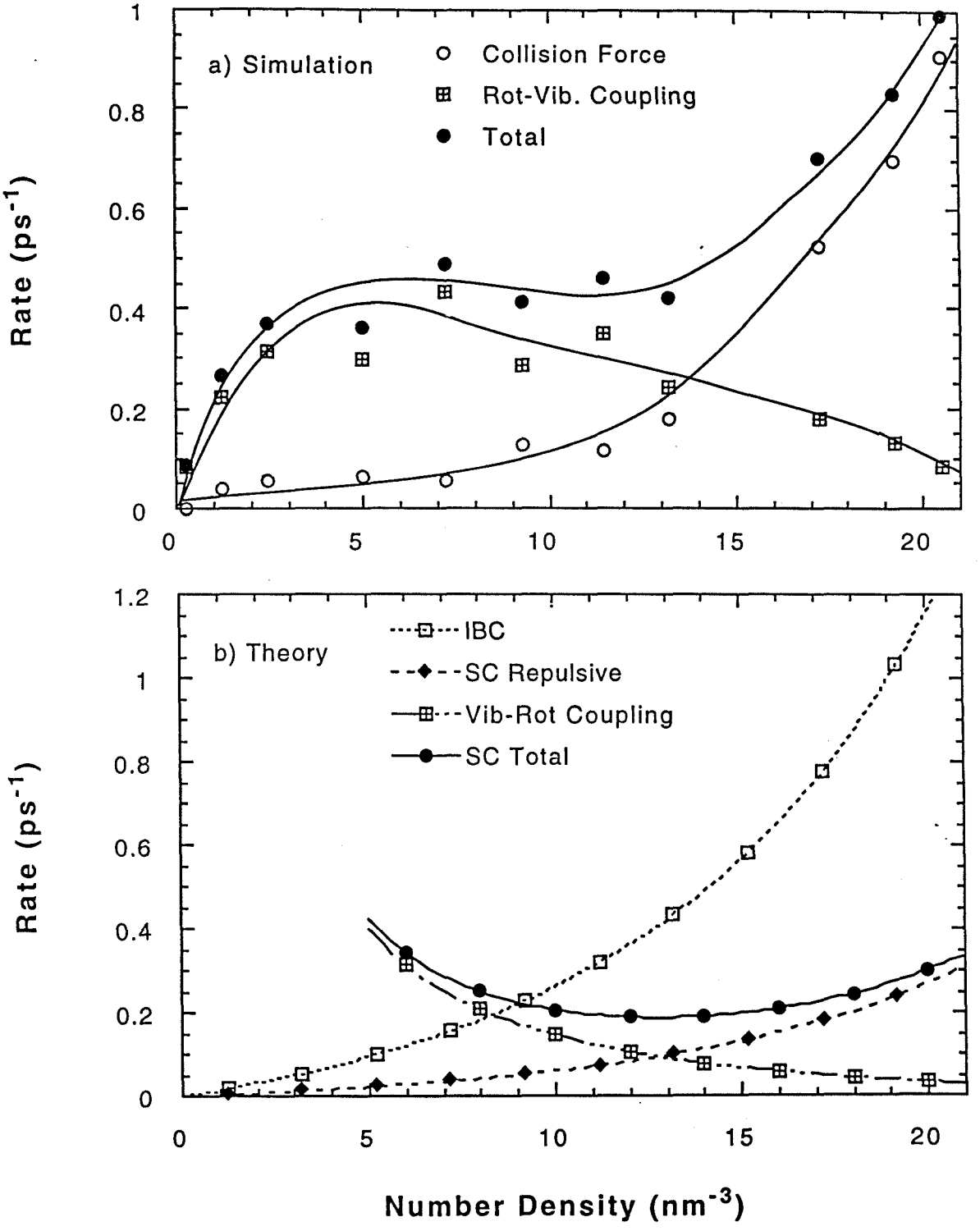
a) Simulation
Collision Force
Rot-Vib. Coupling
Total
Rate (ps^{-1})
b) Theory
IBC
SC Repulsive
Vib-Rot Coupling
SC Total
Rate (ps^{-1})
Number Density (nm^{-3})

Figure 24

Chapter 5

Femtosecond Studies of Dissociation and Recombination of I_2 in Argon Clusters

5.1 Introduction

In continuation of our efforts to examine the ultrafast dynamics of solvated reactions (see articles in reference [1]), we give here a full account of our earlier reports on the studies of atomic reactions in large clusters. This and the accompanying paper [2] focus on the dynamics of dissociation, recombination, and coherence of iodine in large clusters of argon atoms. The iodine system is often employed as a solute because of its two-atom simplicity, long history [3], and well known gas-phase potentials and dynamics [see, *e.g.*, ref. 4-8]. The dynamics of the nuclear motion in isolated gas-phase iodine occur on the femtosecond time scale and depend on the state excited [7-8], as discussed below. In the 1930s, Franck and Rabinowitch [3] proposed that, in solution, the solvent acts to confine the dissociating atoms and force them back close enough to one another to reform the chemical bond. Over the years, intensive efforts have been devoted to the study of dissociation and recombination processes in solution, high pressure gases, clusters, and solids [see ref. 9-41].

Atomic and molecular clusters provide unique systems for studying the solvation dynamics of dissociation and recombination, as it is possible to form real solvent shells around the solute. The number of solvent atoms or molecules can potentially be controlled, allowing one to study the the dependence of solvation on cluster size [42-50]. The reduced number of degrees of freedom in these finite systems also offers an opportunity to examine the microscopic effects of the solvent cage on the nuclear motion of the solute molecule. Previous real-time studies have examined the vibrational and

electronic predissociation of neutral I_2 in relatively small clusters of rare gases, $I_2 \cdot X_n$ ($n = 1$ to 4 and X = He, Ne, and Ar)[51-53], focusing on the rates of dissociation to $I + I + X$ and $I_2^* + X$, and the mechanisms of the reaction. Single atom caging has been examined since the early 1980s [54-59] and the origin of this novel phenomena has been explored by a number of research groups [for recent reviews see ref. 59-60].

In order to study, in real time, the nuclear motion of iodine during the course of dissociation, recombination and relaxation, we have applied the femtosecond methodology, utilizing laser-induced-fluorescence (LIF) as the detection technique. Neutral $I_2 \cdot Ar_n$ clusters were generated in a molecular beam. We used the spectroscopic assignment of Heaven and Tellinghuisen [see ref. 27] and the scaling rules of Buck and Krohne [61] to identify cluster sizes. The I_2 molecules were excited to the dissociative regions of the A, B and Π_{1u} states and to the predissociative region of the B state. Surprisingly, a coherent recombination following direct dissociation of the I_2 on the A state was observed, providing the first direct observation of the caging process on the sub-picosecond time scale. Apparently, the solvent confines the atoms in a "frozen" cage; a picture which is confirmed by molecular dynamics [2]. Following this coherent, direct caging we have observed vibrational relaxation as the two recombining atoms reach the equilibrium geometry. The B state dynamics are fundamentally different and involve dissociation and recombination on a picosecond time scale, as detailed below.

Coherent dynamics in real time were observed in mass-selected ionic clusters of $I_2^- \cdot (CO_2)_n$ by Lineberger's group [44-45]. They observed recombination and vibrational relaxation, and showed that full shells of solvent molecules were necessary for both the observation of the coherent feature and a high quantum yield of geminate recombination [44-45]. The long-range Coulomb interactions induced by the negative charge play a key role in the dynamics and in the solvent localization. For our neutral clusters, we used spectroscopic shifts instead of mass selection to distinguish large clusters from small clusters and bare iodine. Our interest here is to focus on large clusters with one or more solvent shells and not on the size identification of small clusters as in previous work on $I_2 \cdot X_n$ (X = He, Ne, and Ar; n = 1 to 4) [51-53].

For iodine in Ar clusters, a red shift of the LIF emission (D'→A') was observed and assigned to the lowering of the ion-pair states relative to the valence states [27]. This red-shift has been found to depend on the size of the cluster cages, reaching a limiting value of 4200 cm^{-1} (from 342 nm to 400 nm) for large clusters ($N \geq 40$) [27-28]. Monitoring the red-shifted emission (400 nm) is then equivalent to monitoring the dynamics in the large clusters. We assume that the valence states (*e.g.* A/A', B, and Π_{1u}/ Π_{1g}) of iodine are not strongly perturbed by the presence of the argon atoms and, therefore, use gas-phase potentials for these states (Fig. 1), modified to include the solvent-induced barrier. This is consistent with the findings in high pressure Ar gas (up to 2500 bar) [31-32] and in Ar matrices [24] where small changes in the valence-state potential energy surfaces were found. The relevant potential energy surfaces are shown in

Fig. 1. The dotted lines in Fig. 1 represent the solvated ion-pair states [27], which are lower than their gas phase counterparts by 4200 cm^{-1}.

According to the scaling rule developed recently by Buck and Krohne, from their molecular beam scattering study [61], the average size of the clusters formed under our experimental conditions was estimated to change from 8 to 40 atoms, as the backing pressure was varied from 400 to 1100 Torr. The probability of forming more than one I_2 in a single argon cluster is negligible because of the low iodine partial pressure (0.3 Torr) used in the co-expansion [58]. The binding energy between iodine and argon (~ 230 cm^{-1}) [62] is about three times larger than that between argon atoms (~ 80 cm^{-1}), which supports the model of the iodine molecule at the center of the cluster as lowest energy state [2]. If I_2 is on the surface of the cluster, the femtosecond dynamics would be totally different as shown below.

In our experiments, the pump wavelength was tuned from 460 to 700 nm in order to examine both the direct dissociation and predissociation. We also varied the probe wavelength systematically in order to follow changes along the reaction coordinate in the process of recombination and vibrational relaxation. At pump wavelengths longer than 580 nm, direct dissociation on the A state appeared to be the dominant pathway in the clusters and a coherent recovery of I_2 signal was observed. At shorter pump wavelengths (between 500 and 580 nm), a predissociation out of the B state was observed, which was followed by a gradual recombination and relaxation on a much longer time scale. The cluster size dependence of the dissociation and recombination dynamics was also

explored. We varied the stagnation pressure (backing pressure) of the expanding gas mixture so as to change the average size of clusters formed in the beam [61,64-65]. To compare the cluster dynamics with that of isolated systems, we have also examined the LIF spectra and transients for an I_2-He beam. The results are shown to compare with that for the I_2-Ar beam.

To help visualize the motion and to understand the microscopic interactions involved, molecular dynamics (MD) simulations were carried out. We refer to some of the simulation results in the discussion to compare the experimental results to theoretical analyses of the solute-solvent and solvent-solvent interactions. A detailed description of the MD simulations is given in the accompanying publication [2].

This paper is organized as follows. In section II, we briefly describe our femtosecond laser system, the molecular beam apparatus, and the pump-probe LIF detection methodology. In Section III, the experimental results are presented, including (a) LIF spectra, (b) pump wavelength dependence, (c) probe wavelength dependence, (d) 342-nm transients from the iodine-argon beam, (e) backing pressure dependence, and (f) polarization dependence. In Section IV, we discuss the experimental results and present a microscopic picture of the ultrafast solvation dynamics of the reaction.

5.2 Experimental Setup

A tunable linear-cavity dye laser (Coherent Satori) was synchronously pumped by the frequency-doubled output (532 nm) of a CW mode-locked Nd:YAG laser (Coherent Antares 76-S) at a repetition rate of 76 MHz. A prism-pair inside the dye laser was used to compensate for group-velocity-dispersion (GVD). Rhodamine 610/ethylene glycol (EG) and DODCI/EG jets were used as the gain medium and saturable absorber, respectively, to generate 120-fs (FWHM) laser pulses at 614 nm. These laser pulses were passed through a home-built four-stage pulsed dye amplifier (PDA). The PDA was pumped by the frequency-doubled output (532 nm) of a 20-Hz *Q*-switched Nd:YAG laser (Quanta Ray DCR-2). The pump laser was synchronized by fast electronics (Quanta Ray SM-1) to selectively pump 20 out of the initial 76 million pulses generated by the Satori dye laser per second. The unamplified residual pulses as well as the amplified spontaneous emission (ASE) were absorbed by a malachite green/EG saturable absorber jet inside this PDA. Kiten red 620/water and Rhodamine 640/water were used as gain media, and two spatial filters were used to further reduce the ASE. In addition, the final stage was designed for double pass to enhance the amplification. After the PDA, the integrated pulse energy was measured to be about 1 mJ with 10% energy fluctuation and 5% ASE. A double-pass prism compressor was placed after the PDA to compensate for the GVD it induced. The pulse duration was measured to be 120 fs (FWHM) after the compression with a central wavelength of 614 nm and a spectral width of 5 nm (FWHM). For probe-wavelength dependent measurements, the prism compressor was

removed because higher pulse energy was required. Without the compressor, the pulse duration was measured to be 650 fs.

To perform multi-color pump-probe LIF experiments, the amplified laser beam was passed through a beam splitter. For the pump-wavelength dependent measurements, one beam was delayed by a computer-controlled, sub-micrometer resolution translation stage and subsequently frequency-doubled by a 0.5-mm type-I KDP crystal to serve as the probe. This 307-nm probe beam had a spectral width of 5 nm with an estimated pulse energy of 50 μJ. The other beam was focused into a water cell to generate a supercontinuum. A 10-nm bandpass filter, centered at the desired pump wavelength, was used to isolate the pump beam which was then sent into a second three-stage PDA. Depending on the selected wavelength, either part of the doubled (532 nm) or tripled (355 nm) output of the *Q*-switched Nd:YAG laser was used in pumping this PDA and appropriate gain dyes dissolved in methanol or water were chosen as gain media. In this fashion, the central wavelength of the pump beam was tuned from 460 to 700 nm with a spectral width of 10 nm. Following compression in another prism pair, the beam was measured to have a duration on the order of 200 fs and a pulse energy from 50 to 300 μJ depending on the wavelength with about 5% ASE. For the probe-wavelength dependent measurements, the KDP crystal after the translation stage was removed to give a 614 nm beam which was used as the pump while the probe beam was the doubled output of the second dye amplifier. The second prism compressor was also removed in these experiments. The probe wavelength was tuned from 280 to 350 nm with a 5-nm spectral

width. In both cases, the pump and probe beams were recombined by a dichroic beam splitter (BS) outside the vacuum chamber and were sent collinearly into the molecular beam apparatus to perform the experiments.

Figure 2 shows the schematics of the optical setup together with the molecular beam system. The recombined pump and probe beams were focused collinearly into the molecular beam chamber by a UV lens L1 ($f = 30$ cm). A mixture of iodine-argon or iodine-helium gas was prepared by passing argon/helium gas (99.99%) through a tube containing powdered iodine crystals. This mixture was then expanded through a pulsed solenoid valve (d = 500 μm; General Valve series 9) into a vacuum chamber (10^{-4} Torr) to generate a supersonic molecular beam. The backing pressure of argon was varied from 400 to 1,100 Torr to control the formation condition of iodine-argon clusters, while that of helium was fixed at 900 Torr. The pulsed nozzle was synchronized with the 20-Hz *Q*-switched Nd:YAG laser pulses, while the time delay and the duration of the nozzle opening were adjusted to optimize temporal overlap between the molecular beam and the laser beams. The focused (lens L1, $f = 30$ cm) laser beams intersected the molecular beam at right angles 1.5 cm (x/d ~ 30) from the nozzle opening, well after the termination of cluster formation. The crossing region was optimized by adjusting the nozzle position from outside the chamber, as shown in Fig. 2.

The laser-induced fluorescence (LIF) was collected by a convex lens L2 ($f = 5$ cm) and a convex mirror M2 ($r = 5$ cm), as shown in Fig. 2. The collected radiation was then focused by another UV lens L3 ($f = 15$ cm) into a computer-controlled 10-cm

monochromator (*f*/3.5) and was detected by a photon-counting photomultiplier tube (PMT). The spectral resolution of the monochrometer was adjusted in this experiment from 2 to 16 nm. The signal output from the PMT was averaged by a gated boxcar integrator (PARC Model 162 & 164) with a gate width of about 50 ns and an integration time of 0.25 seconds. Five laser shots were, therefore, averaged over each integration period. The integrated signal was then sent to an A/D converter and was processed by a microcomputer.

For each set of measurements, the spectral information of the LIF was obtained by scanning the calibrated monochromator in wavelength with a 2- or 4-nm resolution. Spectra were taken at both a positive and negative delay between the pump and probe pulses. Background spectra due to the pump or probe beam alone were also recorded. The monochromator was then fixed at a certain wavelength (342 or 400 nm) with a broader spectral resolution (4-8 nm). The LIF transient was obtained by scanning the delay line from a negative time delay to a positive time delay between the pump and probe laser pulses.

LIF spectra and transients were obtained for both iodine-argon and iodine-helium expansions. This procedure was repeated for each combination of the pump and probe wavelengths and each backing pressure of argon. To achieve good statistics, all the transients obtained were averaged over 40 scans of the delay line, corresponding to an average of 200 laser shots for each data point. The linearity of the detection system was carefully checked and verified with calibrated neutral-density filters. The transients

obtained at different intensities of the pump and probe beams showed identical behavior. This indicates that the absorption of either the pump or the probe pulses was below the saturation limit in our experiments.

5.3 Results

5.3.1. Laser-induced-fluorescence spectra

At a certain time delay between the pump (480 to 700 nm) and probe (307 nm) pulses, we scanned the monochrometer from 320 to 460 nm and recorded the emission spectra from both the iodine-helium and iodine argon beam with a spectral resolution of 2 nm. The emission spectra from the iodine-helium beam appeared identical to those obtained from iodine gas cells with the same pump-probe combination and with the same spectral resolution (~ 2 nm). Within the wavelength range of 320 to 460 nm, only a 342 nm band was observed to be dependent on the pump-probe time delay. The emission spectra from the iodine-argon beam, on the other hand, showed two emission bands that were dependent on the time delay: one around the 342 nm, the other extended from approximately 370 to 420 nm. As reported earlier [27-28], the center of this broad band shifted from 375 nm to 400 nm as the stagnation pressure of argon gas was increased from 650 Torr to 1100 Torr. The relative amplitude of this broad band to that of the 342 nm emission increased with the increase of the argon backing pressure. This broad emission band became too weak to detect as we lowered the argon backing pressure to near or below 400 Torr. In contrast, the 342 nm emission became stronger as we lowered the argon backing pressure.

Figure 3 shows the LIF spectra for two different pump wavelengths (510 and 614 nm) while the probe wavelength is at 307 nm. To record these spectra (thick lines in Fig. 3) the probe pulse was delayed by 100 ps (positive time delay) relative to the pump pulse. The spectra obtained when the pump and probe pulses overlapped in time (zero

time delay) appeared identical to the thick lines in Fig. 3. At negative time delays, *i.e.* when the probe pulse preceded the pump pulse, the emission band around 342 or 400 nm either disappeared or decreased, depending on the pump wavelength (thins lines in Fig. 3). The emission spectra obtained with only the pump beam (the probe beam was blocked) were identical to those obtained at negative time delays, suggesting that the background signal around 342 or 400 nm was caused by the multi-photon absorption of the pump beam. The background signal at 355 nm (Fig. 3.a) came from the scattered light of the tripled output of the DCR-YAG laser (the pump laser of the PDA).

5.3.2. Pump wavelength dependence

With the pump wavelength tuned from 480 to 700 nm and the probe wavelength fixed at 307 nm, we scanned the pump-probe time delay and obtained LIF transients from both the iodine-helium and iodine-argon beams by detecting fluorescence at 342 and 400 nm, respectively. The stagnation pressure was fixed at 1100 Torr for the iodine-argon expansion and at 900 Torr for the iodine-helium expansion. We first scanned the relative time delay between the pump and probe pulses on a long time scale (from –20 to 180 ps) to examine the long-time behavior of the transients. We then shortened the scanning range to time resolve the dynamics within a few picoseconds of the pump excitation of the system. In the following we shall first describe the transient behavior for iodine in the helium expansion and then present the corresponding results from the iodine-argon expansion on short (–2 to 14 ps) and long (–20 ps to 180 ps) time scales separately.

(1) IODINE-HELIUM TRANSIENTS

At pump wavelengths shorter than 500 nm or longer than 614 nm, the LIF transients from the iodine-helium expansion showed only a single peak with pulse-width limited rise and decay (~200 fs) at zero time delay. The insets of Figs. 4.c & 5.a show iodine-helium transients on a short time scale (–1 to 4 ps). These transients were fit by a Gaussian function to estimate the pump-probe cross correlation and to calibrate the zero time delay (time zero). At pump wavelengths between 500 and 590 nm, the iodine-helium transients all displayed a plateau after the initial pulse-width-limited rise at zero time delay. Some of these transients taken at 510, 580, and 590 nm pump wavelengths are shown on a short time scale (insets of Fig. 4.a and Fig. 5.b & 5.c). A modulation appeared on the 510-nm transient, showing a period of 900 fs in agreement with gas phase results [8, 66]. The initial rises were also used to calibrate the cross correlation of the pump/probe pulses and the time zero. For the pump wavelength at 614 nm, an initial peak occurred at time zero which then promptly decayed to a constant signal level (inset of Fig. 4.b). The relative amplitude of the constant level to that of the initial maximum was about 50%. This transient was also used for the purpose of calibration, as discussed below.

(2) IODINE-ARGON TRANSIENTS ON A SHORT-TIME SCALE

Monitoring the 400 nm fluorescence, we recorded the corresponding LIF transients from the iodine-argon beam with the stagnation pressure fixed at 1100 Torr and with the probe wavelength at 307 nm. The 614-nm iodine-argon transient shown in Fig. 4.b is typical of "A-state type" behavior. An initial peak appeared at the zero time delay

with a pulse-width limited rise and decay (~ 200 fs), which is coincident with the time zero in the iodine-helium transient (inset of Fig. 4). After decaying to almost zero, the signal promptly recovered to a level that is comparable to the initial maximum. This recovery occurred on a time scale (~ 300 fs) that was close to the cross correlation (~ 320 fs, FWHM) of the pump and probe pulses. At longer delay time (2 to 30 ps approximately) , the signal increased almost linearly and much more slowly (see also Fig. 6.d). For pump wavelengths ranging from 590 to 700 nm (λ_{probe} = 307 nm), the transients exhibited similar behavior. Due to the broader pump pulse duration at wavelengths other than 614 nm, the pulse-width limited rise-decay-recovery feature was not as well time resolved in the other A-state type transients (Fig. 4.a & 4.c) as in the 614 nm one (Fig. 4.b). A shoulder instead of a peak was observed at the zero time delay for a 700 nm transient (Fig. 4.c).

The iodine-argon transients at pump wavelengths between 500 and 580 nm displayed a monotonic decay after the initial pulse-width limited rise on the short-time scale. As a typical example, the transient taken at a pump wavelength of 510 nm is shown in Fig. 5.b. For comparison, the transient taken from the iodine-helium expansion at the same pump/probe combination is shown in the inset with a modulation period of 900 fs. At pump wavelengths between 510 and 590 nm, bare iodine molecules are mostly prepared on the B state [5] and undergo bound oscillatory motion [7, 8] with lifetimes on the order of ~ 1 μs [67]. For iodine-argon transients, the behavior changes from the "B-state type" to the "A-state type" when the pump wavelength is tuned from 580 to 590 nm.

For iodine in a helium beam, the transient behavior, on the other hand, did not show pronounced difference between these two pump wavelengths (insets of Fig. 4.a & 5.c).

For the pump wavelength at 480 nm, the iodine-argon transient displayed a plateau following the initial pulse-width limited rise on this short-time scale (Fig. 5.a). The corresponding iodine-helium transient, in contrast, shows just a sharp peak at zero-delay-time (inset of Fig. 4.a). At this wavelength, bare iodine molecules are excited to the dissociative regions of the B (above its bound limit) or Π_{1u} state [5].

(3) IODINE-ARGON TRANSIENTS ON A LONG-TIME SCALE

On a long time scale, the pump wavelength dependence of the iodine-argon transients is shown in Fig. 6 for pump wavelengths of 480, 510, 614, and 640 nm. Transients with pump wavelengths between 590 and 700 nm displayed single multi-slope rises that reached asymptotic values in 50 ps (Fig. 6.c & 6.d). At pump wavelengths between 500 and 580 nm, the transient signal decayed on a time scale of 10 to 20 ps after the first pulse-width limited rise. After reaching a minimum, the signal increased again and reached a constant level in another 50 ps. As a typical example, Fig. 6.b shows such a "B-state type" transient taken with a 510-nm pump pulse (λ_{probe} = 307 nm). In the 480-nm transient (Fig. 6.a), the LIF signal appeared to stay constant for 10 ps following the initial pulse-width limited rise and then increased gradually to a higher asymptotic value in another 50 ps.

5.3.3. Probe wavelength dependence

To examine the probe wavelength dependence of the transient signals at 400 nm, we have tuned the probe wavelength from 280 to 350 nm. The pump wavelength was fixed at 614 nm and the stagnation pressure of the argon gas was maintained at 1100 Torr. The cross correlation of the pump and probe pulses used in this investigation was measured to be 0.8 ps. Detecting the 400 nm fluorescence, we scanned the pump-probe time delay over certain ranges. The results obtained are shown in Fig. 7 on a long time scale (–20 to 180 ps). At λ_{probe} = 350 nm, the LIF signal rose quickly to a maximum within 3 ps and then decayed to almost the ground level in another 12 ps (Fig. 7.a). At shorter probe wavelengths (up to 307 nm), both the rise time and decay times became longer (Fig. 7.b-d). In addition, a constant signal level after the initial rise and decay became more significant at shorter probe wavelengths, except for the 280 nm probe. The rise time (from zero intensity level to maximum) became 10 ps at λ_{probe} = 330 nm, 18 ps at λ_{probe} = 320 nm, and 50 ps at λ_{probe} = 307 nm. The decay time (from maximum to the constant level) was 12 ps at λ_{probe} = 350 nm, 50 ps at λ_{probe} = 330 nm, and 70 ps at λ_{probe} = 320 nm. The decay was not apparent at λ_{probe} = 307 nm (Fig. 7.d). At λ_{probe} = 280 nm, the rise and decay times became fast again: the rise time was 8 ps and the decay time was 15 ps (Fig. 7.e). At λ_{probe} = 280, 307, and 320 nm, the transient signal first reached a certain value after a fast rise (2 ps) and then increased more slowly and almost linearly for another 6 to 20 ps.

5.3.4. The 342 nm emission

At certain wavelength combinations and relative time delays of the pump (480 to 700 nm) and probe (307 nm) pulses, we scanned our monochrometer and obtained the LIF emission spectra from both the iodine-argon and iodine-helium beams. Within the 2-nm spectral resolution of our detector, the spectra obtained from these two beams displayed a similar fluorescence band around 342 nm. We then monitored this 342 nm emission and scanned the pump-probe delay line. The LIF transients obtained from the iodine-helium beam appeared similar to those from iodine gas cells and were described previously. For the iodine-argon beam, the probe wavelength was fixed at 307 nm and the argon backing pressure was kept at 1100 Torr. A transient obtained from the iodine-argon beam at λ_{pump} = 510 nm and λ_{probe} = 307 nm is shown in Fig. 8.b, as a typical example of the transients obtained at pump wavelengths between 480 and 550 nm. The main features displayed by these transients appeared similar to those obtained with detection of the same situation at 400 nm emission (Fig. 8.a). For a pump wavelength of 614 nm, an initial peak with a pulse-width limited rise and decay was observed at zero-time-delay, which was then followed by a slow, almost linear rise after the initial decay reached the zero intensity level (Fig. 9.a). The fast recovery, apparent in the corresponding 400-nm transient (Fig. 9.b), was absent from the 342-nm transient.

5.3.5. Backing-pressure dependence

The internal temperature and average size of the clusters are dependent on the backing pressure of the expanding gas [61,64-65]. We have varied the backing pressure

of argon from 400 to 1,100 Torr corresponding to cluster sizes from approximately 8 to 40 atoms. We scanned the pump-probe time delay and separately monitored the 400 and 342 nm signals from the iodine-argon beam. The transients thus obtained for the pump/probe combination of 510/307 nm were fit by a bi-exponential function for both the 400 (Table 1) and 342 nm transients (Table 2). For the 400-nm transients, the relative amplitude of the long-time asymptote to the initial maximum increased with the backing pressure. The decay time after the initial pulse-width limited rise was relatively insensitive to the backing pressure change while the following recovery time became shorter as the backing pressure became higher. For the 342-nm transients, both the decay and rise times decreased as the pressure increased. At pressures of 670 and 1,100 Torr, we also obtained 400-nm transients with the 614/307-nm pump/probe wavelength combination. The component of the fast recovery appeared to be slightly smaller and slower for the transient obtained at a lower backing pressure. On a longer time scale, the two transients (not shown here) appeared almost identical.

5.3.6. Polarization dependence

At the 614/307-nm pump-probe wavelength combination, we adjusted the relative polarization angles of the pump and probe beams. Detecting 400 nm emission, with the Ar backing pressure at 1100 Torr, we recorded transients with the polarization of the pump and probe beams at parallel (0°) and perpendicular (90°) orientations. They appeared identical within the noise level (not shown). We also took iodine-helium transients (λ_{probe} = 307 nm; detecting 342 nm emission, helium backing pressure at 900

Torr) for which the angles between the pump and probe polarization directions were set at 0°, 45°, and 90°. The relative amplitude of the initial peak to the long-time asymptote differed slightly for different polarization angles: the largest for 45° and the smallest for 90°. At a pump wavelength of 510 nm, we conducted a similar measurement on the iodine-argon expansion (1100 Torr). The transients obtained (λ_{probe} = 307 nm; detecting 400 nm fluorescence) for different polarizations between the pump and probe beams did not display a significant difference.

5.4 Discussion

5.4.1. Cluster size and spectra

According to the gas phase absorption coefficients [5], the pump pulses (460 to 700 nm) used in our experiments could excite I_2 from the X state to either the B, Π_{1u} or A state depending on the wavelength, as shown in Fig. 1. The probe pulse (280 to 350 nm) further reaches ion-pair states through allowed electronic transitions (*e.g.* B $\rightarrow$ f, A $\rightarrow$ β, A' $\rightarrow$ D', and X $\rightarrow$ D) [6]. In the gas phase, collision induced non-radiative energy relaxation promptly quenches all ion-pair excitations into the ground state of the lowest ion-pair state D' [68], from which the characteristic fluorescence (342 nm, D' $\rightarrow$ A') of uncomplexed I_2 is emitted. For I_2 in Ar, the ion-pair states are solvated by the surrounding argon atoms leading to a lowering of the ion-pair potentials relative to the valence states [9,24,27-28,31-32]. In argon matrices, the emission was red shifted by as much as 2900 cm^{-1} to 380 nm [24]. Recent studies on I_2 in high pressure argon showed that the center of this emission band gradually shifts from 342 nm to 374 nm at room temperature as the pressure of argon gas increases from 0 to 2000 bar [31-32].

Fei *et al.* observed a broad 400 nm emission as well as the 342 nm band, using nanosecond LIF detection of clusters. [27] The center of the 400-nm band was observed to shift from 375 nm to a limiting value of about 400 nm as the backing pressure was increased from 1140 to 1900 Torr, in their argon expansion conditions (d = 0.3 mm). The relative amplitude of the 400-nm band to that of the 342-nm band was also enhanced as the backing pressure was raised. This red shifted emission was assigned to large $I_2 \cdot Ar_n$

clusters formed in their iodine-argon expansion. Effective solvation of the ion-pair states by the argon cage was suggested to account for the 4200 cm^{-1} red shift of the fluorescent emission. The 342-nm emission was assigned, in their work, to the population of bare iodine molecules in the molecular beam. In our experiment, we also observed the two-band features in the LIF spectra: one at 342 nm and the other shifting from about 375 to 400 nm as the argon backing pressure was increased from 400 Torr to 1100 Torr. At backing pressures near or lower than 400 Torr, the red-shifted band almost disappeared while the 342 nm signal was even stronger. Unlike rigid matrices, the clusters under study have the most compact structure [65], which enables them to solvate iodine as effectively as low temperature liquids. [27,69]

Using the scaling rule developed by Hagena, *et al.* [64], we estimated the average size of the $I_2 \cdot Ar_n$ clusters in our beam (nozzle diameter 0.5 mm) to range from 25 to 130 as the backing pressure was varied from 400 to 1100 Torr. Buck and Krohne [61] have recently characterized the size distributions of Ar clusters in their crossed beam experiments, in which the scattering cross-section and distribution of the helium beam was correlated with the cluster size distributions in the argon beam. Their measurement suggested that the previous scaling rule overestimated the average size of the clusters. According to their newly developed relation between the average cluster size $\overline{N}$ and the backing pressure P(in mbar), the nozzle diameter d (in μm), and the nozzle temperature T (in K), $\overline{N} = 86.95 \times P^{1.64} \cdot d^{1.394} \cdot T_0^{-3.752}$, the average size of argon clusters formed in our molecular beam at P ~ 1100 Torr was estimated to be 40. Clusters of this size form

almost two full layers of argon atoms and suffice to cage the dissociated iodine atoms, as was shown by the MD simulations [2]. As mentioned above, particles in clusters tend to form the most compact structure [65] and the solvation of the iodine states is therefore more complete in the clusters (4200 cm^{-1}) [27] than in the argon matrix (2900 cm^{-1}) [24]. At a backing pressure of 400 Torr, the average size of our clusters was estimated to be about 8. Most of the clusters at this backing pressure were not large enough to cause red shifted emissions, as discussed below. The inclusion of I_2 in the cluster can be deduced from the observed femtosecond dynamics (free *vs.* caged wave packet) and is consistent with the larger binding energy between iodine and Ar compared with Ar-Ar, as discussed in the introduction.

The probe pulses used in these experiments excited the iodine systems to the ion-pair states (*e.g.* f, D, β and D') with some excess energy with respect to the bottom of the lowest ion-pair state D'. The radiative lifetimes of these ion-pair states are on the order of several nanoseconds [6] for bare iodine systems. If the lifetimes are on the same order of magnitude in the clusters, then the efficient non-radiative relaxation on these ion-pair states may transfer most of the population into the bottom of the D' state and pass the excess energy to the surrounding argon atoms. Some argon atoms with enough kinetic energy could evaporate from the clusters. If we assume that the average binding energy of each argon atom to the cluster [45] is on the order of 1000 cm^{-1}, then 7 to 8 argon atoms may be evaporated by an excess energy of 7500 cm^{-1}. This excess energy is estimated by subtracting the photon energy of the fluorescence (400 nm) from the photon

energy of the probe pulses (307 nm). When clusters with a small number of argon atoms ($n \leq 8$) are excited by the probe pulses, this non-radiative relaxation in the ion-pair states may evaporate all of the surrounding argon atoms and reduce these clusters to bare iodine molecules by the time fluorescence occurs. In addition, the vibrational relaxation on the A/A' ,B, or X state could also cause the evaporation of some argon atoms at longer pump-probe delay times, as was demonstrated by the MD simulations [2]. This may explain why the 342-nm transients from the iodine-argon expansion differed totally from those obtained from bare iodine systems (detecting 342 nm). On the other hand, the clusters that eventually fluoresce at 400 nm must initially have much more than 8 argon atoms in order to provide a solvation energy of 4200 cm^{-1} throughout the relaxation and evaporation processes. This explanation is further supported by the different 340-nm transients observed in the iodine-argon expansion from the ones observed in the iodine-helium expansion.

The LIF spectra from the iodine-helium expansion showed only a 342 nm emission in the 300- to 500-nm region. The transients obtained by monitoring this 342 nm signal from the iodine-helium beam are very similar to those from bare iodine molecules in gas cells. At the moderate backing pressure (900 Torr) used, He is very inefficient in forming iodine-helium complexes. The van der Waals interaction between I_2 and He (14 cm^{-1}) is much weaker than that between I_2 and Ar (230 cm^{-1}) [62]. The iodine dynamics would not be significantly affected by the He attachment even if some small $I_2 \cdot He_n$ complexes were formed in the beam. There is, however, difference between

the iodine system in the He expansion and the bare iodine system at room temperatures in a gas cell. The He expansion provides a collision free environment and a lowering of the vibrational/rotational temperatures of the iodine molecules to around 30 K. The transients obtained from these systems, therefore, characterize the dynamics of cold isolated iodine.

We have therefore three conclusions regarding the LIF spectra: (1) the 400 nm fluorescence comes essentially from large iodine-argon clusters and the detection of the 400 nm emission provides a unique way to monitor the wave packet motion of iodine molecules inside neutral argon clusters.; (2) the 342 nm emission from the iodine-argon expansion, on the other hand, originates partially from small iodine-argon clusters and partially from residual population of bare iodine molecules; (3) the 342 nm emission from the iodine-helium expansion characterizes cold isolated iodine systems. The solvent shift observed here can be related to the large dipole moment of the ion-pair states, and this has been treated in the papers by Lienau *et al* [31-32].

5.4.2. Probe windows

As shown in Fig. 1, the probe pulses (λ_{probe} = 280 nm to 350 nm) used in our experiments excites the I_2 to the ion-pair states through allowed electronic transitions, *e.g.* B $\rightarrow$ f, A $\rightarrow$ β, A' $\rightarrow$ D', and X $\rightarrow$ D. [4,6] The relative strength of the fluorescence following the probe pulses depends on several factors: The I_2 population on the intermediate states (B, A/A' or high vibrational levels of X), the absorption cross section of the probe photons at these states, and the fluorescent quantum yield from the ion-pair

states. The laser intensities were kept constant throughout the delay range in our experiment. In the argon clusters, non-radiative relaxation on the ion-pair states occurs on a much shorter time scale (100 ps) than the fluorescent emission (4.5 to 8 ns) so that most of the excited states were quenched non-radiatively into the bottom of D' state before the fluorescence occurred. The quantum yields for fluorescence were thus nearly the same for all excitations. The relative amplitude of the LIF signal was then dependent on the population and the probe pulse absorption. For bare iodines at room temperature, the absorption cross-section from X to D was measured to be 0.92 $\dot{A}^2$ at 183 nm probe [9], and that from A' to D' was measured to be 0.61 $\dot{A}^2$ at 300 nm probe [70]. For $I_2 \cdot Ar_n$ clusters, we assumed that the solvation effect simply pulled down the ion-pair states by 4200 cm^{-1}, as shown by the dotted lines in Fig. 1. Using gas phase potentials for the valence and ground states, we calculated Franck-Condon distributions as functions of probe wavelengths. For the ground state, the maximum absorption shifts to lower vibrational levels as the probe wavelength becomes shorter. At 307 nm, the optimal absorption is centered around 7500 cm^{-1} below the dissociative limit (or 5000 cm^{-1} above the bottom) of the ground state, according to this calculation.

The X to B pump excitation (pumped at 480 to 620 nm) of I_2 is a parallel electronic transition. The transition induced by the probe absorption from B to f is also parallel. The LIF signal near time zero will be enhanced by a factor of three if the pump and probe pulses are short enough and their polarization are aligned in the same direction [71]. The X to A transition, on the other hand, is perpendicular. The subsequent A to β

probe absorption is again parallel. The pump-probe LIF signal upon excitation of the A state is thus favoring the perpendicular alignment of the pump and probe beams. At a pump wavelength of 614 nm, the LIF signal was probably a combination of both A and B state excitation. The polarization dependence of the LIF signal from the I_2 in He beam, therefore, did not favor either the perpendicular or the parallel alignment of the pump and probe pulses. In the large $I_2 \cdot Ar_n$ clusters, no explicit polarization dependence of the LIF transients was observed. This may indicate that the symmetry of the ion-pair states were at least partially destroyed by the Ar solvent shells. We must, however, consider all three processes, pump/probe/fluorescence, in order to calculate the magnitude of the anisotropy expected [1].

5.4.3. Direct dissociation and recombination

Monitoring the 342 nm emission from the iodine-helium beam, we obtained LIF transients at different pump wavelengths (480 to 700 nm) while the probe wavelength was fixed at 307 nm (insets of Figs. 4 & 5). Beginning at a pump wavelength of 614 nm pump (inset of Fig. 4.b), a dissociative channel became important and dominant as the pump wavelength became longer, as illustrated by the pulse-width limited peak at zero time delay. This dissociative channel is attributed to pump excitation to the A state. At room temperature, about 30% of the iodine molecules are excited to the A state at 614 nm [5]. The LIF transients (not shown here) obtained by detecting the 342 nm emission from iodine gas cells with the same pump and probe combination (614/307 nm) at room temperature, however, did not show a significant peak at zero time delay, suggesting that

A state excitation was less important at room temperatures (gas cell environment) than at lower temperatures (in the He expansion) for the same pump wavelength. This interpretation is supported by Tellinghuisen's work [72] which indicated that the X to B absorption of bare iodine was dependent on the vibrational/rotational temperature of the molecule. At pump wavelengths longer than 580 nm, this X to B absorption becomes less efficient at lower temperatures.

The X to A absorption may, therefore, be relatively enhanced at long wavelengths (614 to 640 nm) for cooled (30 K) I_2 molecules in helium and argon expansions. Furthermore, the X to B absorption was previously observed to be blue-shifted by 13 cm^{-1} per Ar atom in the $I_2 \cdot Ar_n$ clusters because of different degrees of X and B state solvation [54]. If we assume that in a full layer (~ 20) of Ar atoms, each atom incites the same blue-shift, then the X to B absorption will be shifted to shorter wavelengths by as much as 260 cm^{-1}, or 10 nm near 614 nm. This solvation-induced blue-shift may may partially explain why the $I_2 \cdot Ar_n$ transients displayed A-state type behavior at λ_{pump} = 590 nm (Fig. 4.a), a wavelength at which the corresponding bare I_2 transient from the He beam displayed bound B-state behavior (inset of Fig. 4.a). On the other hand, I_2 excited to its B state by light near 590 nm (v' ~ 12 to 14) predissociates very rapidly both in $I_2 \cdot Ar_n$ clusters [59] and in high pressure Ar gas [31-32]. At λ_{pump} = 620 nm, the predissociation time of the B state was measured to be about 1 ps at an Ar pressure of 2000 Bar [31-32]. In a recent time-resolved experiment on the I_2 in liquid n-hexane by Scherer *et al.* [73] the predissociation time of the B state following 580 nm excitation was obtained to be on

the order of 300 fs. In large $I_2 \cdot Ar_n$ clusters, strong coupling between the B and the Π_{1u}/Π_{1g} states may have caused direct dissociation of I_2 below the 590 nm excitation level ($v' \sim$ 12 to 14). The initial peak in the LIF signal observed in A-state type transients (Fig. 4) could, therefore, have some contribution from this dissociative region of the B state as well as from the A state. At pump wavelengths longer than 640 nm, dissociation following A state excitation dominated in both the iodine-argon beam and the iodine-helium beam, as was demonstrated by the transients shown in Fig. 4.c and the inset.

The recovery of LIF signal observed in the transients of $I_2 \cdot Ar_n$ clusters is direct proof of geminate recombination. After reaching a zero intensity level, the LIF signal (400 nm emission) from the $I_2 \cdot Ar_n$ clusters recovered on a time scale of 300 fs. The recovery of signal was best resolved in the 614-nm transient (Fig. 5.b) which was obtained with the shortest pump and probe pulses (120 fs). The time scale of the prompt recovery was comparable to the pump-probe cross correlation which was characterized by the pulse-width-limited rise and decay of the initial peak. This indicates that the coherence of the wave packet motion was preserved for as long as 660 fs throughout the dissociation and recombination process and manifested in the damped oscillations at longer times [2]. We have ruled out the possibility that this fast recovery could have been caused by a vibrational motion on the B state, because its vibrational period at this energy (614-nm pump) is around 300 fs for bare I_2 [8,66] and I_2 in high pressure Ar gas [31-32]. At 300 fs of time delay, the signal level dropped to almost zero (Fig. 4.b), indicating that either the B state became dissociative or the probe photon (307 nm) absorption on the B

state was very inefficient at this pump excitation energy (614 nm) in argon clusters (compared to the A state absorption). At longer pump wavelengths (640 to 700 nm) the LIF transients obtained from the iodine-argon beam displayed coherent features similar to the 614-nm transients. At pump wavelengths between 700 and 590 nm, the A state is dissociative with excess energies of 1700 to 4400 cm^{-1}. The fast recovery of signal at 660 fs, therefore, represents a coherent recombination of I_2 following direct dissociation in the argon cage.

As emphasized in our earlier report [30], the key to this coherence lies partially in the fact that the cluster structure was initially cold and rigid when the dissociation occurrs. This view is supported by MD simulations [2]. The Ar atoms act collectively in colliding with the dissociating iodine atoms. After the first series of collisions, some of the iodine atoms bounce back adiabatically on the original A state and give rise to the coherent recovery of LIF signal. The non-exponential rise following the coherent recovery comes mainly from vibrational relaxation on the A/A' states. For an initially warm (60 to 90 K) cluster, the cluster cage melts and its soft structure excludes coherent motion [2]. The cluster size may also play a role in determining whether coherent recombination is possible. As shown by Fig. 9.a, the coherent recovery was absent from the transients obtained by monitoring the 342 nm emission, which characterizes smaller clusters, from the iodine-argon beam. Coherent caging had not been previously observed in the liquid phase or in high pressure gases because of the induced thermal averaging. Aside from the necessary ultrashort laser pulses, the observation of such coherence

requires a relatively cold and rigid solvent as well as an ultrashort dissociation time (direct dissociation) [30].

Upon recombination in the cluster cage, the I···I atom pair may be formed either on the A/A' or X state. The recombination takes less than 2 ps following direct dissociation on the A state dissociation [2]. The A and A' states have well depths of 1640 and 2500 cm^{-1}, respectively, for bare iodine systems [4,74-75]. In argon matrix [24], these states were reported to have radiative lifetimes of 143 μs (A) and 6 ms (A'), much longer than the time scale of our interest. If the Franck-Condon region is centered near the bottom of these states, the LIF transients are expected to show a plateau following a monotonic rise, with the rise time reflecting the relaxation time on these states. The transient obtained at a probe wavelength of 307 nm did show such a behavior , with a rise time of about 50 ps (see Fig. 6c), which is two to three times longer than the A/A' relaxation time calculated from the MD simulations [2]. This may indicate that the MD simulations tend to over-estimate the vibrational relaxation rate [20]. At the probe wavelength of 307 nm, the LIF signal remained constant at long pump-probe time delays (up to 200 ps). This led us to conclude that the LIF signal from iodine which recombined on the X state was not important, if there was any. Otherwise, at all the probe wavelengths that we invoked (280 to 350 nm), we would have observed a rise and decay in the signal as the population relaxed into and out of the Franck-Condon maximum of the probe pulse.

The transients obtained in the probe-dependent experiments are shown in Fig. 7 for five different probe wavelengths (280 to 350 nm). These transients were all obtained at the same Ar backing pressure (1100 Torr), with the same pump wavelength (614 nm), and monitoring the same fluorescent emission (400 nm). Probed at 350 nm, the rise time was about 3 ps. It increased to about 6 ps at λ_{probe} = 330 nm and up to 10 ps at λ_{probe} = 320 nm. The time scale of the subsequent signal decay increased from 5 ps at 350 nm to 30 ps at 330 nm and up to about 40 ps at 320 nm. As the probe wavelength was tuned from 350 to 307 nm, the absorption maximum of the probe pulses shifted from high to low vibrational levels of the A/A' states. If the iodine molecules recombined into the A/A' states and underwent vibrational relaxation, we would see the LIF signal increase as the population steps into the absorption maximum and then decrease as the population moves past this maximum. Both the rise time and the decay time should become longer, as the probe wavelength becomes shorter, because the lower the vibrational level, the slower the relaxation rate. This is consistant with the above results.

At probe wavelengths shorter than 307 nm, the rise and decay appeared again (see Fig. 7e, for 280 nm probe). This indicates that the Franck-Condon maximum has shifted toward higher vibration levels along the opposite side of the A/A' state potential well (relative to longer probe wavelengths). It is also possible that the ground state population became visible at these short probe wavelengths and contributed to this signal rise and decay on top of signal from the A/A' states.

When probed at 350 nm, the transient signal decayed to nearly zero after a maximum was reached, indicating that no signal came from the bottom of the A/A' states at this probe wavelength. As the probe was tuned to shorter wavelengths (330 and 320 nm), the signal decayed to a constant level whose relative amplitude increased with the decrease of probe wavelength (Fig. 7b and Fig. 7c). When probed at 307 nm, the transient simply displayed a plateau following a 50 ps rise (Fig. 7d). As mentioned above, we have assigned the asymptotic signal to the lowest vibrational levels on the A/A' states. For iodine molecules at room temperature, the maximum probe absorption from the A' state was measured to be around 300 nm [18]. This maximum corresponds to resonant absorption from the lowest vibrational levels on the A' state. In solvents, the absorption is expected to be red shifted because of the lowering of the ion-pair states. In liquid CCl_4, the shift was reported to be ~ 20 nm near the 320 nm probe wavelength [18]. The red-shift in Ar clusters was expected to be slightly smaller than that in liquid CCl_4 since the polarizability of the Ar atom (1.64×10^{-24} cm^3) is smaller than that of the CCl_4 molecule (11.2×10^{-24} cm^3) [76]. Meanwhile, the fluorescence (D' to A') red shift in the clusters under study was as much as 4200 cm^{-1}. It was therefore concluded that the A' state absorption maximum at the bottom of the well had been shifted to 307 nm in these clusters. The A and A' state absorptions are expected to be similar because of their similarity in potential energy surfaces. In principle, the populations at intermediate levels of the X state could also be probed at wavelengths from 280 to 350 nm. Vibrational relaxation on the X state takes a few hundred picoseconds [2] for the population to move

out of these intermediate regions and reach the lower levels of the well. Accordingly, if an X state contribution had been significant in our experiment, we should have observed rise and decay features in all our transients independent of the probe wavelength. The fact that we did not observe any decay in the 307-nm-probe transient on the time scale of 200 ps indicates strongly that X state absorption was not important in our experiment, at least for the probe wavelength of 307 nm. This conclusion is consistent with work on high pressure systems [31, 32, 41].

Many of the A-state type transients (Fig. 7) displayed multi-slope rises after the pump excitation. In the transient UV absorption experiments conducted in Harris' group on I_2 in CCl_4 [19], similar multi-slope rises, followed by multi-slope decays, in the transient absorption were observed on a long time scale (from 80 ps to a few nanosecond). In their experiment (with a pump wavelength of 590 nm and a probe wavelength of 295 to 400 nm), the rise times of the A/A' state signal, which characterizes the vibrational relaxation on these two states, were estimated to be about 20 ps. A faster decay (5 to 20 ps depending on the probe wavelength) component was assigned to the predissociation of the B state, and a slower decay component (~ 400 ps) was assigned to the A/A' to X non-radiative relaxation. In our experiment, however, we found that either the B state was directly dissociative or its contribution to the LIF signal (400 nm) was insignificant at pump wavelengths below 590 nm.

5.4.4. Predissociation and recombination

At pump wavelengths between 500 and 580 nm, the LIF transients from the isolated systems in the He beam indicated a pump excitation to the B state which was stable on the time scale of interest (200 ps). The corresponding iodine-argon transients displayed a very different behavior. They were characterized by a pulse-width limited rise at time zero, a following ~ 10 ps decay and a subsequent slower recovery that occurred on a 50 ps time scale. The pulse-width limited rise in both the He and Ar beams characterizes the coherent excitation of I_2 to the B state (there could be some percentage of excitation to the Π_{1u} state at 510 or 500 nm, as shown in Fig. 1). The subsequent decay in the iodine-argon transients on the 10 ps time scale demonstrates the predissociation of the B state I_2 in the cluster cages. This predissociation is due to collision-induced non-adiabatic couplings between the B and Π_{1g} states [59,77]. The signal recovery after the predissociation is again attributed to geminate recombination of the I_2 molecules inside the cluster cages. These B-state type transients were obtained both as functions of Ar backing pressure and as functions of the pump wavelengths (Fig. 4.a-b & Fig. 5). We have used a bi-exponential decay-and-rise function convoluted with a Gaussian to fit these transients. The fit results are listed in Tables 1 and 2. The fit function has an additional fit parameter Δt_0 to allow for a certain time delay between the decay and the rise. Such a delay often appears in the experimental transients and is related to the recombination time following the predissociation.

After I_2 is excited to high vibrational levels ($v' > 14$) of the B state by the pump pulses (500 to 580 nm), subsequent vibrational relaxation efficiently transfers kinetic energies from the I_2 vibrational mode to the thermal vibrational modes of the cluster. Warmed up by this energy transfer, the cluster cage becomes soft and some of the argon atoms evaporate as they acquire enough kinetic energy. When the I_2 predissociates, the soft cluster cage can no longer confine the dissociating I atoms within a small radius. The two iodine atoms are able to separate to a greater internuclear distance, allowing argon atoms to intercede [2]. In order for the I_2 to re-form, the iodine atoms, relaxed through collisions with the Ar atoms, have to diffuse within the clusters until they reach an appropriate internuclear separation. It takes, therefore, a longer time for iodine to recombine after predissociation than it does after direct dissociation in cold clusters. The average recombination time ranges from 5 ps to more than 10 ps, depending on the excitation energy [2]. The internuclear separation of the two iodine atoms following the predissociation reaches as far as 9 Å.

Intuitively, the shorter the pump wavelength, the more excess energy the cluster receives from the relaxation on or predissociation from the B state. The recombination time is thus longer at shorter pump wavelengths. The predissociation time is also dependent on the excitation energy. As observed by Burke and Klemperer [59], in their study of $I_2 \cdot Ar$, the predissociation rate on the B state is a modulated function of the vibrational level. The overall trend is an increase in the probability for predissociation at lower vibration energies. In agreement with this argument, the transients obtained for

pump wavelengths between 580 and 510 nm displayed both a longer decay time and a longer delay time as the pump wavelength became shorter. The transients for pump wavelengths shorter than 510 nm (480 and 500 nm) displayed an opposite trend. This is because excitation to the dissociative Π_{1u} state becomes more significant as the pump wavelength becomes shorter than 510 nm. The percentage of pump excitation to the Π_{1u} state changes from 22% at 510 nm to 34% at 500 nm and up to 47% at 480 nm (Fig. 1). The transient behavior following Π_{1u} excitation should be similar to that following A state excitation [2]. The overlap of a Π_{1u} transient on a B transient causes the apparent shortening of the time delay between the initial decay and the following rise, as shown by the MD simulations [2]. In the specific case of the 480 nm pump, this overlap may have caused the predissociation-related decay to disappear (Fig. 4.a).

At 480 nm, the pump pulse excites the iodine to a region of the B state that is above its gas phase dissociation limit. Inside the argon clusters, however, the dissociation limit of the B state may be higher as suggested by the blue-shift of the X to B absorption [54]. Accordingly, the B state dynamics at this excitation energy is similar to those described for the 510 nm pump. Alternatively, direct caging (back to the B state) might occurr after the dissociation (into $I + I^*$) followed by vibrational relaxation and electronic predissociation on the recombined B state [2]. These two descriptions may prove to be equivalent if the direct caging is interpreted as have been caused by the solvent-induced formation of a potential barrier along the dissociation path (in to $I + I^*$).

Following predissociation/recombination in the cluster cages, vibrational relaxation on the recombined A/A' and X states is expected to be similar to that following direct-dissociation/recombination. More Ar atoms are expected to evaporate from the cluster following B state excitation because more energy is injected into the system by pump photons of shorter wavelengths [2]. No explicit effect of this evaporation on the relaxation dynamics was observed in our experiments. That is probably because the groups of clusters that gave rise to the 400 nm emission are too large to be affected by an evaporation of a few Ar atoms. The fact that the recovered signal at longer time delays was even stronger than the initial maximum clearly indicates that the probe absorption on the A/A' states is stronger than that for the B state. If the probe absorption coefficients are comparable for all the states (B and A/A') involved, the caging efficiency is then suggested to be near unity. Simulations on clusters containing 44 argon atoms suggests that such a size was sufficient to provide a 100% recombination yield [2].

5.4.5. Dynamics of small clusters

As pointed out earlier, the 342-nm transients obtained from the iodine-argon beam represent the dissociation and recombination dynamics in small clusters, in addition to a bare iodine background. This was further verified by a transient obtained by detecting the 342 nm emission from the iodine-argon expansion (1100 Torr) at a 614/307 nm pump/probe combination (Fig. 9.a). Following the initial peak, which characterized the pump excitation at 614 nm, the signal dropped to almost zero at 300 fs and started to increase again on a 10 ps time scale. The coherent recovery apparent in the

corresponding 400 nm transient (Fig. 9.b, detecting 400 nm emission) was absent from this 342 nm transient, indicating that the complexes that gave rise to the 342 nm fluorescence were not large or rigid enough to directly cage the iodine. The fact that the signal dropped to ground level after the initial peak verifies that the population of I_2 which is excited to the B state either is directly dissociative or is insignificant for the cluster dynamics at this pump-probe combination (λ_{pump} = 614 nm; λ_{probe} = 307 nm).

At shorter pump wavelengths (480 to 580 nm), the transients obtained by monitoring the 342 nm fluorescence appeared somewhat similar to the corresponding 400 nm transients (see Fig. 8). As shown in Fig. 8, the relative amplitude of the long time asymptote to the initial peak is smaller in the 342 nm transients than in the corresponding 400 nm ones (at the same Ar backing pressures), suggesting that the caging yield is lower in small clusters than that in large clusters. Among the 342 nm transients, this ratio becomes smaller at lower backing pressures. At 400 Torr, a constant signal level instead of a rise was observed following the decay. This constant level is attributed to LIF emission from bare I_2 molecules, the population of which becomes greater at lower backing pressures. The absence of recombination (rise) at this backing pressure (400 Torr) is also consistent with the absence of red shifted emission in the corresponding spectral measurements. These 342 nm transients were also fit by the bi-exponential decay-and-rise function. The fit results are listed in Table 2. The rise times τ_2, which characterize the recombination/relaxation time constants, became shorter as the pressure became larger (Table 2) and are longer than their counterparts in the 400-nm transients

(compare Table 1 and Table 2). It should be noted that the bi-exponential decay-and-rise functions could not fit the experimental transients perfectly. It is likely that neither the decay nor the rise can be treated as single or double exponential functions. The fit results for τ_1 are particularly rough, because of the small number of data points along the decay curves.

Within the ensemble of small clusters, the distribution shifts to larger sizes as the backing pressure is increased. The initial cluster temperature also becomes colder as the pressure becomes higher. Accordingly, the relaxation/predissociation and recombination/relaxation rates increases with the backing pressure. As the clusters grow larger, forming two or more full layers, the relaxation/predissociation rates becomes insensitive to the outer shells. This may explain the relative constant decay times τ_1 observed in the 400-nm transients (Table 1) at different backing pressures.

5.4.6. Comparison with ionic clusters, dense fluids, and matrices

Lineberger's group studied the photodissociation and recombination dynamics of I_2^- in size-selected $I_2^-\cdot(CO_2)_n$ clusters by using pump-probe ion detection techniques [44-45]. In their studies, the absorption recovery of the probe pulse in large clusters (n = 14-17) consists of two components: a coherent recurrence at 2 ps and an slower gradual recovery on a longer time scale (~ 10 ps). The short-time feature has been assigned to coherent I···I$^-$ motion following photodissociation. The long-time absorption recovery is attributed to the vibrational relaxation in lower electronic states. For smaller cluster sizes

($n \leq 12$), no coherent recurrence was observed and the absorption recovery time increases to about 40 ps.

The above results are similar to ours in that a coherent recombination of dissociative iodine atoms can be observed in clusters, although the two systems are different in nature. The charge induced long-range Coulomb attraction between the dissociating iodine-$(CO_2)_n$ radicals is critical to the coherent reforming of the I_2^- in the clusters. The potential surfaces of $I_2^-\cdot(CO_2)_n$ during dissociation and recombination may be strongly perturbed from those of the uncomplexed I_2^- potential surfaces due to charge redistribution. In our case, the weaker and shorter-ranged van der Waals interactions between the iodine and Ar atoms are the dominant forces and are dependent on the rigid structure of the larger neutral $I_2\cdot Ar_n$ clusters. The coherent recombination of a dissociative neutral I···I pair observed in large Ar clusters is primarily due to the collective solvent collision force. It would be interesting to repeat our experiments using neutral $I_2\cdot(CO_2)_n$ clusters, and to compare with Lineberger's system.

Previous studies in the liquid phase of various solvents have not reported the coherent caging discussed here. For dense fluids, the coherent motion of the wave packet during dissociation was observed and examined [26, 31-33], but the prompt (coherent) recombination was only evident at the highest Ar densities. For liquids and dense fluids, the temperature (300 K) in both cases is much higher and long-range order is absent. The solvent distribution around the iodine is random in nature. It is, therefore, anticipated that coherence in the dissociation-recombination dynamics would diminish [2, 30].

Furthermore, due to their high temperature and mobility, the solvent particles can easily intercede between the separated iodine atoms following the iodine dissociation. The diffusive channel would then play a more important role in the caging dynamics.

If the solvent structure is made more rigid than the cluster, an enhanced coherence is expected [30]. Recent time-resolved studies of I_2 in Ar and Kr matrices systems have observed the coherent feature in the dissociation-recombination process and showed clear persistent oscillations [37-38]. For similar pump and probe wavelengths, the LIF transients obtained in the iodine-argon matrix system appears similar to those from the large clusters reported here. The coherence extended to longer times in the argon matrix, due to the lattice structures.

5.5 Conclusions

Using the femtosecond methodology, with LIF detection techniques, the dissociation, geminate recombination, and coherence dynamics of I_2 in $I_2 \cdot Ar_n$ clusters ($\overline{n}$ ~ 8 to 40) has been studied. The primary and secondary processes of caging have been observed and the mechanism critically depends on the time scale of dissociation in the solvent cage. After the system was excited to the dissociative A state with pump wavelengths ranging from 590 to 700 nm, a direct dissociation of I_2 was accomplished in 300 fs. A subsequent direct recombination took place in another 360 fs in large $I_2 \cdot Ar_n$ clusters ($\overline{n}$ 40 or larger), indicating that the coherence of the wave packet motion following direct dissociation was preserved for at least 660 fs in cluster cages. Damped oscillations [2] are part of a long-time recovery. This coherent caging dynamics is determined by bond breakage characteristics within the solvent cage (dissociation time), energy exchange between the fragments and the solvent cage (chaperon time), and nature of collective solvent properties (geometry, structure, and temperature). For liquids and supercritical gases at room temperature, there is a lack of collective binding forces and the coherent recombination feature is therefore not expected.

Recombination after predissociation from the B state displays a diffusive nature. The cluster structure is softened by the energy transfer from the I–I electronic/vibrational mode into the thermal vibrational modes of the $I_2 \cdot Ar_n$ clusters. The diffusive motion of the separated I atoms is confined by the finite boundary of the cluster, which give rise to a relatively narrow distribution of recombination times. In liquids and high-pressure gases,

on the other hand, the two far-separated iodine atoms can recombine through slow diffusive motion and, therefore, both primary and secondary recombination can occur.

The time scale for vibrational relaxation on the recombined A/A' states is found to be sensitive to the vibrational level, ranging from 3 ps (probed at 350 nm) near the dissociation limit (into I + I) to 50 ps for energy levels near the bottom of the well (probed at 307 nm). For the high vibrational levels, the iodine atoms can move to larger internuclear separations and their interactions with the argon atoms are enhanced and lead to faster energy relaxation. In addition, due to the anharmonicity of the A/A'-state potential surfaces, the vibrational-level energy difference is greater around low vibrational levels. The coupling between the cluster mode and the I_2 vibrational mode is therefore relatively weaker, leading to a slower energy relaxation at lower vibrational energies.

In the accompanying paper, we present MD calculations for the same system. We examine the different regimes realized experimentally and compare the theoretical results to their experimental counterparts. The effects of reaction time, caging time, and solvent characteristics (structure, temperature, etc.) are all part of the MD study [2].

5.6 References

1. Zewail, A. H. *Femtochemistry: Ultrafast Dynamics of the Chemical Bond*; World Scientific: Singapore, 1994; and articles therein.
2. Liu, Q.; Wang, J.-K.; Zewail, A. H. *J. Phys. Chem.* **1995**, the following paper in this issue.
3. Franck, J.; Rabinowitch, E. *Trans. Faraday Soc.* **1934**, 30, 120.
4. Mulliken, R. S. *J. Chem. Phys.* **1971**, 55, 288.
5. Tellinghuisen, J. *J. Chem. Phys.* **1982**, 76, 4736.
6. Lawley, K.; Jewsbury, P.; Ridley, T.; Langridge-Smith, P.; Donovan, R. *Mol. Phys.* **1992**, 75, 811.
7. Bowmann, Dantus, Zewail, I2 work (check??)
8. Gruebele, M.; Zewail, A. H. *J. Chem. Phys.* **1993**, 98, 883; and references therein.
9. Julien, L. M.; Person, W. B. *J. Phys. Chem.* **1968**, 72, 3059.
10. Chuang, T. J.; Hoffman, G. W.; Eisenthal, K. B. *Chem. Phys. Lett.* **1974**, 25, 201.
11. Nesbitt, D. J.; Hynes, J. T. *J. Chem. Phys.* **1982**, 77, 2130.
12. Otto, B.; Schroeder, J.; Troe, J. *J. Chem. Phys.* **1984**, 81, 202 and references therein.
13. Bado, P.; Dupuy, C.; Magde, D.; Wilson, K. R.; Malley, M. M. *J. Chem. Phys.* **1984**, 80, 5531.
14. Kelley, D. F.; Abul-Haj, N. A.; Jang, D. *J. Chem. Phys.* **1984**, 80, 4105.
15. Hynes, J. T. *Ann. Rev. Phys. Chem.* **1985**, 36, 573 and references therein.
16. Hippler, H.; Otto, B.; Schroeder, J.; Schubert, V.; Troe, J. *Ber. Bunsenges. Phys. Chem.* **1985**, 89, 240.
17. Abul-Haj, N. A.; Kelley, D. F. *J. Chem. Phys.* **1986**, 84, 1335.
18. Harris, A. L.; Bergh, M.; Harris, C. B. *J. Chem. Phys.* **1986**, 84, 788 and references therein.
19. Smith, D. E.; Harris, C. B. *J. Chem. Phys.* **1987**, 87, 2709.

20. Brown, J. K.; Harris, C. B.; Tully, C. T. *J. Chem. Phys.* **1988**, 89, 6687.

21. Harris, A. L.; Brown, J. K.; Harris, C. B. *Ann. Rev. Phys. Chem.* **1988**, 39, 341 and references therein.

22. Paige, M. E.; Harris, C. B. *Chem. Phys.* **1990**, 149, 37.

23. Harris, C. B.; Smith, D. E.; Russell, D. J. *Chem. Rev.* **1990**, 90, 481.

24. Macler, M.; Heaven, M. C. *Chem. Phys.* **1991**, 151, 219 and references therein.

25. Xu, X.; Yu, S.-C.; Lingle, R. Jr., Zhu, H.; Hopkins, J. B. *J. Chem. Phys.* **1991**, 95, 2445.

26. Zewail, A. H.; Dantus, M.; Bowman, R. M.; Mokhtari, A. *J. Photochem. Photobiol. A: Chem.* **1992**, 62, 301.

27. Fei, S.; Zheng, X.; Heaven, M. C.; Tellinghuisen, J. *J. Chem. Phys.* **1992**, 97, 6057 and references therein.

28. Potter, E. D.; Liu, Q.; Zewail, A. H. *Chem. Phys. Lett.* **1992**, 200, 605.

29. Ben-Nun, M.; Levine, R. D.; *J. Phys. Chem.* **1992**, 96, 1523.

30. Liu, Q.; Wang, J.-K.; Zewail, A. H. *Nature* **1993**, 364, 427.

31. Lienau, Ch.; Williamson, J. C.; Zewail, A. H. *Chem. Phys. Lett.* **1993**, 213, 289.

32. Lienau, Ch.; Zewail, A. H. *Chem. Phys. Lett.* **1994**, 222, 224. *J. Chim. Phys.* **1995**, 92, 566.

33. Whitnell, R. M.; Wilson, K. R.; Yan, Y. J.; Zewail, A. H. *J. Mol. Liq.* **1994**, 61, 153; see also *Chem. Phys. Lett*, (check??)

34. Gerber, R. B.; McCoy, A. B.; Garcia-Vela, A. *Ann. Rev. Phys. Chem.* **1994**, 45, 275.

35. Syage, J. A. *Faraday Discussions* **1994**, 97, 401.

36. Raz, T.; Schek, I.; Ben-Nun, M.; Even, U.; Jortner, J.; Levine, R. D. *J. Chem. Phys.* **1994**, 101, 8606.

37. Zadoyan, R.; Li, Z.; Ashjian, P.; Martens, C. C.; Apkarian, V. A. *Chem. Phys. Lett.* **1994**, 218, 504.

38. Zadoyan, R.; Li, Z.; Martens, C. C.; Apkarian, V. A. *J. Chem. Phys.* **1994**, 101, 6648.

39. Syage, J. A. *J. Chim. Phys.* **1995**, 92, 248.

40. Xu, J.; Schwentner, N.; Hennig, S.; Chergui, M. *J. Chim. Phys.* **1995**, 92, 541.

41. Materny, A.; Lienau, Ch.; Zewail, A. H. to be published.

42. Felker, P. M.; Zewail, A. H. *J. Chem. Phys.* **1983**, 78, 5266.

43. Breen, J. J.; Peng, L. W.; Willberg, D. M.; Heikal, A. A.; Cong, P.; Zewail, A. H. *J. Chem. Phys.* **1990**, 92, 805.

44. Papanikolas, J. M.; Vorsa, V.; Nadal, M. E.; Campagnola, P. J.; Gord, J. R.; Lineberger, W. C. *J. Chem. Phys.* **1992**, 97, 7002.

45. Papanikolas, J. M.; Vorsa, V.; Nadal, M. E.; Campagnola, P. J.; Buchenau, H. K.; Lineberger, W. C. *J. Chem. Phys.* **1993**, 99, 8733.

46. Wei, S; Purnell, J.; Buzza, S. A; Snyder, E. M. Castleman, A. W. Jr. in *Femtosecond Chemistry*, eds. Manz, J; Wöste, L; VCH: New York, 1994. (??)

47. Syage, J. A. in *Femtosecond Chemistry*, eds. Manz, J; Wöste, L; VCH: New York, 1994; see also *J. Phys. Chem.* 1995, (??)

48. Gerber, R. B.; McCoy, A. B.; Garcia-Vela, A. in *Femtosecond Chemistry*, eds. Manz, J; Wöste, L; VCH: New York, 1994.

49. Dugourd, P.; Rayane, D.; Labastie, P.; Pintar, B.; Chevaleyre, J.; Broyer, M.; Wöste, L. *J. Phys.* IV **1991**, 1, 509.

50. Jortner, J. *J. Chim. Phys.* **1995**, 92, 205; and references therein.

51. Breen, J. J.; Willberg, D. M.; Gutmann, M.; Zewail, A. H. *J. Chem. Phys.* **1990**, 93, 9180.

52. Willberg, D. M.; Gutmann, M.; Breen, J. J.; Zewail, A. H. J. *Chem. Phys.* **1992**, 96, 198.

53. Gutmann, M.; Willberg, D. M.; Zewail, A. H. *J. Chem. Phys.* **1992**, 97, 8037, 8048.

54. Saenger, K. L.; McClelland, G. M.; Herschbach, D. R. *J. Phys. Chem.* **1981**, 85, 3333.

55. Valentini, J. J.; Cross, J. B. *J. Chem. Phys.* **1982, 77**, 572.

56. Philippoz, J.-M.; van den Berg, H.; Monot, R. *J. Phys. Chem.* **1987**, 91, 2545.

57. Philippoz, J.-M.; Melinon, P.; Monot, R.;van den Berg, H. *Chem. Phys. Lett.* **1987**, 138, 579.

58. Philippoz, J.-M.; van den Berg, H.; Monot, R. *J. Chem. Phys.* **1990**, 93, 8676.

59. Burke, M. L.; Klemperer, W. *J. Chem. Phys.* **1993**, 98, 1797, 6643.

60. Roncero, O.; Halberstadt, N.; Beswick, J. A. in Reaction Dynamics in Clusters and Condensed Phases, eds. Jortner, J.; Levine, R. D.; Pullman, B.; Kluwer Academic Publishers: Dordrecht, 1994.

61. Buck, U.; Krohne, R. *Phys. Rev. Lett.* **1994**, 73, 947.

62. Blazy, J. A.; Dekoven, B. M.; Russell, T. D.; Levy, D. H. *J. Chem. Phys.* **1980**, 72, 2439.

63. Perera, L.; Amar, F. G. *J. Chem. Phys.* **1990**, 93, 4884.

64. Hagena, O. F.; Obert, W. *J. Chem. Phys.* **1972**, 56, 1793.

65. Farges, J.; de Feraudy, M. F.; Raoult, B.; Torchet, G. *J. Chem. Phys.* **1986**, 84, 3491.

66. Bernstein, R. B.; Zewail, A. H. *Chem. Phys. Lett.* **1990**, 170, 321.

67. Capelle; G. A.; Broida, H. P. *J. Chem. Phys.* **1973**, 58, 4212.

68. Guy, A. L.; Viswanathan, K. S.; Sur, A.; Tellinghuisen, J. *Chem. Phys. Lett.* **1980**, 73, 582.

69. Lawrence, W.; Okada, F.; Apkarian, V. A. *Chem. Phys. Lett.* **1988**, 150, 339.

70. Tellinghuisen, J.; Phillips, L. F. *J. Phys. Chem.* **1986**, 90, 5108.

71. Zewail, A. H. *J. Chem. Soc. Faraday Trans.* II **1989**, 85, 1221.

72. Tellinghuisen, J. *J. Quant. Spectrosc. Radiat. Transfer* **1977**, 19, 149.

73. Scherer, N. F.; Jonas, D. M.; Fleming, G. R. *J. Chem. Phys.* **1993**, 99, 153.

74. Viswanathan, K. S.; Sur, A.; Tellinghuisen, J. *J. Mol. Spectrosc.* **1981**, 86, 393.

75. Tellinghuisen, J. *J. Mol. Spectrosc.* **1982**, 94, 231.

76. see *CRC Handbook of Chemistry and Physics*, 70th ed., eds. Weast, R. C. et al.; CRC Press: Florida, 1990.

77. Kubiak, G.; Fitch, P. S. H.; Wharton, L.; Levy, D. H. *J. Chem. Phys.* **1978**, 68, 4477.

5.7 Tables

Table1. Parameters fit for the λ_{LIF} = 400 nm transients. λ_{probe} = 307 nm.

The transients were fit by convoluting a decay-and-rise function:

$f(t) = A_0 + A_1 e^{-(t-t_0)/\tau_1} + A_2 e^{-(t-t_0-\Delta t_0)/\tau_2}$ with $g(t) = e^{-t^2/\tau_0^2}$.

(a) Pump wavelength dependence (backing pressure = 1100 Torr)

λ_{pump} (nm)	τ_1 (ps)	τ_2 (ps)	Δt_0 (ps)	A_1/A_2
502	17.4±3.4	16.6±1.4	12.0±0.8	0.40±0.09
510	17.4±1.3	15.1±0.78	12.0±0.4	0.62±0.06
550	15.9±2.2	11.9±1.0	10.7±0.5	0.52±0.09
570	16.3±4.5	14.8±1.5	8.4±0.6	0.30±0.07
580	15.2±4.7	11.4±2.7	4.8±0.7	0.46±0.11

(b) Backing pressure dependence (λ_{pump} = 510 nm)

Backing Pressure (Torr)	τ_1(ps)	τ_2(ps)	Δt_0(ps)	A_1/A_2
1100	17.4±1.3	15.1±0.78	12.0±0.4	0.62±0.06
900	18.4±3.4	34.2±2.6	19.0±1.6	0.6±0.2
650	13.0±2.1	53.6±5.0	25.1±2.5	0.83±0.07

Table 2. Parameters fit for the λ_{LIF} = 342 nm transients, where λ_{probe} = 307 nm.

The transients were fit by convoluting a decay-and-rise function:

$f(t) = A_0 + A_1 e^{-(t-t_0)/\tau_1} + A_2 e^{-(t-t_0-\Delta t_0)/\tau_2}$ with $g(t) = e^{-t^2/\tau_0^2}$.

(a) Pump wavelength dependence (backing pressure = 1100 Torr)

λ_{pump} (nm)	τ_1 (ps)	τ_2 (ps)	Δt_0 (ps)	A_1/A_2
502	15.0±1.1	22.2±0.91	19.0±0.7	0.53±0.08
510	15.0±0.88	19.9±0.75	18.7±0.5	0.57±0.07
550	15.7±1.4	22.6±1.3	15.6±0.9	0.66±0.10

(b) Backing pressure dependence (λ_{pump} = 510 nm)

Backing Pressure (Torr)	τ_1 (ps)	τ_2 (ps)	Δt_0 (ps)	A_1/A_2
1100	15.0±0.88	19.9±0.75	18.7±0.5	0.57±0.07
900	20.5±2.4	41.1±2.2	27.2±1.6	0.70±0.13
650	17.7±1.8	45.4±2.1	15.2±2.1	1.22±0.09
400	22.0±1.9	∞	—	∞

5.8 Figure Captions and Figures

Fig. 1 Relevant potential energy surfaces of iodine. The dotted lines are obtained by lowering the I_2 ion-pair states by 4200 cm^{-1} and are used here to represent the solvated ion-pair states [27]. The wavy line represents fluorescence from the solvated D' state to A' state. The dependencies of relative absorption cross sections for the A, B, and Π_{1u} states on the pump wavelength are represented by the curves shaded from darkest to lightest respectively [5]. The arrows indicate the corresponding photon energies for the pump wavelengths 480, 510, 614, and 700 nm from highest to lowest. The potential energy values are measured from the bottom of the X state.

Fig. 2 Schematics of the molecular beam system and the two femtosecond-pulse arrangement.

Fig. 3 LIF spectra from the iodine-argon expansion. The backing pressure was kept at 1100 Torr. The probe wavelength was 307 nm. The solid lines were obtained with the probe pulses preceded by the pump pulses (positive delays); the dashed lines obtained with negative delays, which is identical to spectra obtained with the pump beam alone. The peak around 355 nm (part a) came from the scattering of the tripled output of the YAG laser (DCR-2).

Fig. 4 A-state type LIF transients from the iodine-argon beam on a short time scale. The backing pressure is 1100 Torr. The probe wavelength is 307 nm. These transients were obtained by monitoring the 400 nm emission from the beam. Pulse widths are about 120 fs for the 614 nm transient and about 300 fs for the others. The insets are transients that were obtained with the same pump and probe arrangements but from the iodine-helium beam (monitoring 342 nm emission) at a backing pressure of 900 Torr.

Fig. 5 B-state type LIF transients from the iodine-argon beam, on a short time scale. The backing pressure is 1100 Torr. The probe wavelength is 307 nm. These transients

were obtained by monitoring the 400 nm fluorescence from the beam. In the insets are corresponding transients (monitoring the 342 nm emission) obtained from the iodine-helium beam with the same pump and probe pulses.

Fig. 6 LIF transients from the iodine-argon beam. The backing pressure is 1100 Torr. The probe wavelength is 307 nm. These transients were obtained by scanning the pump/probe delay over a long time scale (– 20 to 180 ps) and monitoring the 400 nm emission from the beam. The pump wavelength was tuned from 480 to 700 nm.

Fig. 7 A-state type transients obtained with different probe wavelengths (detecting 400 nm emission). The backing pressure is 1100 Torr. The pump wavelength is kept at 614 nm. The probe wavelength was tuned from 280 to 350 nm.

Fig. 8 B-state type LIF transients obtained by monitoring a) the 400 nm emission; b) the 342 nm emission from the iodine-argon expansion. The backing pressure is kept at 1100 Torr. The pump and probe wavelengths are 510 and 307 nm, respectively.

Fig. 9 A-state type LIF transients obtained by monitoring (a) 342 nm; (b) 400 nm emission from the same iodine-argon beam. The backing pressure is 1100 Torr. The pump and probe wavelengths are 614 and 307 nm, respectively. The pulse widths are about 200 fs for the 342 nm transient, and about 120 fs for the 400 nm transient.

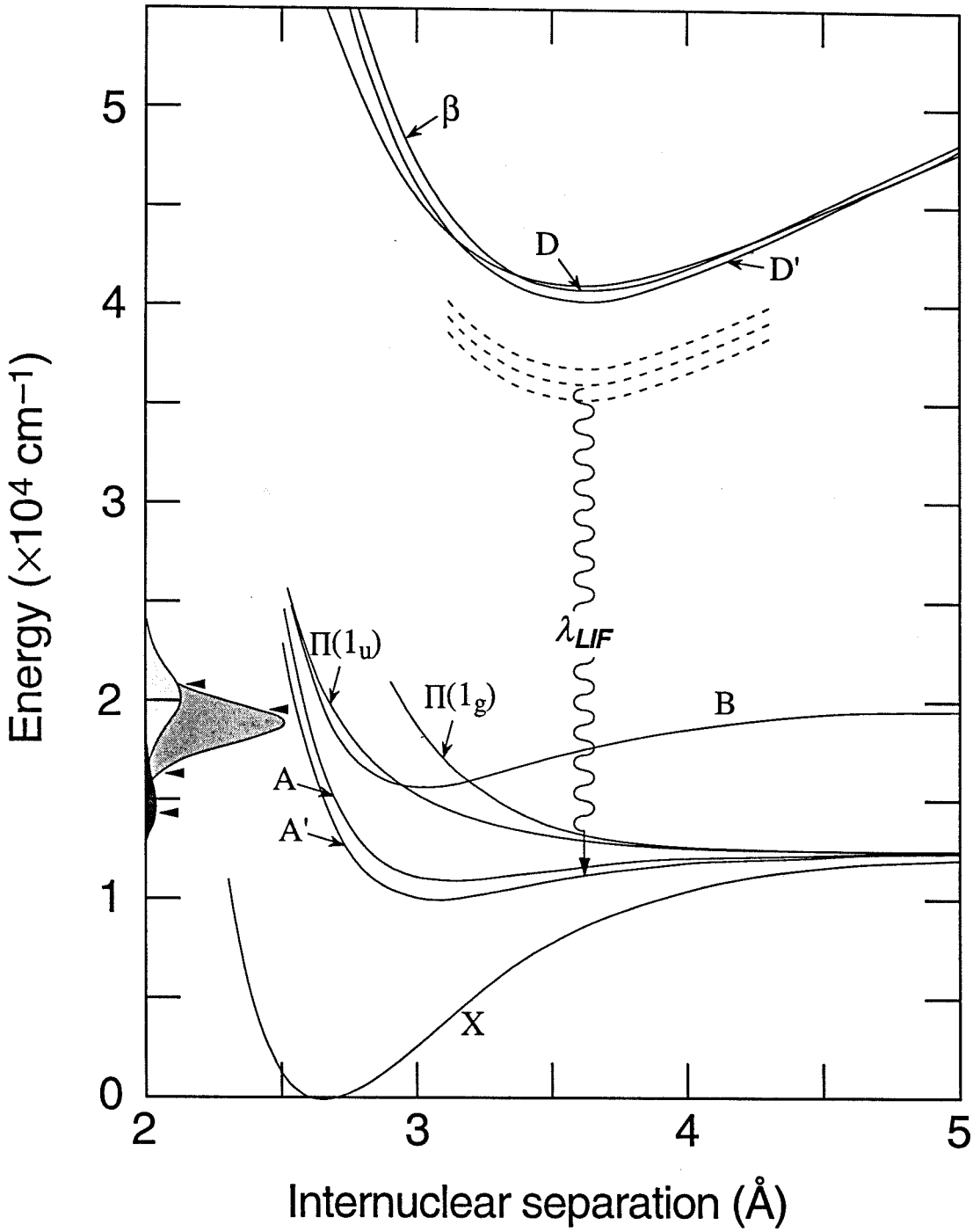
Energy (×10⁴ cm⁻¹)
Internuclear separation (Å)
β
D
D'
λLIF
Π(1u)
Π(1g)
B
A
A'
X
0
1
2
3
4
5
2
3
4
5

Figure 1

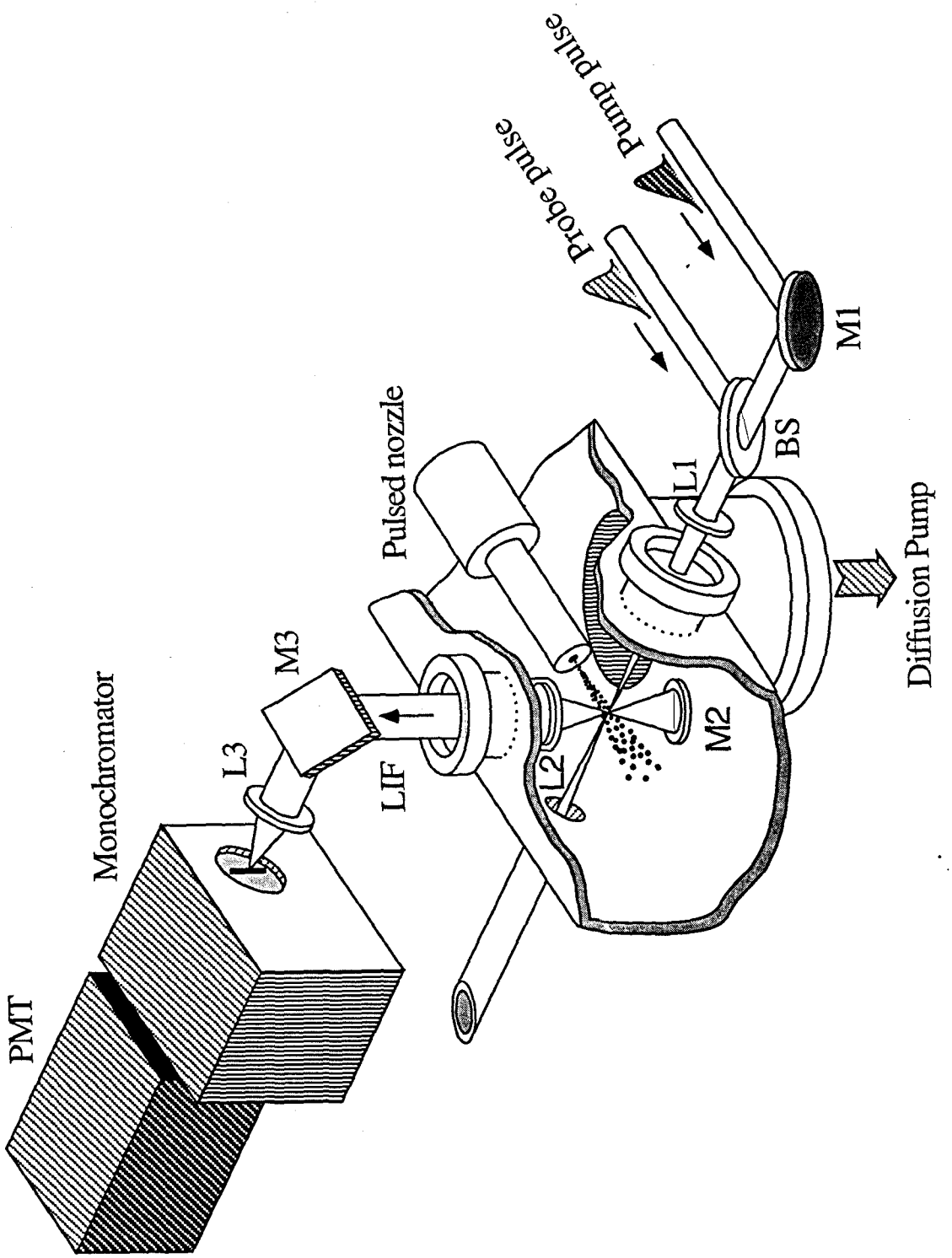
PMT
Monochromator
L3
M3
LIF
Pulsed nozzle
L2
M2
L1
BS
M1
Probe pulse
Pump pulse
Diffusion Pump

Figure 2

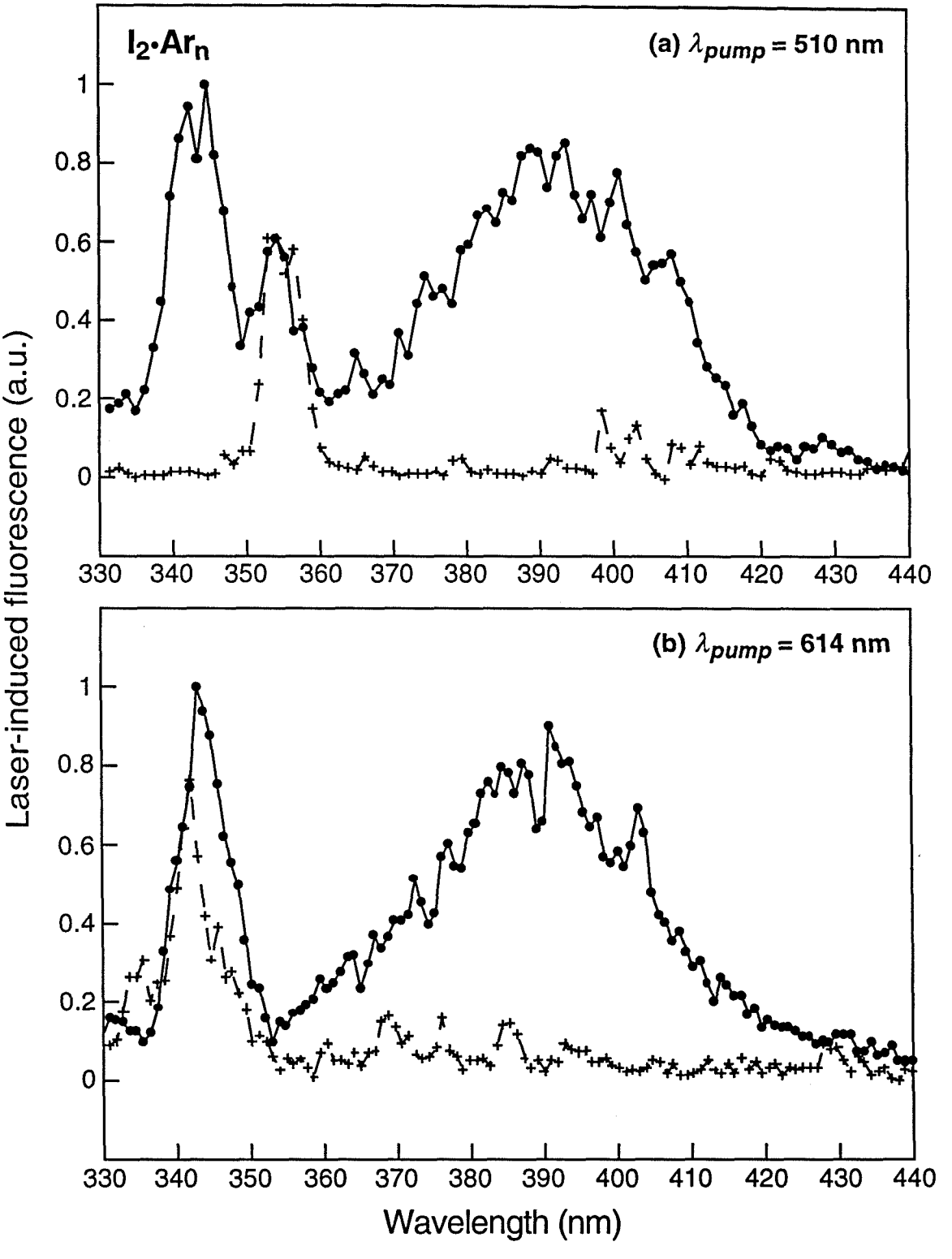
I_2•Ar_n
(a) λ_{pump} = 510 nm
(b) λ_{pump} = 614 nm
Laser-induced fluorescence (a.u.)
Wavelength (nm)
0
0.2
0.4
0.6
0.8
1
330
340
350
360
370
380
390
400
410
420
430
440

Figure 3

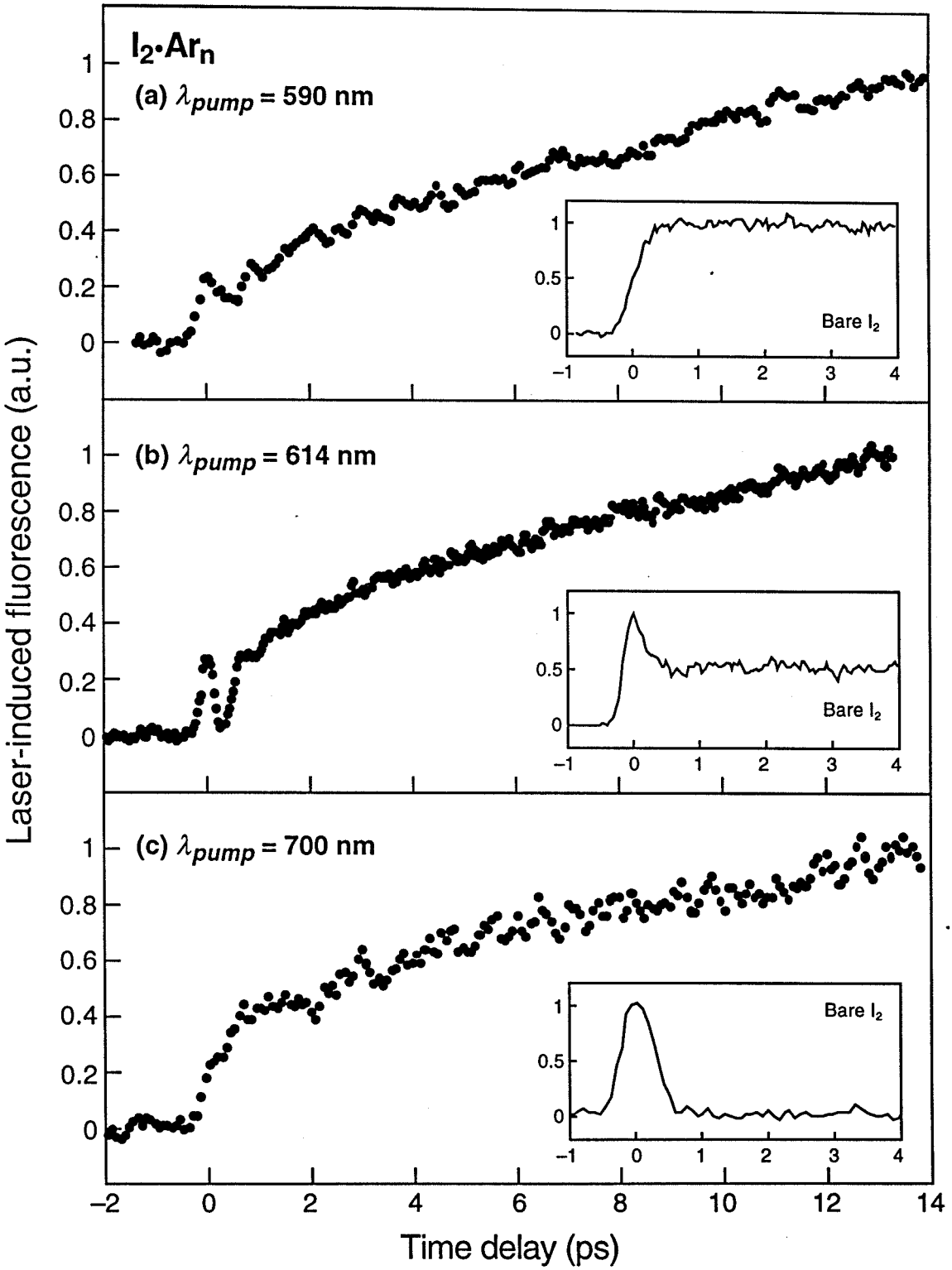
$I_2 \cdot Ar_n$
(a) λ_{pump} = 590 nm
(b) λ_{pump} = 614 nm
(c) λ_{pump} = 700 nm
Bare I_2
Laser-induced fluorescence (a.u.)
Time delay (ps)

Figure 4

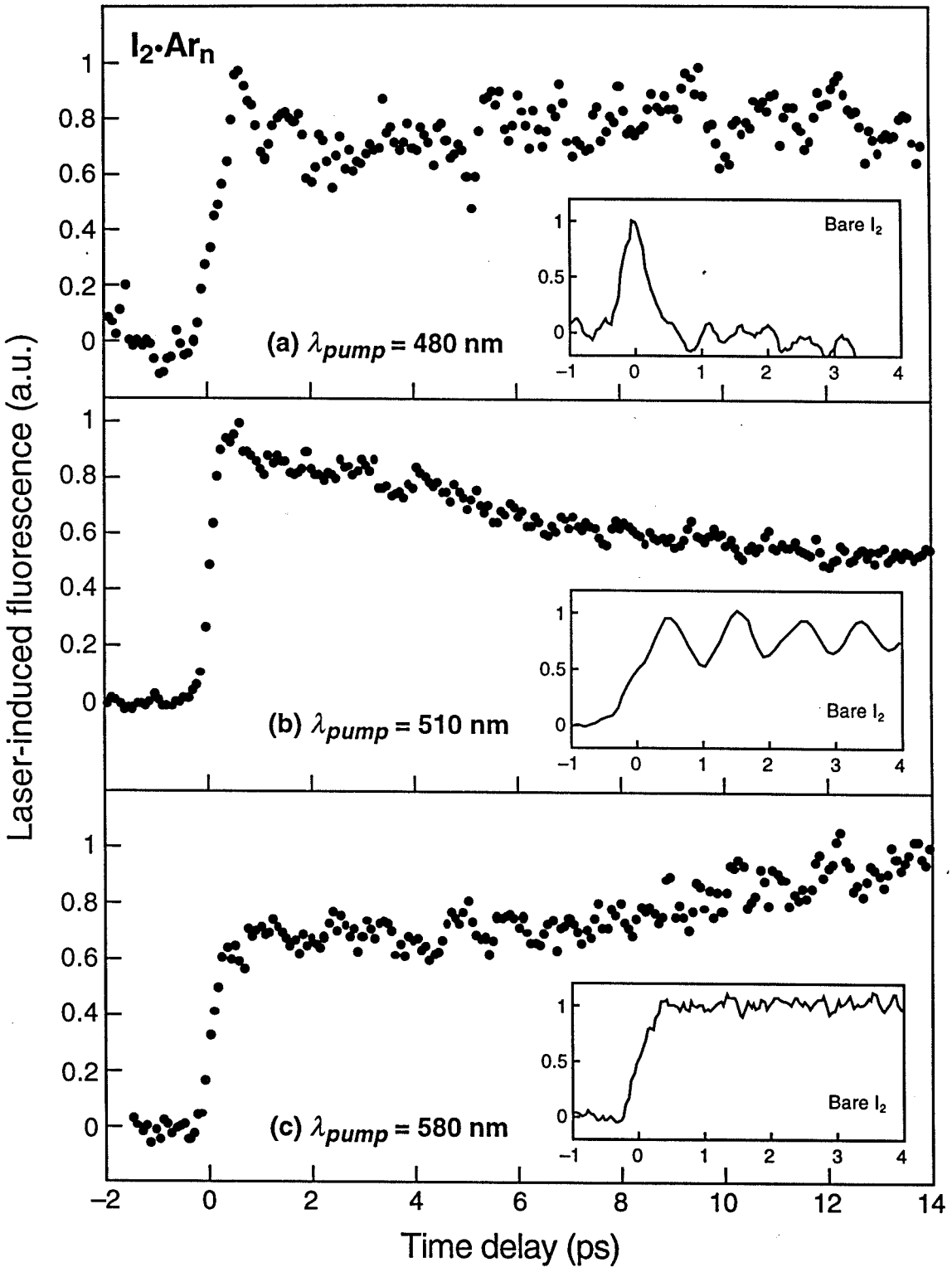
I_2·Ar_n
(a) λ_{pump} = 480 nm
(b) λ_{pump} = 510 nm
(c) λ_{pump} = 580 nm
Bare I_2
Laser-induced fluorescence (a.u.)
Time delay (ps)

Figure 5

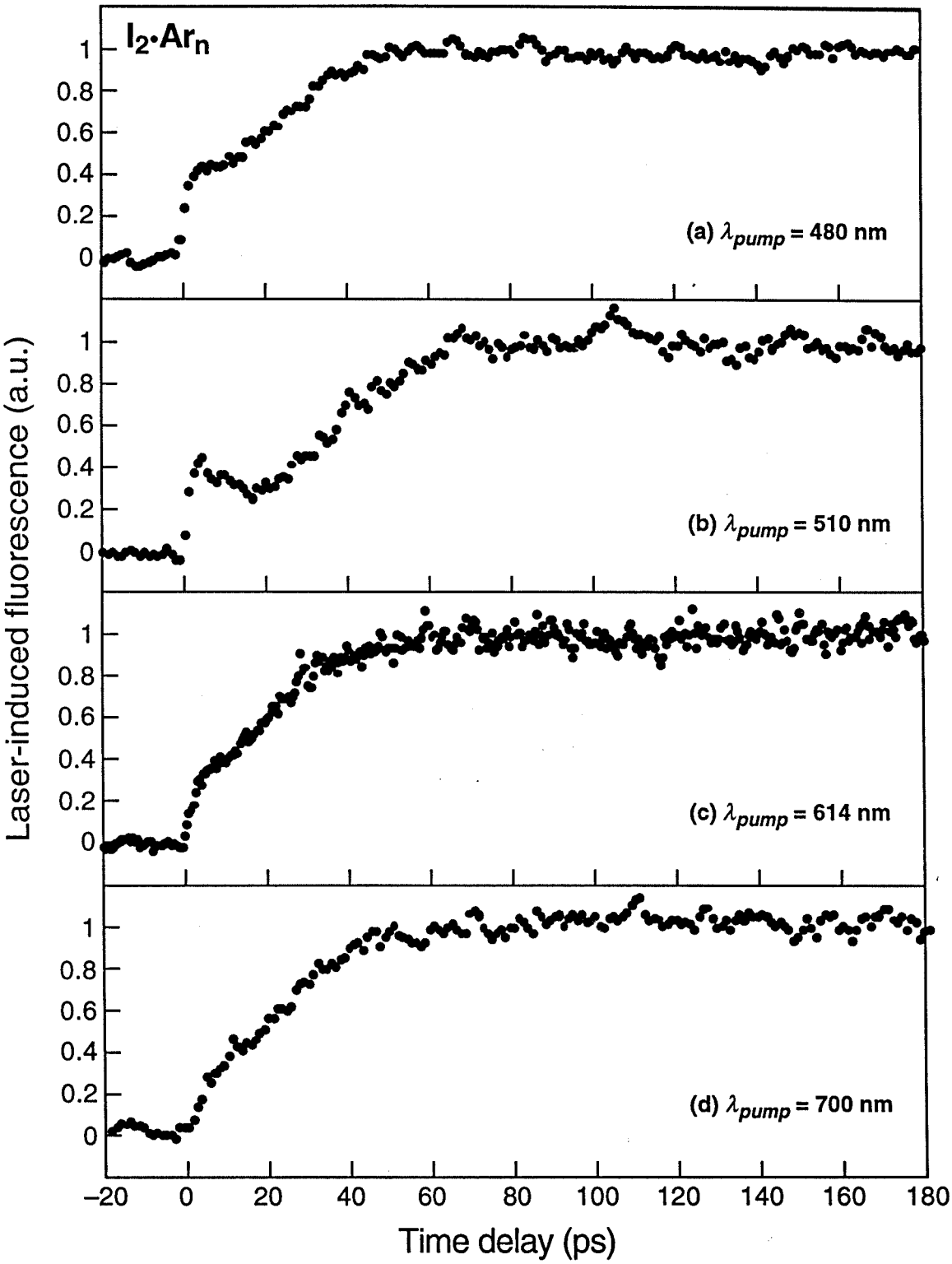
$I_2 \cdot Ar_n$
(a) λ_{pump} = 480 nm
(b) λ_{pump} = 510 nm
(c) λ_{pump} = 614 nm
(d) λ_{pump} = 700 nm
Laser-induced fluorescence (a.u.)
Time delay (ps)
0
0.2
0.4
0.6
0.8
1
−20
0
20
40
60
80
100
120
140
160
180

Figure 6

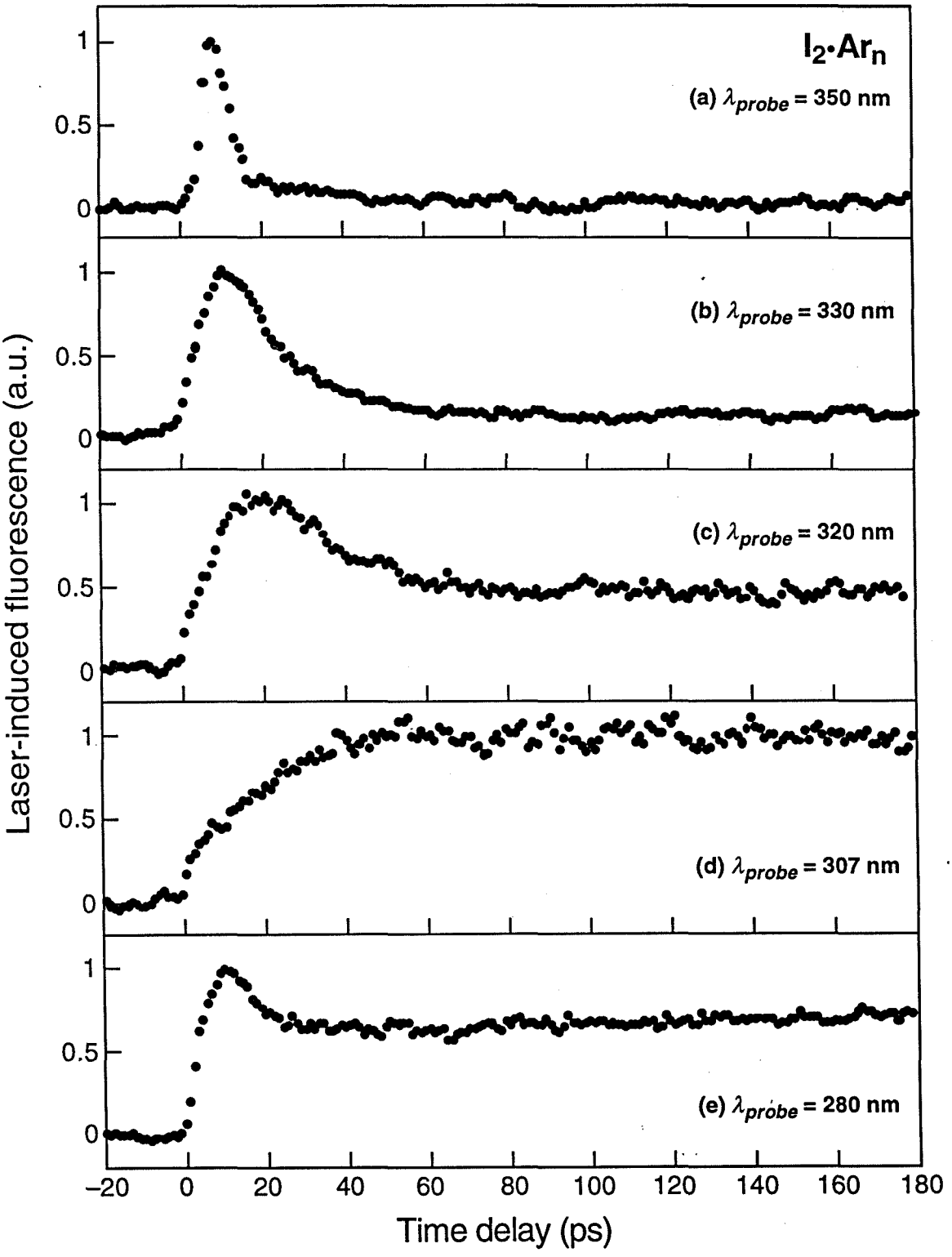
$I_2 \cdot Ar_n$
(a) λ_{probe} = 350 nm
(b) λ_{probe} = 330 nm
(c) λ_{probe} = 320 nm
(d) λ_{probe} = 307 nm
(e) λ_{probe} = 280 nm
Laser-induced fluorescence (a.u.)
Time delay (ps)
0
0.5
1
−20
0
20
40
60
80
100
120
140
160
180

Figure 7

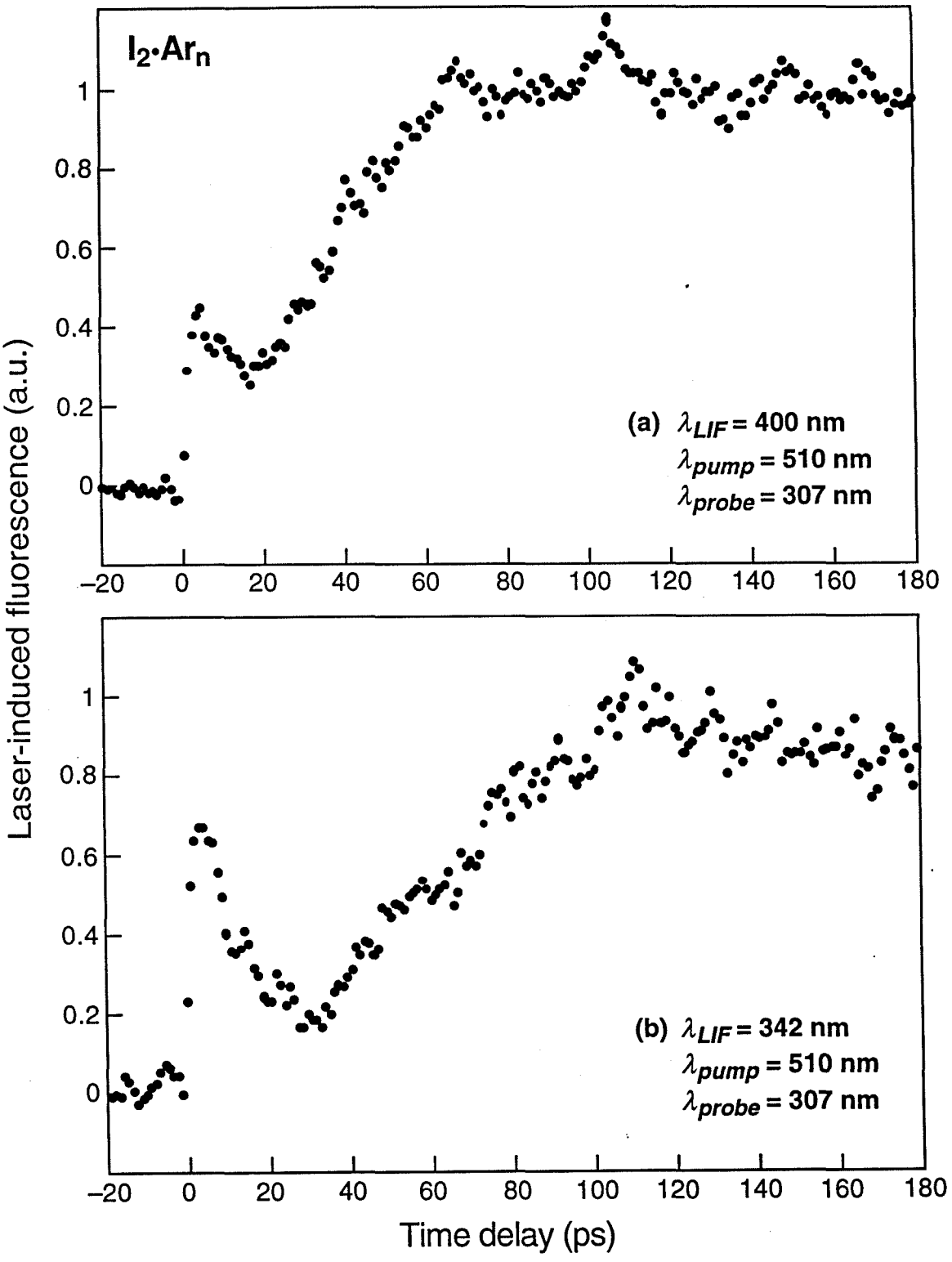
$I_2 \cdot Ar_n$
(a) λ_{LIF} = 400 nm
λ_{pump} = 510 nm
λ_{probe} = 307 nm
(b) λ_{LIF} = 342 nm
λ_{pump} = 510 nm
λ_{probe} = 307 nm
Laser-induced fluorescence (a.u.)
Time delay (ps)
0
0.2
0.4
0.6
0.8
1
−20
0
20
40
60
80
100
120
140
160
180

Figure 8

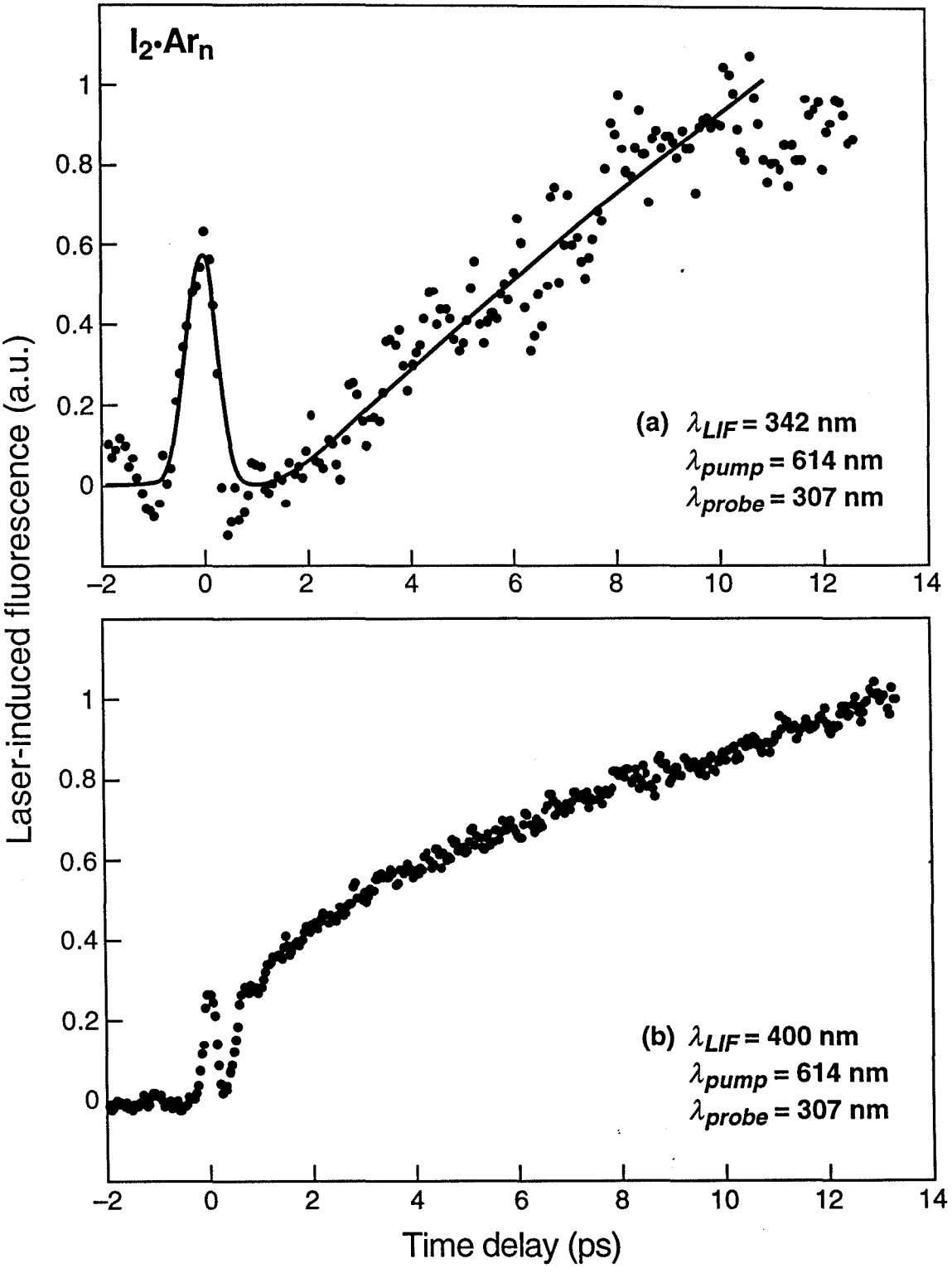
I_2·Ar_n
(a) λ_{LIF} = 342 nm
λ_{pump} = 614 nm
λ_{probe} = 307 nm
(b) λ_{LIF} = 400 nm
λ_{pump} = 614 nm
λ_{probe} = 307 nm
Laser-induced fluorescence (a.u.)
Time delay (ps)

Figure 9

Chapter 6

Molecular Dynamics Studies of Dissociation, Recombination, and Coherence

6.1 Introduction

This paper focuses on the use of molecular dynamics (MD) to investigate the dissociation and recombination of iodine in large argon clusters and to compare with the experimental results of the preceding paper [1]. The simulations provide an opportunity to examine the changes in the structure and dynamics of the system with time and to correlate them with the experimental observables. For the iodine-argon cluster system, we invoke MD, using classical mechanics, to obtain trajectories of the motion. The nuclear masses involved are heavy enough to justify a classical approximation. Given the relatively short time scales involved (femtoseconds to picoseconds) and the finite nature of cluster systems, efficient and accurate trajectory calculations can be carried out on modern computers. For a microscopic description, the MD simulations are particularly helpful in identifying the key forces controlling dissociation, recombination and vibrational relaxation.

In the MD calculations we consider the system of an iodine molecule, excited either to the A or B state (see Fig. 1), surrounded by large number of argon atoms. The number of argon atoms varies from 17 to 44 with the MD calculation specific to a given size. The excitation is realized in the simulation by instantaneously switching the iodine potential from the ground state (X) to the excited state (A or B) appropriate to the excitation energy. The time of excitation is sampled from a Gaussian distribution function representing the finite width of the initial pump pulse. Following the excitation, positions and velocities of the iodine and argon atoms are calculated according to the acting forces as functions of time. From an average of many such trajectories, we can

monitor the dynamic changes of the separation, energy and electronic states of the iodine atoms, as well as the response of the cluster cage to the dissociation as a function of the initial temperature, size and structure of the system. Following excitation to the continuum of the A state, we closely examine the coherent nature of the dissociation and recombination and relate this coherence to the initial structure of the cluster as well as to the time scale of bond breaking. Following excitation to the bound B state, we focus on the electronic predissociation to a repulsive state and the consequences of this relatively long-time scale bond breaking.

The MD approach used here for cluster systems has some similarities to previous studies, but with a different focus. Amar and Berne simulated the dissociation and recombination dynamics of Br_2 in Ar clusters of different sizes [2]. Their study showed the influence of the cluster size and geometry on the caging efficiency. Li et al. studied the relaxation and evaporation rate of an $I_2 \cdot Ar_{13}$ cluster following the excitation of iodine to its B state [3]. The effect of a single solvent atom on the caging and electronic predissociation from B-state iodine has been studied both theoretically and experimentally and an excellent review of the results can be found in Gerber's article [4]. For ionic clusters, recent MD and Monte Carlo simulations carefully studied the influence of the charge distribution on the structure and dynamics of the $I_2^- \cdot (CO_2)_n$ clusters [5]. A novel study of the theoretical femtochemical dynamics of large iodine argon clusters was carried out by Raz et al, where iodine dissociation could be induced by the cluster collision with a surface [6].

Our approach here focuses on the elementary femtosecond dynamics of coherence, bond-breakage and bond-reformation, and the subsequent relaxation on the picosecond time scale. The simulations are specifically designed to provide a microscopic picture and support for the interpretation of the experimental results discussed in Ref. 1. The paper is organized as follows. Section 6.2 describes the MD methodology and Section 6.3 presents the MD results and discussion. The paper is concluded in Section 6.4.

6.2 Methodology

6.2.1. Cluster trajectories

The MD simulations are based on ensemble averages of many independent cluster trajectories, which in turn were obtained by numerically integrating Hamilton's equations over a certain period of time (for a summary, see Ref. 7). For the iodine-argon clusters containing n argon atoms and two iodine atoms, Hamilton's equations are written as:

$$\dot{q}_{ij} = \partial H/\partial p_{ij}; \qquad \dot{p}_{ij} = -\partial H/\partial q_{ij} \qquad (i = 1,2,\cdots,n+2; j = x,y,z), \tag{1}$$

where H is the Hamiltonian of the system, and is given by

$$H = \sum_{i=1}^{n+2} \sum_{j=x,y,z} \frac{p_{ij}^2}{2m_i} + V(q) \cdot \tag{2}$$

The potential function V is taken to be a sum of pairwise interactions.

The X, A', A and B states of iodine are represented by Morse functions:

$$V(r) = D\left\{\exp\left[-2\beta\left(r-r_e\right)\right] - 2\exp\left[-\beta\left(r-r_e\right)\right]\right\} + E_\infty, \tag{3}$$

where r is the internuclear separation, r_e is its equilibrium value and E_∞ is the dissociation energy. Parameters for these four states are listed in Table 1. The repulsive Π_{1u} and Π_{1g} states are represented by a polynomial function:

$$V(r) = Ar^{-n} + B, \tag{4}$$

where $n = 9$, A = 5.24×10^7 cm^{-1}, and B = 0 for Π_{1u} [8]; and $n = 10$, A = 3.455×10^8 cm^{-1}, and B = -134 cm^{-1} for Π_{1g} [9].

The Ar–Ar and I–Ar internuclear interactions are modeled by Lennard-Jones functions:

$$V(r) = 4\varepsilon\left[(\sigma/r)^{12} - (\sigma/r)^{6}\right]. \qquad (5)$$

The parameters for the close contact distance σ and for the dissociation energy ε are also listed in Table 1.

The integration was carried out by using a velocity Verlet algorithm [10] with a fixed step size of 1 fs (1×10^{-15} second). A fourth-order Runge-Kutta integrator was used to initialize the integration. Energy conservation was maintained at better than 1 part in 10^5 over a period of 90 ps. For each set of simulations, more than 200 independent trajectories were computed to achieve good statistical averages.

6.2.2. Curve-crossing and curve-hopping

To compare with the corresponding experimental results, we have simulated the excitation of I_2 to dissociative regions of the A, B and Π_{1u} states as well as the pre-dissociative region of the B state. The non-adiabatic coupling between the B and $\Pi_{1u}(\Pi_{1g})$ states is modeled by a Landau-Zener-Stückelberg approximation [11]. The probability for the B state to cross over to the Π state is calculated according to the following equation:

$$P(v_{I-I}; W_{B-\Pi}) = 1 - \exp\left\{-\frac{2\pi}{\hbar}\cdot\frac{W_{B-\Pi}^2}{v_{I-I}\Delta F(R_x)}\right\}, \qquad (6)$$

where R_x is the crossing point; $W_{B-\Pi}$ is the coupling matrix element between the B and Π state; v_{I-I} is the relative radial velocity between the two iodine atoms above the crossing point; $\hbar$ is the reduced Planck's constant; and

$$\Delta F(R_x) = \left| \left(\partial V_B / \partial R - \partial V_\Pi / \partial R \right)_{R=R_x} \right| \tag{7}$$

is the difference in the slopes of the two potentials at the crossing point. The effective crossing region around R_x is given by

$$\delta R = 4W_{B-\Pi} / \Delta F(R_x) \, . \tag{8}$$

For the trajectory calculations, Eq. 6 was only evaluated when R_{I-I} fell between $R_x - \delta R$ and $R_x + \delta R$. If the probability was larger than a random number (between 0 and 1), then the potential was instantaneously switched from the B to Π state. The crossing point between the B and Π states was computed from the model potentials (Table 1) used in the simulations. The coupling matrix element $W_{B-\Pi}$ was chosen to be around 15 cm^{-1}, corresponding to a time scale of about 10 ps for the B state predissociation at a pump wavelength of 570 nm.

Following I_2 dissociation, the potential energy surface of the I···I system becomes a mixture of the X, A/A', Π, and other valence states at large R_{I-I} values as a result of solvation by the Ar cage. This state mixing causes the dissociating I···I to effectively hop from one state to the other. To simplify the problem, we specified a certain value of R_{I-I} (4.5 Å) beyond which the curve-hopping was assumed to occur with given probabilities, and within which curve-hopping was not allowed. To satisfy energy conservation, the

change in potential energy upon curve-crossing or curve-hopping was compensated for by an opposite change in the relative kinetic energy along the I–I coordinate.

6.2.3. Laser-induced fluorescence (LIF)

To simulate the LIF signals, we first assigned Franck-Condon regions for each of the iodine states involved. We used a model potential of the solvated D state to represent the manifold of ion-pair states. The Franck-Condon regions were then located by matching the probe photon energies (280 to 350 nm) to the energy difference between the D and valence states (B, A, and A'). In previous experimental studies [1,12-14], the D'→ A' fluorescence emission was found to be red-shifted by as much as 4200 cm^{-1} in large $I_2 \cdot Ar_n$ clusters relative to the gas phase. As discussed in Ref. 1, this red-shift is due to solvation of the ion-pair states by the Ar atoms which leads to a lowering of these states relative to the valence states. In argon matrices, this red-shift was measured to be 2900 cm^{-1} and the A/A' states were reported to have a solvation energy of ~ 250 cm^{-1} relative to the ground state [15]. Assuming that the solvation of the A/A' states is proportional to the red-shift of the D'→A' emission, the A/A' states are estimated to be lowered by ~ 350 cm^{-1} in the clusters under study. The potentials for the ion-pair states are modified from their Rittner form [16] by the addition of an extra term: $-C(R-R_s)/R$ to represent the solvation effect in Ar clusters. The parameters C and R_s are chosen to be 15,576 cm^{-1} and 2.72 Å, respectively, so that the bottom of the modified D state is lower than its gas phase value by about 4200 cm^{-1} and the energy difference between the D and A' states, near the A' state equilibrium separation, is close to the photon energy of a 307 nm probe pulse.

During the trajectory calculation, when the R_{I-I} fell within the assigned Franck-Condon regions, the delay-time dependent LIF signal $S_{LIF}(t)$ was computed using the following formula:

$$S_{LIF}(t) = f_0 \cdot \left\{1+\left[\Delta V_{I-I}\left(R_{I-I}(t)\right)-\hbar\omega_{probe}\right]^2 \Big/ \gamma^2 + \left[0.5\mu_{I-I}v_{I-I}^2(t)\right]^2 \Big/ \Gamma^2\right\}^{-1}, \quad (9)$$

where f_0 is a scaling factor, $\Delta V_{I-I}\left(R_{I-I}(t)\right)$ is the potential energy difference between the solvated ion-pair states and the valence states at given R_{I-I} which in turn is a function of the delay time t, $\hbar\omega_{probe}$ is the photon energy of the probe pulse, γ is a combination of the probe spectral width and the inhomogeneous broadening of the ion pair state, μ_{I-I} is the reduced mass of the I···I system, v_{I-I} is the relative radial velocity between the two iodine atoms, and Γ represents the absorption bandwidth. In using equation (9), both energy and momentum conservation have been accounted for and the simulated LIF transients are not very sensitive to the parameters used. The parameters used in this calculation are listed in Table 2. The LIF transients obtained were all averaged over more than 200 independent trajectories.

6.3 Results and Discussion

6.3.1. Cluster structures

Pure argon clusters have icosahedral or polyicosahedral structures, depending on their size [17]. With an embedded iodine molecule, this structure is altered to some degree to compensate for the differing size and potential of the iodine atoms. Since the van der Waals interactions between an iodine and an argon atom are considerably stronger than those between two argon atoms, it is reasonable to assume that a structure with the iodine molecule in the center of the cluster is the most stable configuration. We assigned the initial positions of 19 argon atoms in accordance with an icosahedral structure for the $I_2 \cdot Ar_{17}$ system and of 46 Ar atoms to a polyicosahedral structure for the $I_2 \cdot Ar_{44}$ system. The two central Ar sites were then replaced by two iodine atoms and their distance was adjusted to the ground state (X) equilibrium value (2.67 Å). Random velocities, sampled from a Gaussian distribution function, were assigned to all the atoms before the system was allowed to relax for about 10 ps. During this relaxation, the iodine was maintained in its ground state and the average kinetic energy of the system, *i.e.* the cluster temperature T was evaluated. After 10 ps, the velocities of all the atoms were scaled by $\sqrt{T_0/T}$ and the process was repeated until T was within 10% of T_0, the experimental temperature of the cluster.

The coordinates of the iodine and argon atoms were then recorded and used for 3-dimensional plots of the cluster structure as well as for the radial and angular distribution calculations. Typical structures of the clusters are shown in Figures 2a and 2b for a 17-Ar

and a 44-Ar cluster, respectively. At 30 K, the iodine remains enclosed by the argon shell after relaxation. The first layer of argon atoms appears to have kept a symmetric structure with respect to the iodine molecule, similar to the original icosahedral arrangement (Fig. 2a). The second layer (for larger clusters) is less well confined to its original configuration, and very often becomes asymmetric with respect to the iodine molecule (Fig. 2b). This is probably caused by the finite thermal energy (30 K) of the system and the weaker interaction between the outer layer and the iodine molecule.

The radial distributions of Ar atoms relative to the I_2 center of mass are shown in Fig. 3 for two different cluster sizes and three different temperatures. At low temperatures (around 30 K), the well defined inner shell structure of the clusters can be seen in Fig. 3a (for 17 Ar) and Fig. 3b (for 44 Ar) by the first two sharp peaks in the radial distributions. The third peak in Fig. 3b becomes broader and smeared out, indicating that the outer layer is less confined as mentioned above. As the temperature is increased to 60 and 90 K, the mobility of the argon atoms increases and the structure of the cluster becomes less distinguishable (Figures 3c and 3d).

The corresponding angular distributions with respect to the iodine bond axis are shown in Fig. 4. In Figures 4a and 4b, the argon atoms have well localized azimuthal distributions at low temperatures (30 K). The structure is particularly clear for clusters with only 17 argon atoms (Fig. 4a). For larger clusters, the angular distribution is somewhat compromised by the average over the floppy outer shell and the confined inner

shell. At higher temperatures (60 to 90 K), the argon atoms no longer have preferred locations and are highly mobile in the cluster, as shown in Figures 4c and 4d.

As discussed below, the iodine dissociation and recombination dynamics are very sensitive to the cluster temperature. The temperature of the cluster reflects the mobility of the argon atoms and, therefore, serves as an indication of how well the local structure around the iodine differs from one system to the other in a micro-canonical group. At 30 K, the clusters are effectively in a solid phase, with Ar atoms localized in a specific geometric structure. While from 60 to 90 K, the clusters are melted and behave like liquid droplets. This is consistent with the simulations done by Farges *et al.* [17]

6.3.2. Dynamics following A state excitation

(A) DISSOCIATION

After preparation of the cluster, the I_2 potential was instantaneously switched from the X to the A state at a level ~ 3750 cm^{-1} above its dissociation limit (to I + I). This corresponds to excitation by a 614 nm photon. In the subsequent dissociation, the two iodine atoms move away from one another until reaching a certain maximum separation, $R_{max}(I-I)$, where the recombination process begins. This $R_{max}(I-I)$ value was recorded for each individual trajectory so that distributions of $R_{max}(I-I)$ among all the trajectories could be studied. Shown in Fig. 5a is such a distribution obtained from 700 trajectories of $I_2 \cdot Ar_{17}$ clusters (with an initial temperature of 30 K). About 54% of the trajectories gave rise to a maximum I–I separation between 4 and 5.5 Å. For $I_2 \cdot Ar_{44}$ clusters with the same initial temperature, more than 90% of the trajectories had a

maximum I–I separation smaller than 5.5 Å (Fig. 5b). For larger clusters (with 44 Ar), all of the 800 trajectories calculated resulted in the iodine atoms caged within the cluster, whereas for smaller clusters (with 17 Ar), about 21% of the trajectories ended up with one or both of the iodine atoms outside the bounds of the cluster.

As the initial temperature (T_{init}) was increased, the distribution of $R_{max}(I-I)$ spread out to larger values (Figures 5c and 5d). The probability for $R_{max}(I-I)$ to be smaller than 5.5 Å dropped from 90% at T_{init} = 30 K to 50% at T_{init} = 60 K and to 20% at T_{init} = 90 K.

(B) RECOMBINATION

At large I–I distances, the potential energy difference between the A and A' states becomes insignificant, so that a state mixing occurs. Depending on the details of this mixing, the iodine will have a certain probability of being on either the A or A' state upon recombination. In our simulations, we assumed that the state mixing was not significant until the I–I distance reached 4.5 Å, after which the probability for the iodine state to switch from A to A' was 50%. As shown in Figures 5a-d, certain trajectories had a maximum I–I separation smaller than 4.5 Å (as many as 20% for the $I_2 \cdot Ar_{44}$ clusters at T_{init} = 30 K). For such trajectories, the iodine was simply bounced back on the A state by the stiff cluster wall before it had a chance to hop to the A' state.

To quantify the time scale of recombination, we have defined and monitored the caging time (t_{cage}) during the trajectory calculation; t_{cage} was defined as the time period from the start of dissociation to the moment when the I–I distance decreased to 3.5 Å

again and the total I–I energy fell to 200 cm^{-1} below the dissociation limit. (Note that in a rigid solvent cage, the gas phase dissociation limit is modified by the solvent barrier. However, for consistency at all times, we use the –200 cm^{-1} criterion with the gas phase potentials.) The distribution of t_{cage} was obtained from more than 400 independent trajectories for each size and temperature configuration of clusters. The distribution for $I_2 \cdot Ar_{17}$ at T_{init} = 30 K is shown in Fig. 6a. Among 700 trajectories calculated, 64% of them had the iodine recombined within 10 ps after the dissociation. The caging efficiency for this cluster is then assigned to be 64%. The probability for iodine to recombine within 500 femtoseconds is ~ 15% and the probability for t_{cage} to be between 0.5 and 1.5 picoseconds is also ~ 15%. As shown in Fig. 6a, there are two distinct peaks to represent these two channels of caging. The distribution also has a long tail extending from 1.5 ps to longer than 10 ps as some trajectories did not end up with the iodine recombined within this period of integration.

At the same temperature for a larger cluster (with 44 Ar), the distribution looks similar, but the second peak (between 0.5 to 1.5 ps) becomes more prominent, accounting for as much as 73% of all the trajectories calculated (Fig. 6b). The first peak accounts for 20% in this case. The tail of the distribution only extends from 1.5 ps to about 3 ps, accounting for less than 10% of all trajectories. The caging efficiency was 100% in this case, which means iodine recombined within 10 ps for all of the 800 trajectories calculated. As the temperature increases, the first peak drops from 20% at 30 K to 17% at 60 K and to 4% at 90 K, while the second peak drops from 73% at 30 K to 27% at 60 K

and to only 4% at 90 K (see Fig. 6b-d). The second peak is no longer distinguishable at 90 K. It becomes part of a long tail at this high temperature (Fig. 6d). The caging efficiency is 76% at 60 K and is 34% at 90 K.

The two peaks represent two different channels of direct caging. The first channel involves a head-on collision between iodine and Ar atoms which are closely packed on top of both iodine atoms at the moment when dissociation occurs. Each of these head-on collisions can transfer as much as 72.8% of the total available kinetic energy from the iodine atoms to the cage. The total available kinetic energy is about 5,700 cm^{-1} for the dissociating iodine atoms when their separation is near the equilibrium distance of the A state (3.1 Å). Thus, an optimum head-on collision leaves the total energy (potential energy plus kinetic energy) of iodine more than 400 cm^{-1} below its A state dissociation limit. Following this head-on collision, the iodine will be stabilized before its separation reaches about 4.5 Å. This is verified by the comparison between the caging time distributions (Figures 6a-d) and the distributions of maximum I–I separation. The trajectories which had caging times less than 500 fs also had a maximum I–I separation less than 4.5 Å. This caging channel will be closed if the initial excitation energy is so high that a head-on collision fails to stabilize the iodine, even when the collision occurs around the equilibrium distance of the A state. For instance, if the excitation energy is more than 18,000 cm^{-1} (or wavelength less than 555 nm), assuming that the iodine could still be excited to the A state, the total available kinetic energy near 3.1 Å will be about

7,500 cm^{-1}. An optimum head-on collision would still leave iodine above the A state dissociation limit.

To verify this point, we changed the excitation energy to 18,000 cm^{-1} (555 nm). With the initial temperature at 30 K and 44 argon atoms in the cluster, we calculated 200 independent trajectories and obtained both the caging time distribution and the distribution of maximum I–I separation. The results are shown in Fig. 7 with the corresponding results of a 614 nm excitation. In the caging time distribution (Fig. 7a), the first peak virtually disappeared, while the second peak is still very strong. For almost all of the trajectories, the maximum I–I separation is greater than 4.5 Å, as shown in Fig. 7b. As a comparison, when the excitation energy is lower than 18,000 cm^{-1}, the head-on caging channel is present even when the cluster temperature is as high as 90 K (Fig. 6d), or when the cluster has fewer argon atoms (Fig. 6a).

The second caging channel, which has a caging time around 1 ps, involves multiple collisions between the iodine atoms and the solvent shells. Upon dissociation, the iodine atoms lose their excess kinetic energy through a sequence of encounters, none of which is as drastic as a head-on collision. The duration of the iodine-argon encounter may be long enough in this case for the iodine motion to be correlated with the stretching motion of the cluster wall. If the cluster is stiff enough the iodine atoms will be pushed back to recombine by the reverse motion of the cluster wall. We will show in the following that this is indeed what happens with the large cluster (44 Ar) at low temperature (30 K).

(C) DYNAMICS

We have monitored the time dependence of the total I–I energy (E_{I-I}), I–I distance (R_{I-I}), cluster temperature ($T_{cluster}$) and cluster size (N_{ar}) in each of the trajectories and averaged the results over 200 to 800 trajectories. If one looks at the iodine as a sub-system within the cluster, the behavior of the total iodine energy over time will then display the dynamic energy exchange between this sub-system and the argon shells. Figures 8a and 8b show the time evolution of the total I–I energy in a large cluster (44 Ar) at 30 K following excitation at 614 nm and 555 nm, respectively. Despite the difference in excitation energies, the two curves look very similar. The iodine energy drops very quickly over the first one to two hundred femtoseconds, followed by a local minimum at 450 fs for 614 nm excitation and at 650 fs for 555 nm excitation (see the inserts of Figures 8a and 8b). After this minimum, the iodine energy increases by about 25 cm^{-1} before it undergoes a long time decay.

As mentioned earlier, at the excitation energy of 18,000 cm^{-1} (555 nm), the head-on caging channel does not exist. That the amount of energy-recovery is the same as that at a lower excitation energy (614 nm), is an indication that the energy-recovery feature comes from the second caging channel discussed above. As a comparison, even at the lower excitation energy (614 nm), the energy-recovery behavior disappeared when either the size of the cluster was changed to 17 argon atoms (Fig. 8c) or the initial temperature was changed to 60 K (Fig. 8d). The iodine reaches zero kinetic energy at its maximum separation (see Fig. 9a). The fact that the iodine gained some energy during its

recombination indicates that the cluster is at least partially elastic. Following an iodine collision, the cluster expands then contracts undergoing another collision with the iodine atoms and transferring some of the original kinetic energy back to the photofragments. The argon atoms appear to have acted collectively, in very much the same way as in a matrix [18]. In doing so, the coherence of the iodine nuclear motion is preserved or partially preserved, as have been observed experimentally [1].

The preserved coherence can also be seen in the plot of I-I distance versus time (Fig. 9a). The average I-I distance becomes less than 3.5 Å at about 1 ps as the caging process is complete, but a modulation remains for another few picoseconds, which indicates that the nuclear motion following the recombination is still coherent. Immediately after the recombination, the iodine is in high vibrational levels of the A or A' state. Subsequent interactions between the iodine and the Ar atoms lead to vibrational relaxation of the iodine. Although the total iodine energy continues to decrease as a result of this vibrational relaxation, the rate of relaxation becomes increasingly slower as the vibrational energy approaches the minimum. The whole relaxation process takes about 15 ps on the A state and more than 30 ps on the A' state.

The plot of cluster temperature versus time displays high values (between 70 and 90 K) for the first 2 to 3 ps after the I_2 dissociation (see Fig. 9b). The average value drops to a more stable level of about 55 K in 3 ps. The photon excitation of I_2 provides a localized (I–I mode) energy deposition into the cluster system within a very short period of time (less than 200 fs). The prompt I_2 dissociation following this excitation causes a

localized energy transfer between the iodine and nearby Ar atoms. There is not enough time for the system to dissipate all the absorbed energy to reach a thermal equilibrium within the first 2 to 3 ps. The values in the plot, therefore, only represent average kinetic energies of the cluster elements (I and Ar atoms) for the first few picoseconds. After 3 ps, the system gradually approaches a thermal equilibrium, with an average temperature of about 55 K. Notice that there is a also a drop-and-recovery feature before 1 ps, similar to what has been shown in the plot of iodine energy versus time (see insert of Fig. 8a). In fact it is caused by the same effect described for the energy-recovery. Near the end of iodine dissociation, some of the extra energy is transferred into the potential energy of the cluster, so that the total kinetic energy of the whole system reaches a minimum value. This potential energy is then quickly converted into both vibrational modes of the cluster and transitional modes of some individual atoms. In the later case, some of the argon atoms will be evaporated from the cluster after they have obtained enough energy.

Figure 9c shows that the number of Ar atoms within 25 Å from the cluster center on the average drops from 43 to about 41.5 between 2.5 and 3.5 ps. The cluster size decreases much more slowly at longer time. The prompt evaporation of one or two Ar atoms is the result of the cascade kinetic energy transfer from inner cluster shells to the outermost Ar atoms. This energy transfer is very efficient as shown below, and its direction is preferentially along the iodine dissociation axis as momentum has to be conserved. The expulsion of the first one or two Ar atoms occurs around 3 ps, in good agreement with the timing of the prompt "temperature" drop shown in Fig. 9b. According to Figures 9b and 9c, the total kinetic energy of the cluster differs by about 1000 cm^{-1}

before and after the first one to two argon atoms are ejected from the cluster. The Ar atoms are counted outside the cluster if and only if their distance from the center of mass (CM) of the system is greater than 25 Å. From the initial radial distribution (Fig. 3b), we know that these Ar atoms are initially located within a distance of 7 Å from the CM. With kinetic energies around 1000 cm^{-1}, the argon atoms have to spend about 2 ps in traveling the extra 18 Å of distance. Thus, these atoms must obtain this excess energy within one picosecond to correspond with the drops in cluster temperature and number at about 3 ps.

We have also monitored the population distribution on various states in the simulation. For excitation of the large clusters (44 Ar) at 614 nm, the time dependence of state distributions for three different initial temperatures: 30, 60 and 90 K are shown in Figures 10a-c, respectively. In our simulations, we have allowed the iodine to recombine onto both the A and A' states. The contribution of the ground state in the caging dynamics will be discussed later in this paper. The transient state is defined as the state when the separation of iodine is greater than 4.5 Å or the total energy of iodine is above the dissociation limit (into I + I). According to this definition, the lifetime of the transient state will represent how long the two iodine atoms remain separated under given conditions. The prompt increase in the A state population and the rapid decrease in the X state population near time zero represent the wave packet excitation. The A state rise and decay time represents the finite pulse width (200 fs).

At 30 K, the population in the A and A' states quickly builds up following the fast decay of the A state population (Fig. 10a). The time scale of this build-up is comparable to the pulse width, which indicates that the recombination process is direct and coherent, in agreement with the experimental observation [1]. In about 1 ps, the population reaches a constant level, indicating that the recombination process is complete. Vibrational relaxation then follows, which results in further lowering of the total I–I energy (Fig. 8a). Notice that the transient state lifetime (full-width-at-half-maximum) is about 500 fs in this case, consistent with the rise time of the A/A' state recovery. At higher temperatures, the transient state has a much longer lifetime: about 4 ps for 60 K and more than 10 ps for 90 K. Correspondingly, the recovery of A or A' population takes much longer than in the low temperature case.

(D) TRANSIENT SIMULATIONS

For the same system, what we have directly observed experimentally are LIF transients — the laser-induced-fluorescence signal versus pump-probe delay time [1]. For a direct comparison with the experimental observables, we have simulated the transient signals using the simple models described in Section 6.2. The parameters used are listed in Table 2. The result for an $I_2 \cdot Ar_{44}$ cluster (T_{init} = 30 K) following A state excitation (614 nm) is shown in Fig. 11a on a short time scale. Its experimental counterpart is shown in Fig. 11b. The two transients appear to be very similar: the initial peak at time zero, the coherent recovery around 660 fs, the slope of the slow rise, and even some of the modulations are reproduced by the simulation. The simulated transients

are not very sensitive to the parameters used. This robustness confirms that the transient behavior reproduced here represent the microscopic physical picture rather than numerical fittings. The LIF signals from the A and A' states are both shown in Fig. 11a. Both of these two states contribute to the coherent recovery of the LIF signal, as the iodine recombines into either of them promptly following dissociation. The slow rise after 1 ps is caused by vibrational relaxation, through which the iodine relaxes to lower vibrational levels of the A/A' states where the Franck-Condon overlap for probing is more efficient. The signal from the A' state is slightly delayed relative to that from the A state. The periods of their modulation are also slightly different, as a result of the details of the two potential energy surfaces. The overlap of their individual contributions makes the final modulation look irregular, just like what has been experimentally observed (see Fig. 11b). The recovery and oscillations directly reflect the coherent motion in the solute-solvent potential.

To demonstrate the effect of the size and temperature of the cluster on the transient behavior, Fig. 12a shows a simulation obtained for a smaller cluster with 17 argon atoms; and Fig. 12b was obtained for a higher initial temperature (60 K). In both of these two transients, the prompt recovery of signal around 660 fs has virtually disappeared. Fig. 12a appears similar to the experimental transient obtained from small clusters (Fig. 12c) [1].

On a longer time scale (90 ps), the simulated transients are shown in Fig. 13 with their experimental counterparts for two different probe wavelengths. At 307 nm, both the

simulated and experimental transients show a slow non-exponential rise before the signal reaches a constant level. The rise time for the simulation characterizes the time it takes for the A and A' states to relax to their potential minima, where the Franck-Condon overlap is the maximum for a 307 nm probe wavelength. For a 330 nm probe, the Franck-Condon region shifts to higher vibrational levels of the A and A' states. It then takes less time for the iodine population to relax into these intermediate levels, as shown in Fig. 13c and Fig. 13d by the faster rises. As the population relaxes further, it will eventually move out of the maximum Franck-Condon region, causing the signal to decay again (see Fig. 13c and Fig. 13d). The simulation results are consistent with the experimental results on this trend of variations, though the simulation appears to have over-estimated the relaxation rate on the A and A' states. This over-estimation is likely to be caused by the overlook of the quantum effect during the relaxation process, especially at long times. While classically the iodine can constantly exchange its vibrational energies with the argon atoms, there will be limitations imposed by the quantum mechanics which would only allow quantized energy transfers between a bound iodine state and the argon atoms in the clusters. These limitations can potentially lower the effective rate of vibrational relaxation.

The fact that the experimental signal remains constant at very long times (more than 200 ps) indicates that the iodine system has reached a relatively stable state on this time scale. This is not the X state, because the photon energy used (307 nm) can only probe its intermediate vibrational levels. These intermediate levels are not stable in the clusters as the relaxation process continues. The time scale for the X state relaxation was

estimated to be less than 200 ps according to our simulation. The A and A' states are, on the other hand, relatively stable on this time scale. The lifetimes of the A and A' states are a few microseconds and milliseconds, respectively, in argon matrices [15]. We expect their lifetimes in argon clusters to be comparable. It is possible that iodine recombines onto the X state as well. In fact Fei, et al have observed the absorption spectra from recombined X state in similar cluster systems [14]. The LIF signal from the X state, if there is any, will decay away on long time scales (200 ps or so). This long time decay was not observed experimentally (see Fig. 13b)[1], which suggests that either direct caging into the X state is not significant or the probing of the X state is far less efficient than that of the A and A' states. In argon solutions [19] the caging on the X state was found experimentally to be negligible, consistent with the cluster work [1], and we will not consider contributions from the X state for most of our discussion here.

6.3.3. Dynamics following B state excitation

The dynamics following B state excitation were similarly simulated. After the initial preparation of the cluster, the potential of I_2 was instantaneously switched from the X to the B state with the excitation energy varied between 17,500 cm^{-1} (570 nm) and 20,800 cm^{-1} (480 nm). The coupling between the B and Π_{1u}/Π_{1g} states was simulated by the Landau-Zener-Stückelberg model to allow predissociation. The exact values for the coupling matrix elements between the B and Π states are not known to us. The results reported here were obtained using $W_{B-\Pi_{1g}} = 15$ cm^{-1} and $W_{B-\Pi_{1u}} = 5$ cm^{-1}.

The time dependence of state populations is shown in Fig. 14a for an excitation wavelength of 570 nm. After a prompt excitation at time zero, the B state population decays on a time scale of about 6 ps. The population of the transient state, as defined previously, covers a broad distribution from a few to more than 60 picoseconds. The recombination to the A and A' states is delayed by about 4 ps, and the rise time of the population on these states is on the order of 30 ps. The results for shorter excitation wavelengths (510 nm and 480 nm) are similar, except that the B state decay time and the A/A' delay time become longer. Based on the model potentials used for the B and Π_{1u}/Π_{1g} states, the curve-crossing points are near the bottom of the B state [9,20]. The coupling is not efficient unless the vibrational energy is very close to the crossing points according to the Landau-Zener-Stückelberg model used. For lower excitation energy (570 nm), it takes less time for iodine to relax into the efficient curve-crossing regions, causing the B-state decay to be faster.

Following the B-state predissociation, the iodine atoms are well separated so that argon atoms can intercede between them, as shown in Fig. 14b. In order to recombine, the iodine atoms have to approach each other diffusively within the cluster. For higher excitation energies (or shorter wavelengths), the cluster absorbs more kinetic energy from the iodine and becomes softer which allows the iodine atoms to separate further upon dissociation.

The influence of excitation energy on the time scales of recombination is clearly demonstrated by the caging time distribution introduced earlier. As shown in Fig. 15, the

distribution shifts to longer times when the excitation wavelength is changed from 570 nm to 510 nm. The most probable value for the caging time is about 10 ps for 570 nm excitation, and is about 18 ps for 510 nm excitation. The distribution of maximum I–I separation, which is not shown here, also shifts to longer distances when the excitation wavelength is changed to shorter wavelengths (or higher energies)

The dynamics following either A or B state excitation are compared in Fig. 16. Following B state excitation, the I_2 energy is transferred to the argon atoms through vibrational relaxation and electronic predissociation, both of which occur on a picosecond time scale. The recombination also occurs on a much longer time scale following the predissociation than that following the direct A state dissociation (Fig. 16a). This difference in time scales is also illustrated by comparing the time dependence of cluster temperature (Fig. 16b) and cluster size (Fig. 16c). Following A state excitation, the temperature (or average value of kinetic energy) and number of argon atoms change dramatically within the first few picoseconds (Fig. 16b and Fig. 16c, dotted lines). The cluster is quickly stabilized after 4 ps with a temperature of about 55 K (Fig. 16b, dotted line). The temperature then decays on a very long time scale (a few nanoseconds), as the cluster slowly cools down through evaporation (Fig. 16c, dotted line).

Following B state excitation, the temperature rises to a maximum value of about 65 K in about 20 ps (Fig. 16b, solid line). The temperature then decays on a much longer time scale. For A state excitation, within the first few picoseconds, one to two argon atoms are ejected from the cluster through concerted collisions (see Fig. 16c, dotted line).

This does not happen in the case of B state excitation, in which argon atoms have to undergo thermalized evaporation in order to leave the cluster. As a result, the evaporation rate is much slower following B state excitation than following A state excitation for the first 4 ps. At longer times, thermalized evaporation becomes dominant for both cases. The cluster is hotter following B state excitation (Fig. 16b), because the excitation energy is higher and the average energy taken away by the first few argon atoms is lower. The rate of evaporation then becomes higher for the B state excitation than for the A state excitation (Fig. 16c).

For 570 nm excitation, the simulated LIF transient is shown in Fig. 17 along with the corresponding experimental result. The two transients appear to be similar in nature. The simulated transients for higher excitation energies (not shown here) also generally agree with their experimental counterparts [1]. The signal decay following initial excitation is caused by the relaxation and electronic predissociation on the B state, the time scale for which increases as the excitation energy is increased (from 570 to 510 nm). The slow recovery of the LIF signal comes from the recombination and relaxation onto the A and A' states. The onset of the recovery appears to be delayed relative to time zero as is the case when we try to fit the experimental transients [1]. This delay is caused by the fact that the iodine atoms have to remain separate for a finite period of time before the onset of recombination (see the caging time distribution in Fig. 15).

At 480 nm, the iodine is excited to the B state above the dissociation limit (into I + I*), according to the gas phase potential. For all of the 400 trajectories that we have

computed (for the larger cluster with 44 Ar), the iodine atoms are promptly bounced back to the B state below its dissociation limit. The B-state transient behavior appears to be similar at 480 nm to that at 570 nm, except that both B state decay time and the delay time before recombination are longer. Experimentally the LIF transient at 480 nm displayed an initial plateau followed by a slow rise that reached a second constant level some 30 ps later [1]. This behavior is attributed to the extra contributions from the directly excited Π_{1u} state at this pump wavelength. The percentage of excitation to the Π_{1u} state is estimated to be ~46% according to the gas phase absorption spectra [21]. The transient behavior following excitation of the Π_{1u} state is similar to that following the A state excitation on long time scales (like the one shown in Fig. 13a). By overlapping the B-state and Π_{1u}-state transients, we were able to reproduce the experimental results (not shown here). The dynamics above the B-state dissociation will be published separately, as new rich experimental and theoretical results are now available [22].

6.4 Conclusions

In this contribution, we studied the molecular dynamics of iodine in argon clusters in order to examine the microscopic atomic motions and to compare with the experimental femtosecond results presented in the preceding paper.

At low temperatures (30 K or lower), the cluster system displayed well defined structures. The Ar atoms are well localized and the I_2 molecule is enclosed by at least one full shell in large clusters. For larger clusters (with 44 argon atoms), the collective binding force of the Ar atoms is strong and the cluster cage is elastic. The excited iodine atoms are not able to break the cage upon direct dissociation on the A state. The prompt reflection of iodine atoms from this cage causes the iodine molecules to be coherently reformed within 1 ps after the direct dissociation. Aside from this concerted caging, we have revealed another channel of direct caging. The iodine molecule can be promptly stabilized by argon atoms that are located head on with the iodine atoms along the dissociation axis. This channel is purely dependent on the geometry and kinetics of the systems involved. At higher temperatures (above 60 K), the Ar clusters are melted much like a liquid droplet. The high mobility of the Ar atoms allows the iodine atoms to penetrate through the inner Ar shells following the dissociation. It then takes longer for the well separated iodine atoms to diffusely approach each other and form a bond again.

The time scales for dissociation are found to play an important role in the subsequent dynamics of recombination. When the dissociation is prompt (direct dissociation of I_2 on the A state), the Ar cage does not have enough time to rearrange

itself before the I_2 separation occurs. The excitation process is equivalent to a localized energy deposition. The subsequent motion of the cluster then preserves some of the initial coherence for a certain period of time depending on the dissipative nature of the system. Since the caging process is so fast (less than 1 ps) following the direct dissociation, the early time dynamics are insensitive to atoms/molecules that are far away from the iodine. It was originally proposed that similar systems in a cold matrix environment should display similar coherent features in the caging dynamics [13], which has recently been observed experimentally for iodine in argon and krypton matrices [18].

When the dissociation is indirect (predissociation on the B state), the vibrational-transitional energy transfer tends to warm up the Ar cage before the I_2 separation actually takes place. Upon dissociation, the iodine atoms are able to depart far from each other, allowing the argon atoms to intercede between them. The recombination, therefore, takes longer, because the well separated iodine atoms have to approach each other diffusively.

The comparison between MD and experiments is satisfactory and brings to focus the nature of the motion under different conditions that we studied: (1) angular and radial distribution; (2) temperature and size of the cluster; (3) state prepared and state of caging; (4) wave packet motion; and (5) the change in energy and bond distance for iodine in the solvent cage. Figures 18 and 19 summarize the MD of the wave packet in the solvent cage and the associated snapshots for different cluster sizes. The above concepts give the *molecular basis* for the dissociation and recombination phenomena: The bond breakage time is critical to the subsequent caging dynamics, and caging is a mechanism described

by a dominant (coherent) energy release from the solute to the solvent (lowering of energy below dissociation limit) and only at very long times by the physical motions of the solvent (diffusive process).

6.5 References

1. Wang, J.-K.; Liu, Q.; Zewail, A. H. *J. Phys. Chem.*, **1995**, preceding paper.
2. Amar, F. G.; Berne, B. J. *J. Phys. Chem.* **1984**, 88, 6720.
3. Li, Z.; Borrmann, A.; Martens, C. C. *J. Chem. Phys.* **1992**, 97, 7234.
4. Gerber, R. B.; McCoy, A. B.; Garcia-Vela, A. *Ann. Rev. Phys. Chem.* **1994**, 45, 275.
5. Papanikolas, J. M.; Maslen, P. E.; Parson, R. *J. Chem. Phys.* **1995**, 102, 2452.
6. Raz, T.; Schek, I.; Ben-Nun, M.; Even, U.; Jortner, J.; Levine, R. D. *J. Chem. Phys.* **1994**, 101, 8606.
7. Allen, M. P.; Tildesley, D. J. *Computer Simulation of Liquids*; Oxford University Press: New York, 1992.
8. Nesbitt, D. J.; Hynes, J. T. *J. Chem. Phys.* **1982**, 77, 2130.
9. Tellinghuisen, J. *J. Chem. Phys.* **1985**, 82, 4012.
10. Swope, W. C.; Andersen, H. C.; Berens, P. H.; Wilson, K. R. *J. Chem. Phys.* **1982**, 76, 637.
11. Landau, L. D. *Physik Z. Sowjetunion* **1932**, 2, 46; Landau, L. D.; Lifshitz, E. M. *Quantum Mechanics*; Pergamon Press: Oxford, 1977; Zener, C. *Proc. Roy. Soc. London*, **1932**, A137, 696; ibid. **1933**, A140, 660; Stückelberg, E. C. G. *Helv. Phys. Acta.*, **1932**, **5**, 369.
12. Potter, E. D.; Liu, Q.; Zewail, A. H. *Chem. Phys. Lett.* **1992**, 200, 605.
13. Liu, Q.; Wang, J.-K.; Zewail, A. H. *Nature* **1993**, 364, 427.
14. Fei, S.; Zheng, X.; Heaven, M. C.; Tellinghuisen, J. *J. Chem. Phys.* **1992**, 97, 6057; and references therein.
15. Macler, M.; Heaven, M. C. *Chem. Phys.* **1991**, 151, 219; and references therein.
16. Tellinghuisen, J. *Can. J. Phys.* **1984**, 62, 1933.
17. Farges, J.; de Feraudy, M. F.; Raoult, B.; Torchet, G. *J. Chem. Phys.* **1983**, 78, 5067.
18. Zadoyan, R.; Li, Z.; Ashjian, P.; Martens, C. C.; Apkarian, V. A. *Chem. Phys. Lett.* **1994**, 218, 504; Zadoyan, R.; Li, Z.; Martens, C. C.; Ashjian, P.; Apkarian, V. A. *J. Chem. Phys.* **1994**, 101, 6648.

19. Lienau, Ch.; Zewail, A. H. *Chem. Phys. Lett.* **1994**, 222, 224; Materny, A.; Lienau, Ch.; Zewail, A. H. to be published.

20. Burke, M. L.; Klemperer, W. *J. Chem. Phys.* **1993**, 98, 1797.

21. Tellinghuisen, J. *J. Chem. Phys.* **1982**, 76, 4736.

22. Works to be published.

6.6 Tables

Table 1. Potential parameters used in the simulation.

(a) Morse functions for the iodine X, A, A' and B states:

$$V(r) = D\{\exp[-2\beta(r-r_e)] - 2\exp[-\beta(r-r_e)]\} + E_\infty$$

State	r_e (Å)	β(Å^{-1})	D (cm^{-1})	E_∞(cm^{-1})
X [a]	2.67	1.91	12547.2	0
A' [b]	3.073	2.104	2856	0
A [b]	3.1	2.104	1990	0
B [a]	3.03	1.75	4381.8	7605.0

a. see reference 8.

b. see reference 18. Modified in accordance with the solvation in Ar clusters.

(b) Lennard-Jones functions for the Ar-Ar and the I-Ar interactions:

$$V(r) = 4\varepsilon\left[(\sigma/r)^{12} - (\sigma/r)^{6}\right]$$

Pair	σ(Å)	ε (cm^{-1})
Ar-Ar [a]	3.405	83.3
I-Ar [b]	3.617	130.3

a. see reference 2.

b. see reference 3.

Table 2. Parameters for the LIF [a]:

State	f_0	$\gamma(cm^{-1})$	$\Gamma(cm^{-1})$
X	100	100	200
A'	100	100	200
A	100	100	200
B	100	100	200

a. see text.

6.7 Figure Captions and Figures

Fig. 1 The iodine potential energy curves that are relevant to the dissociation and caging dynamics. Wave packets and arrows are drawn to illustrate the dynamical processes under study. a) I_2 is excited to the A state above its dissociation limit (into I + I). Following direct dissociation, the iodine is caged by the surrounding argon cluster. b) I_2 is excited to the B state, followed by predissociation through non-adiabatic couplings between the B and Π states and subsequent recombination onto the A/A' and X states.

Fig. 2 Snapshots of typical cluster structures at 30 K with different number of argon atoms: (a) 17 argon atoms; (b) 44 argon atoms.

Fig. 3 Radial distributions of Ar atoms with respect to the CM of the iodine. a) $I_2 \cdot Ar_{17}$ at 30 K; b) $I_2 \cdot Ar_{44}$ at 30 K; c) $I_2 \cdot Ar_{44}$ at 60 K; d) $I_2 \cdot Ar_{44}$ at 90 K.

Fig. 4 Angular distributions of Ar atoms with respect to the iodine bond axis. a) $I_2 \cdot Ar_{17}$ at 30 K; b) $I_2 \cdot Ar_{44}$ at 30 K; c) $I_2 \cdot Ar_{44}$ at 60 K; d) $I_2 \cdot Ar_{44}$ at 90 K.

Fig. 5 Distribution of the maximum I–I separation following A state excitation (614 nm). a) $I_2 \cdot Ar_{17}$ at 30 K; b) $I_2 \cdot Ar_{44}$ at 30 K; c) $I_2 \cdot Ar_{44}$ at 60 K; d) $I_2 \cdot Ar_{44}$ at 90 K.

Fig. 6 Caging time distribution following A state excitation (614 nm). The excitation pulse width was set to be 200 fs. a) $I_2 \cdot Ar_{17}$ at 30 K; b) $I_2 \cdot Ar_{44}$ at 30 K; c) $I_2 \cdot Ar_{44}$ at 60 K; d) $I_2 \cdot Ar_{44}$ at 90 K.

Fig. 7 (a) Distributions of caging time and (b) distribution of maximum I-I separation following A state excitation at 555 nm (solid lines) and at 614 nm (dashed lines) for $I_2 \cdot Ar_{44}$ at 30 K.

Fig. 8 Time dependence of the total iodine energy (kinetic energy plus potential energy). a) $I_2 \cdot Ar_{44}$ at T_{init} = 30 K with an excitation wavelength of 614 nm; b) $I_2 \cdot Ar_{44}$ at T_{init} = 30 K with an excitation wavelength of 555 nm; c) $I_2 \cdot Ar_{17}$ at T_{init} = 30 K

with an excitation wavelength of 614 nm; d) $I_2 \cdot Ar_{44}$ at T_{init} = 60 K with an excitation wavelength of 614 nm. The critical regions near 1 ps are plotted in the corresponding inserts.

Fig. 9 Time dependence of a) I–I distance, b) cluster temperature and c) cluster size (number of Ar) on a short time scale following the excitation of $I_2 \cdot Ar_{44}$ at 614 nm. Recombination onto the X state is not considered.

Fig. 10 The time dependence of the population distribution on various states: a) $I_2 \cdot Ar_{44}$ at an initial temperature of 30 K; b) $I_2 \cdot Ar_{44}$ at an initial temperature of 60 K; c) $I_2 \cdot Ar_{44}$ at an initial temperature of 90 K. The excitation wavelength is 614 nm and recombination onto the X state is not considered.

Fig. 11 LIF transients following A state excitation at 614 nm. a) Simulation results for an $I_2 \cdot Ar_{44}$ cluster with an initial temperature of 30 K. The signal is calculated in accordance with a probe wavelength of 307 nm. b) Experimental transient obtained by monitoring the red-shifted fluorescence (400 nm) from an iodine-argon co-expansion with the probe wavelength at 307 nm. See Ref. 1 for more detail.

Fig. 12 LIF transients following A state excitation. a) Simulation results for an $I_2 \cdot Ar_{17}$ cluster with an initial temperature of 30 K. The signal is calculated in accordance with a probe wavelength of 307 nm. b) Simulation results for an $I_2 \cdot Ar_{44}$ cluster with an initial temperature of 60 K. The signal is calculated in accordance with a probe wavelength of 307 nm. c) Experimental transient obtained by monitoring the iodine fluorescence at 342 nm from an iodine-argon co-expansion with the probe wavelength at 307 nm. See Ref. 1 for more detail.

Fig. 13 Probe dependence of the LIF transients: a) simulation results for $I_2 \cdot Ar_{44}$ (T_{init} = 30 K) with the probe wavelength at 307 nm; b) experimental result with the probe wavelength at 307 nm; c) simulation result for $I_2 \cdot Ar_{44}$ (T_{init} = 30 K) with the probe

wavelength at 330 nm; d) experimental result with the probe wavelength at 330 nm. The excitation (pump) wavelength is 614 nm. The iodine is assumed to be excited to the A state and recombine onto both A and A' states in the simulations.

Fig. 14 Time dependence of a) state populations and b) argon insertion following B state excitation at 570 nm. The cluster simulated is $I_2 \cdot Ar_{44}$ with an initial temperature of 30 K. The coupling between the B and Π states is considered. Recombination onto the X state is not included.

Fig. 15 The distribution of caging times for B state excitation: a) the excitation wavelength is 570 nm; b) the excitation wavelength is 510 nm. The cluster simulated is $I_2 \cdot Ar_{44}$ with an initial temperature of 30 K. The coupling between the B and Π states is considered. Recombination onto the X state is not included.

Fig. 16 The time dependence of a) I–I energy; b) cluster temperature; and c) cluster size following A (614 nm, dotted lines) and B state excitation (570 nm, solid lines). The simulation was performed for an $I_2 \cdot Ar_{44}$ cluster with an initial temperature of 30 K.

Fig. 17 LIF transients following B state excitation at 570 nm: a) simulation results for an $I_2 \cdot Ar_{44}$ cluster (T_{init} = 30 K) with the probe wavelength at 307 nm; b) experimental results obtained with the same pump and probe wavelengths.

Fig. 18 Wave packet motion as a function of time. The wave packet was treated classically as representing the spacial distributions of I–I distances at given times. The distributions were obtained by averaging over 1000 independent trajectories.

Fig. 19 Snapshots of the clusters at different times. (a) For a cluster with 17 Ar atoms. At the time of iodine dissociation (t = 0), one iodine atom is not capped by argon atoms so that the subsequent recombination takes more than 4 ps. (b) For a cluster with the same size (17 Ar), the iodine molecule is fully enclosed and the recombination following dissociation is direct. (c) For larger clusters with 44

argon atoms or more, the iodine is almost always fully enclosed. The caging is, therefore, direct and coherent.

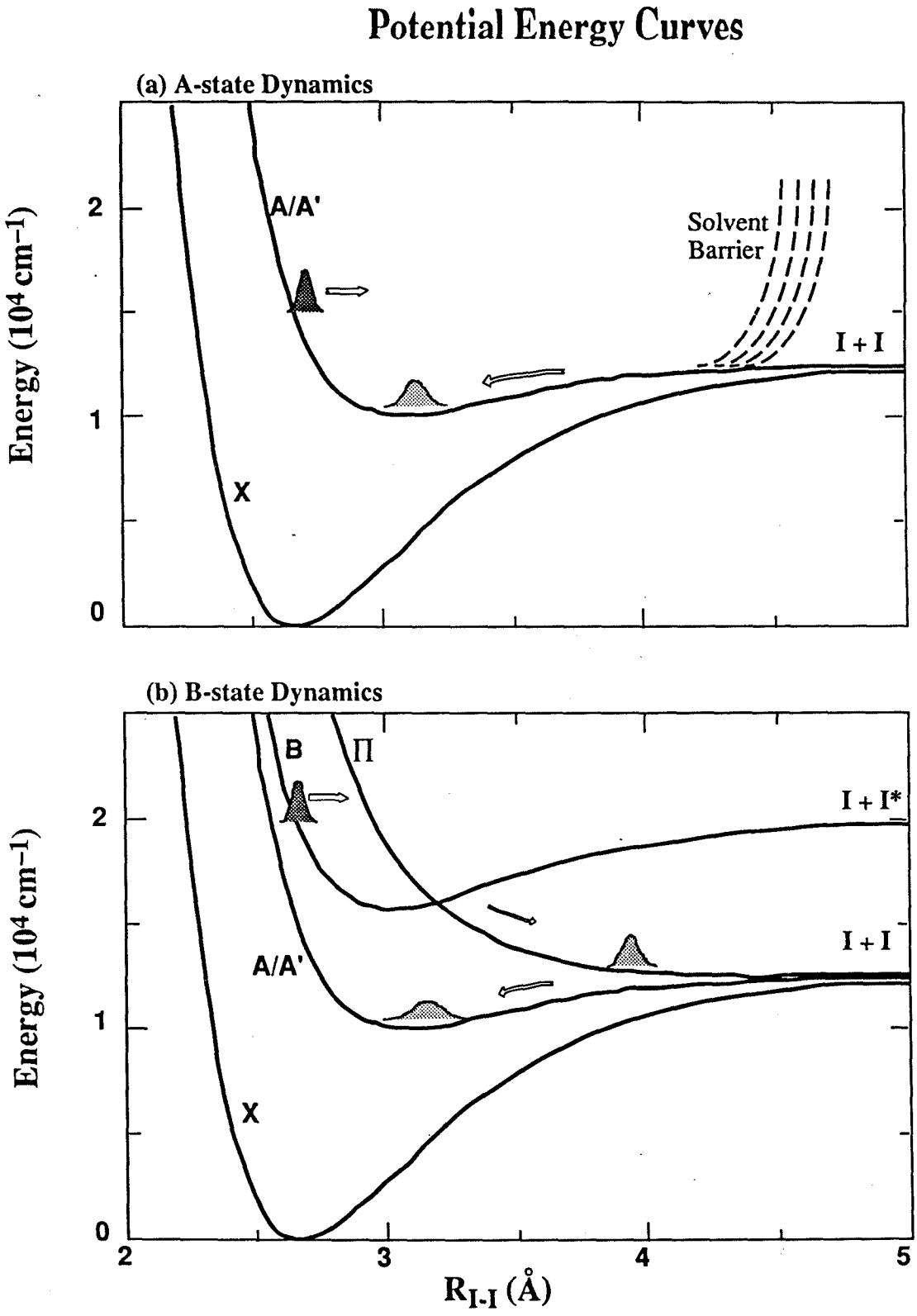
Potential Energy Curves
(a) A-state Dynamics
Energy (10^4 cm^{-1})
2
1
0
A/A'
Solvent
Barrier
I + I
X
(b) B-state Dynamics
B
Π
I + I*
I + I
A/A'
X
2
3
4
5
R_{I-I} (Å)

Figure 1

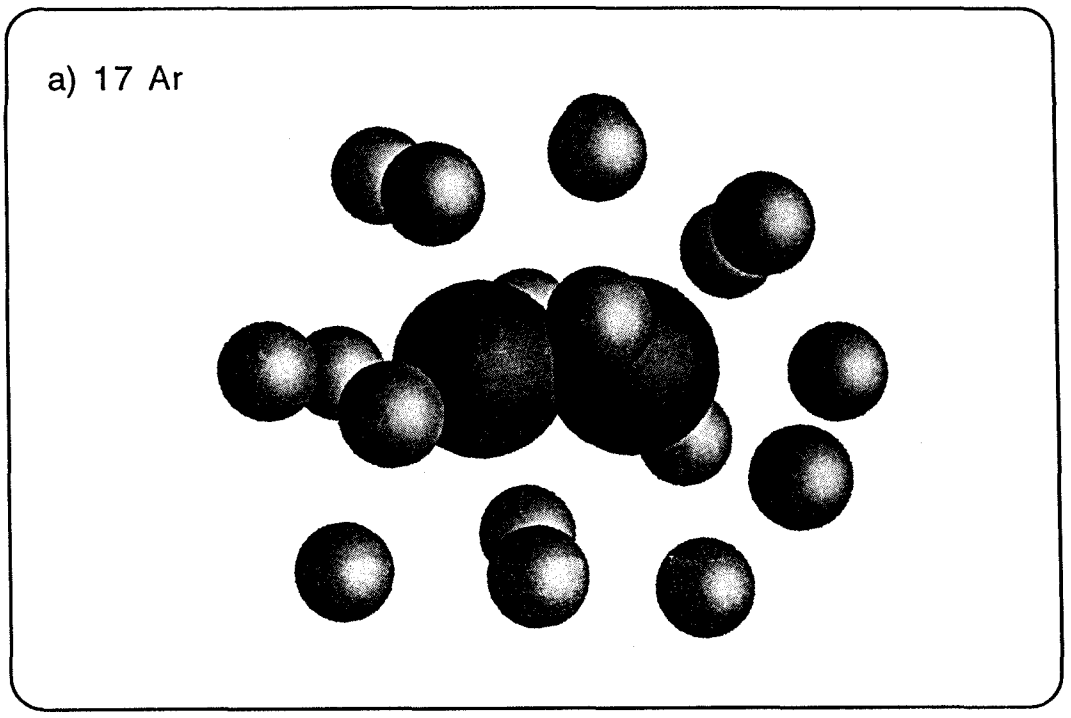

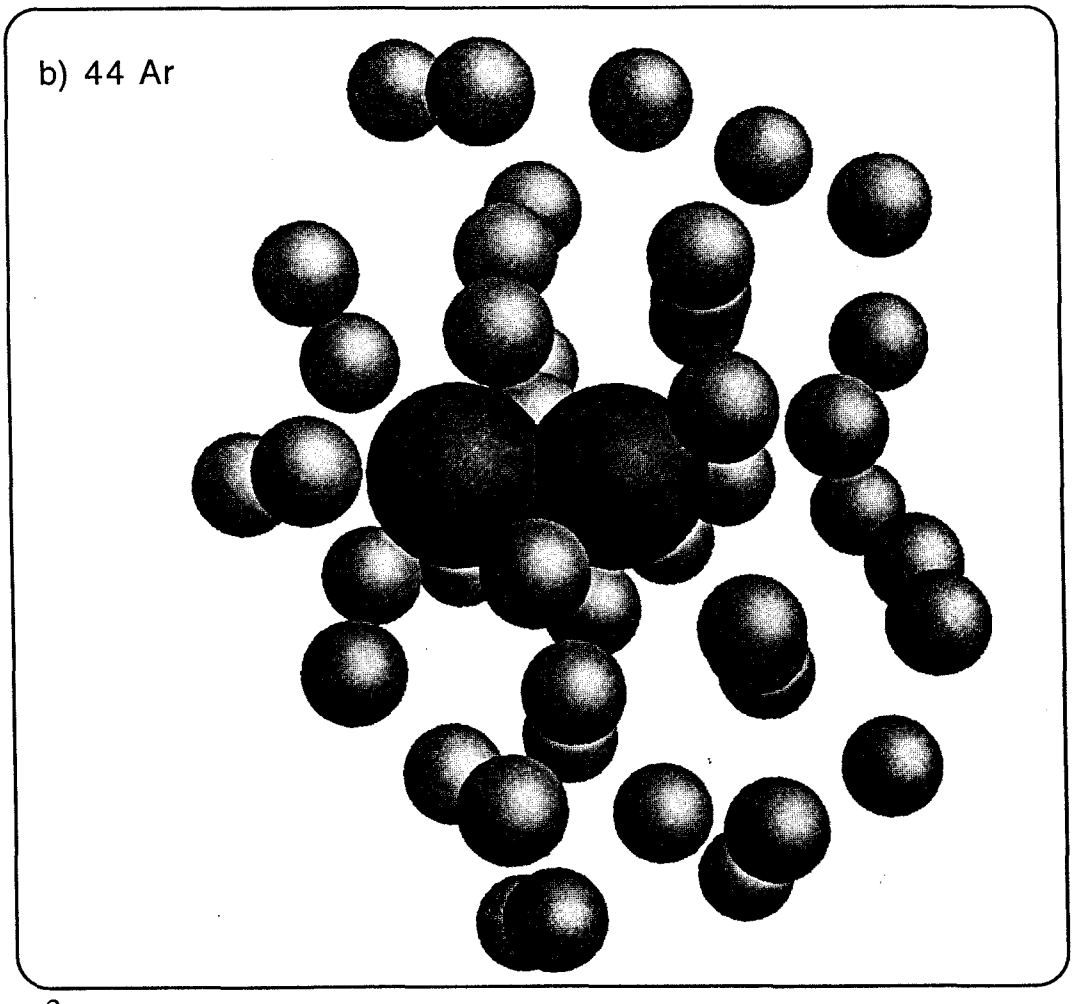

Figure 2

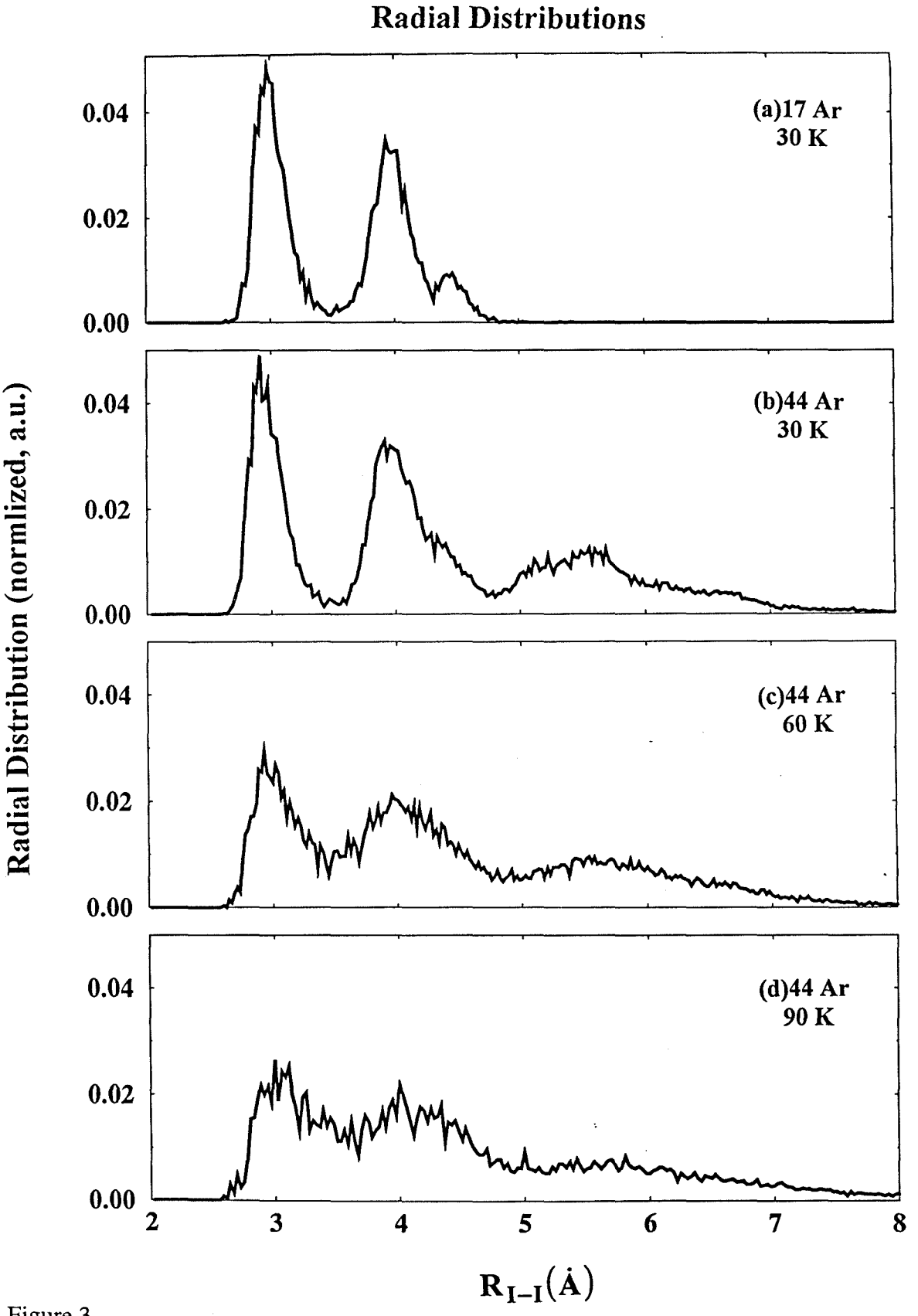
Radial Distributions
(a)17 Ar
30 K
(b)44 Ar
30 K
(c)44 Ar
60 K
(d)44 Ar
90 K
0.04
0.02
0.00
Radial Distribution (normlized, a.u.)
2
3
4
5
6
7
8
R I–I (Å)

Figure 3

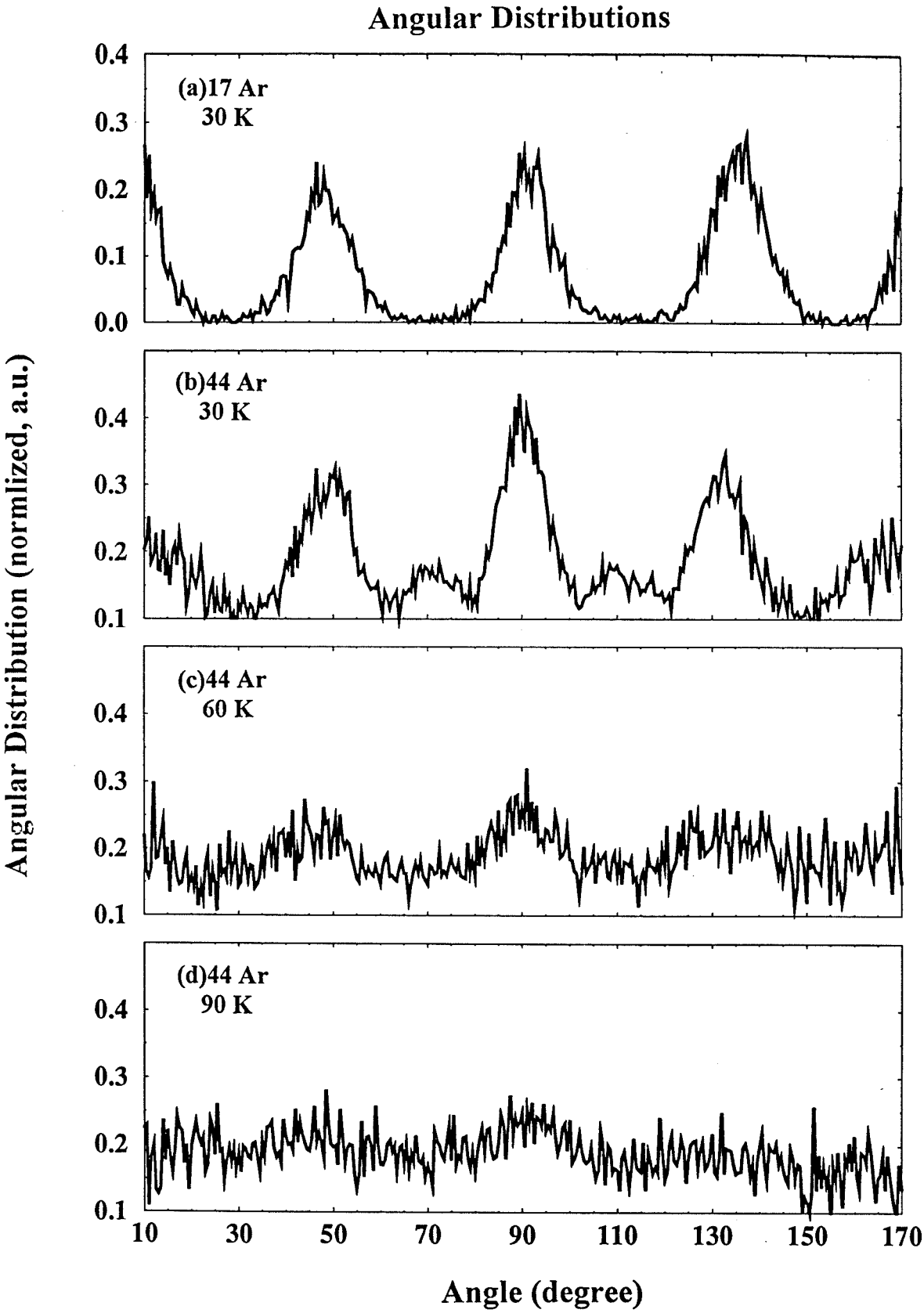
Angular Distributions
(a)17 Ar
30 K
(b)44 Ar
30 K
(c)44 Ar
60 K
(d)44 Ar
90 K
Angular Distribution (normlized, a.u.)
Angle (degree)
0.0
0.1
0.2
0.3
0.4
10
30
50
70
90
110
130
150
170

Figure 4

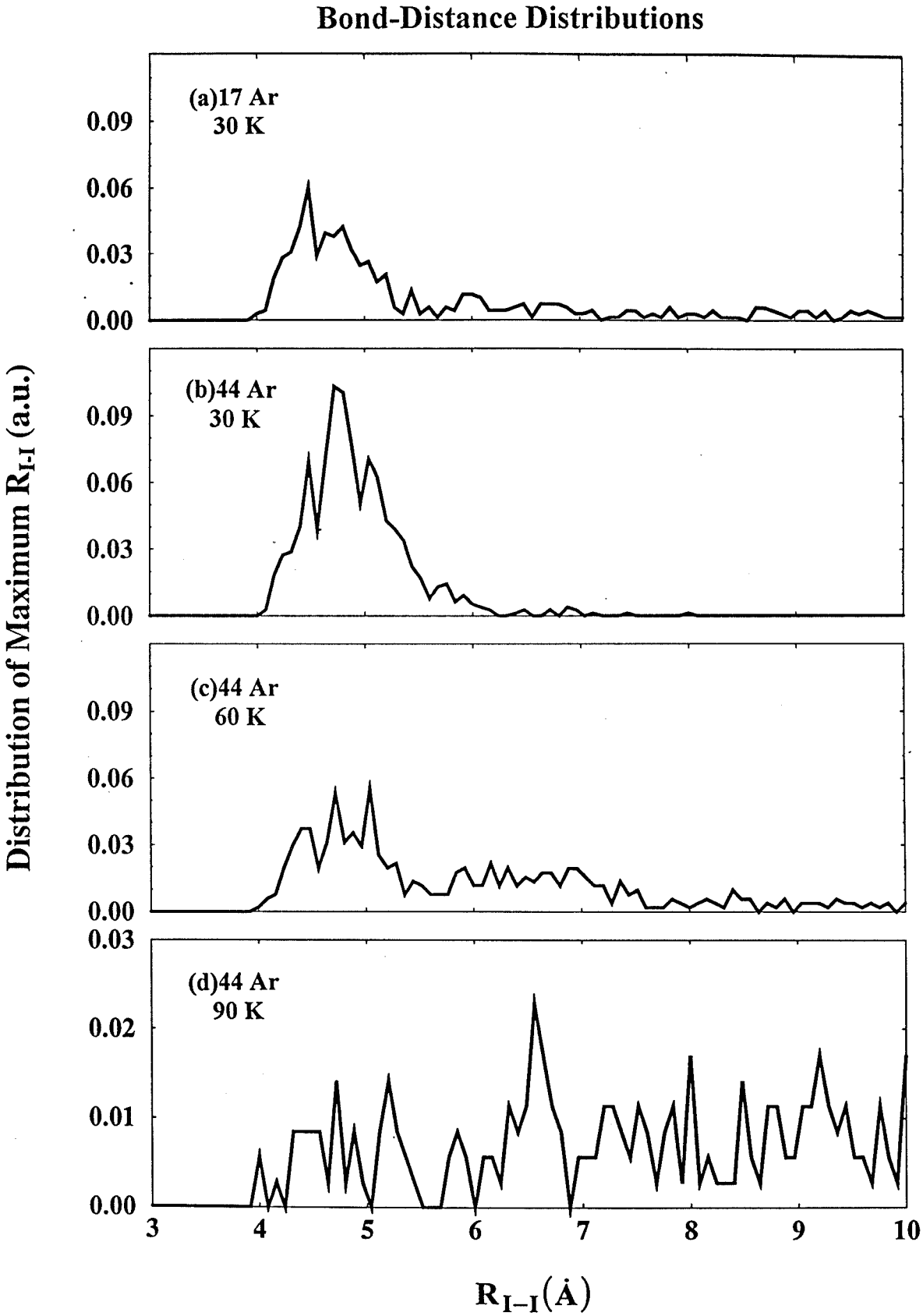
Bond-Distance Distributions
(a)17 Ar
30 K
(b)44 Ar
30 K
(c)44 Ar
60 K
(d)44 Ar
90 K
Distribution of Maximum R_{I-I} (a.u.)
R_{I-I}(Å)
0.09
0.06
0.03
0.00
0.02
0.01
3
4
5
6
7
8
9
10

Figure 5

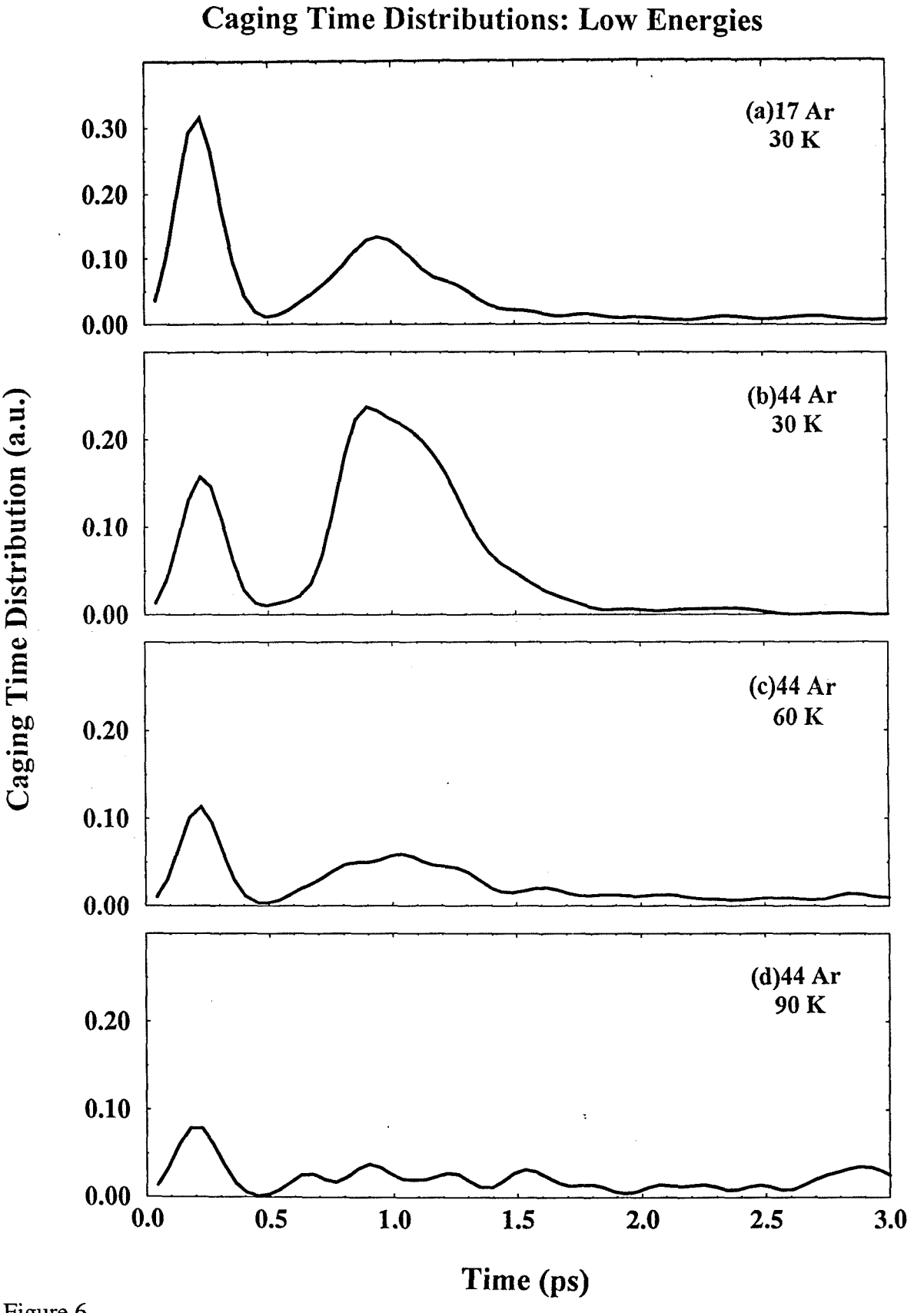
Caging Time Distributions: Low Energies
(a)17 Ar
30 K
(b)44 Ar
30 K
(c)44 Ar
60 K
(d)44 Ar
90 K
Caging Time Distribution (a.u.)
0.30
0.20
0.10
0.00
0.0
0.5
1.0
1.5
2.0
2.5
3.0
Time (ps)

Figure 6

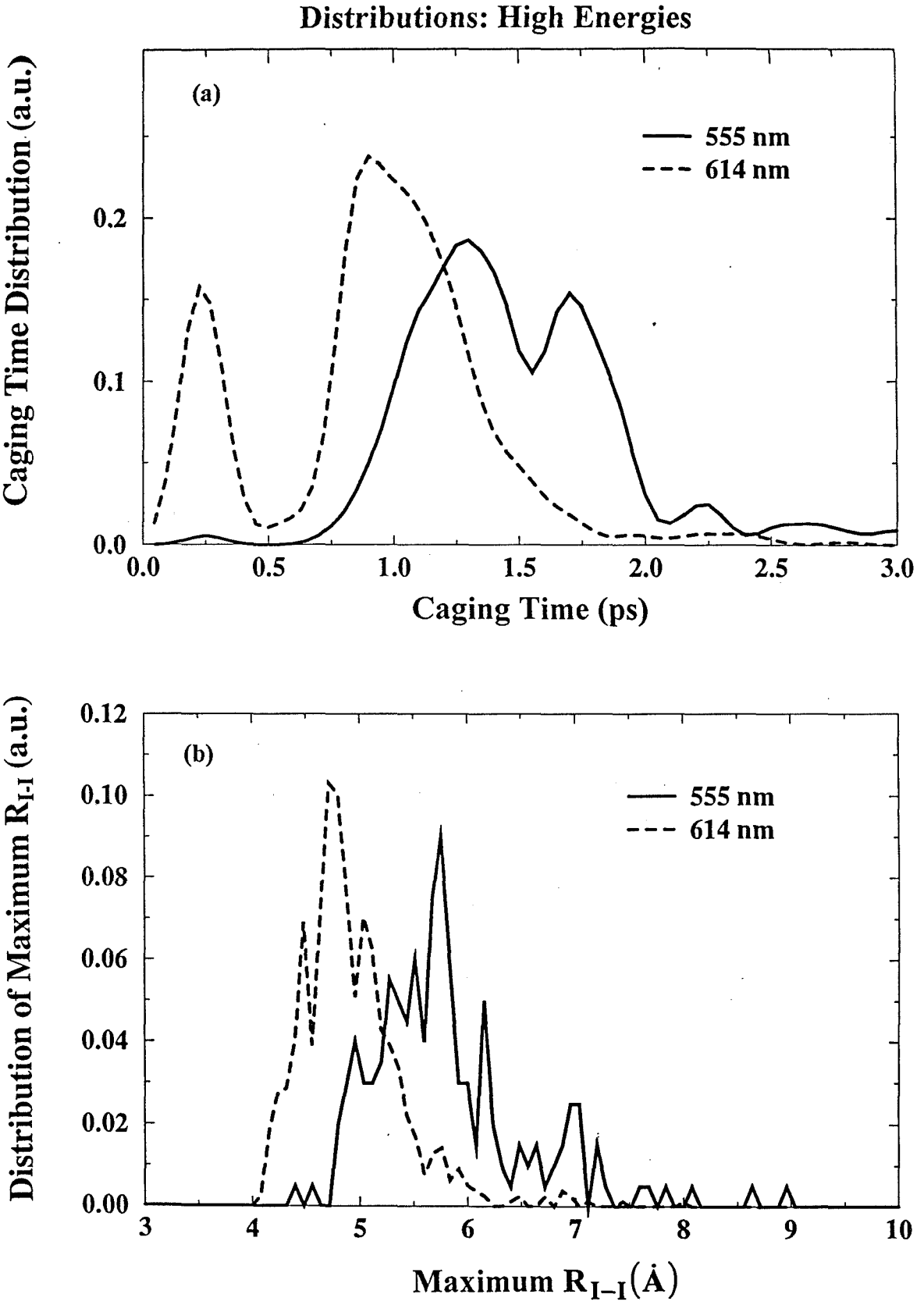
Distributions: High Energies
(a)
555 nm
614 nm
Caging Time Distribution (a.u.)
0.0
0.1
0.2
0.0
0.5
1.0
1.5
2.0
2.5
3.0
Caging Time (ps)
(b)
555 nm
614 nm
Distribution of Maximum R_{I-I} (a.u.)
0.00
0.02
0.04
0.06
0.08
0.10
0.12
3
4
5
6
7
8
9
10
Maximum R_{I-I}(Å)

Figure 7

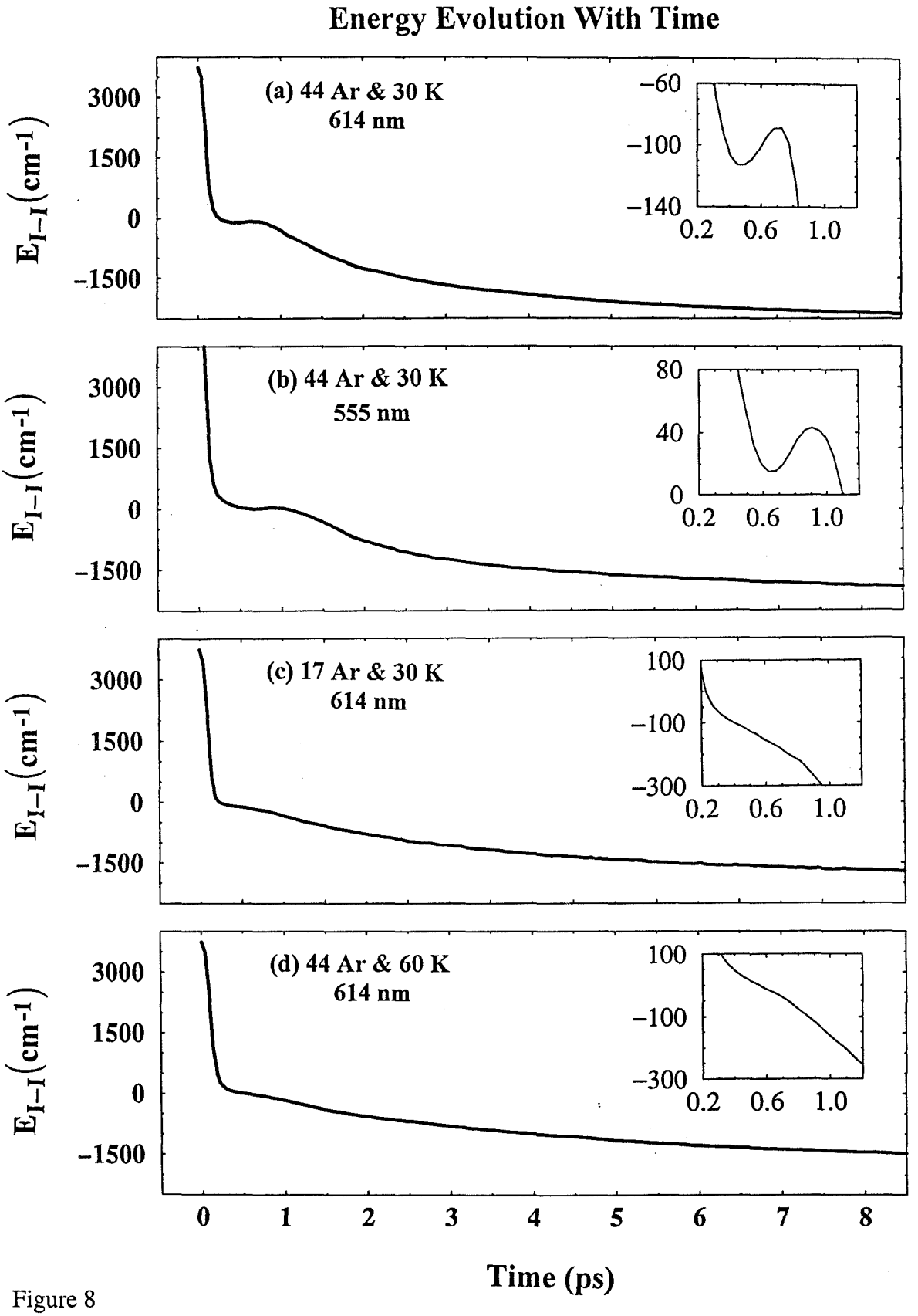
Energy Evolution With Time
(a) 44 Ar & 30 K
614 nm
(b) 44 Ar & 30 K
555 nm
(c) 17 Ar & 30 K
614 nm
(d) 44 Ar & 60 K
614 nm
$E_{I-I}(cm^{-1})$
3000
1500
0
−1500
−60
−100
−140
80
40
100
−300
0.2
0.6
1.0
0
1
2
3
4
5
6
7
8
Time (ps)

Figure 8

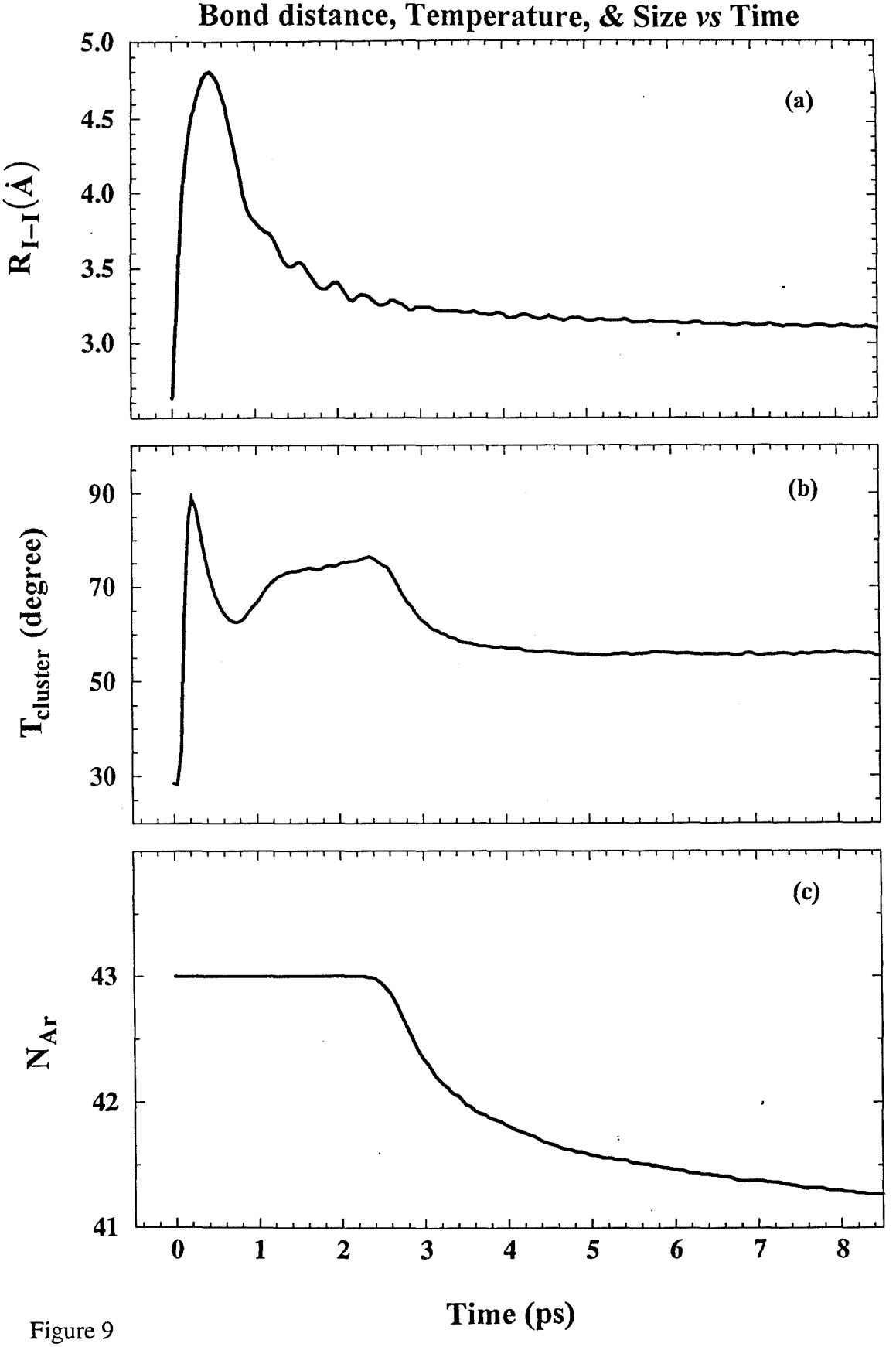
Bond distance, Temperature, & Size vs Time
(a)
(b)
(c)
R_{I-I}(Å)
$T_{cluster}$ (degree)
N_{Ar}
Time (ps)
5.0
4.5
4.0
3.5
3.0
90
70
50
30
43
42
41
0
1
2
3
4
5
6
7
8

Figure 9

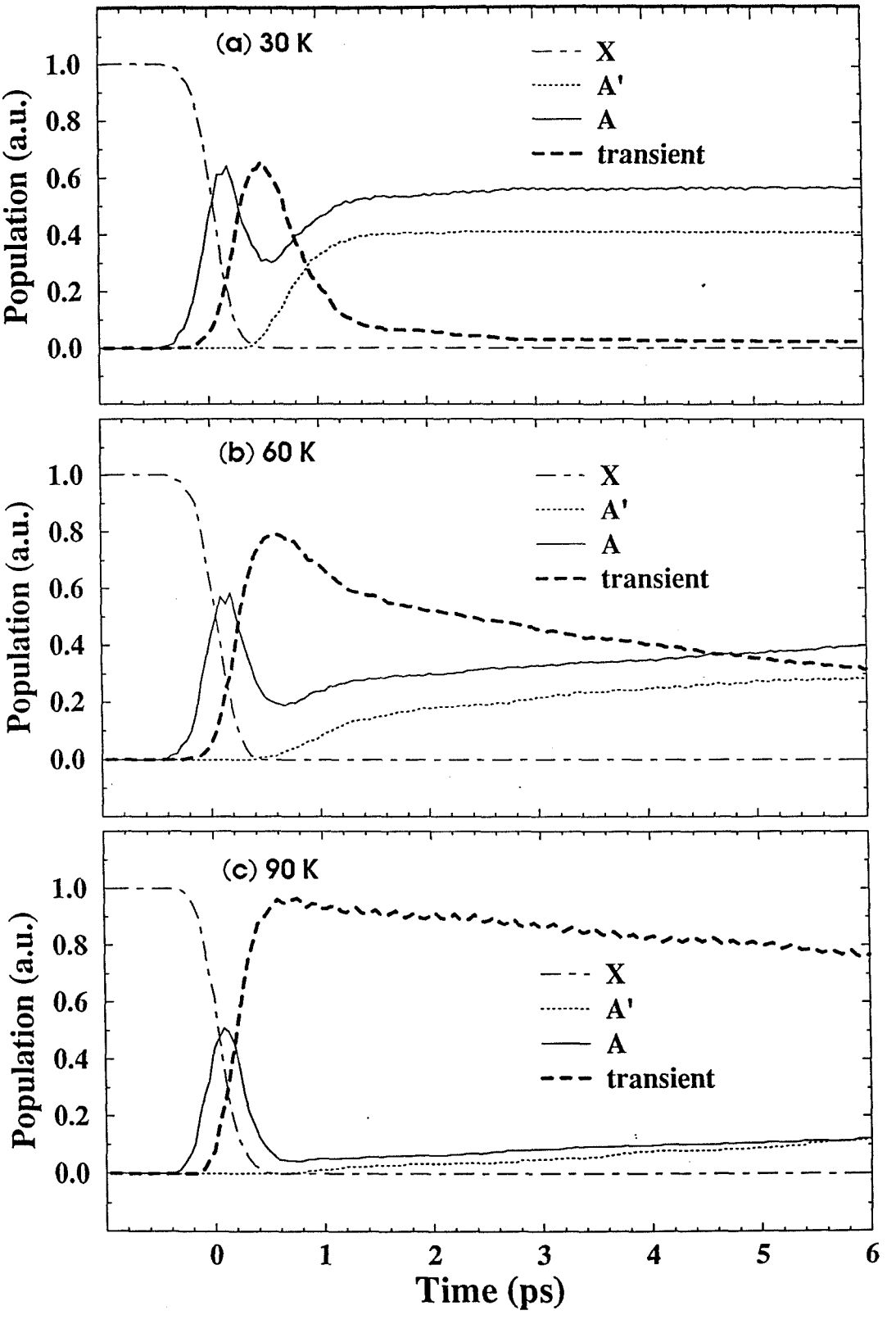
State Population Distributions
(a) 30 K
(b) 60 K
(c) 90 K
X
A'
A
transient
Population (a.u.)
1.0
0.8
0.6
0.4
0.2
0.0
0
1
2
3
4
5
6
Time (ps)

Figure 10

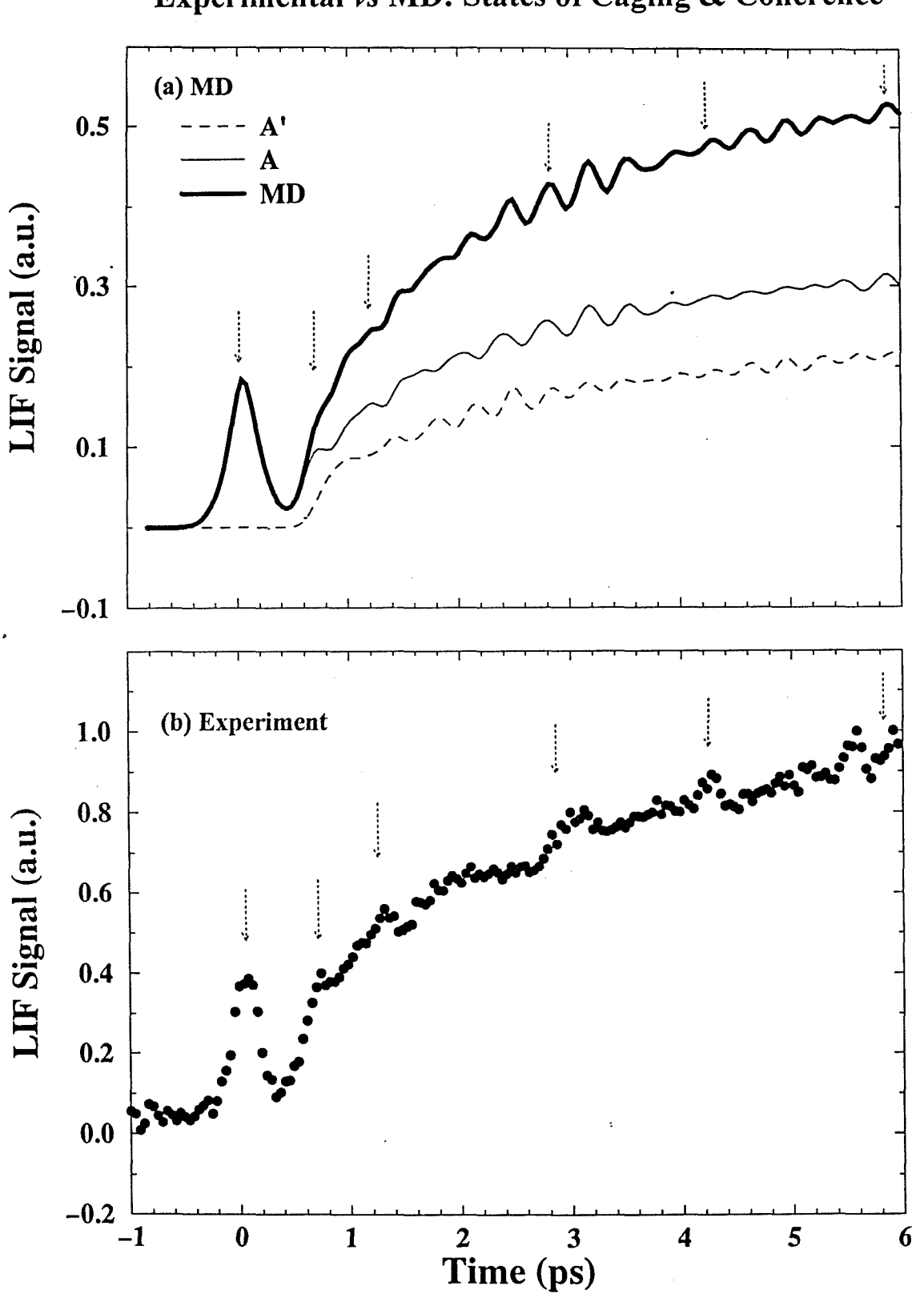
Experimental *vs* MD: States of Caging & Coherence
(a) MD
A'
A
MD
LIF Signal (a.u.)
0.5
0.3
0.1
-0.1
(b) Experiment
LIF Signal (a.u.)
1.0
0.8
0.6
0.4
0.2
0.0
-0.2
-1
0
1
2
3
4
5
6
Time (ps)

Figure 11

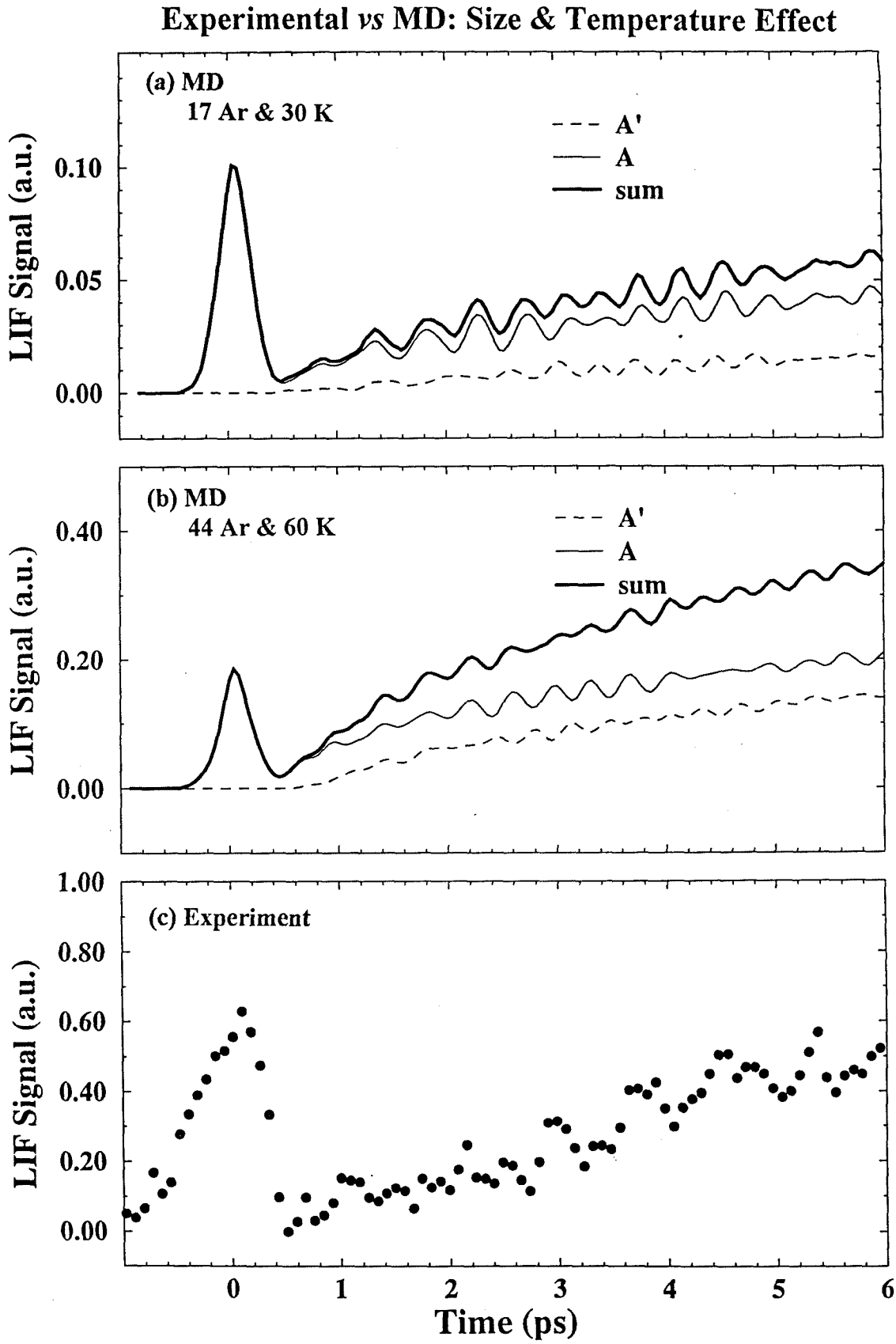
Experimental vs MD: Size & Temperature Effect
(a) MD
17 Ar & 30 K
A'
A
sum
LIF Signal (a.u.)
0.10
0.05
0.00
(b) MD
44 Ar & 60 K
A'
A
sum
LIF Signal (a.u.)
0.40
0.20
0.00
(c) Experiment
LIF Signal (a.u.)
1.00
0.80
0.60
0.40
0.20
0.00
0
1
2
3
4
5
6
Time (ps)

Figure 12

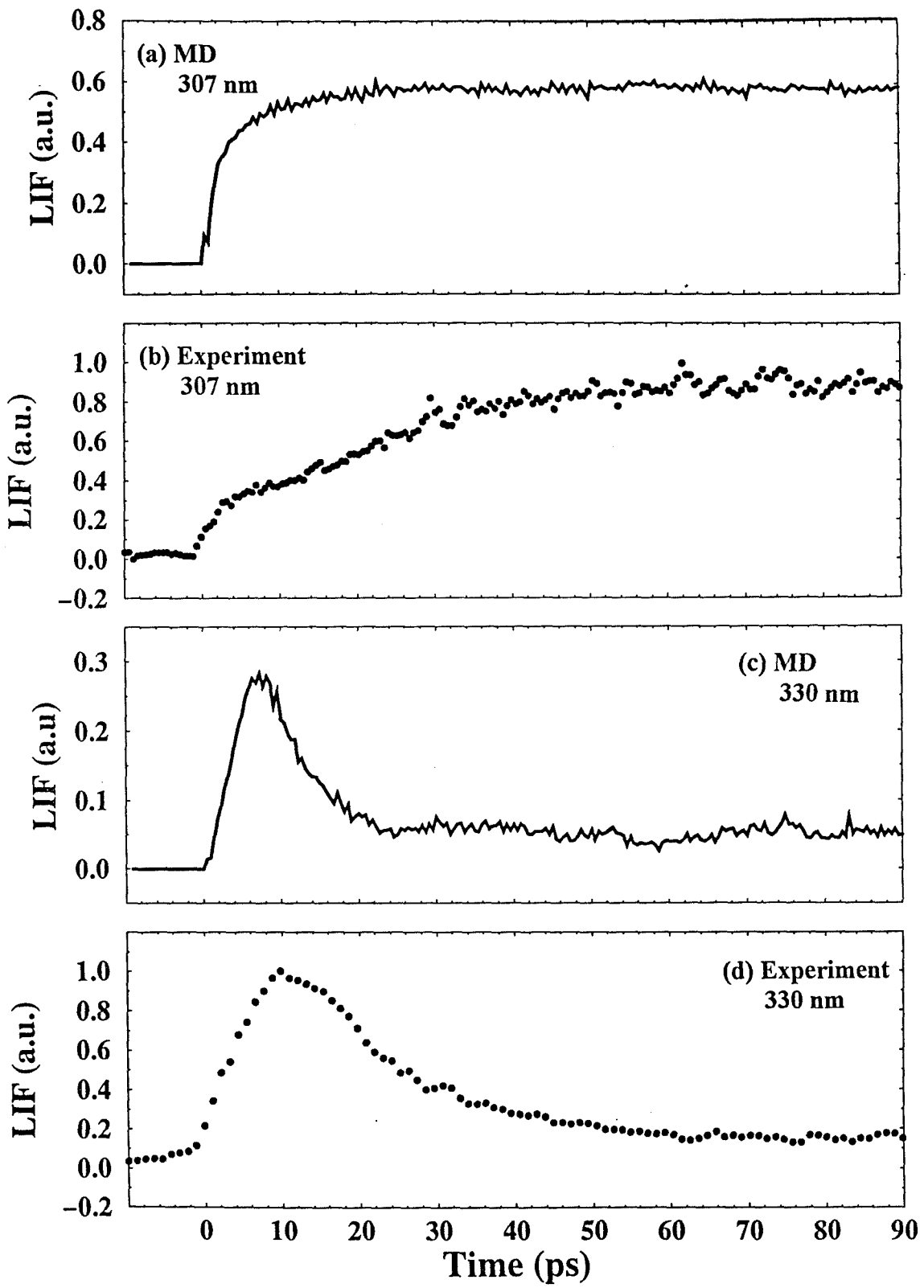
Experimental vs MD: Longer Time Scales
(a) MD
307 nm
(b) Experiment
307 nm
(c) MD
330 nm
(d) Experiment
330 nm
LIF (a.u.)
LIF (a.u)
Time (ps)
0.8
0.6
0.4
0.2
0.0
1.0
0.8
0.6
0.4
0.2
0.0
-0.2
0.3
0.2
0.1
0.0
1.0
0.8
0.6
0.4
0.2
0.0
-0.2
0
10
20
30
40
50
60
70
80
90

Figure 13

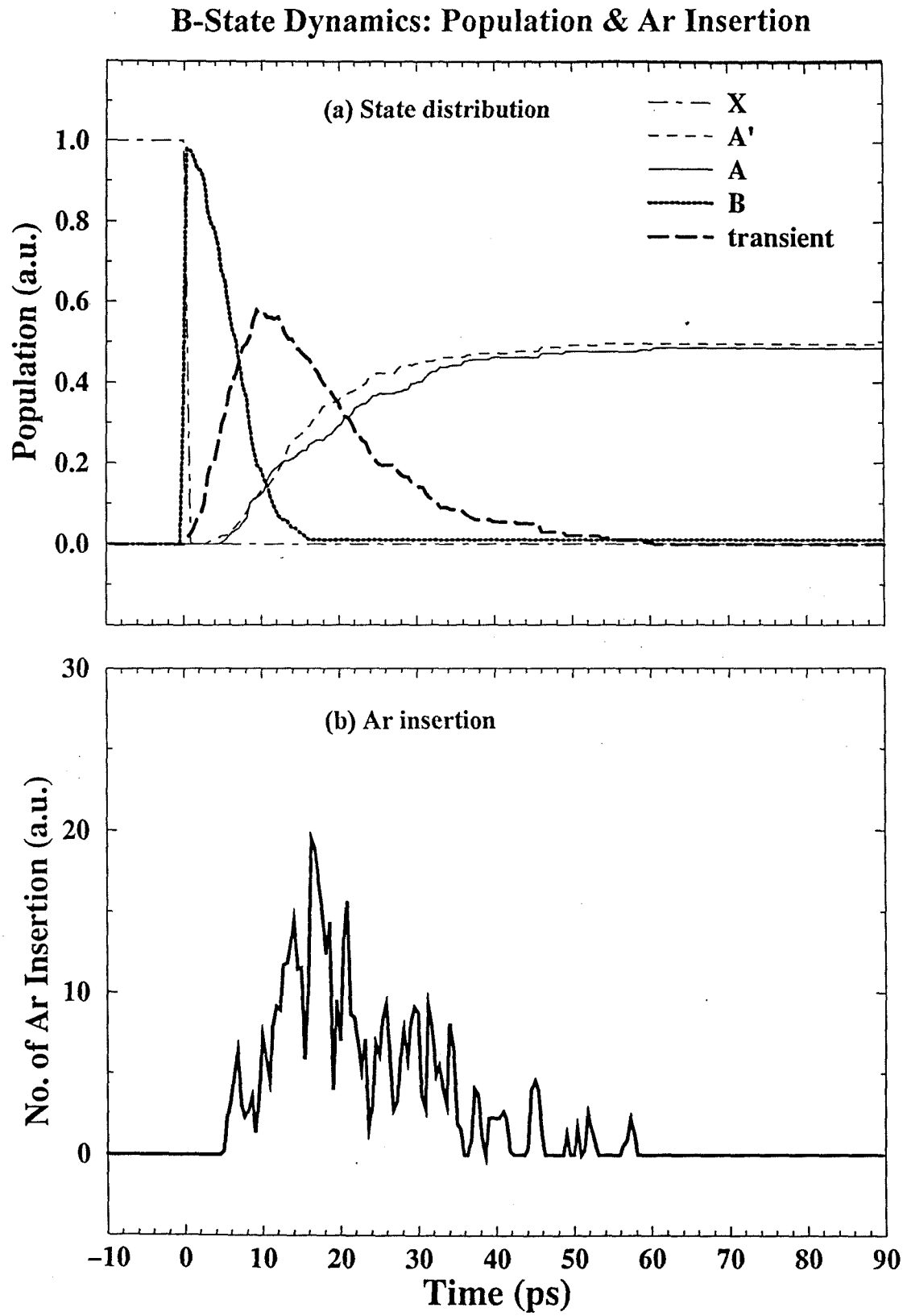
B-State Dynamics: Population & Ar Insertion
(a) State distribution
X
A'
A
B
transient
Population (a.u.)
1.0
0.8
0.6
0.4
0.2
0.0
(b) Ar insertion
No. of Ar Insertion (a.u.)
30
20
10
0
−10
0
10
20
30
40
50
60
70
80
90
Time (ps)

Figure 14

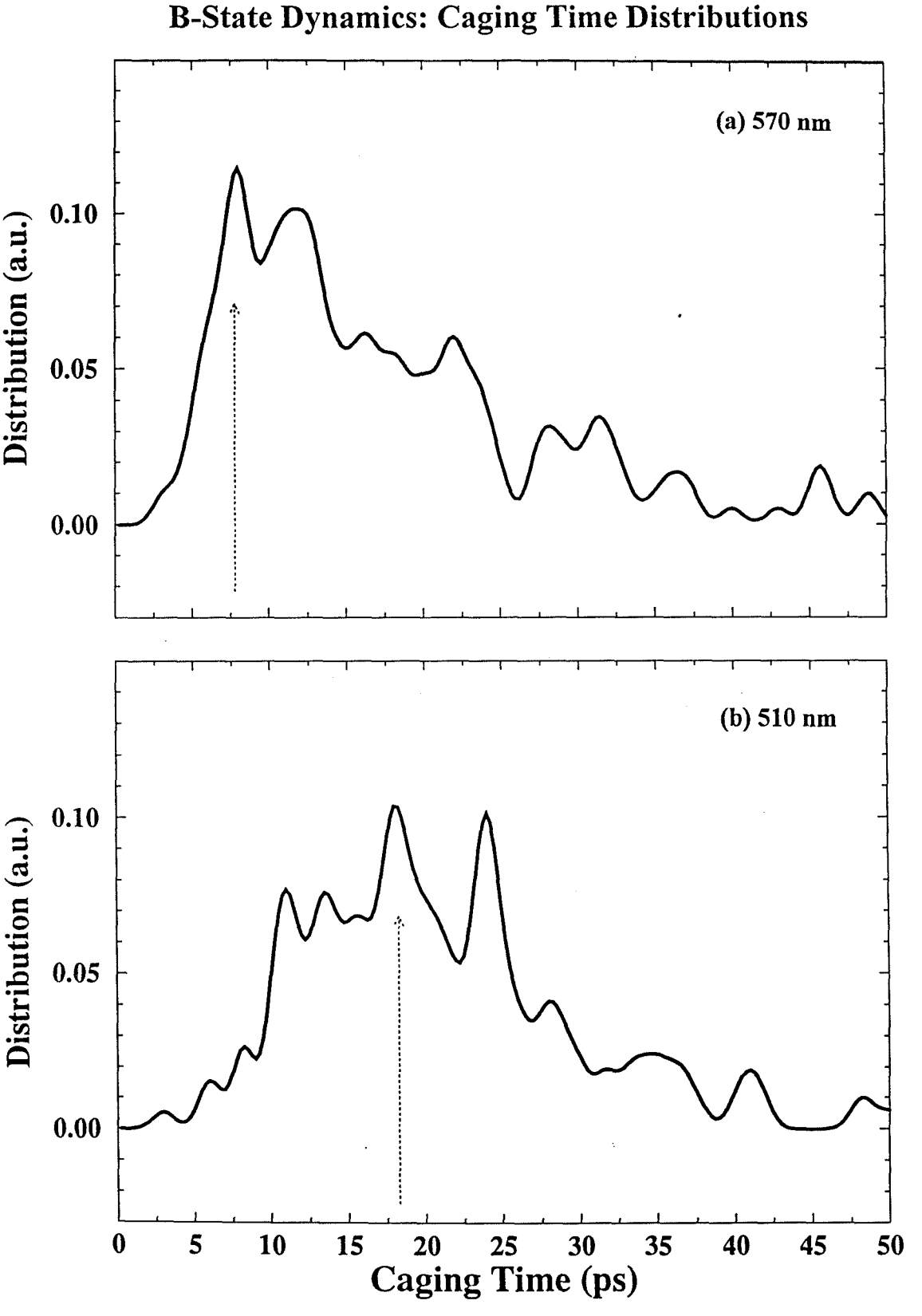
B-State Dynamics: Caging Time Distributions
(a) 570 nm
(b) 510 nm
Distribution (a.u.)
0.10
0.05
0.00
0
5
10
15
20
25
30
35
40
45
50
Caging Time (ps)

Figure 15

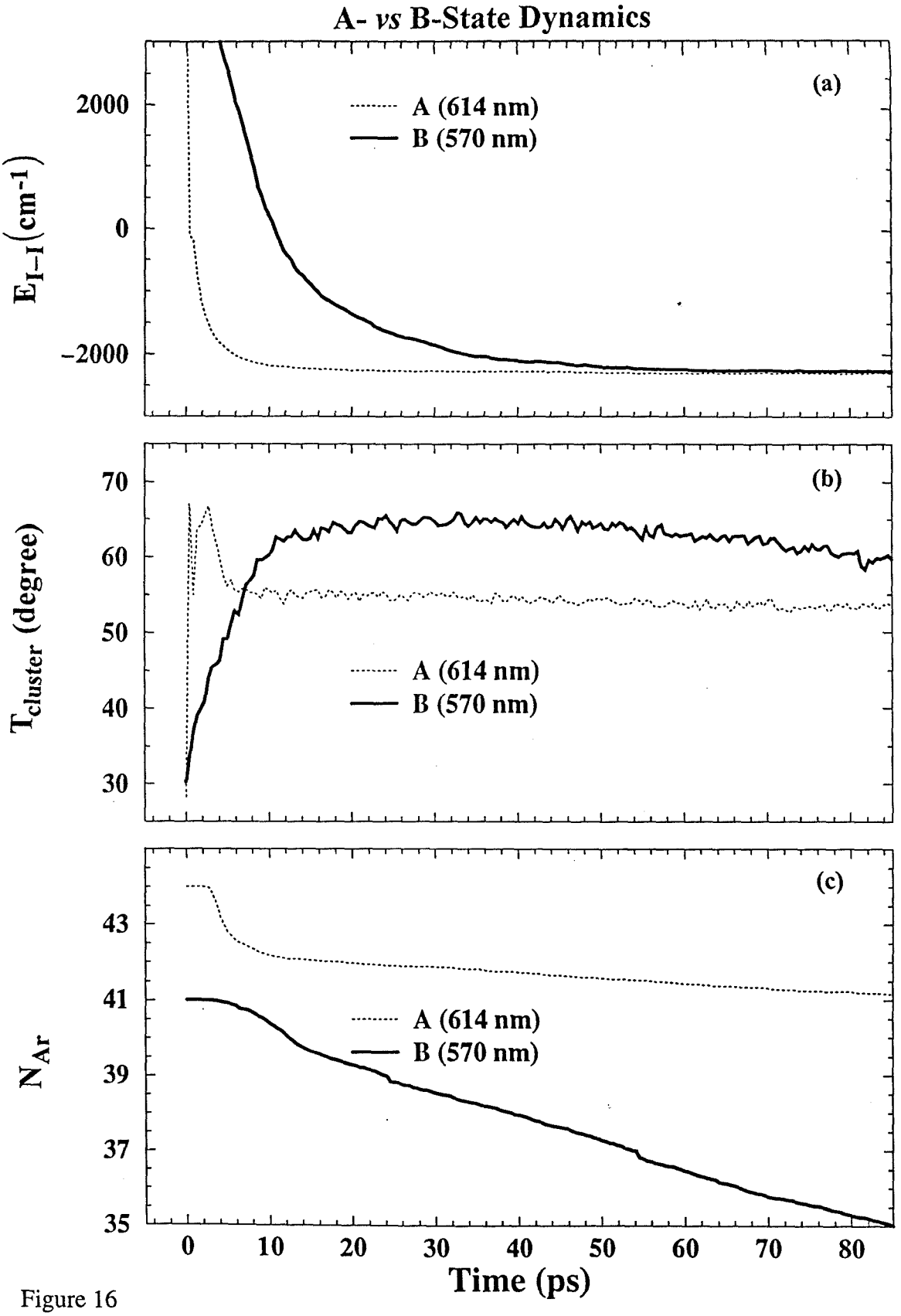
A- vs B-State Dynamics
(a)
A (614 nm)
B (570 nm)
2000
0
-2000
$E_{I-I}(cm^{-1})$
(b)
A (614 nm)
B (570 nm)
70
60
50
40
30
$T_{cluster}$ (degree)
(c)
A (614 nm)
B (570 nm)
43
41
39
37
35
N_{Ar}
0
10
20
30
40
50
60
70
80
Time (ps)

Figure 16

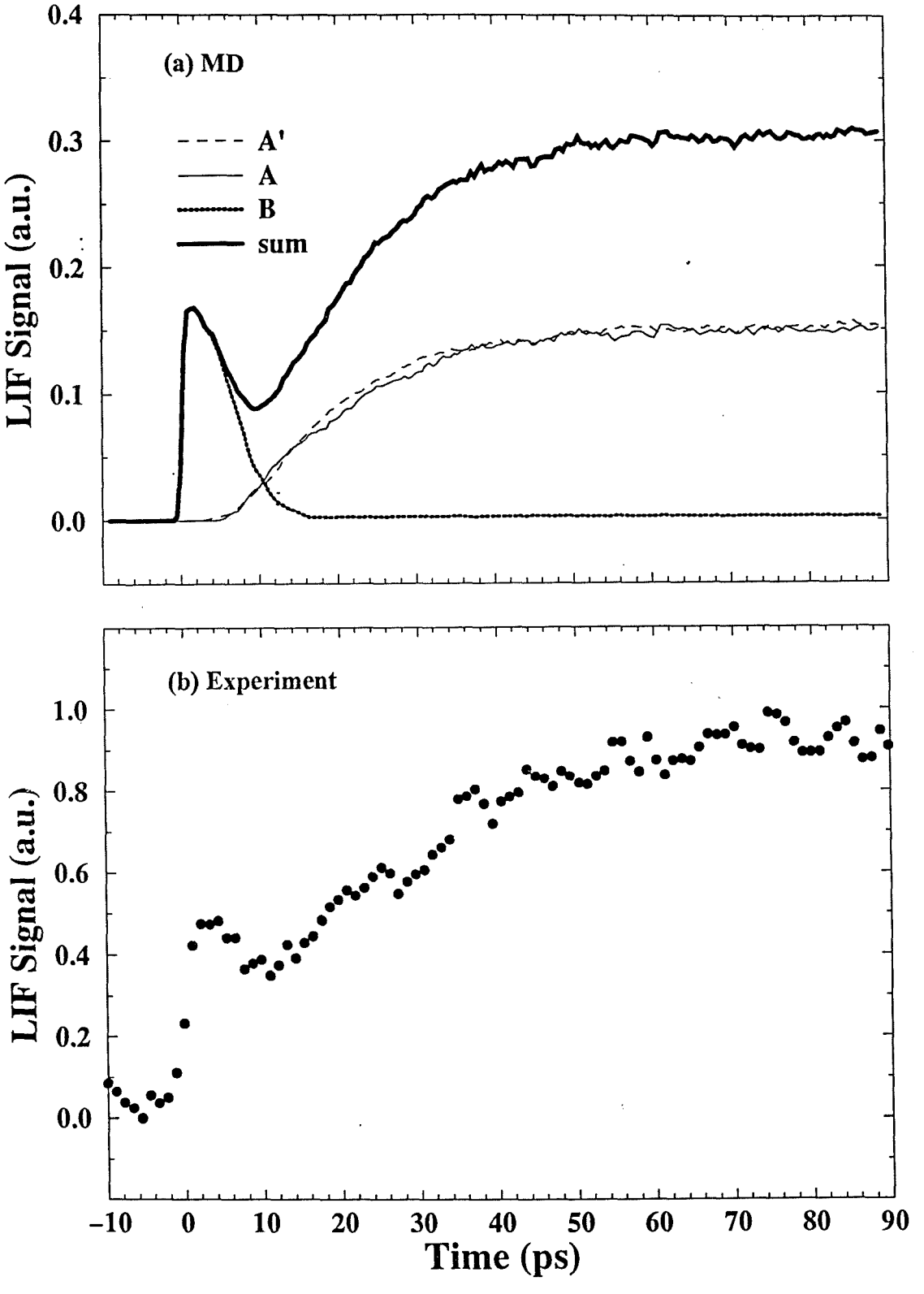
B-State Dynamics: Experimental vs MD
(a) MD
A'
A
B
sum
LIF Signal (a.u.)
0.4
0.3
0.2
0.1
0.0
(b) Experiment
LIF Signal (a.u.)
1.0
0.8
0.6
0.4
0.2
0.0
-10
0
10
20
30
40
50
60
70
80
90
Time (ps)

Figure 17

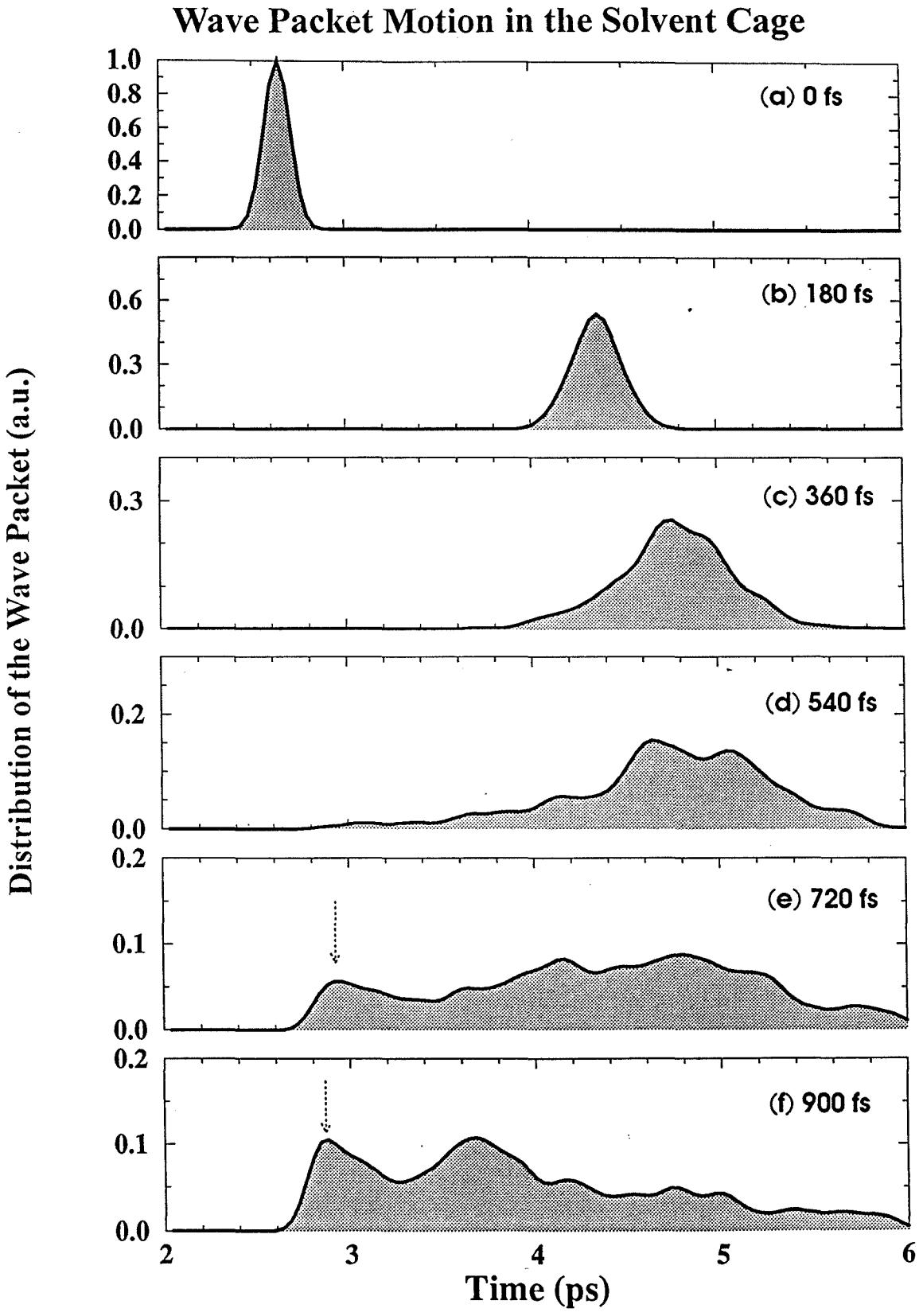
Wave Packet Motion in the Solvent Cage
Distribution of the Wave Packet (a.u.)
(a) 0 fs
(b) 180 fs
(c) 360 fs
(d) 540 fs
(e) 720 fs
(f) 900 fs
Time (ps)

Figure 18

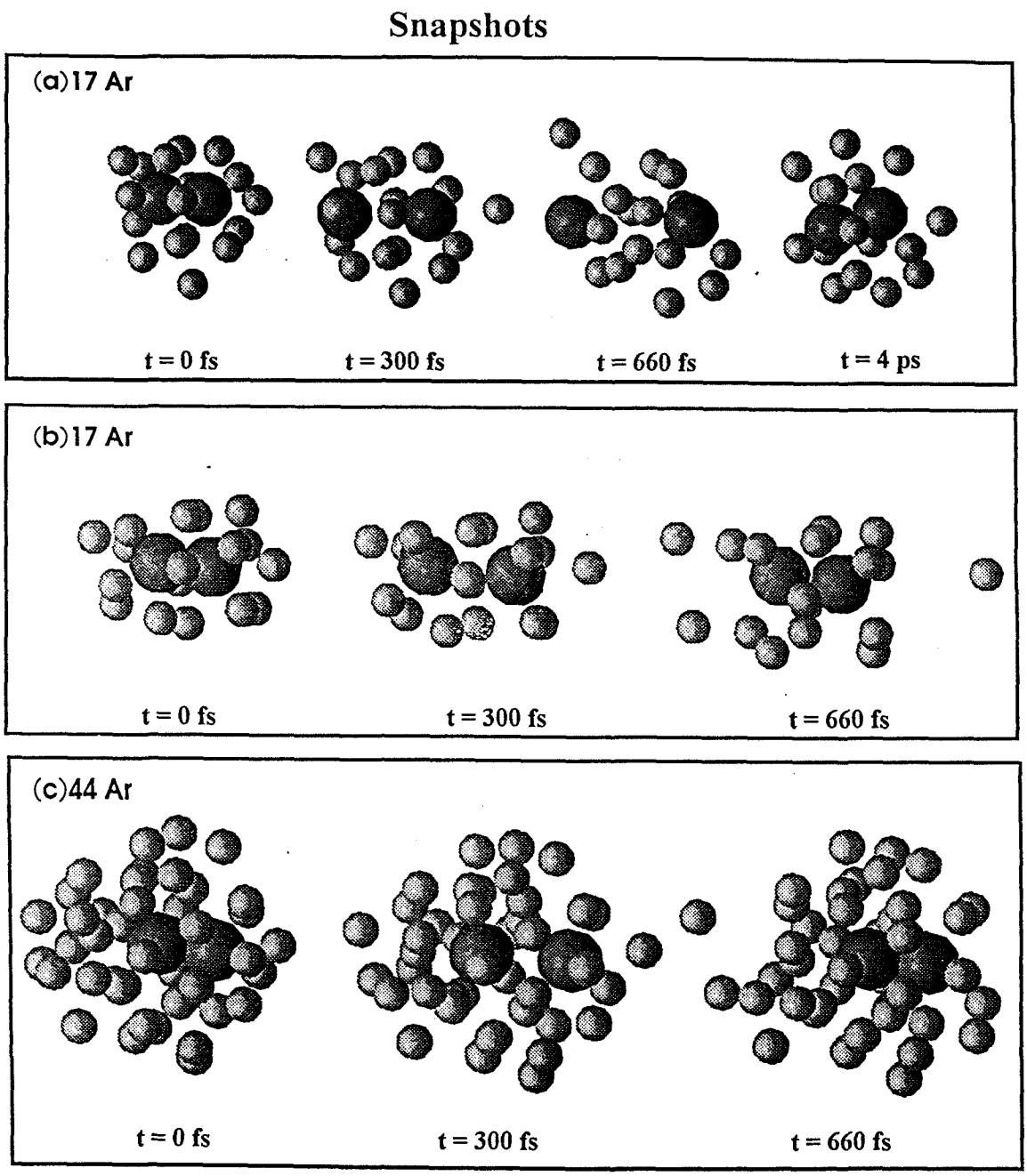
Snapshots
(a)17 Ar
t = 0 fs
t = 300 fs
t = 660 fs
t = 4 ps
(b)17 Ar
t = 0 fs
t = 300 fs
t = 660 fs
(c)44 Ar
t = 0 fs
t = 300 fs
t = 660 fs

Figure 19